Compact Pin-Cathode S-band Gun

Dissertation
zur Erlangung des Doktorgrades
an der Fakultät fär Mathematik, Informatik
und Naturwissenschaften
Fachbereich Physik
der Universitt Hamburg

vorgelegt von
Reza Bazrafshan

Hamburg
2023

Hiermit erkläre ich an Eides statt, dass ich die vorliegende Dissertationsschrift selbst verfasst und keine anderen als die angegebenen Quellen und Hilfsmittel benutzt habe.

I hereby declare upon oath that I have written the present dissertation independently and have not used further resources and aids than those stated in the dissertation.

Hamburg, 20.06.2023

Ort, den | City, date

Unterschrift | Signature

Gutachter der Dissertation:	Prof. Dr. Franz X. Kärtner Dr. Klaus Flöttmann
Zusammensetzung der Prüfungskommission	Prof. Dr. Franz X. Kärtner Dr. Klaus Flöttmann Prof. Dr. Daniela Pfannkuche Prof. Dr. Wolfgang Hillert Dr. Seyedmoein Seyedfakhari
Vorsitzende der Prüfungskomission:	Prof. Dr. Daniela Pfannkuche
Datum der Disputation:	10.08.2023
Vorsitzender des Fach-Promotionsausschusses PHYSIK	Prof. Dr. Günter H. W. Sigl
Leiter des Fachbereichs PHYSIK:	Prof. Dr. Wolfgang J. Parak
Dekan der Fakultät MIN:	Prof. Dr.-Ing. Norbert Ritter

Meiner ganzen Familie und geliebte Marziyeh.

Abstract

S-band RF-guns are highly developed for producing low emittance relativistic electron bunches, but require powerful klystrons for driving. Here, I present the design and first experimental tests of a compact S-band gun that is capable of accelerating electrons up to 180 keV powered by only 10 kW peak power using a compact rack-mountable solid-state amplifier. A pin-shaped cathode with a flat 0.8 mm diameter tip is used to produce an extraction field strength of 100 MV/m as in large-scale S-band guns. The compact gun will serve two purposes: (i) it can be used directly for ultrafast electron diffraction (UED); (ii) as an injector into a THz accelerator (AXSIS) consisting of a THz booster of electron bunches from 0.3 MeV to 2 MeV and a THz linear accelerator generating 20 MeV. For ultrafast electron diffraction (UED) applications, the compact portable electron source can generate a high-brightness electron beam with a temporal resolution of 10 fs, a spatial emittance of 0.1 mm-mrad, and a transverse coherence length of 2.0 nm for 10 fC bunch charge, which are essential beam parameters for achieving nm-fs space-time resolution with this technique. Multipacting, one of the experimental challenges in this RF gun, was studied through three-dimensional numerical simulations as well as by systematic measurements, resulting in an excellent correlation between simulations and experiments. In this thesis I describe the progress in the construction and characterization of this elegant and compact solution to achieving relativistic electron beams in an RF-photogun and provide an outlook for exciting prospects in structural dynamics experiments.

Zusammenfassung

Moderne S-Band-HF-Guns sind für die Erzeugung von relativistischen Elektronenpaketen mit geringer Emittanz optimiert, dieses erfordert jedoch die Verwendung von hochleistungs Klystrons als HF-Quelle. In dieser Arbeit stelle ich das Design und die ersten experimentellen Tests einer kompakten S-Band-Gun vor.

Die vorgestellte S-Band-Gun basiert auf einem kompakten Halbleiter-Verstärker mit einer Spitzenleistung von nur 10 kW und beschleunigt Elektronen auf bis zu 180 keV. Eine stiftförmige Kathode mit einer flachen Spitze von 0,8 mm Durchmesser wird verwendet, um eine Extraktionsfeldstärke von 100 MV/m zu erzeugen, die ebenbürtig mit konventionellen und deutlich größeren S-Band-Guns ist. Die kompakte Gun wurde für zwei Anwendungsfälle designt: (i) sie kann direkt für die ultraschnelle Elektronenbeugung (UED) verwendet werden; (ii) als Injektor für einen THz-Beschleuniger (AXSIS), bestehend aus einem THz-Booster der Elektronenpakete von 0,3 MeV bis 2 MeV und einem THz-Linearbeschleuniger, der 20 MeV erzeugt. Für die Anwendung der ultraschnellen Elektronenbeugung (UED) kann die kompakte Elektronenquelle einen sehr hellen Elektronenstrahl mit einer zeitlichen Auflösung von 10 fs und einer räumlichen Emittanz von 0,1 mm-mrad sowie einer transversalen Kohärenzlänge von 2,0 nm für eine 10 fC-Elektronenpuls erzeugen, was wesentliche Strahlparameter sind, um mit dieser Technik eine nm-fs-Raum-Zeit-Auflösung zu erreichen. Das Multipacting, eine der experimentellen Herausforderungen bei dieser RF-Gun, wurde durch dreidimensionale numerische Simulationen sowie durch systematische Messungen untersucht, was zu einer hervorragenden Korrelation zwischen Simulationen und Experimenten führte. In dieser Arbeit beschreibe ich die Fortschritte bei der Konstruktion und Charakterisierung dieses eleganten und kompakten RF-Photogun und gebe einen Ausblick auf spannende Perspektiven für Experimente zur Strukturdynamik.

Contents

Chapter 1

Introduction

A photocathode RF gun is a crucial component used in particle accelerators to generate high-quality, high-brightness electron beams. It combines principles from both radiofrequency (RF) technology and photoemission to produce a beam of electrons that can be accelerated to high energies. The operation of a photocathode RF gun begins with the illumination of the photocathode surface by a high-power laser pulse. The laser photons transfer their energy to the electrons within the photocathode material, exciting them and providing sufficient energy to overcome the material's work function. The photocathode is typically made of a semiconducting material, such as cesium telluride or gallium arsenide, which has a low electron affinity [1].

To enhance the beam quality and control its characteristics, the photocathode RF gun incorporates an RF cavity. This cavity is typically a resonant structure that operates at microwave frequencies, usually in the range of a few gigahertz. The RF cavity functions by creating a series of electromagnetic waves that propagate along its length and interact with the electron beam, providing both acceleration and focusing. By carefully controlling the shape and intensity of the RF fields within

the cavity, the beam's energy, bunching, and emittance (a measure of the beam's spread in position and momentum) can be optimized [2].

Photocathode RF guns have evolved over several decades, and their development has been influenced by advancements in accelerator technology and materials science. The first successful demonstration of a RF gun using a metal photocathode was reported at Stanford University in 1979 [3], since then, numerous research groups worldwide have made significant contributions to the field. Recent advancements have focused on developing ultrafast photocathodes that can produce electron beams with extremely short bunch durations, on the order of femtoseconds. These ultrafast beams have enabled novel applications in ultrafast electron diffraction and microscopy. The advancements in laser technology, photocathode materials, cooling techniques, and beam optimization have significantly improved the performance and capabilities of these devices, opening up new possibilities in various fields of research and technology.

The concept of the AXSIS project at the Deutsches Elektronen-Synchrotron (DESY) is the development of a compact X-ray light source which aims to develop a fully THz-powered electron accelerator to serve not only as a source of ultrashort electrons for direct application to ultrafast electron diffractometry, but also for generation of ultrashort pulses of X-rays for pushing the limits of temporal resolution to the attosecond regime [4].

Although the final AXSIS machine is expected to be powered exclusively by THz radiation, intermediate phases may resort to radio-frequencies (RF), i.e. 3 GHz devices which are powered by a rack-mountable RF power supply. In this concept, electrons sourced by photoemission from a 180 keV compact RF gun are first accelerated in a THz-powered booster to the 832 keV level, and subsequently accelerated to the 20 MeV level in a THz-powered LINAC. The electrons are then transported and focused to overlap with the focus of a counter-propagating laser to produce X-rays by inverse-Compton scattering (ICS) [5].

Ultrafast electron diffraction (UED) also known as femtosecond electron diffraction (FED) has become an important tool for probing atomic-scale structure due to the orders-of-magnitude higher interaction cross sections and orders-of-magnitude lower damage per scattering event relative to X-ray diffraction [6]. In addition, electron probes provide increased sensitivity to hydrogen atoms, which are of fundamental importance for understanding biological [7]. These properties, in

conjunction with a significantly lower fabrication cost than comparable X-ray sources, make electron sources highly attractive for ultrafast atomic-scale research.

Traditionally, UED sources are inexpensive, static voltage DC photoelectron guns capable of delivering high-coherence electron bunches with energies typically in the range of 50 – 100 keV. The space charge, however, causes a rapid spatial and temporal expansion of the electron beam in this range of energy, resulting in a decrease in the brightness and temporal resolution of the UED system [8]. An alternative to DC fields for the purpose of rapid acceleration of charged particles to high energies is the application of rf-fields in normal or superconducting cavities which are commonly used for the acceleration of electrons to energies ranging up to the MeV level. The propagation speed of rf waves within these constrained dimensions leads to the fast alternating character of the fields, with frequencies typically ranging in the GHz range.

However, multi-MeV RF guns, typically driven by klystrons, require a level of cost and infrastructure not accessible to the majority of small, university-scale labs. Here, we propose an intermediate solution between the DC-gun and RF-gun technologies which is still low cost and requires low levels of infrastructure, but significantly increases electron energies beyond what is typically feasible with DC guns: a compact RF gun driven by a low-average-power solid-state amplifier which harnesses field-enhancement at a pin-shaped photocathode to increase field strengths, electron energies and hence bunch quality [9]. We will describe the concept and design of this RF gun in Chapter 2, followed by a discussion of the performance of the first prototype in Chapter 3.

High space charge forces rapidly degrade beam quality due to the high peak current and extremely low velocity of the electron bunches after emission from the photocathode. Thus, a high acceleration field at the cathode is of great importance for reaching a high electron beam quality. By using three-dimensionally shaped laser pulses with a well-defined profile, the beam quality can be further optimized. By optimizing the initial electron distribution, it is possible to minimize the expansion and non-linearity of the electron bunch in the phase space. Under the influence of the RF and solenoid fields as well as the space charge force, the initial profile of the beam is modified after it has been extracted from the cathode. An analysis of the electron beam dynamics after extraction from the cathode can be conducted analytically [10] or numerically using simulation codes such as ASTRA [11]. In chapter 4, comprehensive simulations are presented on beam dynamics in

the RF gun and the effect of the laser beam's transverse and longitudinal shape on electron bunch characteristics.

Because of the strong accelerating field in the cavity, electrons may be field-emitted from the copper cavity surface and the photocathode. Dust on the front surface of the cathode may be a strong field emitter as well, resulting in increased dark current. The dark current at the gun may be accelerated together with the electron bunch, therefore it is necessary to investigate the dynamics of the dark current. The amount of dark current can be reduced with rf conditioning [12].

Multipacting peaks are evident during the operation of a gun, and their magnitude depends heavily on the solenoid field profile [13]. For multipacting to be controlled, the point at which multipacting occurs and the multiplication process must be identified. A detailed simulation and experimental study of multipacting is presented in chapters 5 and 6. A specific application of the RF gun for UED will be discussed in chapter 7, together with the UED test setup, beam dynamics, and the latest practical results.

Chapter 2

Compact RF Gun, Prototype I

2.1 RF Gun Components

Photocathode RF guns have been proven to be an excellent electron source for very high-quality beams required for X-ray FELs and Ultrafast Electron Diffraction (UED) [14]. Electron beams are generated in photocathode RF guns by excitation laser pulses and accelerated by the RF field immediately following their generation. Upon emission from the photocathode, electron bunches have a very high intensity and velocity close to zero, resulting in a degradation of beam quality due to high space charge forces. It is therefore extremely important to provide a high accelerating field at the cathode in order to obtain a high quality electron beam.

Further optimization of beam quality may be achieved through the use of three-dimensionally shaped laser pulses with well-defined profiles [15]. With the optimized initial electron distribution, the expansion and nonlinearity of the electron bunch in phase space can be minimized. Under the influence of the RF and the solenoid fields as well as the force of the space charge, the initial profile of the beam is modified after extraction from the cathode.

Field emission from the copper surface of the cavity and from the photocathode is possible due to the strong accelerating field within the cavity. It is also possible that dust present on the front surface of the cathode may act as a strong field emitter, thereby increasing the dark charge. Dark charge at the gun can be accelerated

together with the electron bunch, thus the dark charge dynamics must be investigated. During gun operation, multipacting phenomena are found at the beginning and/or at the end of the RF pulse. There are several factors that affect multipacing, including the solenoid field profile, cavity geometry, and the cleanliness of the surface. The amount of dark charge and multipacting can be reduced by careful conditioning of the gun.

2.1.1 Half-Cell Pillbox RF Cavity

A cavity resonator is a closed metal structure that confines electromagnetic fields in the range of electromagnetic spectrum. As part of the design of a radio frequency cavity for the compact RF gun, it is important to consider a number of factors such as the operating frequency, the quality factor, tuning, the accelerating electric field, etc. These parameters will affect the dynamics of the electron beam, which plays an important role in the design of the cavity.

In Figure 2.1 and Figure 2.2, the geometry of the compact gun cavity is illustrated with the electric field distribution. Electrons emitted from the photocathode are accelerated in a half-cell copper cavity. RF input couplers transfer radio frequency power from the Amplifier (through a coaxial waveguide) to the cavity at a resonance frequency of 2.998 GHz. It has been designed to avoid dipoles and higher order fields in the gun cavity (or sufficiently far from the main resonance frequency) by ensuring perfect cylindrical symmetry of the cavity and coupler components. The asymmetry of the RF field may result in an increase in beam emittance [16].

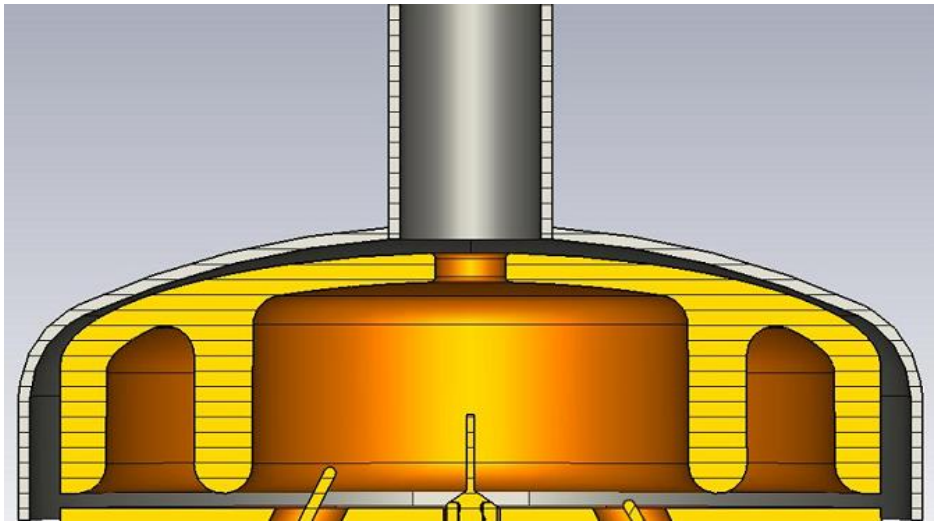

Figure 2.1: Cross sectional view of the cavity with its input and pick-up antennas.

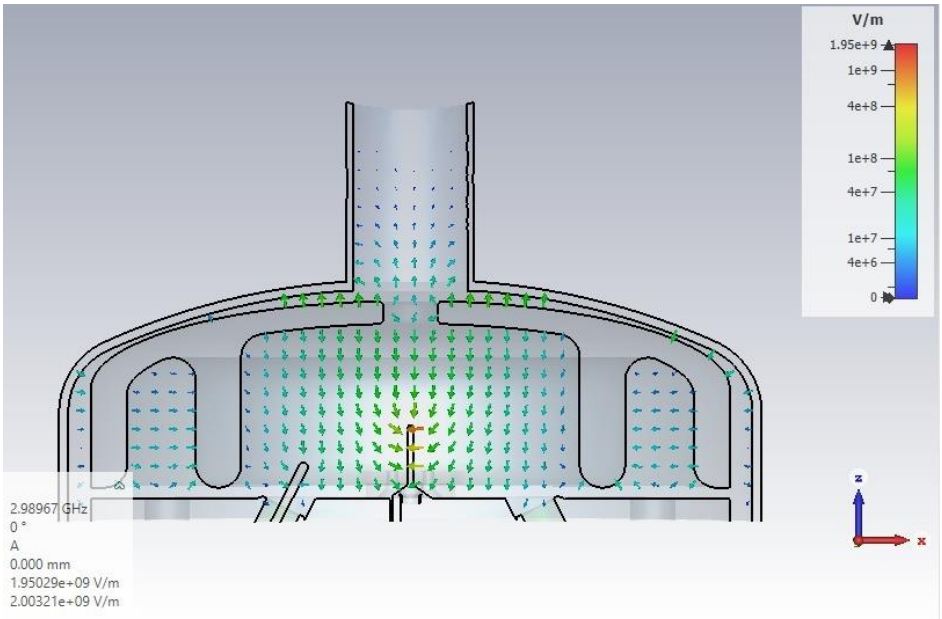

Figure 2.2: The electric field distribution in the cavity, fed by 1 Joule RF energy.

2.1.2 Resonator Theory

The fundamental concepts of waveguides and resonators must be briefly summarized in order to understand the behavior and functionality of the RF system. Based on Maxwell's equations, the wave equation for electric and magnetic fields can be derived [17]. Assuming $\nabla \cdot \mathbf{E} = 0$ (i.e. charge-free space and homogeneous dielectric), the wave equations are as follows:

$$\begin{aligned} \Delta\mathbf{E} - \frac{\epsilon_r \mu_r}{c^2} - \partial_t^2 \mathbf{E} = 0 \\ \Delta\mathbf{H} - \frac{\epsilon_r \mu_r}{c^2} \cdot \partial_t^2 \mathbf{B} = 0 \end{aligned} \tag{2.1}$$

The plane wave solution is also obtained by assuming free space and wave propagation in z direction.

$$E_\perp = E_0 \cdot \exp[i(\omega t - kz)] \tag{2.2}$$

where $k = \sqrt{\epsilon_r \mu_r} \cdot \omega / c$. The fact that $\partial_x = \partial_y = 0$ has been taken into consideration as well. As can be seen from the equation above, these plane waves have no electrical field components in the direction of propagation, which is a critical condition that is needed in order to accelerate particles successfully. It is

possible to avoid this problem by imposing proper boundary conditions, as described below.

First, let us consider boundary conditions that are characterized by metallic boundaries, as in rectangular waveguides, in order to find solutions that have non-zero longitudinal field components.

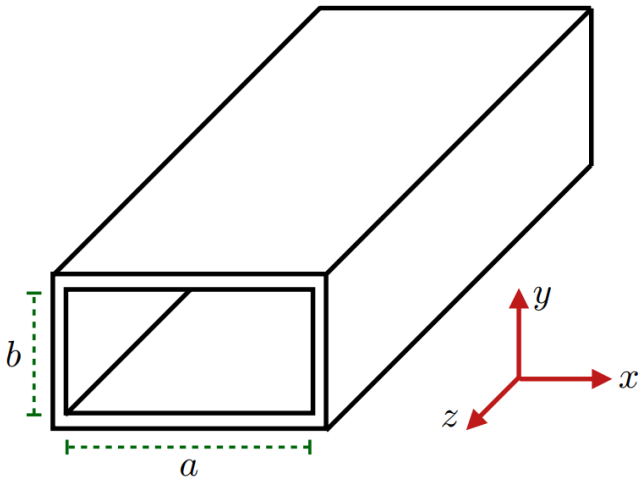

Figure 2.3: Schematic of a rectangular waveguide

Consider $E_z = F_x(x) \cdot F_y(y) \cdot F_z(z)$ as a non-zero function combination obeying equation (2.1). The wave equation can be written as follows:

$$\Delta E_z - \frac{\epsilon_r \mu_r}{c^2} \cdot \partial_t^2 E_z = 0$$

$$\nabla \begin{pmatrix} \partial_x F_x(x) \cdot F_y(y) \cdot F_z(z) \\ F_x(x) \cdot \partial_y F_y(y) \cdot F_z(z) \\ F_x(x) \cdot F_y(y) \cdot \partial_z F_z(z) \end{pmatrix} = -k^2 \big(F_x(x) \cdot F_y(y) \cdot F_z(z)\big) \qquad (2.3)$$

$$\frac{\partial_x^2 F_x(x)}{F_x(x)} + \frac{\partial_y^2 F_y(y)}{F_y(y)} + \frac{\partial_z^2 F_z(z)}{F_z(z)} = -k^2$$

Since k is constant, every term in the equation above must be constant as well, and therefore

$$k^2 \equiv k_x^2 + k_y^2 + k_z^2 \qquad (2.4)$$

With the definition ${k_c}^2 \equiv k_x^2 + k_y^2$ it follows that $k_z = \sqrt{k^2 - k_c^2}$. The phase velocity of the longitudinal electric field component can be expressed as follows:

$$v_{ph} = \frac{\omega}{k_z} = \frac{\omega}{\sqrt{k^2 - k_c^2}} \tag{2.5}$$

Clearly, if $k_c > k$, the phase velocity becomes imaginary, which leads to the phenomenon known as the evanescent wave, an exponentially decaying wave. It is for this reason that k_c is referred to as the cutoff wavenumber. Let us now try to relate the cut-off wavenumber to geometrical properties of a rectangular waveguide with metallic boundaries (see Figure 2.3). Having metallic boundaries leads to the condition that the tangential components of the electric field must vanish. Thus only cosine functions can be correct solutions for $F_x(x)$ and $F_y(y)$. The final solution for the longitudinal electric field is now given by

$$E_z = E_0 \cos\left(\frac{m\pi x}{a}\right) \cos\left(\frac{n\pi y}{b}\right) \exp[i(\omega t - k_z z)] \tag{2.6}$$

Where $m, n \in \mathbb{N}$ define the so called transverse field modes (since the system is now subject to boundary conditions, only discrete solutions are allowed). For the magnetic field component, the solution is as follows:

$$B_z = B_0 \sin\left(\frac{m\pi x}{a}\right) \sin\left(\frac{n\pi y}{b}\right) \exp[i(\omega t - k_z z)]. \tag{2.7}$$

Having found these solutions and recalling that ${k_c}^2 \equiv k_x^2 + k_y^2$, it can now be seen that

$$k_c = \sqrt{\left(\frac{m\pi}{a}\right)^2 + \left(\frac{n\pi}{b}\right)^2} \tag{2.8}$$

which can be used to determine the cut-off frequency (or wavelength) of a particular waveguide mode. Using the wave equation (2.1) and the solutions (2.6) and (2.7), it is possible to write down E_x and E_y in terms of E_z. Inserting the solutions we get:

$$\begin{aligned} E_x &= i\left(k_z\, \partial_x E_z + c k_0\, \partial_y B_z\right)/(k_z^2 - k^2) \\ E_y &= i\left(k_z\, \partial_y E_z - c k_0\, \partial_x B_z\right)/(k_z^2 - k^2) \\ B_x &= i\left(c k_z\, \partial_x B_z - \epsilon\mu k_0\, \partial_y E_z\right)/c(k_z^2 - k^2) \\ B_y &= i\left(c k_z\, \partial_y B_z + \epsilon\mu k_0\, \partial_x E_z\right)/c(k_z^2 - k^2) \end{aligned} \tag{2.9}$$

Where $k_0 = \omega/c$ is the vacuum wavenumber. Looking at equation (7.1) three fundamental classes of field configurations can be distinguished:

(1) $E_z = 0$ $\quad$ TE_{mn}-modes (transverse electric)

(2) $B_z = 0$ TM_{mn}-modes (transverse magnetic)

(3) $E_z = B_z = 0$ TEM_{mn}-modes (transverse electromagnetic)

Since $E_z = 0$ for TE- and TEM-modes, it is clear that the most important modes for particle acceleration are TM-modes. The indices m, n can be understood physically as the number of half-wavelengths along the *x*- and *y*-axis respectively. From equation (2.6) it follows that the lowest TM-mode is the TM_{11} mode. Every waveguide has a so called *dominant mode*. The dominant mode is the mode with the smallest cut-off frequency, or in other words the mode which supports the broadest range of frequencies. There is another important quantity that needs to be considered for waveguides, and that is the waveguide wavelength λ_g. Giving the usual definition of $\lambda = 2\pi/k$, we get:

$$\lambda_g = \frac{2\pi}{k_z} = \frac{2\pi}{\sqrt{k^2 - k_c^2}} \tag{2.10}$$

It is important to note that $\lambda_g > \lambda$, where λ is the wavelength of free space.

Since electrons are accelerated at the compact RF gun using a standing-wave half-cell RF cavity, it is useful to quickly review the waveguide quantities that have been derived above for cylindrical waveguides. In order to derive these properties, it makes sense to switch to cylindrical coordinates. The wave equation for the z-component in cylindrical coordinates is given by

$$\partial_r^2 E_z + \frac{\partial_r E_z}{r} + \frac{\partial_\phi^2 E_z}{r^2} + \partial_z^2 E_z + \frac{\epsilon_r \mu_r}{c^2} E_z = 0. \tag{2.11}$$

The solution of the equation can be found using Bessel's functions of the first kind $J_\alpha(x)$ in integer order (cylindrical symmetry):

$$E_z = E_0 J_m(k_c r)\exp[i(\omega t - m\phi - k_z z)] \tag{2.12}$$

The boundary condition of the waveguide is $E_z = 0$ because of the metallic surfaces. Looking at the solution, it is clear that in order to satisfy this condition at all times, it is necessary to find the roots of the Bessel functions $J_\alpha(k_c a)$, where a is the radius of the waveguide pipe. Moreover, the cut-off wavenumber now depends on the radius of the waveguide in such a way that waves with wavelengths smaller than the pipe diameter cannot be guided. For TM modes, the cut-off wavenumber is now defined as

$$k_c = \frac{j_{\alpha,\beta}}{a} \tag{2.13}$$

where $j_{\alpha,\beta}$ is the β-th root of the Bessel function of the first kind of order α. Accordingly, the cylindrical waveguide modes are now referred to as $\mathrm{TE}_{\alpha,\beta}$ and $\mathrm{TM}_{\alpha,\beta}$. Physically the two indices describe the number of half-wavelengths along one half-circumference (α) and the radius (β) respectively.

In both rectangular and cylindrical waveguides, the phase velocity vph exceeds the speed of light, so neither structure is suitable for particle acceleration since the wave would overrun the particles. One way to overcome this problem is to use standing waves in a cylindrical RF cavity (or pillbox cavity). The simplest cavity resonator would be a waveguide with a short circuit termination at each end. Ideally, the walls would be perfect conductors, which leads to the boundary conditions that have also been discussed above: Electric field lines are perpendicular to the walls, and magnetic field lines are parallel to the walls.

If $L = p \cdot \lambda_g/2$, where L is the cavity length, $p \in \mathbb{N}$ and λ_g the guide wavelength as defined in equation (2.10) the condition for standing waves is fulfilled. Due to the fact that the system is now bounded in the z-direction, an additional index is added to the mode specification. In the case of a cylindrical cavity, the modes are now referred to as $\mathrm{TE}_{\alpha\beta p}$and $\mathrm{TM}_{\alpha\beta p}$. All of the modes are now characterized by their azimuthal (α), radial (β) and longitudinal (p) field configurations. In accelerator physics the usual nomenclature for azimuthal modes is monopol ($\alpha = 0$), dipole ($\alpha = 1$), quadrupole ($\alpha = 2$), and so on ([18]).

TM modes of a cylindrical single-cell cavity can now be calculated in the following way. Noticing that

$$\lambda_g = \frac{2L}{p} = \frac{2\pi}{\sqrt{k_r^2 - k_c^2}} \tag{2.14}$$

Using equation (2.10), it is possible to find k_r, which is the wavenumber that fulfills the resonance condition:

$$k_r^2 = \frac{\pi^2 p^2}{L^2} + k_c^2 \tag{2.15}$$

Inserting equation (2.13) yields

$$f_r = \frac{c}{2\pi} \cdot \sqrt{\frac{j_{\alpha\beta}^2}{a^2} + \frac{\pi^2 p^2}{L^2}} \tag{2.16}$$

In TM-modes, $p = 0$ is the special case where E_z does not exhibit longitudinal dependence. Consequently, the resonant frequency - in this case - is independent of the cavity length. Therefore, in this particular case

$$f_r(\mathrm{TM}_{\alpha\beta 0}) = \frac{c}{2\pi} \cdot \sqrt{\frac{j_{\alpha\beta}^2}{a^2}} \tag{2.17}$$

The lowest monopole mode is called the *fundamental mode* and in the case of a cylindrical single-cell cavity, it is the TM_{010} mode (see figure 2.4). Setting $\alpha = 0$, $\beta = 1$ and $p = 0$, the resonant frequency of this mode can readily be computed using equation (2.16) and $j_{0,1} = 2.4048$:

$$f_r(\mathrm{TM}_{010}) = \frac{c}{2\pi} \cdot \frac{2.4048}{a}. \tag{2.18}$$

As a result, in order to construct a TM_{010} S-band resonator cavity, the radius of the cavity would need to be $a_{3\,GHz} = 3.83\,cm$. All other modes except for the fundamental mode are called HOMs, or *higher order modes*. It is not desirable to use these modes for particle acceleration since the azimuthal fields of these modes can result in particle deflection.

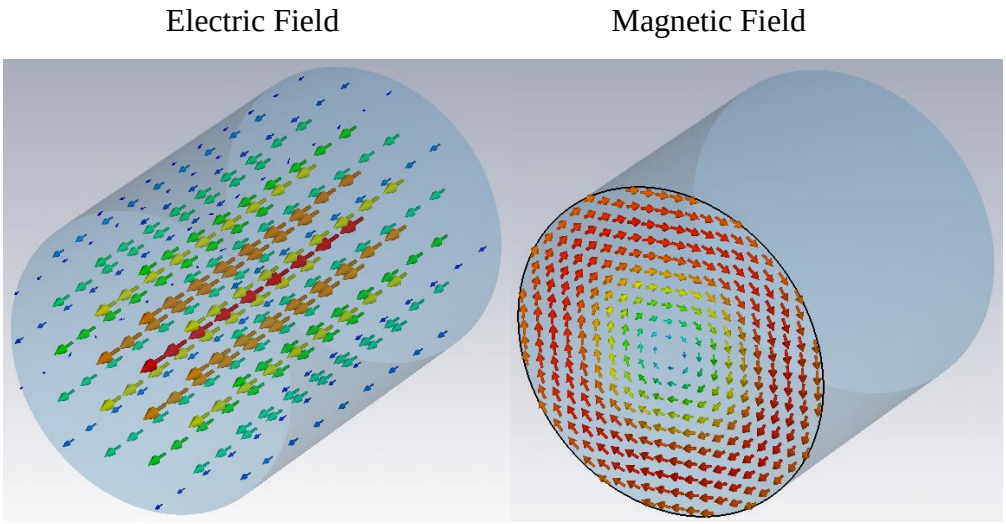

Figure 2.4: Simulation of the TM_{010} mode for a cylindrical single cell cavity.

As a follow-up to the introduction of waveguides and standing wave cavities, it appears useful to summarize a few key aspects of RF cavities. Power is dissipated from resistive losses in the walls of the cavity to maintain the fields. The figure of merit for stored energy U per unit power loss P_d in the cavity walls is the quality factor defined by

$$\mathrm{Q} = \omega \mathrm{U}/P_d. \tag{2.19}$$

But for accelerators we often want to maximize the energy gain per unit power dissipation. Our efficiency figure of merit measures how effective the cavity is in producing an axial electric field per unit power loss. One of the most important quantities is the so called *shunt impedance* expressing the effectiveness of producing an accelerating voltage for a given dissipated RF power P_d inside the cavity, which is defined as follows:

$$R = \frac{|\mathrm{V}|^2}{P_d} \tag{2.20}$$

where U_{acc} is the effective accelerating voltage and P_d is the power loss, or the dissipated power. The effective accelerating voltage is defined by

$$V = \int E_z(z) e^{i\frac{\omega}{\beta c}z} \mathrm{d}z \tag{2.21}$$

where $V_0 = E_0 \mathrm{L}$ is the peak axial voltage for a cavity of length L and average axial field E_0. i.e. the voltage a particle with velocity βc experiences during its transit through the cavity, subject to time variations of the field. Therefore the proportionality factor, which connects V with the time-independent accelerating voltage V_0 is called the *transit time* factor T_β. It is defined by

$$\mathrm{V} = T_\beta \cdot V_0 = \frac{\int E_z(z) e^{i\frac{\omega}{\beta c}z} \mathrm{d}z}{V_0} \cdot V_0 = \frac{\int E_z(z) e^{i\frac{\omega}{\beta c}z} \mathrm{d}z}{\int E_z(z) \mathrm{d}z} \cdot V_0. \tag{2.22}$$

As $E_z(z) = E_0$ is not a function of z in the TM_{010} mode, the transit time factor can be calculated by noticing that the integral in the numerator is now just a Fourier transform of a box function. If $z \in [-L/2, L/2]$, so

$$T_\beta(\mathrm{TM}_{010}) = \frac{\sin\left(\frac{L}{\beta\lambda}\right)}{\frac{L}{\beta\lambda}} \tag{2.23}$$

Where $\omega/\beta c = 2\pi/\beta\lambda$ has been used. The cavity length L must now be chosen according to the free space wavelength λ and β (hence the particle type), such that T_β is maximized, this is called β-matching.

The shunt impedance can be understood as the quantity that defines the efficiency of power transfer to the electron beam through $P_d = \mathrm{R} \cdot I^2$. Considering this, it is clear that R should be maximized. Power losses inside the cavity occur due to the finite conductivity of the cavity walls, which has been neglected in the calculations above. In fact the fields and surface currents penetrate into the cavity walls as deep as the so called skin depth [19].

$$\delta_s = \sqrt{\frac{2}{\mu_0 \mu_w \sigma_w \cdot \omega}} \tag{2.24}$$

Where μ_w and σ_w are the wall permeability and conductivity respectively. The power loss is directly proportional to the skin depth and the square of the cavity voltage [19]. Therefore, shunt impedance is primarily affected by the material used and the shape of the cavity. It is also worthwhile to note that the power loss depends on the particular cavity mode. In accelerator physics, it is common to quote the shunt impedance per unit length, or the so called *specific shunt impedance*. As a rule of thumb, the following formula can be used to estimate the specific shunt impedance for a copper cavity [19]:

$$r\ (\mathrm{M\Omega/m}) \approx 1.28 \cdot \sqrt{f_{\mathrm{rf}}(\mathrm{MHz})} \tag{2.25}$$

The quality factor is another crucial characteristic of the resonator cavity, which will be discussed in more detail in the following section.

A derived parameter which many find useful for cavity design is the ratio of shunt impedance to Q, often called R over Q, which is [20].

$$\frac{\mathrm{R}}{\mathrm{Q}} = \frac{(V)^2}{2\omega \mathrm{U}}. \tag{2.26}$$

We see that R/Q measures the efficiency of acceleration per unit stored energy, and is independent of the power. It is a function of the cavity geometry and is independent of the surface properties that determine the power losses.

2.1.3 Choke Filter

Our design included a choke filter around the cavity in order to prevent the stored electromagnetic energy from leaking out of the gap between the anode and cathode parts. Choke filters perform the same function as quarter wavelength impedance transformers, transforming the open end of the cavity into a short circuit. Additionally, it facilitates access to the interior of the cavity and enables the cavity to be adjusted for optimal coupling. As a result, this cavity can be tuned over a greater bandwidth of +/-3 MHz, which is not possible in cavities without choke filters. On the other hand, gaining access to the cavity allows us to verify our designs, replace cathode pins, etc., as part of this research direction. As shown in Figure 2.5, the designed choke filter can trap the electric field inside the cavity, as evidenced by the field distribution.

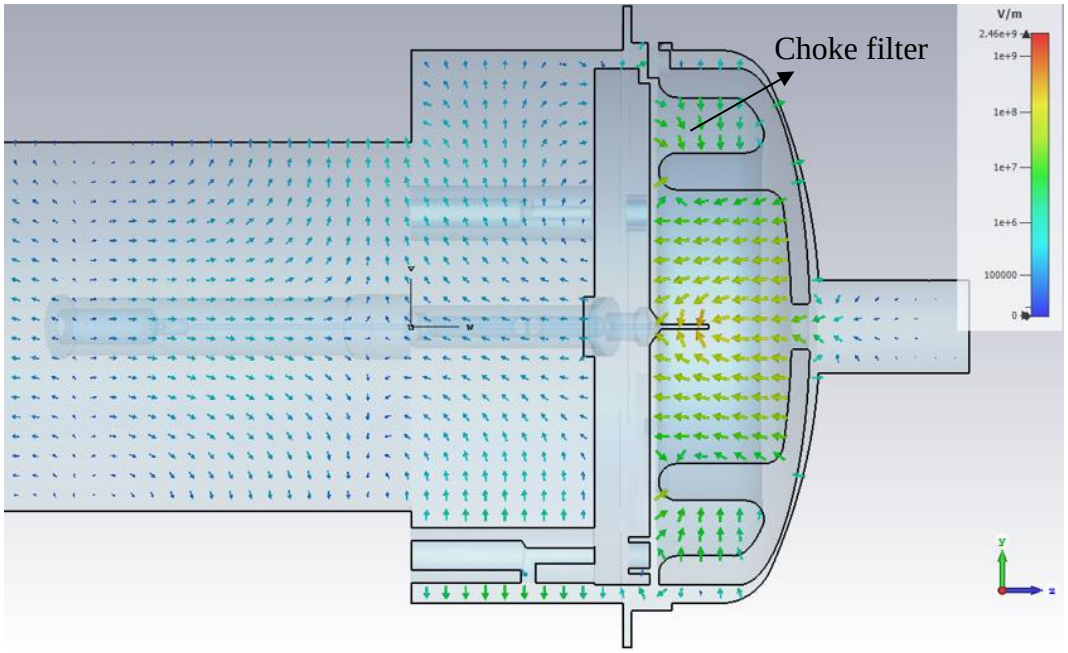

Figure 2.5: Design of a choke filter around the cavity and restricted electric field distribution of RF gun

The choke filter was designed in such a way that it contains two separate parts, so that the interior part of the cavity can be accessed and a better ultra-high vacuum can be achieved with a vacuum pump placed behind the RF gun. Nevertheless, the separation of these two components theoretically means that we no longer have a "*cavity"* since it is not a closed volume. Using the quarter wavelength transformer

we can close the cavity electromagnetically (not physically of course) by transforming the open circuit to short circuit. the quarter wavelength transformer can be realized by a structure called Choke Filter around the cavity.

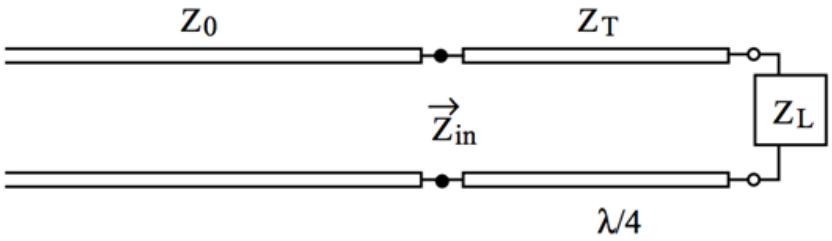

Figure 2.6: Circuit schematic of a quarter-wave transformer

Figure 2.6 illustrates a quarter-wave transformer, a simple impedance transformer used in impedance matching to minimize the amount of energy reflected when a transmission line is connected to a load. Input impedance of a transmission line of length L with characteristic impedance Z_0 connected to a load with impedance Z_L is calculated as follows [21]:

$$Z_{\text{in}} = Z_0 \frac{Z_L + iZ_0 \tan(\beta l)}{Z_0 + iZ_L \tan(\beta l)} \tag{2.27}$$

Since β is the same as the angular wavenumber, $\beta = 2\pi/\lambda$, then for a quarter-wavelength line, $l = \lambda/4$, and $\beta l = \pi/2$. On the basis of the limit, as the tangent function argument approaches $\frac{\pi}{2}$, the impedance becomes:

$$Z_{\text{in}} = \lim_{\beta l \to \pi/2} Z_0 \frac{Z_L + iZ_0 \tan(\beta l)}{Z_0 + iZ_L \tan(\beta l)} = Z_0 \frac{iZ_0}{iZ_L} = \frac{Z_0^2}{Z_L} \tag{2.28}$$

By using a quarter-wave transformer, the load impedance can be matched to the input impedance, and a good estimate of the characteristic impedance Z_0 can be obtained using the formula above which is useful for designing the choke filter.

2.1.4 Compact Rack-Mountable Amplifier

S-band guns are highly developed for the production of low emittance relativistic electron bunches, normally they need powerful klystrons which are bulky and expensive. Here, we present a compact electron source which can accelerate electrons up to 150 keV by only 10 kW from a compact rack-mountable amplifier

as shown in Figure 2.7. The operating frequency of this Solid State High Pulsed Power Amplifier is 2998 MHz +/- 5 MHz. Furthermore, it can be used to cover the pulse repetition rate from 10 Hz to 100 Hz.

Figure 2.7: Compact rack-mountable solid state amplifier

We use feedthroughs and antenna coupling instead of waveguide coupling for the input coupling for several reasons:

- It is more compact
- It is possible to adjust the coupling constant
- In addition to being more compatible with this solid-state amplifier

2.1.5 Pin Cathode

One way to improve the compactness of the accelerator is by eliminating the use of the usual massive and bulky klystrons. Solid state amplifiers in kW range may be a suitable alternative to klystrons for this purpose. Because of the low power of solid-state amplifiers compared to klystrons, typically in the MW range, consideration should be given to the design of cavities so that electrons can be accelerated to relativistic velocities. In Figure 2.8, a simple single-cell pillbox cavity design and electric field distribution are shown operating in the TM_{010} mode at a frequency of 3 GHz.

Using a solid-state amplifier with 10 kW of input power, the field strength would not exceed 5 MV/m, which is insufficient to accelerate electrons and generate high-quality electron beams.

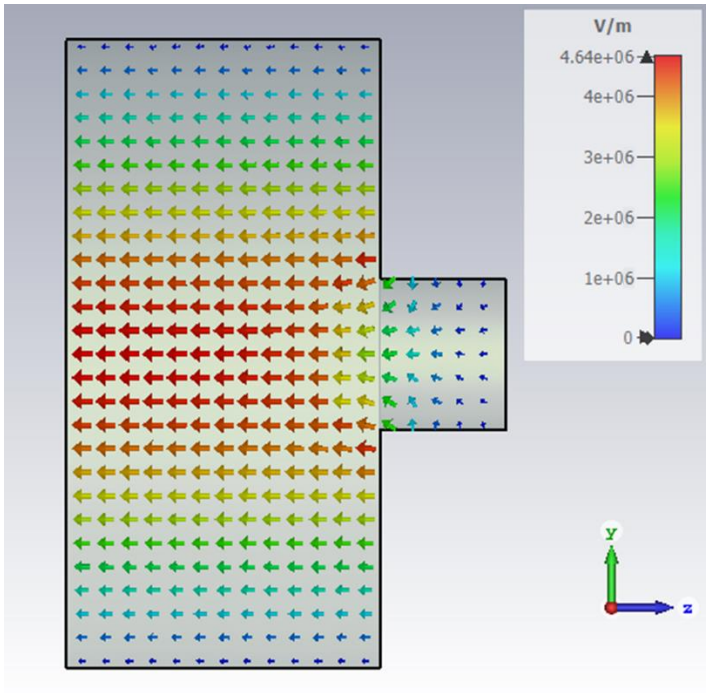

Figure 2.8: Simple single-cell pillbox cavity design and its electric field distribution

A creative way to increase the effective electric field inside this cavity is employing a pin cathode so that the electric fields are efficiently concentrated around the cathode (where photon-emitted electron beams are generated by UV beams striking the cathode) [22], [23].

According to the simulations, if the diameter of this cathode pin is 0.8 mm, the electric field strength on the pin-cathode will exceed 88 MV/m with an input power of 10 kW. This field is sufficient to accelerate electrons more than 100 keV immediately after generation, as well as result in electron bunches with low temporal duration, which will be discussed in more detail in Chapter 4 in the electron beam dynamics section.

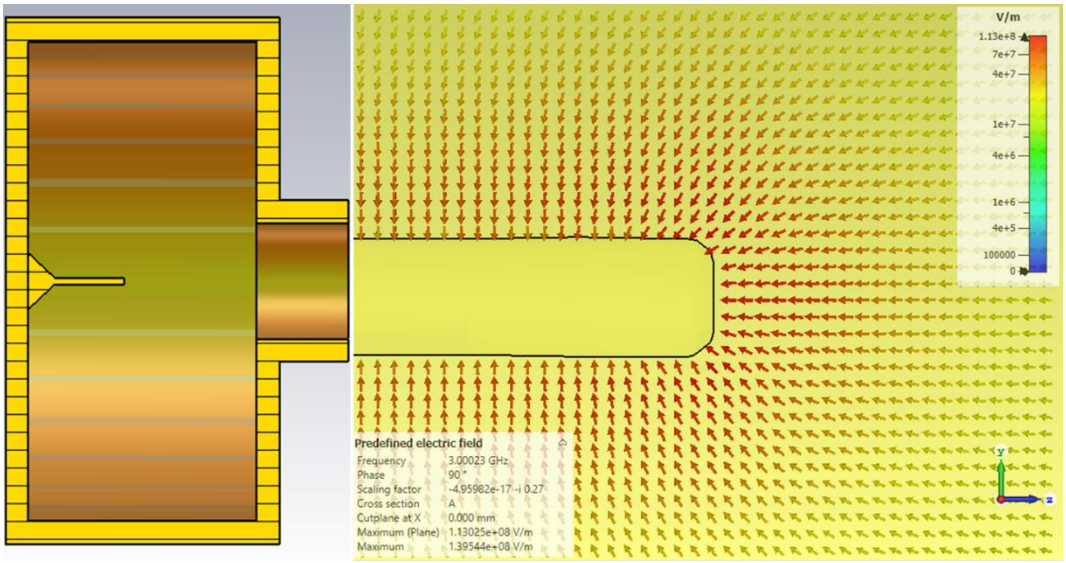

Figure 2.9: left: Cavity design utilizing a pin cathode, and right: distribution of electric fields around the tip

As a result of the solenoid size and vacuum considerations, the solenoid must be located outside of the vacuum chamber. Therefore there must be a flange (typically 20 mm thick) between the cavity and the solenoid. However, this reduces the ability of the solenoid to focus the electron beam immediately following its generation in the cathode, so that the longitudinal and transverse focus points of the electron beam do not coincide at the same point. A solution to this problem is to design the flange so that it is thinner and curved, thus causing the cavity to be curved as well (Figure 2.10).

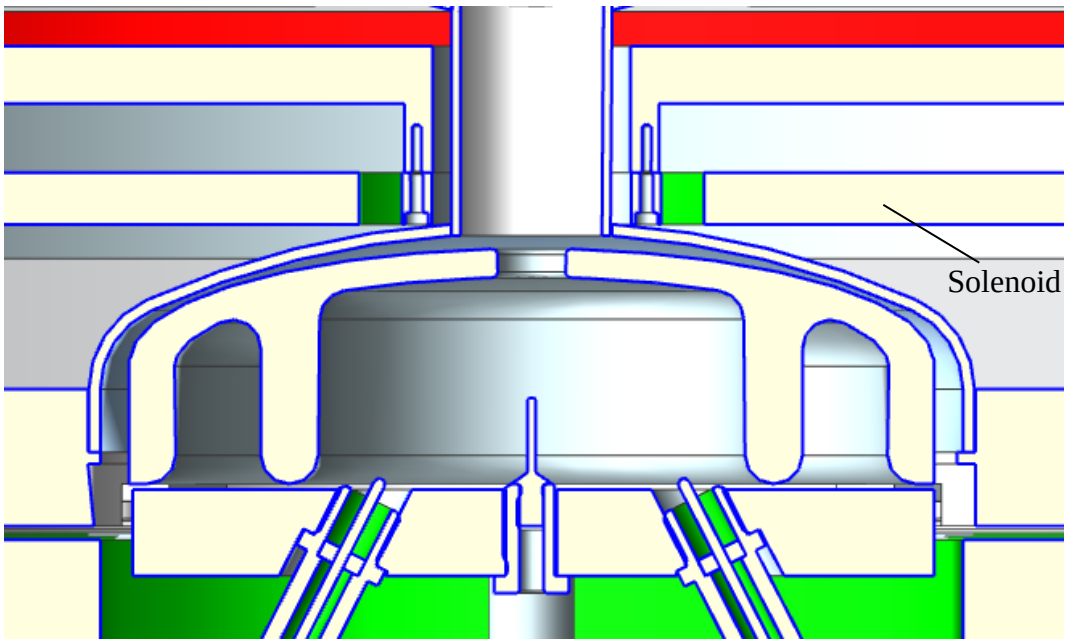

Figure 2.10: A sectional view of the final design of the cavity with the outer curved flange

2.1.6 Solenoid

Due to the space charge effect, the electron beam experiences a strong defocusing during acceleration in the gun cavity. In order to compensate this, a solenoid is employed. The solenoids also aid in compensating for the emittance growth in the gun cavity during acceleration [24].

Solenoids are similar to lenses in an optical setup, with focusing strength based on the integral of the squared magnetic field strength. In contrast to an optical lens, the solenoid does not only focus electrons, but also rotates them around the longitudinal axis due to the radial component of the magnetic field. In order to explain the focusing in a solenoid, Busch's theorem [25] would need to be taken into consideration. According to the theorem, a particle beam's canonical angular momentum is conserved when it travels in the axisymmetric magnetic field of a solenoid. When a charged particle travels through a uniform magnetic field, it starts rotating at the Larmor frequency, which is half the cyclotron frequency. A beam focus is achieved in the solenoid field by the net force that is directed towards the axis of the solenoid. After leaving the solenoid field, the azimuthal velocity of the particle becomes zero and the radial velocity of the particle is proportional to the distance between the particle and the axis of the solenoid.

Our goal in designing this compact RF gun and its solenoid is to focus the beam down to less than 10 μm beam size and 25 μm longitudinal size, with both transverse and longitudinal focus being in the same location. It is known that the focal length of the solenoid depends inversely on $\int B_z^2\, dl$ [26], whereas for a given current $\int B_z\, dl$ is constant. Therefore, the focal length can be decreased by squeezing the magnetic field. In contrast, the growth of emittance proportionally depends on $\frac{\partial^2}{\partial_z^2} B_z^2$ [25]. Thus, in designing the solenoid, a trade-off must be made between the focal length and the emittance. Figure 2.11 illustrates the distribution of magnetic fields of the thin solenoid designed for the compact S-band gun. Additionally, in Figure 2.12 the magnetic field is shown along the axis of the solenoid, with the zero point at the tip of the pin-cathode.

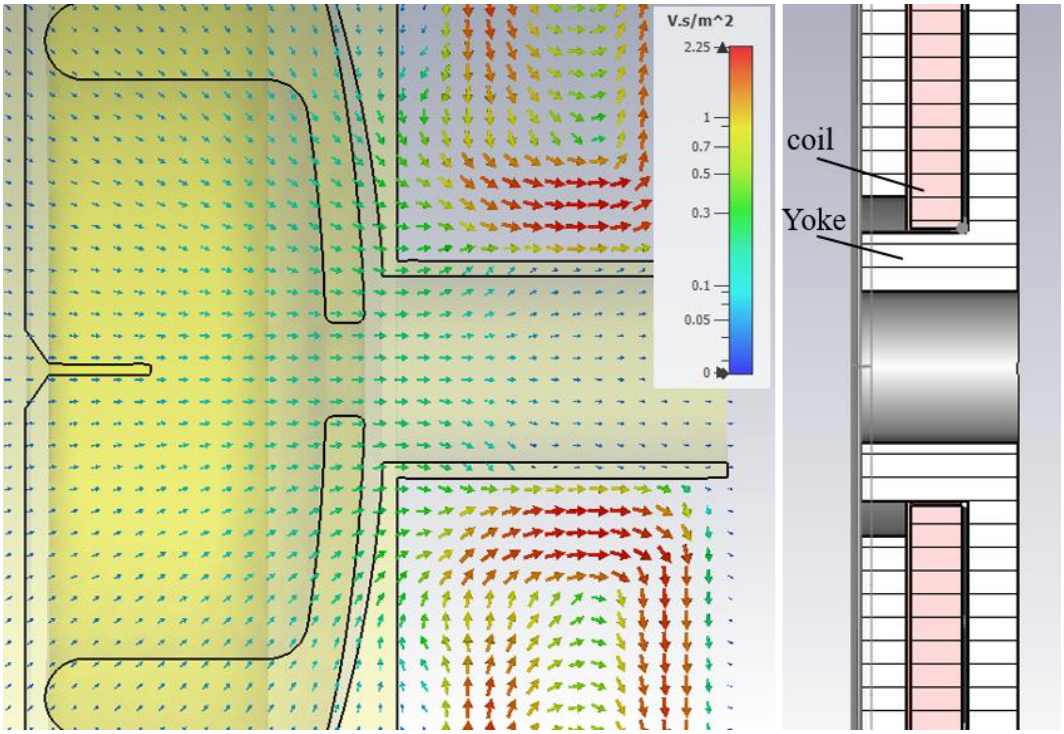

Figure 2.11: Solenoid magnetic flux density distribution and its position in relation to the cavity, along with the cross section of the solenoid illustrating the coil and yoke design

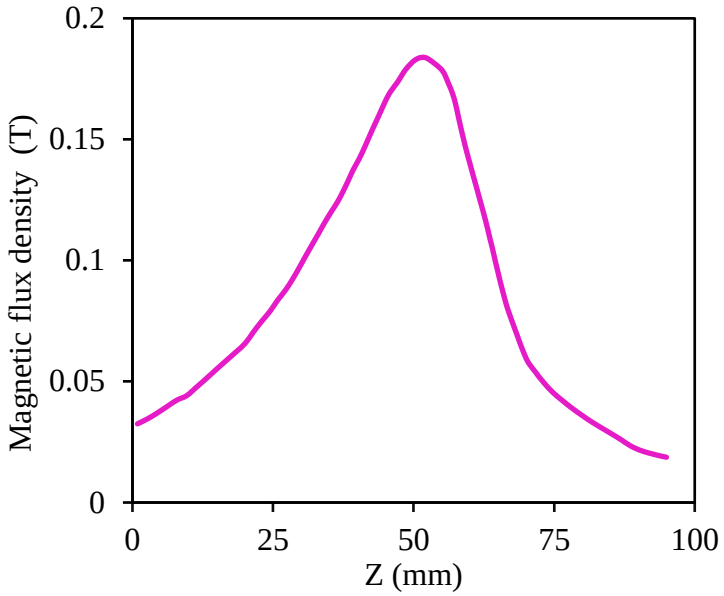

Figure 2.12: Magnetic field value along the axis of the solenoid

This solenoid consists of two parallel coils that are cooled by water. It is necessary for this magnet to be able to support a current of up to 230 A in order to achieve such a magnetic field as described above. Figure 2.13 shows the manufactured coils with an operating voltage and current of 7.5 V and 230 A, respectively. There should be a voltage about 3-5 V overhead for the cables depending on the distance between the power supply and the solenoid. There should be a minimum water pressure of 3 bars and a flow rate of 0.7 liters per minute in each coil, and the two cooling circuits must be connected in parallel.

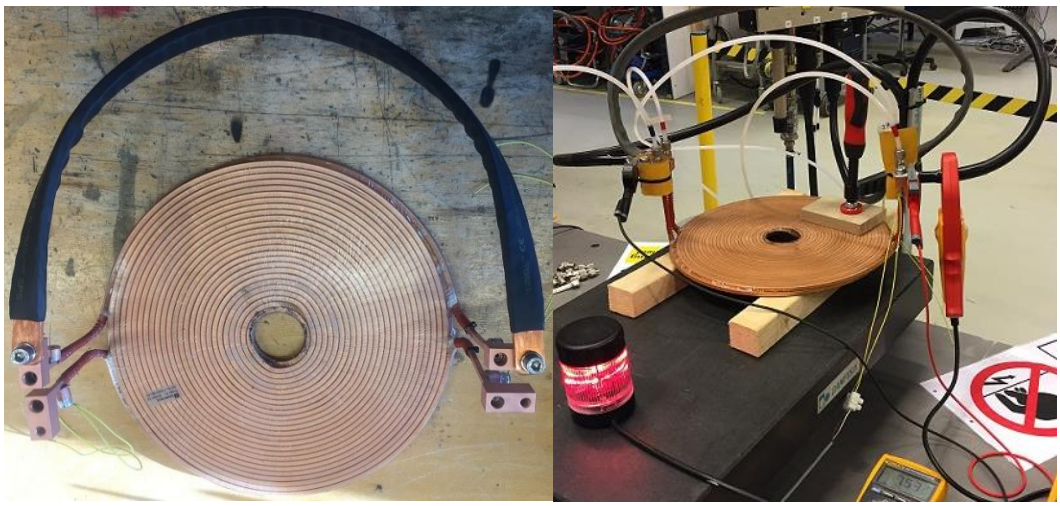

Figure 2.13: Manufactured coils of the solenoid by Danfysik

2.2 Design and Fabrication

The compact RF gun is an S-band gun with a frequency of 2.998 GHz, combining both acceleration and compression of the electron bunch in a single device. By implementing a pin-shaped photocathode with a flat 0.8 mm tip, strong enhancement of the RF-field strength in the vicinity of the cathode is achieved which substantially reduces the power requirements, and hence the cost and complexity of the device.

The maximum power of the compact solid-state amplifier is 10 kW which can accelerate the electrons up to 150 keV according to the simulations have been done for the first prototype of the RF gun. A solenoid is also used just after the gun to focus the electron beam transversely.

Figure 2.14 shows the designed structure. The electrons are generated via photoemission from a circular area at the top of the pin cathode. The 10 kW input power from the compact solid-state amplifier is injected into the cavity with an input antenna via a coaxial feedthrough shown in Figure 2.14. A second antenna is used as the pick-up probe for measuring the electric field inside the cavity. For tuning the cavity, this gun consists of two parts: the anode part is fixed, while the cathode part can be moved by a mechanical translator giving us also the possibility of tuning the cavity by adjusting the distance between the cathode and anode. In addition, the cavity design employs a choke filter which confines the field, and also

facilitating access to the interior of the cavity and tuning the cavity for optimal coupling.

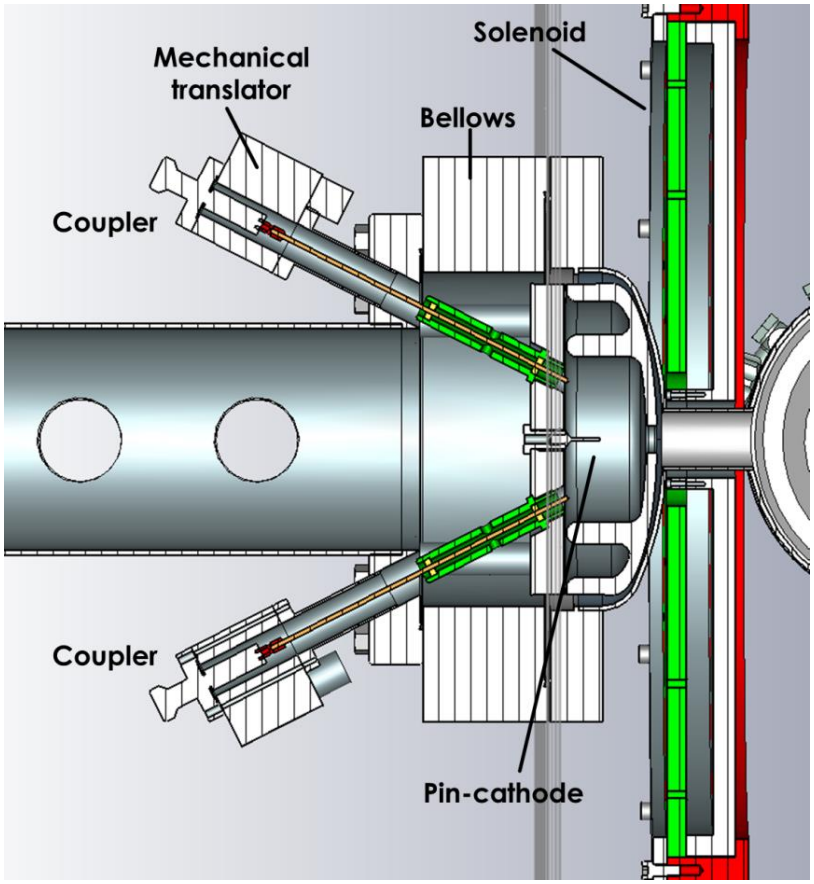

Figure 2.14: Sectional view of AXSIS RF Gun

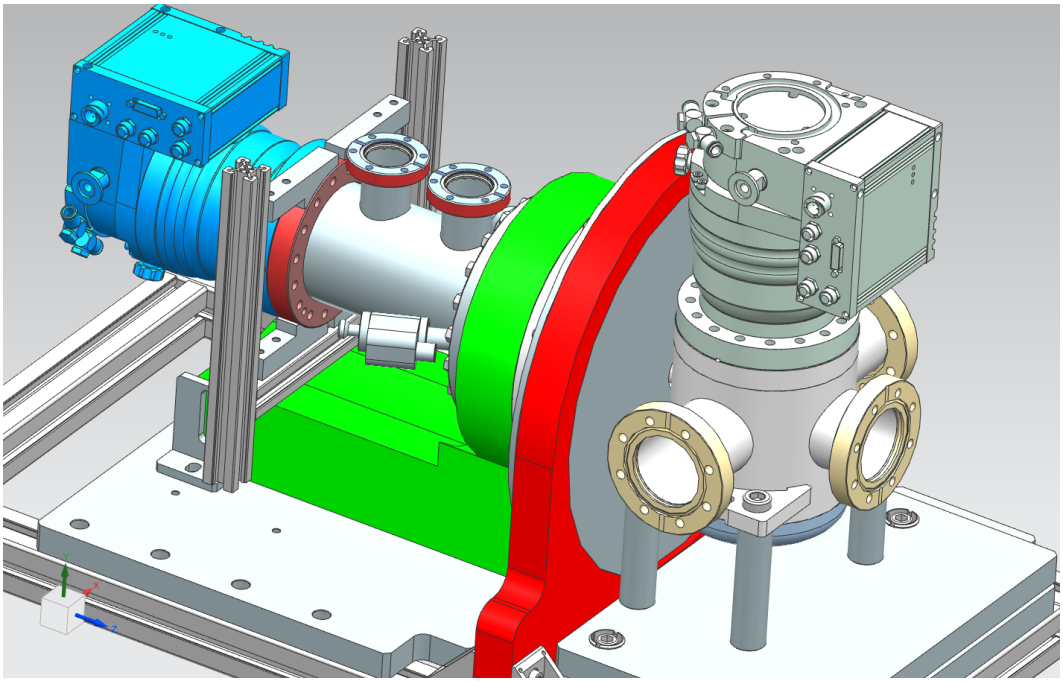

Figure 2.15: 3D CAD drawing of the first prototype of the RF gun

Chapter 3

Characterization Measurement of RF Gun Prototype I

3.1 Quality Factor

The typical layout of the gun RF power flow is shown in Figure 3.1. The system consists of a RF source connected with a waveguide to a RF coupler. Depending upon the frequency and power levels the coupler can be a waveguide, a coaxial line or, as shown in the figure, a side coupled antenna. The RF source power generates the forward power, P_{fwd}, with some going into the gun, P_{cav}, and some being reflected as reverse power, P_{rev}. The total source power is the sum of the cavity and reverse powers, $P_{fwd} = P_{cav} + P_{rev}$.

The RF power enters the gun cavity through a coupling hole or port with a waveguide-cavity coupling parameter $\beta_{coupler}$ defined as

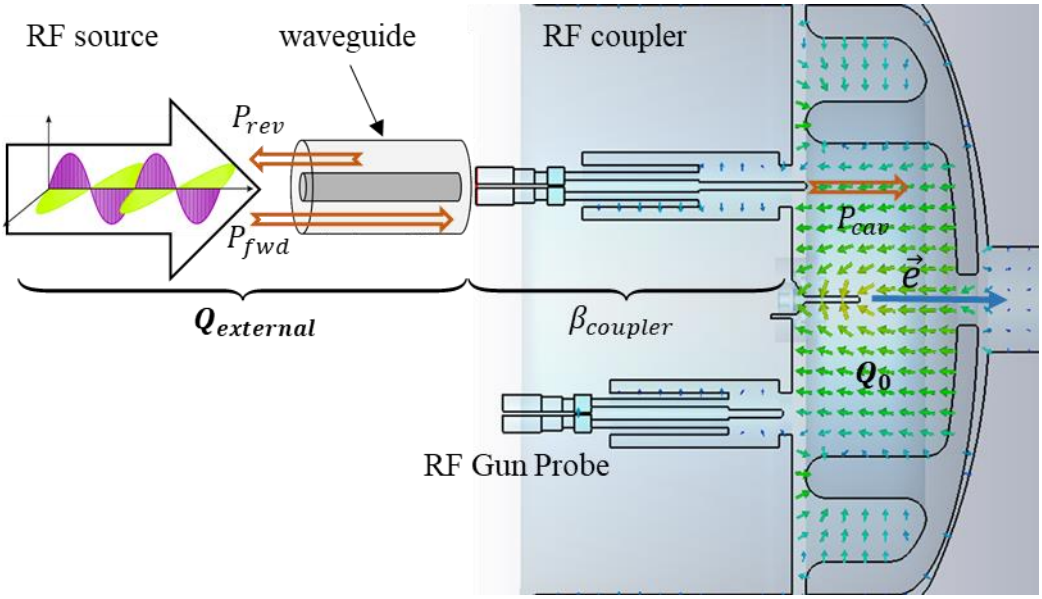

Figure 3.1: Schematic layout of a gun showing RF power flow and gun and waveguide parameters.

$$\beta_{coupler} \equiv \frac{P_{external}}{P_{cav}} \tag{3.1}$$

Here, $P_{external}$ is the rate at which the stored energy in the cavity radiates back into the waveguide when the RF source is turned off. P_{cav} is the steady-state power flowing into the gun. Steady-state is defined as when the fields equilibrate and become time-independent. In steady-state, P_{cav} equals the heat dissipation in the cavity walls and the RF power reflected back to the RF source, P_{rev}. The reverse (or reflected) power is given by

$$P_{rev} = P_{fwd}\left(\frac{\beta_{coupler} - 1}{\beta_{coupler} + 1}\right)^2 \tag{3.2}$$

The external and cavity powers depend upon the external and intrinsic quality factors, which are defined as Q_{external} and Q_0 respectively. For a cavity with a stored energy of U and a resonant frequency, ω_0, the external power is given by

$$P_{external} = \frac{\omega_0 U}{Q_{external}} \tag{3.3}$$

Similarly, for the steady-state power radiating into the cavity

$$P_{\text{cav}} = \frac{\omega_0 U}{Q_0} \tag{3.4}$$

Based on these definitions, the coupling parameter can be expressed in terms of the two quality factors

$$\beta_{\text{coupler}} = \frac{Q_0}{Q_{\text{external}}} \tag{3.5}$$

A resonator used in an oscillator or tuned amplifier, however, may be tightly coupled in order to achieve maximum power transfer. A measure of the level of coupling between a resonator and a feed is given by the *coupling coefficient*. To obtain maximum power transfer between a resonator and a feed line, the resonator should be matched to the line at the resonant frequency; the resonator is then said to be *critically coupled* to the feed [27]. Three cases can be distinguished:

1. $\beta < 1$: The resonator is said to be undercoupled to the feedline.
2. $\beta = 1$: The resonator is critically coupled to the feedline.
3. $\beta > 1$: The resonator is said to be overcoupled to the feedline.

Resonator cavities can be considered as a damped oscillators with external excitation. The damping is again a result of power losses in the cavity walls, as well as an effect of the energy transfer from the field to the electron beam.

$$\mathrm{Q} \equiv \omega \frac{\text{cavity stored energy}}{\text{average power dissipated}} = \frac{\omega \mathrm{U}}{\mathrm{P}}. \tag{3.6}$$

Where the stored energy is:

$$\mathrm{U} = \frac{\varepsilon_0}{2} \int \mathrm{E}^2 \mathrm{dV} + \frac{\mu_0}{2} \int \mathrm{H}^2 \mathrm{dV}. \tag{3.7}$$

In the steady state for any resononant mode, the electric and magnetic stored energies oscillate in time, 90° out of phase. The total stored energy U remains constant. The time-averaged electric and magnetic energies are equal. It is usually easiest to calculate U by using either the electric or the magnetic term alone with the peak value of the field in time.

Loaded and Unloaded Q:

In the steady state the generator supplies the power losses in the cavity walls. If the generator also supplies power to elements external to the cavity, this should be included in the calculation of the Q. We define Q_0 as the quality factor of the cavity

unloaded by the extemal elements. The total (loaded) power supplied by the generator is

$$\mathbf{P}_{\mathrm{T}} = \mathbf{P}_{\mathrm{cavity}} + \mathbf{P}_{\mathrm{external}} \tag{3.8}$$

If the loaded quality factor is $Q_L \equiv \frac{\omega U}{P_T}$, then

$$\frac{1}{Q_L} = \frac{1}{Q_0} + \frac{1}{Q_{\mathrm{ext}}} \tag{3.9}$$

where $Q_{\mathrm{ext}} = \frac{\omega U}{P_{\mathrm{external}}}$.

Looking at the definitions of both the shunt impedance and the quality factor, one notices that both depend on the power loss in the system, which is connected to the material properties. A more general figure of merit can be found by looking at the ratio between the shunt impedance and the quality factor, R/Q, which is hence called *R over Q*. It is given as

$$\frac{R}{Q} = \frac{(T_\beta V_0)^2}{\omega \mathrm{U}} \tag{3.10}$$

R over Q only depends on the shape of the cavity (independent from the surface losses) and is therefore a useful characteristic quantity for resonator cavities.

3.1.1 Quality Factor measurement

At room temperature, the Q values of RF cavities are usually calculated from the resonance bandwidth measured at -3 dB level by a network analyzer which excites and picks up RF signal through the ports located at the opposite sides of a cavity [28]. The resonant curve distortion is caused by the resonance split due to the ellipticity caused by manufacturing tolerances, and RF ports. Therefore, the measured Q values are usually lower than the simulated or theoretical Q values.

The measurement method relies on the classical definition of the Q-factor of a resonator [29], namely

$$\mathrm{Q}_L = \frac{f_0}{\Delta \mathrm{f}} \tag{3.11}$$

where f_0 is central (resonance) frequency, and Δf is the bandwidth (on – 3dB level) of the resonator. This value is referred to as the loaded quality factor Q_L.

In order to tune the cavity to a certain frequency, a linear manipulators is installed on the antenna coupler to adjust the length of the antenna within the cavity, and another one is installed on the back chamber of the RF gun to adjust the distance between the anode and cathode (see Figure 2.14). With the adjustment of the distance between the anode and cathode, the operating frequency in the cavity can be set to 2.998 GHz, and the antenna length within the cavity can be adjusted to optimize the coupling between the source and the cavity.

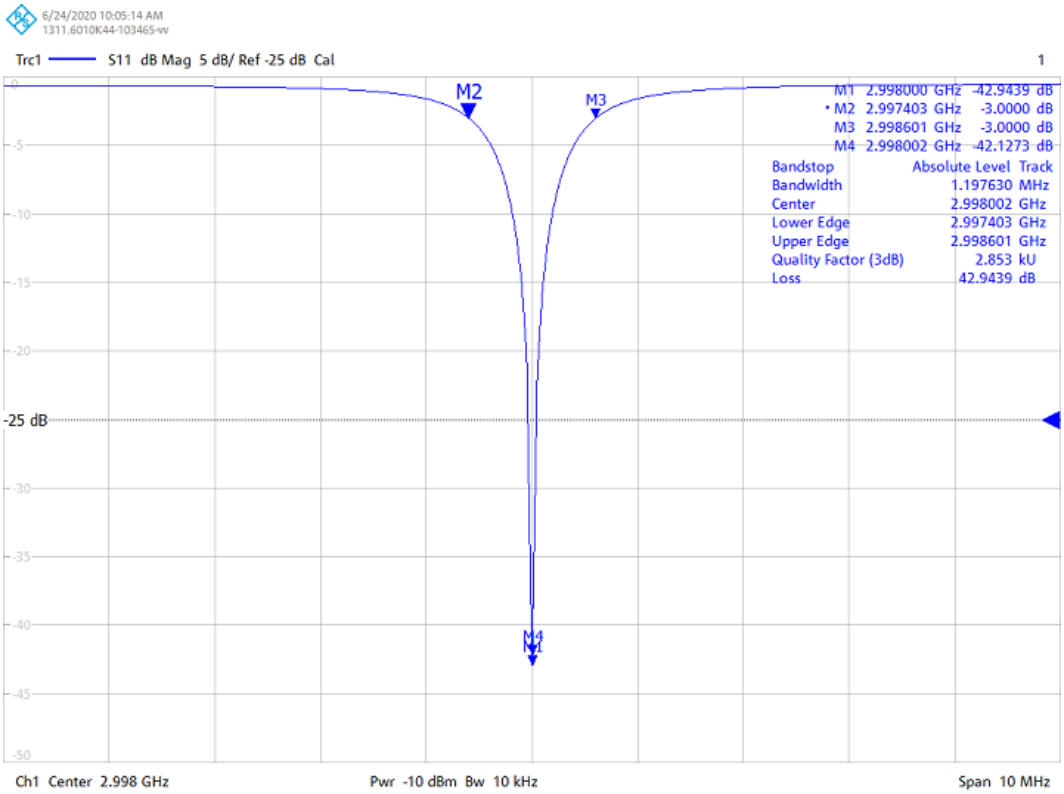

Figure 3.2: frequency response of the cavity using R&S vector network analyzer

According to microwave simulations conducted with the CST software, the unloaded quality factor (which depends on the cavity geometry and material used) is approximately 10,000. Due to the relatively low beam loading in this gun (in the pico-Coulomb range), the coupling coefficient must be close to 1, i.e., the critical coupling. This means that, according to Equ. (3.5), the external quality factor is equal to the unloaded quality factor, and according to Equ. (3.9), the loaded Q should equal half of the unloaded Q. Consequently, we expect to measure a loaded quality factor of about 5000 in the experiment.

In this experiment, using a vector network analyzer with a bandwidth of 4.5 GHz, the frequency response of the cavity was determined. Figure 3.2 shows that, with the span set to 10 MHz, the resonant frequency of 2.998 GHz is clearly coupled in the cavity, with a reflection (S_{11}) reaching below -45 dB. The loaded quality factor for this resonance frequency response is about 2500, which is far below the expected value. In the next section, it will be explained that one of the reasons for this may be the surface quality (primarily surface oxidation) of the RF gun parts. In addition, after about three weeks of conditioning of the RF gun at a power of 10 kW, the quality factor increased by approximately 27%.

3.1.2 RF waveforms measurement during the conditioning

Using a resonant circuit model driven at its resonant frequency, it can be demonstrated that the gun's response time to changes in RF is the $1/e$ response time, τ_{cav}, given as [30]

$$\tau_{cav} = \frac{2}{\omega_0} \frac{Q_0}{1 + \beta_{coupler}} \tag{3.12}$$

Note that the above relations apply only when the gun fields have reached their steady state values, i.e. when $t >> \tau_{cav}$. There are transients that appear when the RF power is first turned on, whose time-dependency is determined by the response time of the gun, often referred to as the cavity fill time.

Figure 3.3 illustrates the measurements of forward, reflection, and gun probe power of the Compact gun being driven by a pulse duration of $\sim 5\ \mu s$. Its duration is sufficient to fill the gun and launch a single bunch of electrons. The measurement was performed at REGAE, it was possible to measure these waveforms after calibration using the DOOCS control panel provided by MSK group for the RF gun. In Figure 3.3, the diagram on the left shows the forward and reflected waveforms, and on the right are the reflection and probe.

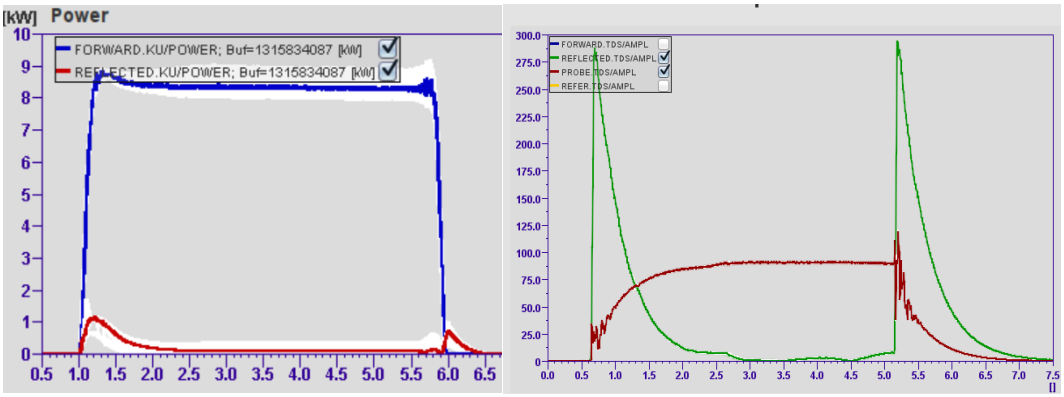

Figure 3.3: RF waveforms measured during high power operation of the S-band gun, *left*: forward (blue) and Reflection (red) signals in kW, *right*: reflection (green) and probe signals in an arbitrary unit.

It is the voltage reflection coefficient, Γ, that determines the behavior of the reverse RF. This coefficient is defined in terms of the forward and reverse voltages, respectively V_{fwd} and V_{ext} [30]

$$\Gamma(t) = \frac{V_{ext}(t)}{V_{fwd}} = \left(1 - e^{-t/\tau_{cav}}\right)\frac{2\beta_{coupler}}{1+\beta_{coupler}} - 1 \qquad (3.13)$$

In this way, power is reflected back toward the RF source in a time-dependent manner corresponding to the forward power times the voltage reflection coefficient squared.

$$P_{rev}(t) = P_{fwd}\,\Gamma(t)^2 \qquad (3.14)$$

Equation (3.13) illustrates that at the start of the RF pulse, $t = 0$, all forward power is reflected regardless of the coupling coefficient. For times longer than the steady-state period, the reflected power is calculated using Equation (3.2), which has three interesting regimes. In the case of $\beta_{\text{coupler}} < 1$, the system is considered to be undercoupled since power is always reflected by the coupler. When $\beta_{\text{coupler}} = 1$, the system is critically coupled, and the reflection is zero after several cavity cycles. If $\beta_{\text{coupler}} > 1$, the system is overcoupled, and the reverse power goes to zero after a short period of time, and then increases again over time to the value given by Equ. (3.2). Figure 3.3 shows measurements for a critically coupled gun in which the reverse power reaches zero after a cavity fill time and then rises to its steady-state value.

3.2 Investigation of resonance frequency stability

The stability of the resonance frequency and coupling is one of the most important parameters for a manufactured cavity, which can be affected by a variety of factors such as cavity design, temperature and mechanical stability of cavity and couplers, vibration level on the system, etc. According to the measurements made using the network analyzer, the resonance frequency was distorted, which will be discussed in this section.

As a means of improving vacuum levels in the cavity, this RF gun has a chamber at the rear that will be equipped with a turbomolecular pump. Due to this, the couplers had to be extended greatly, which made designing the RF gun more challenging. Due to this, even a slight touch on the back or vibration on the body of the RF gun could cause distortions in the frequency resonance and coupling.

According to Figure 3.4, there is an unwanted resonance visible in the frequency response measured with a Vector Network Analayzer (VNA), which may be a result of microwave leakage. The whole structure was modeled with CST in order to identify the cause for the unwanted resonance.

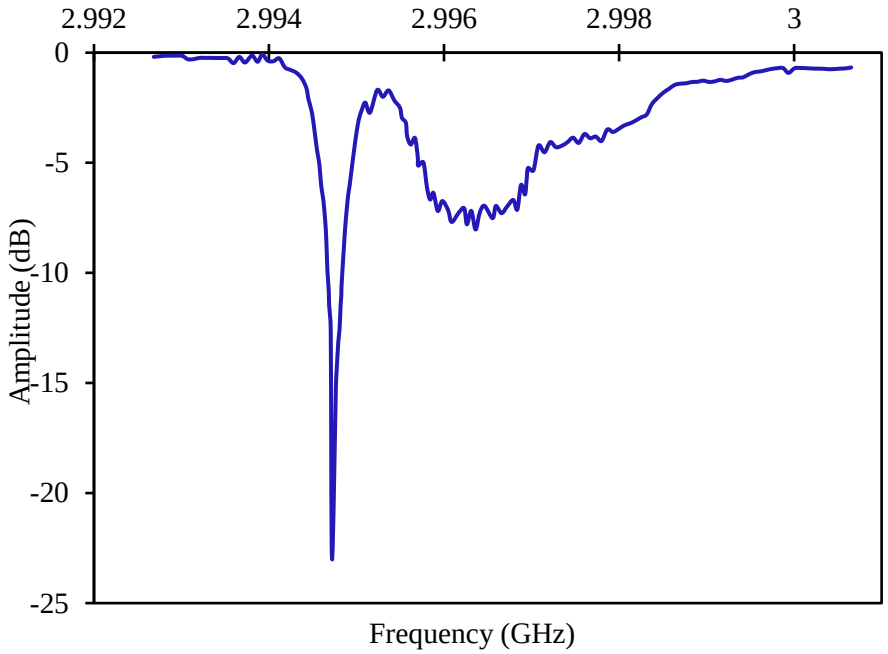

Figure 3.4: Unwanted resonance frequency is observed in S_{11} parameter of a VNA, very close to the main resonance frequency.

Based on the simulation shown in Figure 3.5, it is apparent that firstly the unwanted resonance arises from behind the cavity, and secondly the side resonance occurs at 2.992 GHz. The difference between the simulation and the measured side resonance is due to ignoring the pump connected to the left side of the chamber in the microwave simulation, which adds a volume to the cavity and shifts the resonance frequency slightly. A further evidence supporting this concept is the fluctuation in the resonance curve. In fact, these fluctuations can most likely be attributed to the rotating blades of the turbopump.

The side resonance can be moved by placing a metal grid suited to vacuum in the rear chamber and just behind the cavity. However, it was found that placing a metal tube in the rear vacuum chamber results in a 20 MHz shift in the side resonance which was changed to 2.772 GHz (Figure 3.6). In this way, it is still possible to excite the cavity well at the frequency of 2.998 GHz and perform the conditioning.

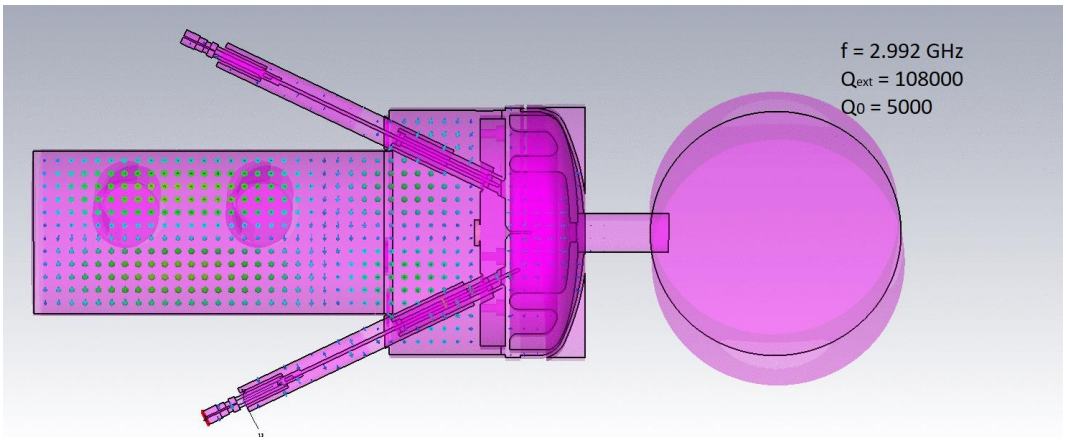

Figure 3.5: Simulation of microwave leakage in the rear chamber using CST software

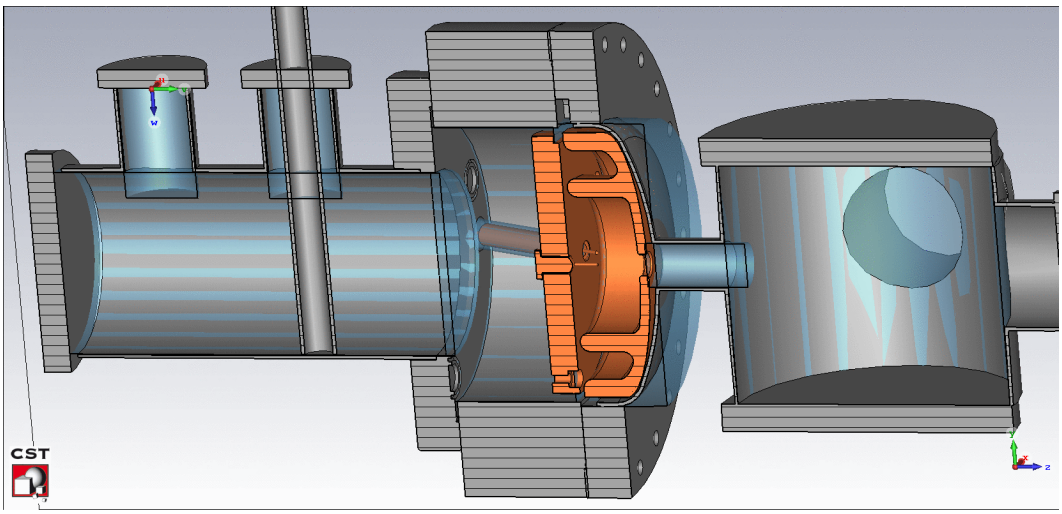

Figure 3.6: A metal tube placed in the rear vacuum chamber results in a shift of 20 MHz in the side resonance

In order to reduce the ultimate pressure inside the cavity of this RF gun as much as possible, two turbo pumps were initially employed (Figure 3.7). Since the blades of the turbo pump and their vibrations caused fluctuations in the resonance frequency, vacuum simulations for an unbaked vacuum chamber were performed using the Molflow+ software [31].

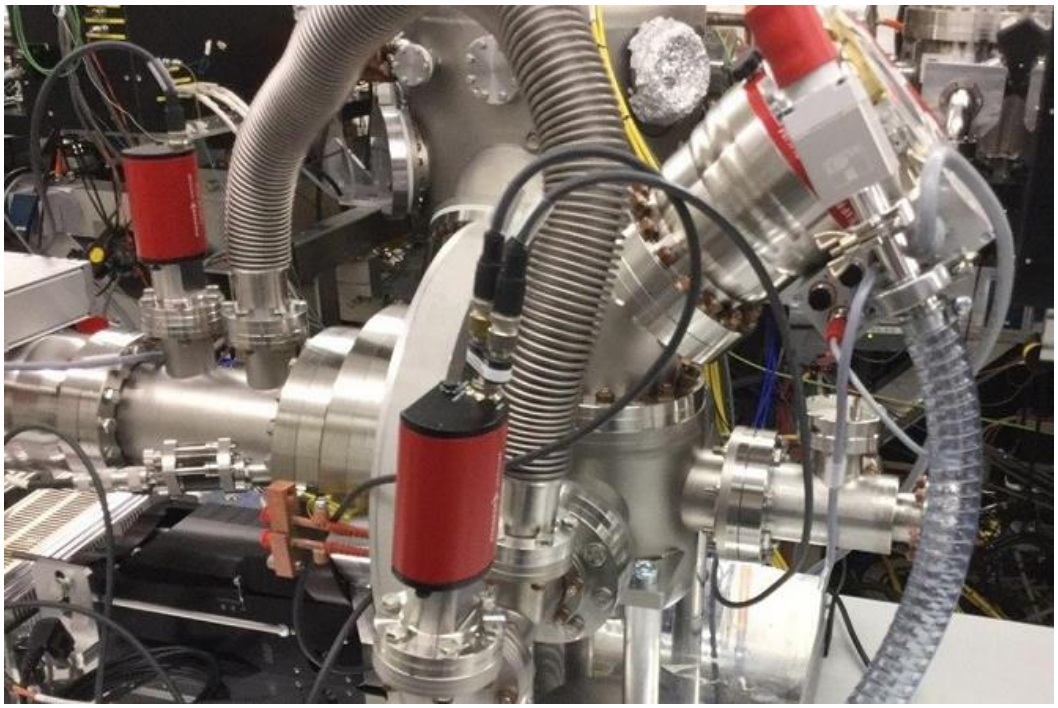

Figure 3.7: RF gun vacuum system utilizing two turbo pumps

As shown in Figure 3.8, there are two different structures, one containing two turbopumps, and the other containing one turbopump, whose pressure profiles are be calculated. Figure 3.9 illustrates the pressure profile along the path of the electron from the pin-cathode up to 30 cm away in the beam line. Based on this comparison, it can be seen that by using a turbopump without bellows, the maximum pressure inside the cavity will be in the range of 2.5×10^{-8} mbar, which is still suitable for the conditioning of the RF gun. It was therefore decided to use only one turbo pump for the experiment, and it led to good results, which will be discussed in the next section.

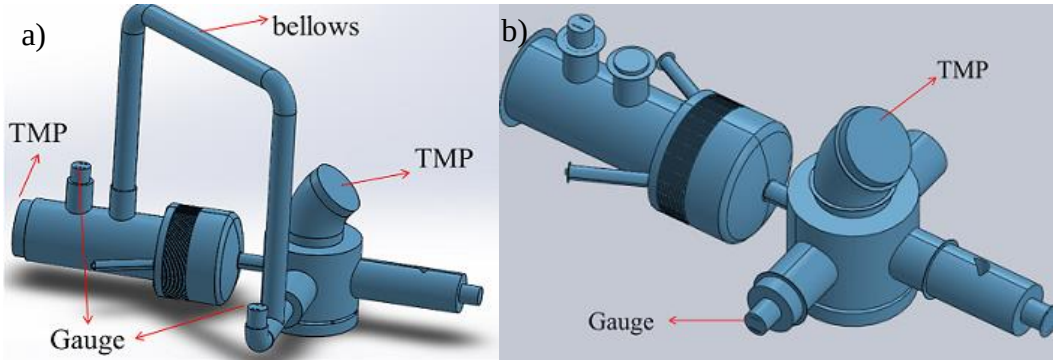

Figure 3.8: Two structures for which the pressure profile will be calculated.

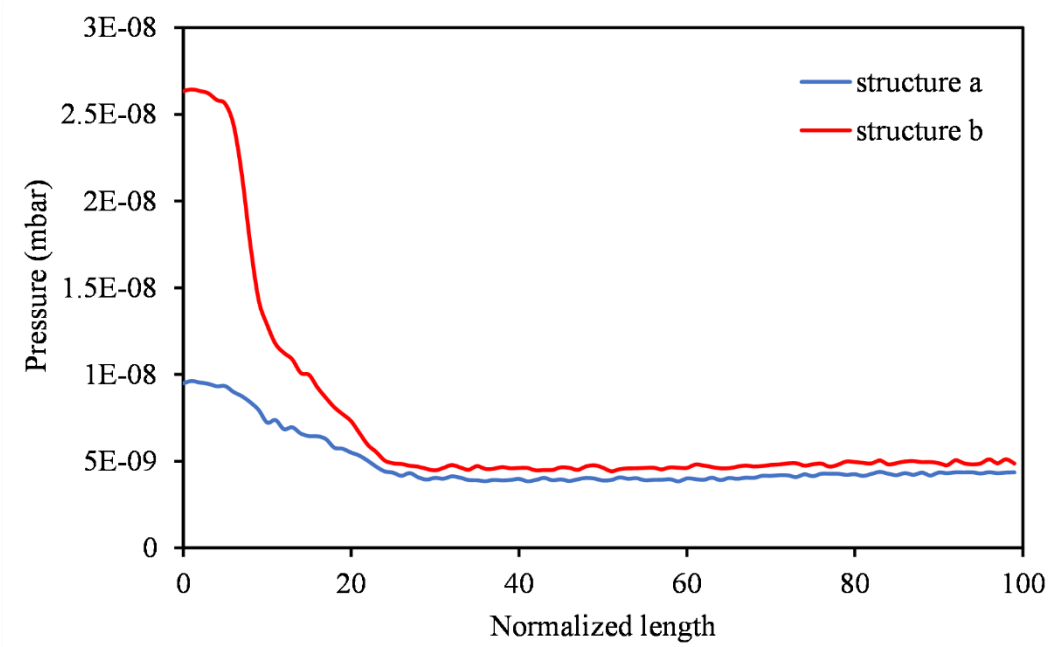

Figure 3.9: Pressure profile of two structures along the path of the electron from the cathode pin up to 30 cm away in the beam line

3.3 RF Gun Conditioning at REGAE

The RF conditioning is a process of intensive RF training of an accelerating structure refers to the preparation and optimization of its operation to achieve the required or the best possible operating parameters, such as high peak power, long pulse length, low failure rate, etc. The RF gun is placed in a ultrahigh vacuum environment to minimize electron scattering and interactions with gas molecules. The vacuum chamber is pumped down to remove any residual gases, ensuring a clean and stable operating environment. The final bakeout must be done when it is at its final place after the cavity installation and connection to an RF system. RF conditioning of a cavity or a coupler, is a surface cleaning process using a low-density plasma in RF fields. Electrical fields cause a field emission, support residual gas ionization and can be a reason for secondary emission. The combined process changes the surface properties and effectively cleans the surface. Long-Term Stability: Once the RF gun is conditioned and the beam parameters are optimized, efforts are made to ensure long-term stability and reliable operation. This involves monitoring and maintaining the necessary conditions, such as vacuum quality, RF power stability, and cathode performance, to ensure consistent beam production over an extended period.

Once initial tests had been performed and the quality factor and resonance frequency stability of the cavity had been identified, this RF gun was transferred to the REGAE tunnel for further experiments, including injection of RF power into the cavity and conditioning of the RF gun. This experiment is also intended to investigate the stability of the power stored in the cavity, as well as the dark charge and multipacting behavior.

The cleanliness of the surfaces of all components used in the RF gun is of great importance since it will affect the vacuum level as well as the amount of dark charge and multipacting, which will directly impact the gun's performance. In the case of the cavity parts, particularly the anode and cathode parts, more detailed cleaning is required. Due to the presence of stains on the copper surfaces inside the cavity, the MVS group was requested to clean the copper parts once again. They first tried a standard cleaning without success on the spots on the surface. That's when they asked to use citric acid because it roughens the copper surface, However was not very effective. Figure 3.10 illustrates the cavity parts that have stains on the surface.

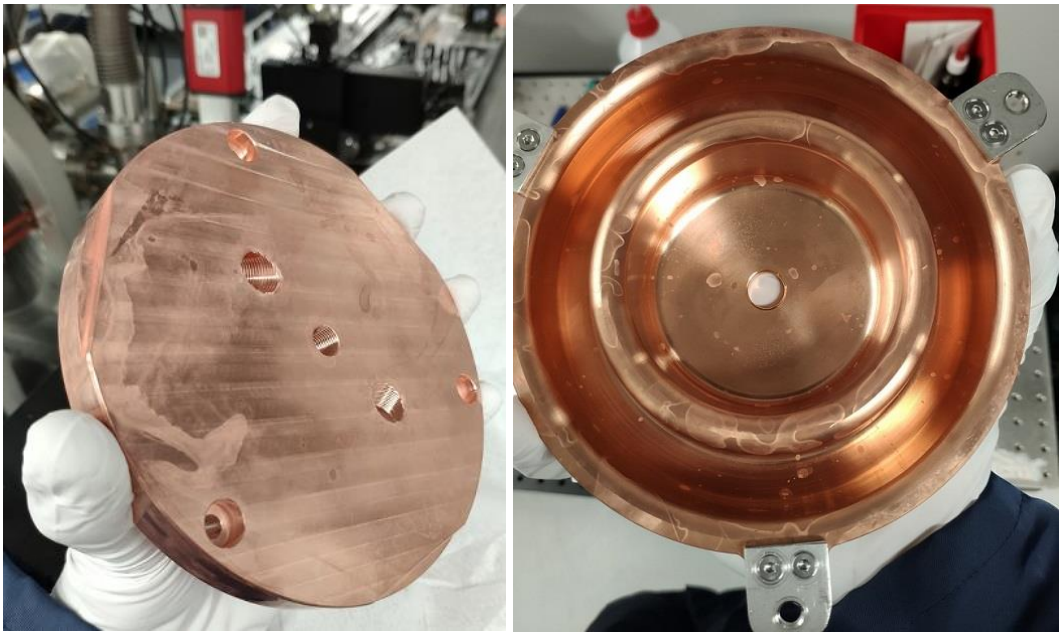

Figure 3.10: Cavity parts (cathode and anode, respectively, from left to right) after cleaning

Prior to operation of the RF gun and injecting RF power from the solid-state amplifier into the cavity, safety considerations must be addressed. According to the "Anzeige von 2 Tisch-Elektronenbeschleunigern" created by Dr. Albrecht Leuschner (D3 department at DESY) RF gun experiments are allowed to have the following maximum beam parameters in the non-shielded lab.

Table 1: Maximum beam parameters of the RF gun in a non-shielded lab provided by safety department

Parameter	Value
Accelerated Particle	Elektronen
Bunch charge	50 fC
Repetition rate	1 kHz
Average beam current	50 pA
Operation time	2000 hrs/yr
Max final energy	1 MeV

The solid-state amplifier, on the other hand, has a peak power of 10 kW, pulse length of 4-10 μs, and repetition rate of 10-100 Hz. This means that the average power put into the RF cavity ($P_{peak} \cdot t_{pulse} \cdot Repitition\ rate$) cannot exceed 10 W. In the first prototype of the Compact RF Gun, electrons are expected to have a maximum energy of 150 keV. Assuming a maximum average beam current of 50 pA is accelerated to 150 keV, the average beam power will be 7.5 µW. Thus, in order to remain within the safety margin, the power conversion from the RF power supply to the electron beam must be less than 10^{-6}.

For safety reasons, this RF gun was tested in the REGAE accelerator tunnel. Following the setting up and conditioning of the RF gun which will be discussed in more detail below, radiation measurements were performed by the D3 safety group at DESY (Figure 3.11). In principle, the impact of electrons on a copper plate mounted at 45-degrees downstream as part of the diagnostic tool should result in Bremsstrahlung radiation emission from the window. The measurements revealed that no signal beyond the background signal could be detected with RF power up to 10 kW and solenoid current up to 180 A. So we have free permission to be in the REGAE tunnel during the conditioning. Moreover, the RF gun experiment for photoemission generation can also be done in the laser lab at CFEL.

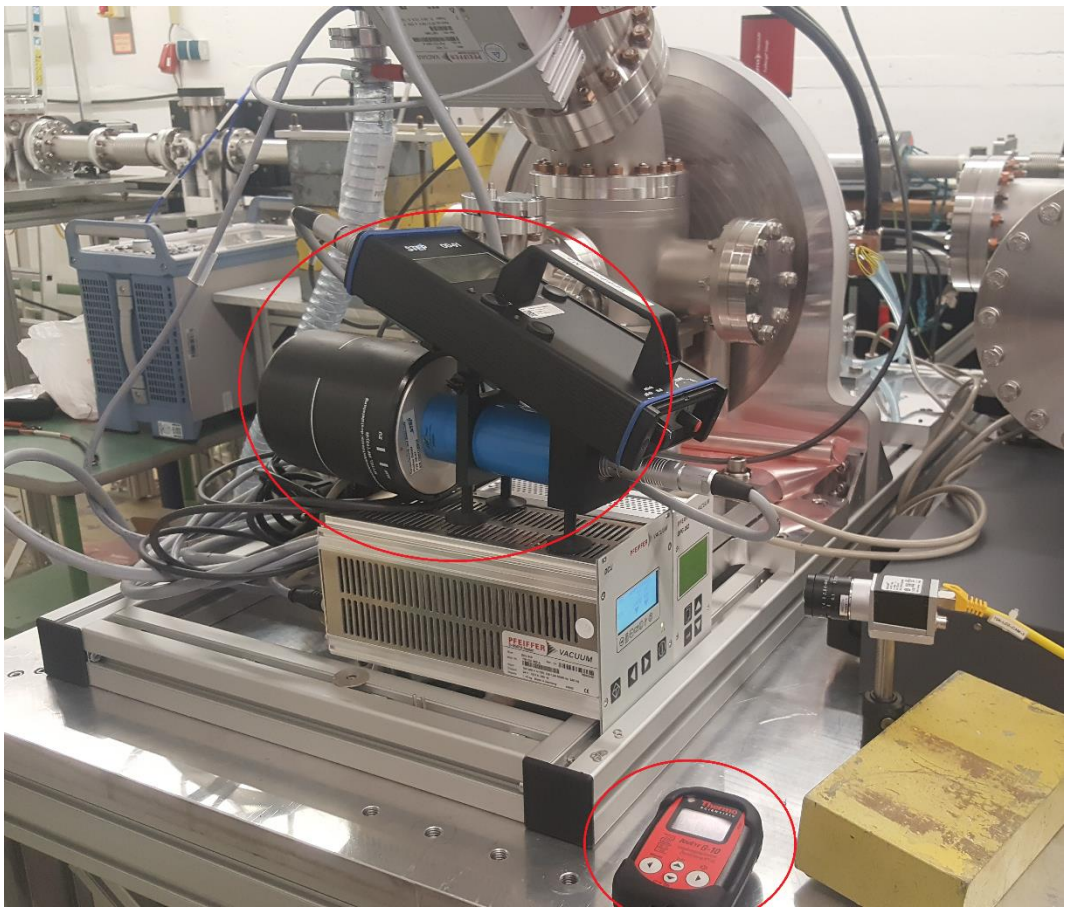

Figure 3.11: Measurements of radiation emitted from the RF gun with an RF power of up to 10 kW and a focusing solenoid of up to 180 A performed by D3 department.

The following is a description of the conditioning procedure of the RF gun:

1. First, a reasonable vacuum level below 10e-7 mbar should be achieved, and the resonance frequency should be set to 2.998 with good coupling in place.
2. Apply RF power and increase the power gradually
3. During the conditioning, it is essential to verify the resonance frequency and RF-coupling using a network analyzer.
4. During RF ramp-up, there will be sparks, then have to start over again.
5. Process takes a few days, depending on number of sparks
6. Presence of sparking is measured via reflection from cavity
7. During the conditioning the Low Level RF (LLRF) control system will indicate the input and reflected power

8. Finished when we can apply maximum field and neither sparks nor constant reflection (can say it's clean)
9. Ready to measure electron beam properties
10. If cavity fails to condition properly, it may need to improve vacuum or cleanliness

Before starting the conditioning of the RF gun, the RF coupler settings have been optimized for best Q-factor, the RF cables were connected to the solid-state amplifier and two cameras for the observation of vacuum pressure and amplifier power were set up. On ramping up the amplifier power, very regular multipacting was observed, resulting in an increase in pressure as well. We continued to ramp up the power every time the pressure was below 5e-7 mbar.

The control panel provided by MSK Group in DOOCS allowed us to view the reflection from the cavity and the probe signal within the cavity. As a result of conditioning and injecting RF inside the cavity, the temperature inside the cavity may change, resulting in a change in resonance frequency inside the cavity. In order to return to optimum conditions, by using the frequency modulation included in the control panel of this RF gun, it is possible to adjust the frequency of the input RF wave into the cavity so that the reflection signal is minimized and the probe signal is maximized, which is a sign of optimum coupling. As an example, when RF power was injected into the cavity for the first time at a power of 1 kW, it was observed that the reflection signal increased slightly. After changing the frequency modulation by +10 kHz, as shown in Figure 3.12, the reflection signal again reached its minimum value.

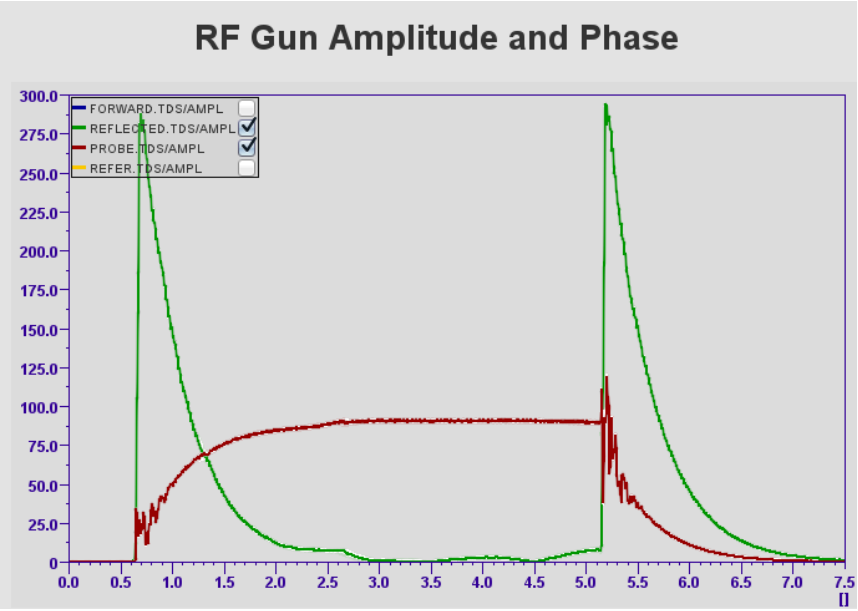

Figure 3.12: Probe signal (red) and reflection signal (green) from the cavity on the control panel of the REGAE accelerator

Multipacting is observed for the first time at a power of 1.5 kW, visible by multiple breakdown and recoveries of the amplitude of the probe signal (blue line in Figure 3.13 shows 3 cycles at 1.5 kW). As shown in this figure, the reflection probe is different from the spark or stable state, which means that in the multipacting phenomenon, electrons absorb more energy from RF power (low amplitude in probe signal) and change the cavity resonance (higher amplitude of reflection signal). As a matter of fact, following the impact of electrons on the inner surface of the cavity, secondary electrons are generated, and then, by synchronizing with the RF frequency, they hit the inner surface of the cavity repeatedly, causing an avalanche of electrons very quickly, and consuming the majority of the power within the cavity.

After some minutes (less than half an hour) multipacting disappeared due to the conditioning effect and the probe signal was stable again, then we ramped up the power of the amplifier to 2.15 kW and then more cycles of the multipacting were observed (Figure 3.14).

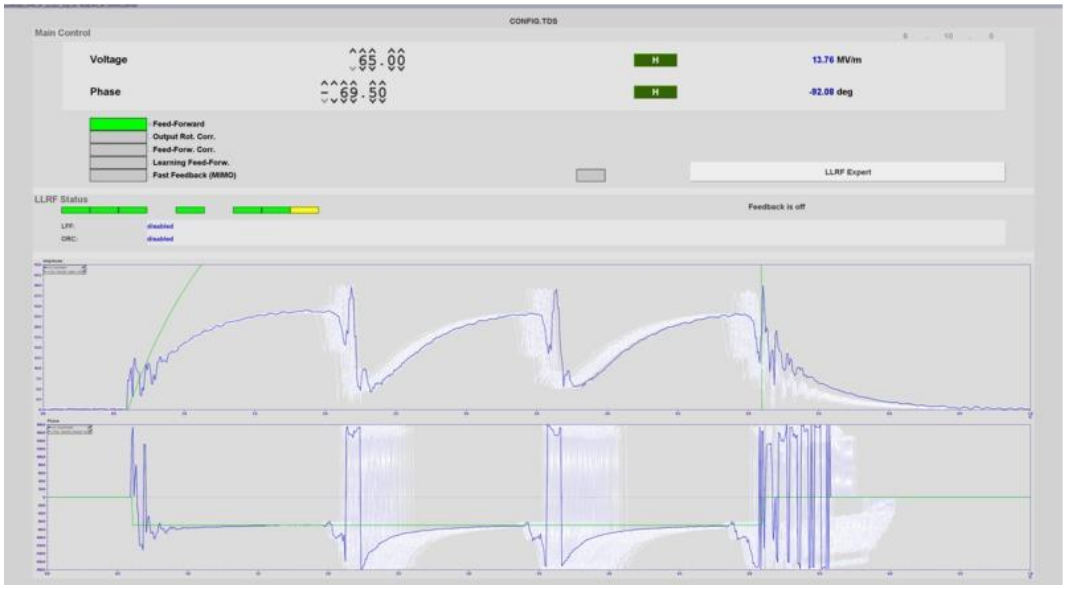

Figure 3.13: Displaying the probe signal from the cavity on the control panel of the REGAE accelerator. Observation of multipacing at 1.5 kW

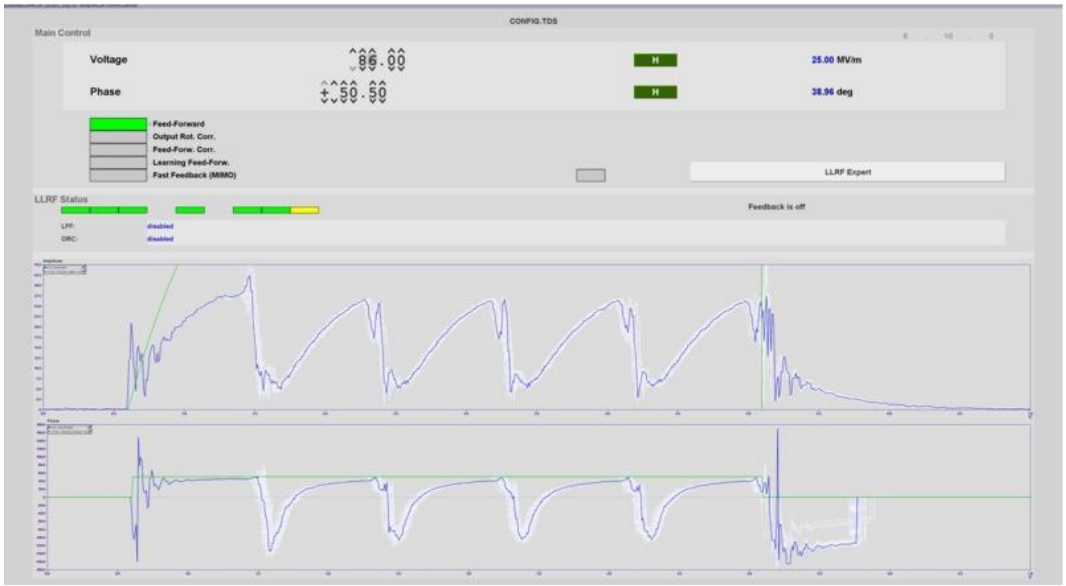

Figure 3.14: Observation of multipacing with 5 cycles at input power of 2.1 kW

At around 3.2 kW, the multipacting disappeared. Going further at 4.1 kW, arcing appeared at each single voltage step but got weaker within minutes. The pressure increased at least one order of magnitude to 10^{-6} mbar range in these arcing phases. At high fields, the typical cyclic multipacting is no longer an issue, though. Instead the arcing reappeared early and has some additional wiggles on it. Figure 3.15

shows the Forward and probe signals when in the spark state. Furthermore, Figure 3.16 illustrates the instability of the probe signal and the increase in the reflection signal.

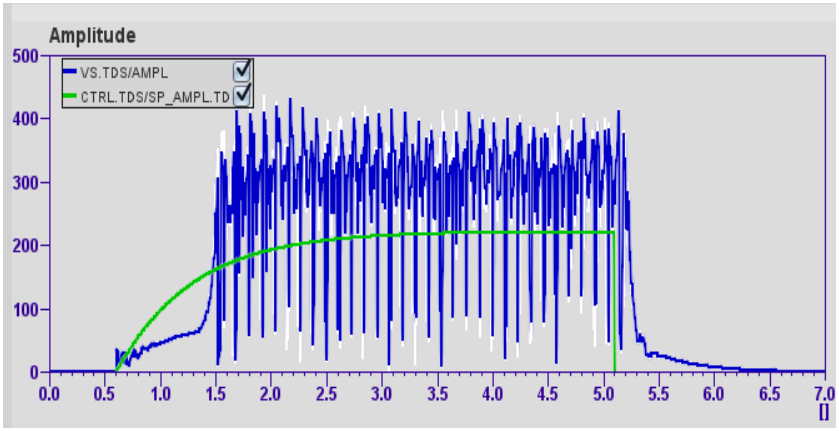

Figure 3.15: The forward (green) and probe (blue) signals of the cavity at 10 kW power in the spark state are shown on the control panel of the RF gun

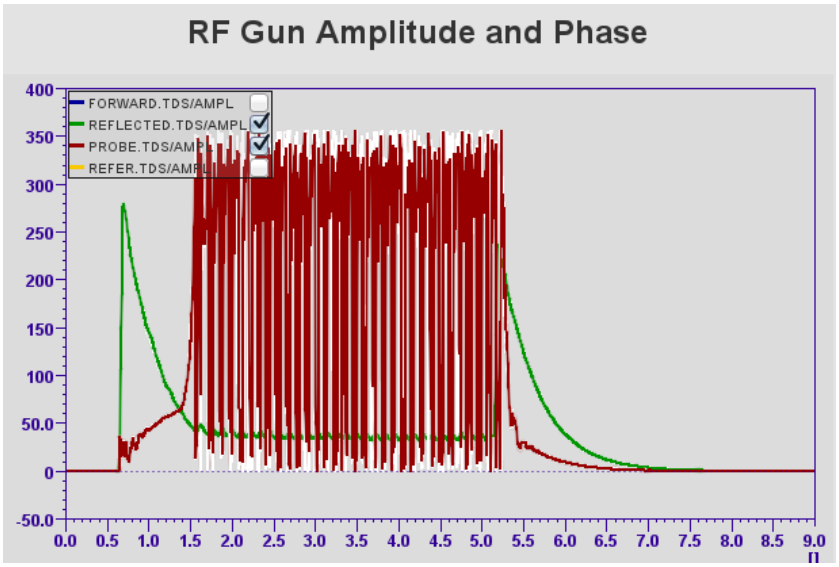

Figure 3.16: The probe (red) and reflection (green) signals of the cavity at 10 kW power in the spark state are shown on the control panel of the RF gun

Experiment with the Solenoid:

After installing the appropriate cables for the solenoid, preparing the power supply, connecting the thermocouples and the thermo-switch on the solenoid, and installing the remote controls, this solenoid was used to continue conditioning of the RF gun.

Based on the simulations related to the multipacting carried out before the experiment and presented in detail in chapter 5, the Multipacting phenomenon will be greatly intensified inside the cavity by applying a solenoid magnetic field, particularly at high currents. At 4.6 kW amplifier power and stable probe signal, the solenoid current was gradually increased. The behavior of the probe and reflection signals in Figure 3.17 indicates that the multipacting in the cavity is much stronger, and takes longer to disappear.

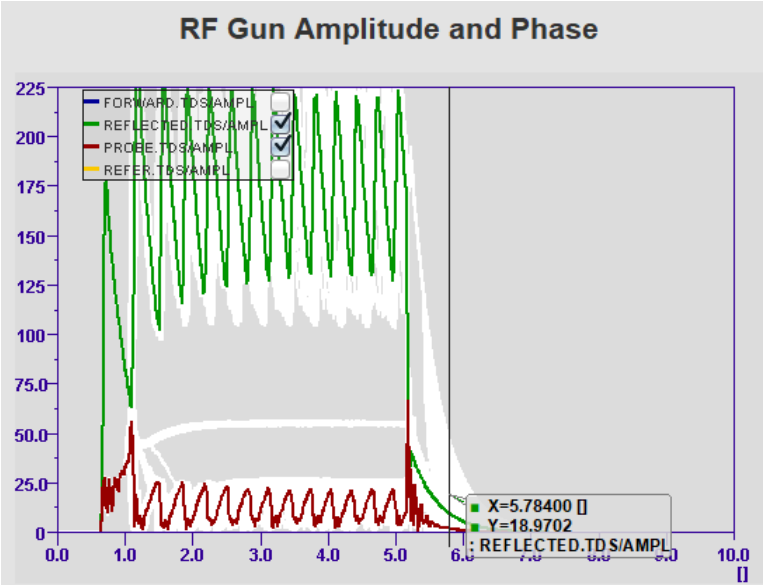

Figure 3.17: The probe (red) and reflection (green) signals at 4.6 kW power and 30 A solenoid current

At 10 kW amplifier power and with the solenoid current setting between 30 and 120 A, the multipacting behavior is similar to before. However, at currents higher than 120 A, the multipacting is much more severe since the probe signal remains constant at its minimum value near zero. The probe and reflection signals are illustrated in Figure 3.18 so that the power injected into the cavity is 10 kW and the solenoid current is 180 A. It will be shown in Chapter 5 that at high currents, electrons are trapped in a certain area around the cavity and cannot leave the cavity, resulting in the generation of more and more secondary electrons, and eventually, they absorb almost all of the RF power within the cavity.

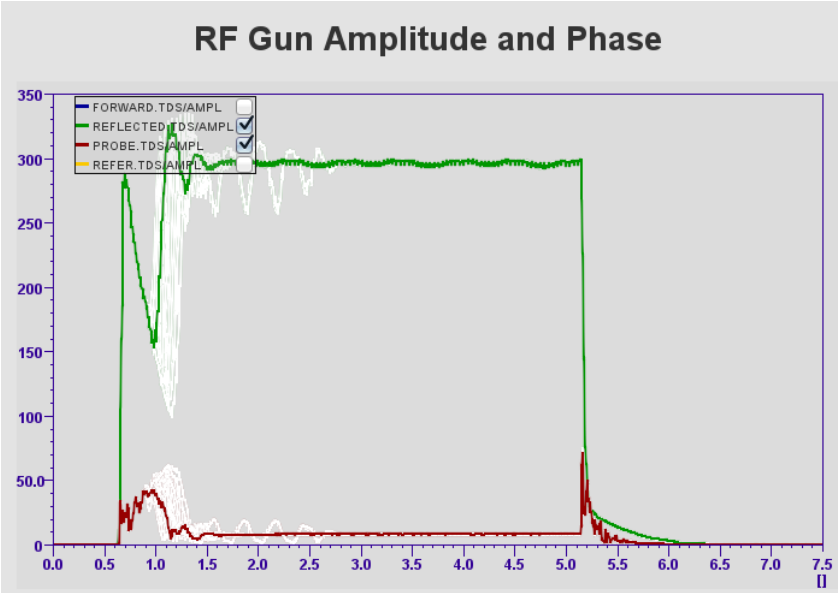

Figure 3.18: The probe (red) and reflection (green) signals at 10 kW power and 180 A solenoid current

In order to measure the dark charge generated inside the cavity, we use a Faraday cup which is attached to the vacuum chamber of the RF gun approximately 30 cm downstream. By connecting the feedthrough to an oscilloscope and triggering it with the RF signal input to the RF gun, a measurement of the dark charge can be accomplished. The maximum amount of dark charge is observed at 10 kW power and 180 A solenoid current, which equals 400 pC (Figure 3.19). For this RF gun, this amount of dark charge is high, and it indicates that there may be some scratches on the tip of the pin cathode. For the next iteration of the RF gun, it is recommended that the pin cathode part be produced with a lower roughness in the nm range.

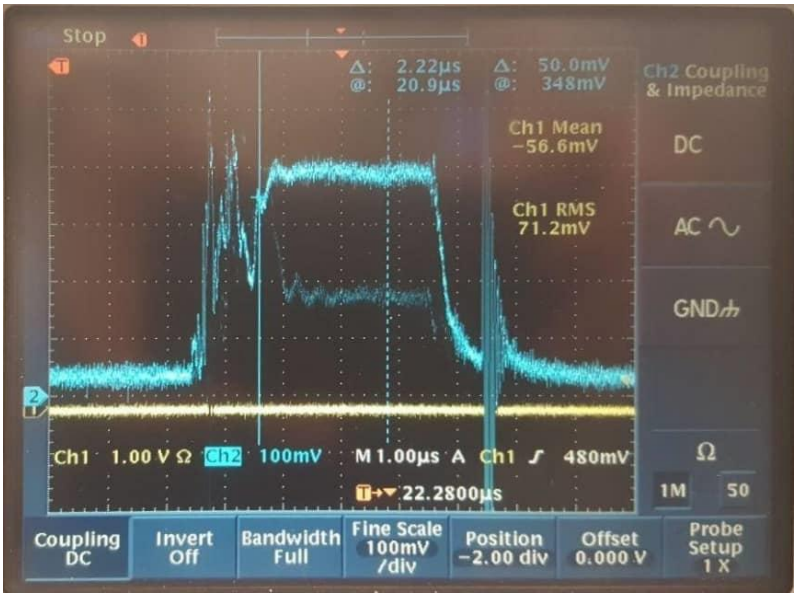

Figure 3.19: Voltage measured by an oscilloscope in order to measure dark charge using a Faraday cup

3.4 Conclusions of the experiments

As we saw in the previous section, despite severe multipacting at high solenoid currents, relatively stable states can be achieved after several days of conditioning. However, the sparks inside the RF gun, which mostly occur at high RF powers, still exist and are the main problem with this gun.

The system has to come to a state where we can switch it on and off without changing its performance, this is part of the conditioning. However, as mentioned earlier, the system is still unstable. The RF gun prototype provided a good experience, however, it would be better to consider another design that includes:

1. Design of stable couplers (vibration-free) by using suitable holders for them, since touching the couplers will change their frequency resonance and coupling.
2. Multipacting: The next generation RF gun can be designed so that electrons do not accumulate densely in the corners of the cavity.
3. Dark charge: Identification of a company that is capable of minimizing roughness in pin cathodes within a range of nanometers.

4. Cleaning the vacuum system: The quality of the internal surfaces of the RF gun, especially in the cavity section, has a significant effect on Dark charge and multipacting, so it is essential to do so as carefully as possible [32].
5. Temperature control is necessary to tune the cavity remotely.
6. Much simpler design with:
    a) fewer sharp points to supress sparking as much as possible
    b) simpler and shorter coupling antennas

We are still working on prototypes and may need more than one iteration. In any case, these experiments provided us with valuable experience and allowed us to demonstrate:

1. The gun is no radiation hazard and we can power it up to 10 kW.
2. Operate the solenoid up to high currents.
3. The vacuum was generally acceptable, and we were able to condition it to some extent.
4. The multipacting could be suppressed by RF conditioning within a month.
5. There is a good agreement between multipacting simulations and experimental results that will be discussed in Chapter 6.
6. We are aware of the parts that need to be improved (cavity and couplers) or removed (for example, the rear housing and turbopump should be removed).

3.4.1 Visual inspection of the gun after conditioning

Upon completion of the conditioning process, it is worth opening the cavity and looking at the inner surface. We will certainly observe spark or multipacting marks on the inner surfaces of the cavity. A prototype designed based on these findings can be developed in the future.

According to Figure 3.20, there were a dark spots located approximately 47 mm away from the tip of the antenna coupler. A comparison with the CAD model (Figure 3.21) reveals that this point corresponds to the location of the venting holes in the coupler design for vacuum improvement. Most likely, this point was responsible for the sparks observed during conditioning at high RF powers. There

were no arcing spots in the coaxial core of the probe coupler because the RF power in this region is relatively low.

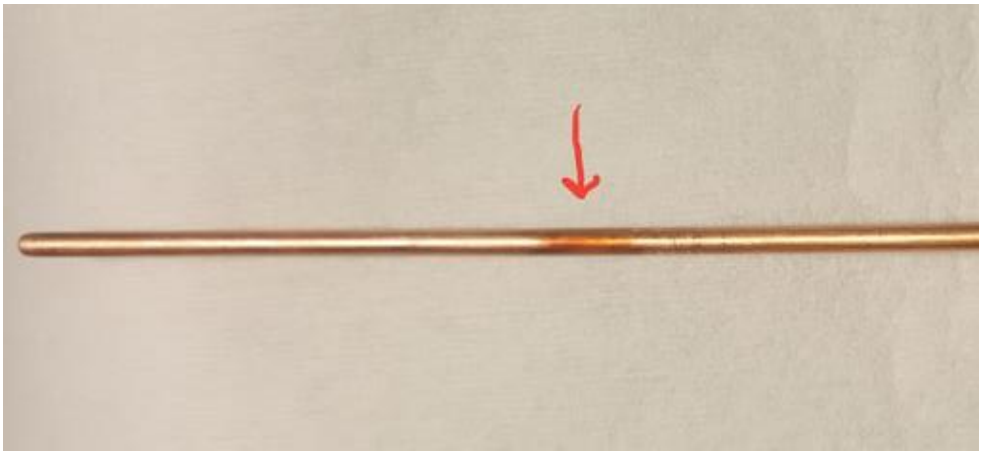

Figure 3.20: A dark spot on the feeding coupler 47 mm away from the tip.

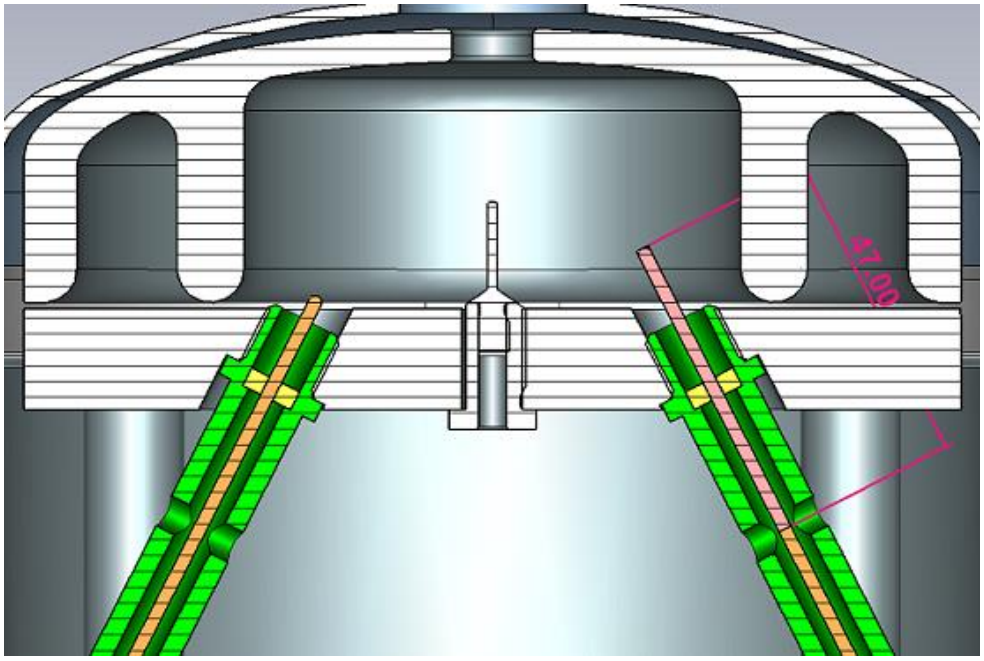

Figure 3.21: A sectional view of the couplers and cavity design illustrates where arcing occurred during the experiment.

Visual inspection of the anode part reveals a few clean spots, especially in the corners of the cavity (red circles in Figure 3.22). These spots are most likely the

result of electron accumulation caused by the multipacting phenomenon, as described in Chapter 5.

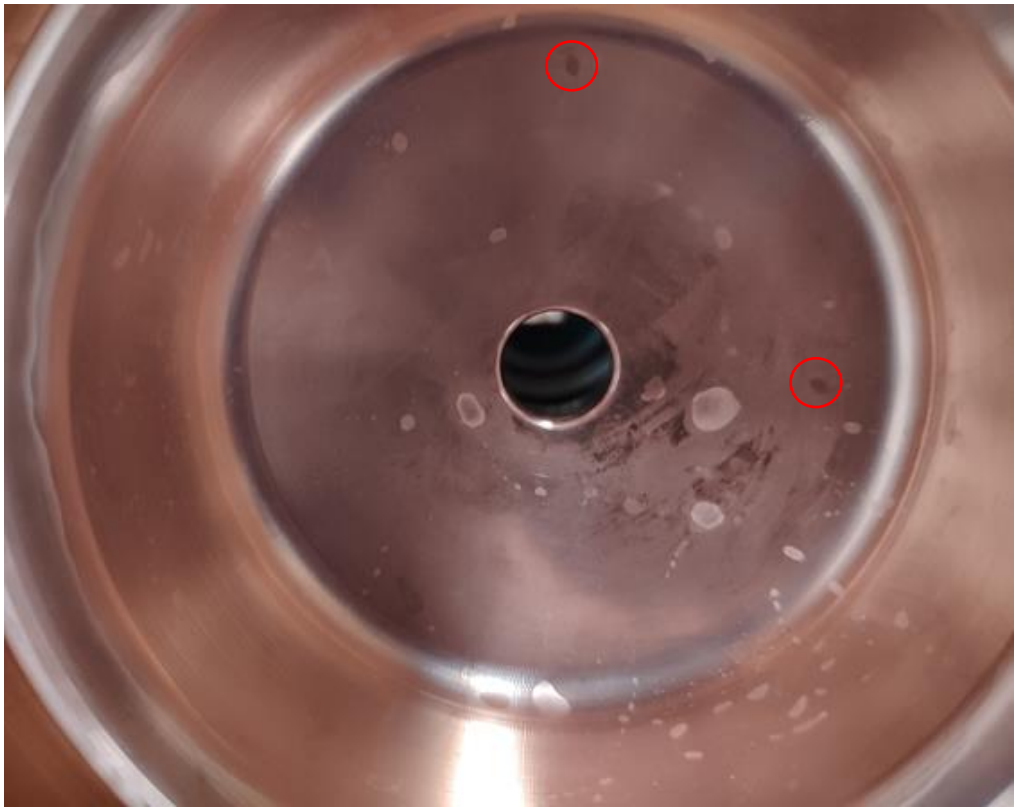

Figure 3.22: Visual inspection of the anode part of the gun after the conditioning.

It can also be seen that the connection between the feedthrough and the antenna in the antenna coupler is darker than the one in the probe (Figure 3.23). Obviously, the antenna coupler has been exposed to a higher RF field, and in addition, the sudden change in the cross-section of the coaxial coupler may lead to more power reflection, which may result in arcing in this region as well.

Using an optical microscope, Figure 3.24 shows the tip of the pin cathode, which has many scratches and cause a high dark charge. The pin cathode should be machined to a roughness much less than 100 nanometers in the next iteration of the RF gun.

Figure 3.23: Visual inspection of the feedthroughs of the couplers after the conditioning.

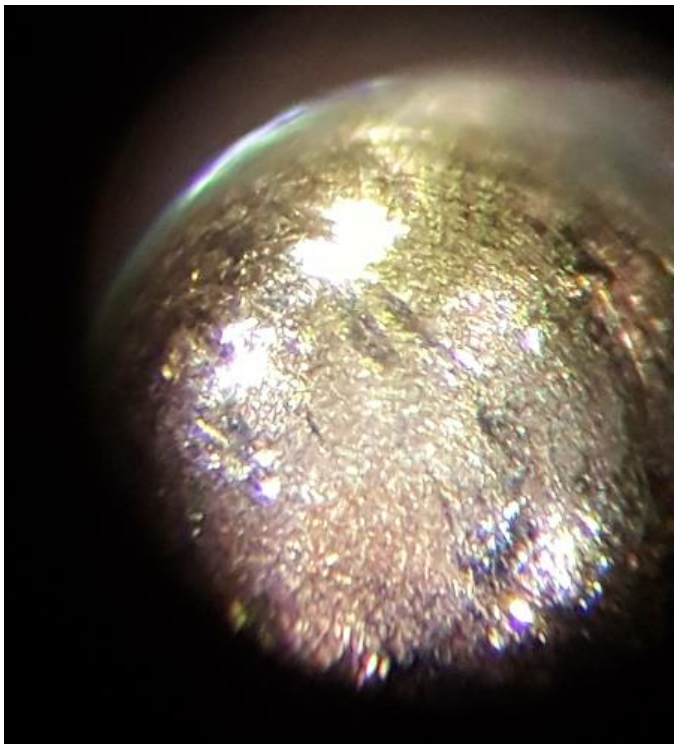

Figure 3.24: Observation of the tip of the cathode pin using an optical microscope

Chapter 4

Compact RF Gun, Prototype II

According to the previous chapter, the first prototype of the RF gun provided valuable experience that we will build on during design and experiment of the second iteration. It is necessary, for instance, to change the design of the couplers, and to reduce the roughness of the pin-cathode to the nm range, as well as to properly clean the cavity in order to decrease dark charge and multipacting. A simpler design should be developed in order to reduce the number of sharp points and prevent sparks.

To ensure that RF leakage is prevented and optimal coupling is designed, detailed microwave simulations have been conducted, which are presented in this chapter. Additionally, a vacuum simulation will be performed in order to determine whether the pressure inside the cavity is in a suitable range. Since the RF gun may be used as a photoinjector into a THz-driven booster, beam dynamic simulations are performed in order to determine the optimal conditions for RF gun operation as well as the influence of laser beam properties, RF phase, and solenoid magnetic field on electron beam quality.

4.1 Microwave simulations

To perform microwave simulations for an enclosed cavity, electromagnetic fields can be decomposed into eigenmodes [33]. Each mode corresponds to a resonant electromagnetic field with a distinct eigen frequency. It is necessary to simulate the Eigenmode mode in order to investigate the resonance frequencies inside the cavity as well as the side frequencies that are present around it. Knowledge of the field distribution in the accelerator cavity helps to optimize the cavity geometry and coupler design. The frequency, quality factor, and (R/Q) of each mode can be determined by solving corresponding eigenvalue problems.

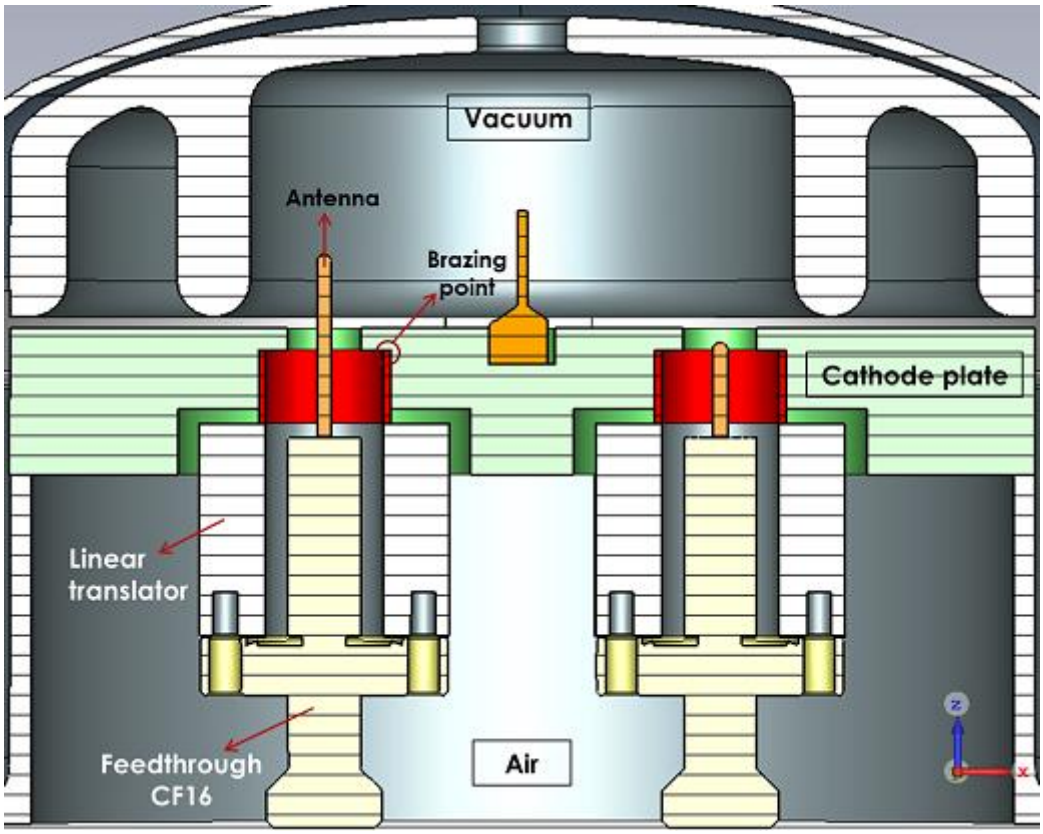

Figure 4.1: Design of the second prototype RF gun with shortened and straight couplers, for eigenmode simulations

The second prototype is designed based on the observations and experience made with the first prototype, and the length of the couplers is minimized in order to stabilize the resonance frequency. Figure 4.1 illustrates the initial design of the second prototype of the cavity used in the 3D eigenmode simulation.

CST Studio Suite® software was used for the microwave simulations, which provides access to multiple electromagnetic (EM) simulation solvers using methods such as the finite element method (FEM). An eigenmode solver is a three-dimensional solver that uses Krylov subspace method (AKS) and Jacobi-Davidson method (JDM) to simulate resonant structures within CST software, allowing cavities in particle accelerators with high Q to be modeled.

In order to simulate the eigenmode, we entered the vacuum geometry according to Figure 4.2 into this solver with PEC (Perfect Electrical Conductivity) as the background. One of the most important aspects of this simulation is determining the external quality factor and comparing it with the unloaded quality factor in order to determine the coupling conditions. To achieve this, we must define a "port waveguide" on the feedthrough which is used for RF power injection. Figure 4.2 illustrates this port along with the structure of the coaxial waveguide feedthrough manufactured by DESY.

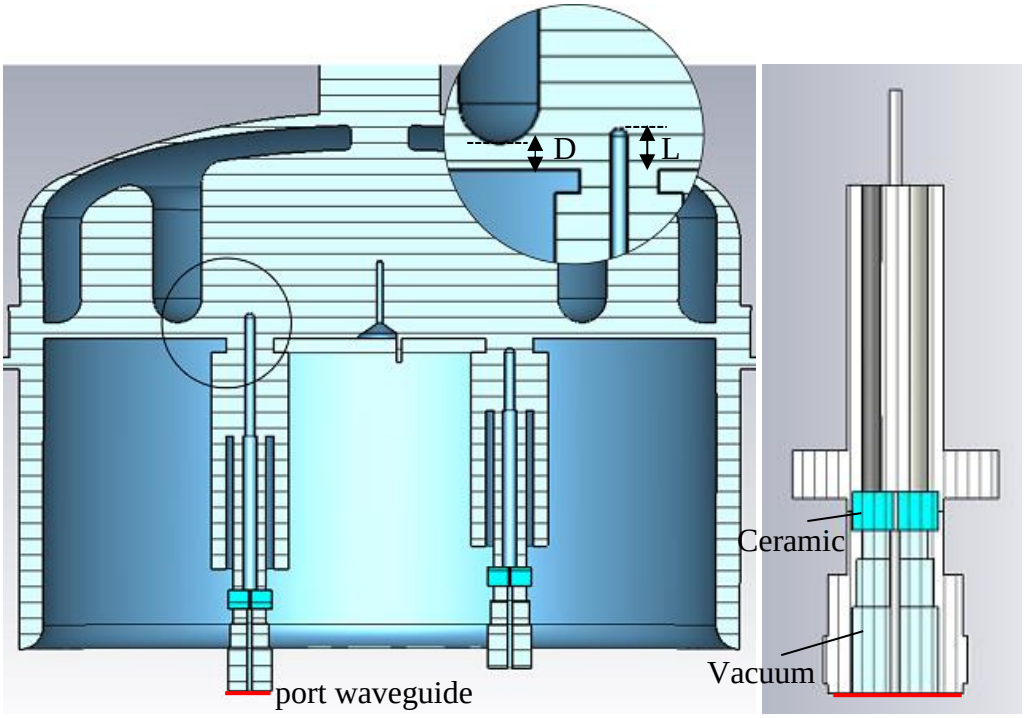

Figure 4.2: Left: 3D model of the vacuum geometry of the cavity in the eigenmode solver, right: coaxial feedthrough and waveguide port

In determining the resonant frequency in this cavity and the optimal coupling, the distance between the cathode and anode (D) and the length of the antenna (L) inside

the cavity are crucial parameters shown in Figure 4.2. For determining the resonant frequency, the distance between the anode and cathode is the most important parameter. By adjusting these two parameters, a point can be reached where the resonance frequency inside the cavity is 2.998 GHz and the coupling coefficient is equal to 1 (the unloaded quality factor is equal to the external quality factor).

A resonant frequency equal to 2.998 GHz inside the cavity can be achieved at a given value of D and L as shown in Figure 4.3. Clearly, the frequency cannot be equal to 2.998 GHz for D values less than 3 mm or greater than 3.4 mm. As discussed in the previous chapter, the frequency inside the cavity is primarily determined by the distance between the anode and the cathode. In order to achieve optimal coupling, it is necessary to determine the coupling coefficient for the points shown in Figure 4.3, where the resonance frequency is 2.998 GHz. According to Figure 4.4, coupling coefficient (β) is equal to 1 when D =3.2 mm. Finally, the cavity will be optimally coupled at 2.998 GHz if D is 3.2 mm and L is 6 mm.

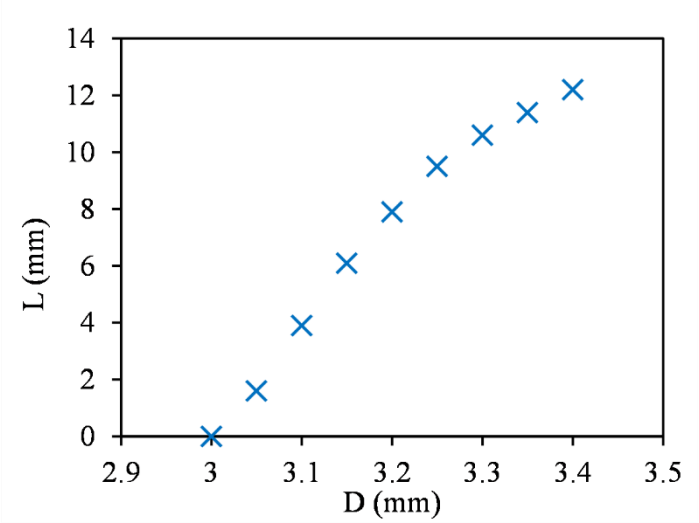

Figure 4.3: The distance between the cathode and anode (D) and the length of the feeding antenna within the cavity (L) that will result in a resonance frequency of 2.998 GHz.

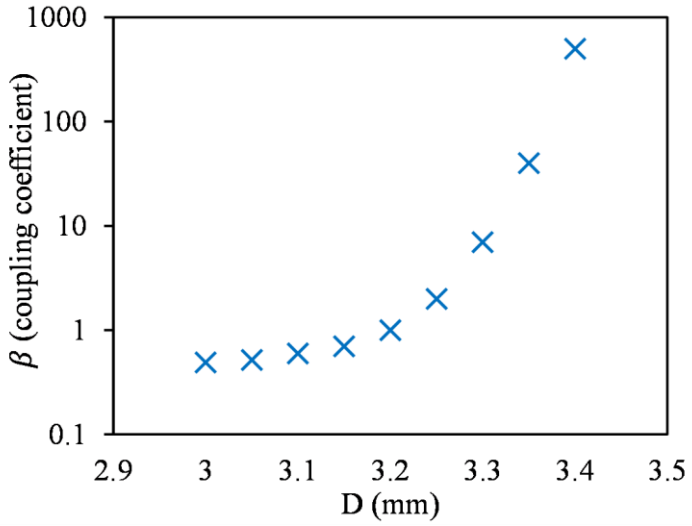

Figure 4.4: Investigating the values of the cavity coupling coefficient for cases in which the resonance frequency is 2.998 GHz.

Several eigenmode simulations were conducted to determine the effect of the length of the antenna inside the cavity (L) on the coupling and resonance frequency. For example, in Figure 4.5, the resonance frequency is shown as a function of the antenna length in which the distance between the anode and the cathode is equal to 3.2 mm. Moreover, in Figure 4.6, the effect of antenna length is shown on the unloaded quality factor and external quality factor, so that the critical coupling conditions can be determined from the intersection of these diagrams.

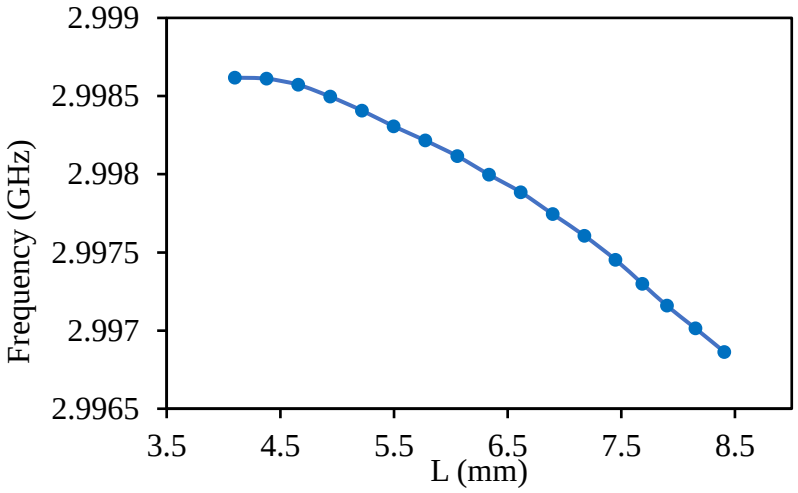

Figure 4.5: The effect of antenna length within the cavity (L) on resonance frequency at 3.2 mm anode-cathode distance

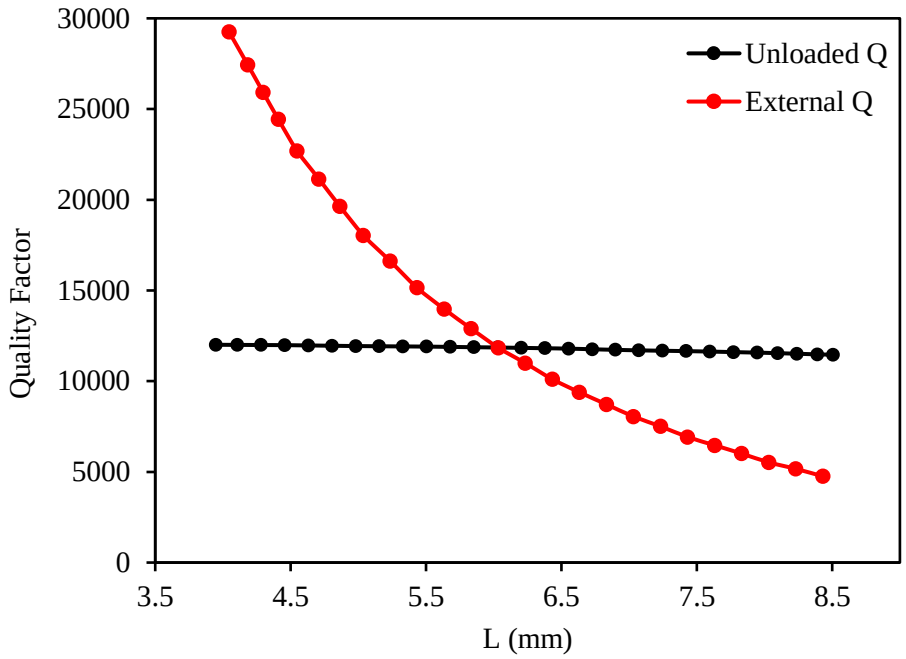

Figure 4.6: An analysis of the impact of the length of the antenna inside the cavity (L) on the external and unloaded quality factors, at 3.2 mm anode-cathode distance

Simulating the eigenmode of the RF gun, which is obtained under optimal cavity conditions, allows us to see how the electric and magnetic fields are distributed in the main mode. The magnitude of the electric and magnetic field resulting from the Eigenmode simulation with CST software is shown in Figure 4.7 and Figure 4.8 under the condition that one joule of RF energy is injected into the cavity. With this optimized cavity, the unloaded quality factor is equal to 11850, which represents an increase of approximately 20% over the previous design.

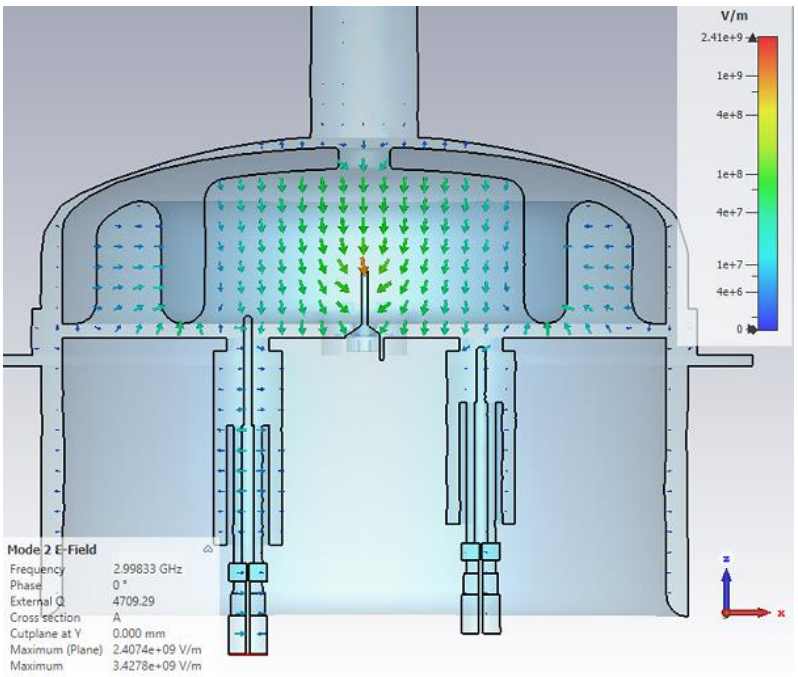

Figure 4.7: The distribution of the electric field in the main mode of an eigenmode simulation with 1 Joule feeding under optimal cavity design conditions.

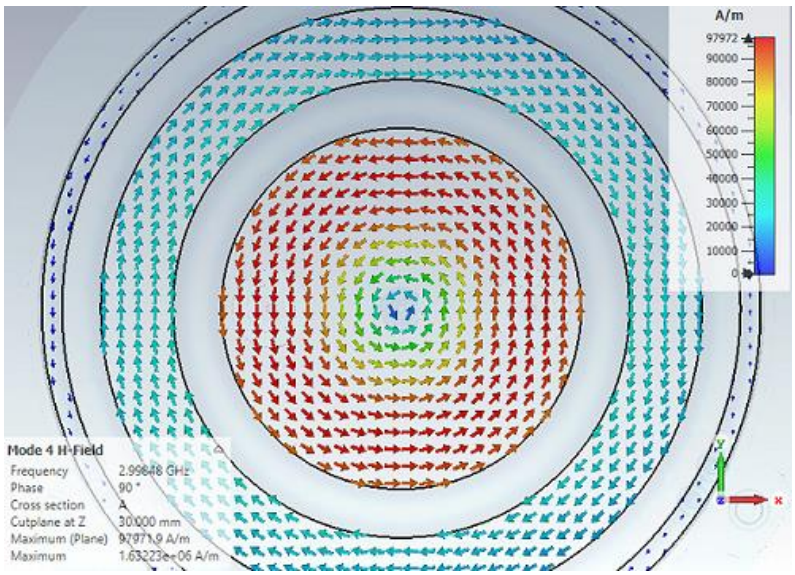

Figure 4.8: The distribution of the magnetic field in the main mode of an eigenmode simulation with 1 Joule feeding under optimal cavity design conditions.

Figure 4.9 illustrates other modes of eigenmode simulations with optimal cavity parameters. These adjacent modes do not resonate inside the cavity, and they are

excited at frequencies of 2.96 and 3.018 GHz, which are sufficiently distant from the frequency of the main mode.

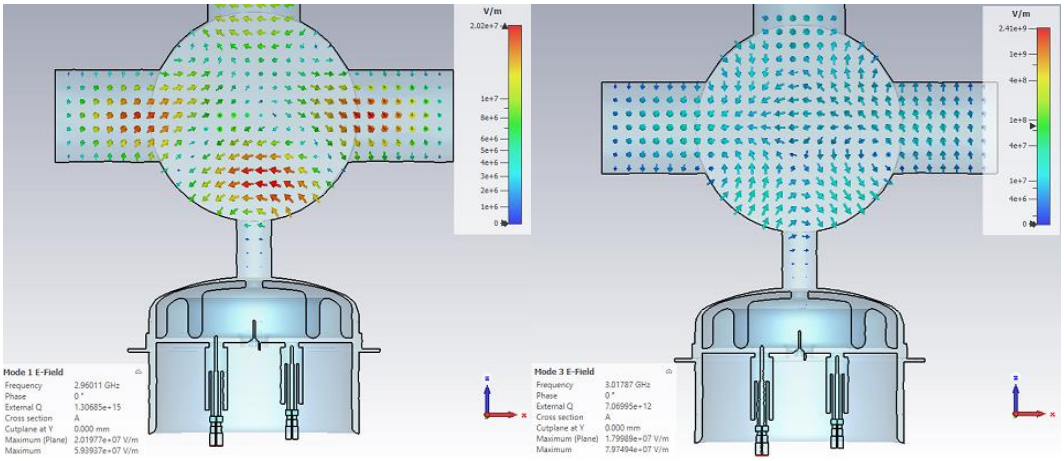

Figure 4.9: The side resonances that appear in the eigenmode simulation show that it has a relatively distant frequency compared to the main resonance frequency of the optimized RF gun at 2.998 GHz.

Besides creating a model with metallic walls it is recommended to fill it with vacuum and make background of PEC (Perfectly Electric Conducting) as shown in Fig.1. This eliminates parasitic mode simulation outside a cavity.

Further to the eigenmode simulation described above, it is recommended to simulate a model with metal walls so that the interior space is filled with vacuum material and the PEC background is considered [34]. The simulation will take longer to run, but it eliminates parasitic mode simulations outside the cavity and the results will likely be more accurate. As shown in Figure 4.10, the complete geometry of the RF gun along with the steel and copper materials is included in the eigenmode simulation. Simulation results are very similar to those described above and the resonance frequency is exactly 2.998 GHz. The only difference is that the unloaded quality factor is equal to 11715, which indicates that there has been very little RF loss in the steel material.

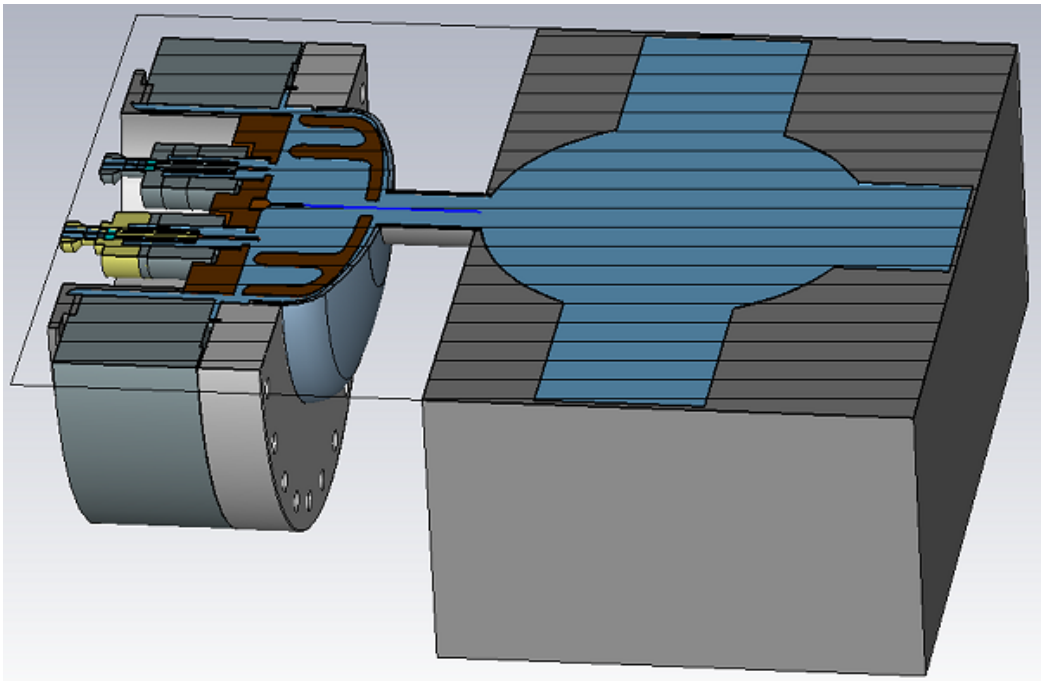

Figure 4.10: The full geometry of the RF gun along with steel and copper materials are included in the eigenmode simulation in order to ensure accuracy.

In addition to eigenmode simulations, the capability of analyzing microwave components in both time domain and frequency domain is highly desirable [35]. Generally, a signal could be described as the sum of many sine waves (Fourier series) that have differing pulses, phases, and amplitudes. Switching between the time domain and the frequency domain and back again, is accomplished by performing mathematical integration using the "Fourier Transform" equations. In fact, when a time-harmonic dependence of the fields and the excitation is assumed, Maxwell's equations may be transformed into the frequency domain.

S-parameters are obtained in CST frequency domain solver by using probe coupled wave ports and the quality factors are calculated thereafter from S_{11}. In the simulation, standard flange mount SMA connectors are modeled on either side of the cavity and excited by two wave ports (on the antenna and probe feedthrough) as shown in Figure 4.2, for extracting the S parameters. The cavity is enclosed by a cylindrical structure of a perfect electric conductor, signifying the metallic walls and hence, the outer conductor is not modeled separately [36]. According to Figure 4.11, S_{11} exhibits a resonance frequency of 2.99808 GHz, along with a quality factor equal to the value obtained from the eigenmode simulation.

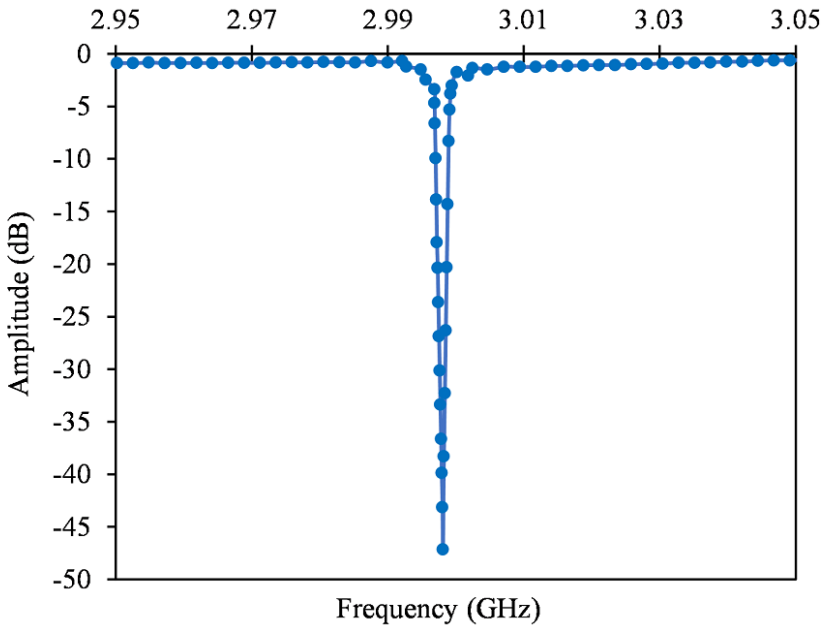

Figure 4.11: S_{11} parameter has been simulated using the frequency domain solver in CST, which indicates a resonance frequency of 2.998 GHz.

In order to adjust the antenna length within the cavity, a linear translator is used, which is equipped with a bellows around the coupler. To avoid sharp points in the RF gun design, an RF finger is integrated around the feedthrough (Figure 4.12). In addition, the cross-section of the coaxial waveguide will be the same from the feedthrough to the cavity entrance, thereby reducing the reflection towards the RF source due to an impedance mismatch. The impact of including this component into the coupler design can be seen in the transient domain solver in CST.

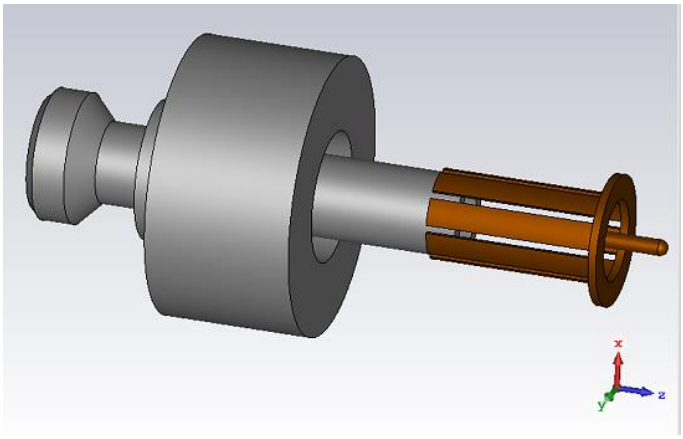

Figure 4.12: The copper RF finger that was employed in the design of the coupler.

In the process of filling the cavity and injecting RF into it, the coupler has a relatively high impedance, resulting in a high electric field around the antenna feedthrough. For this purpose, a transient domain simulation was performed to examine the distribution of the electric field within 10 ns of the RF injection. It can be seen in Figure 4.13 that there is a fairly high electric field around the bellows and in sharper points of the coupler without the RF finger.

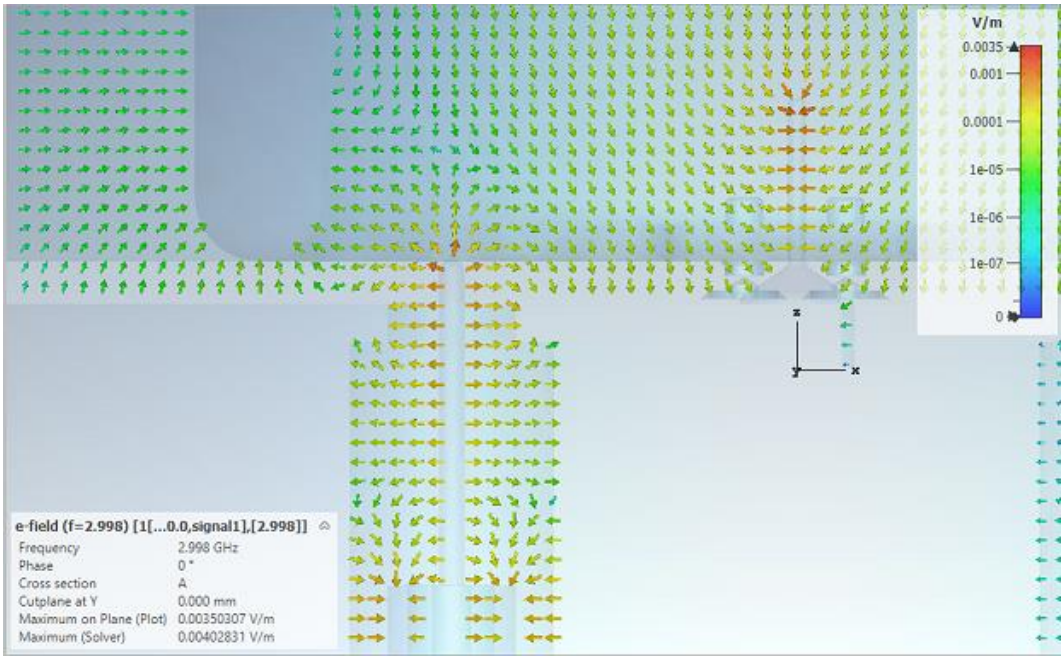

Figure 4.13: Simulation of the electric field distribution after 10 ns of RF injection into the cavity with transient domain solver in CST

The advantage of using the transient domain solver is that points can be regarded as probes in the simulation geometry, and the behavior of the electric field on these probes can be examined at various times during the RF injection. According to Figure 4.14, some probe points have been considered inside and outside the RF finger in order to compare the electric field at these points. As well, a couple of probes were designed on the pin cathode and in the filter choke in order to study the behavior of electric fields in these areas.

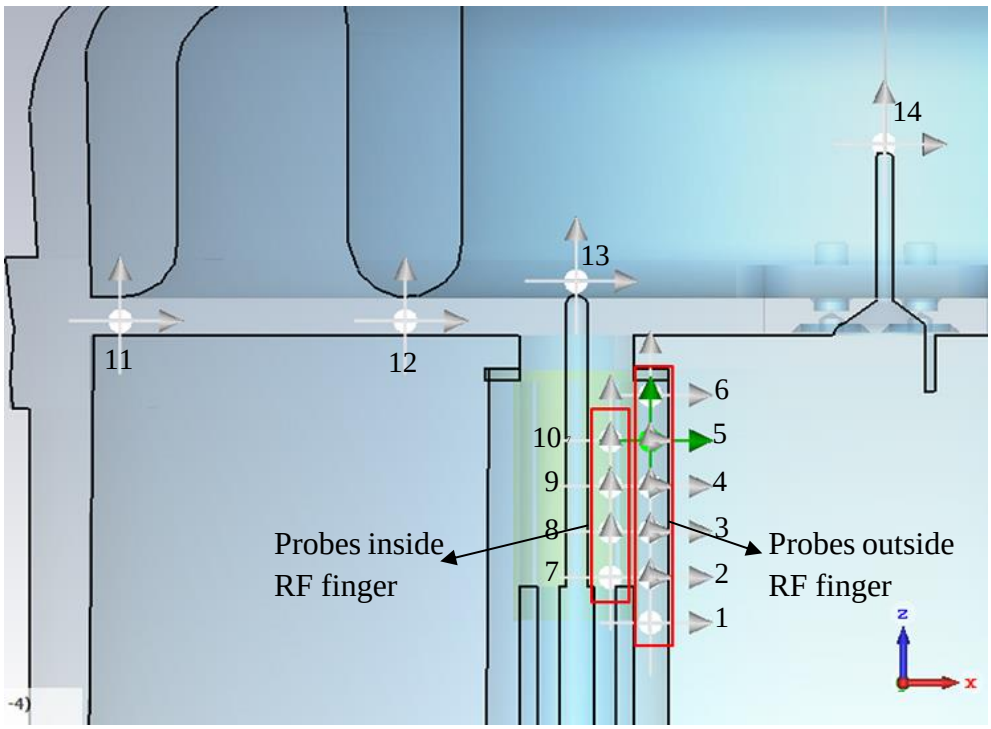

Figure 4.14: Probes are considered in the cavity and coupler for the purpose of studying the behavior of the electric field during RF injection using the transient domain solver.

Based on the comparison between Figure 4.15 and Figure 4.16, it is noticeable that the electric field of the probes outside the RF finger is significantly lower than those inside. Therefore, it is possible to guarantee that by using this RF finger, sparks that may occur at high RF powers are prevented, this issue posed the major challenge during the conditioning of the first RF gun prototype.

The electric field of the probe point near the pin-cathode is shown in Figure 4.17 during the injection time up to 10 ns. By using this microwave simulation solver, the actual filling of the cavity over time can be observed in exquisite detail. According to Figure 4.18, there is a constant electric field on the antenna after a few nanoseconds. Therefore, once the cavity has been filled, the electric field on the antenna will appear much smaller in comparison with the electric field on the cathode, and thus the dark charge will not be significantly affected. In Figure 4.19, the electric field in the choke filter area can also be seen, which is much lower than the electric field inside the cavity, indicating that this filter performs well.

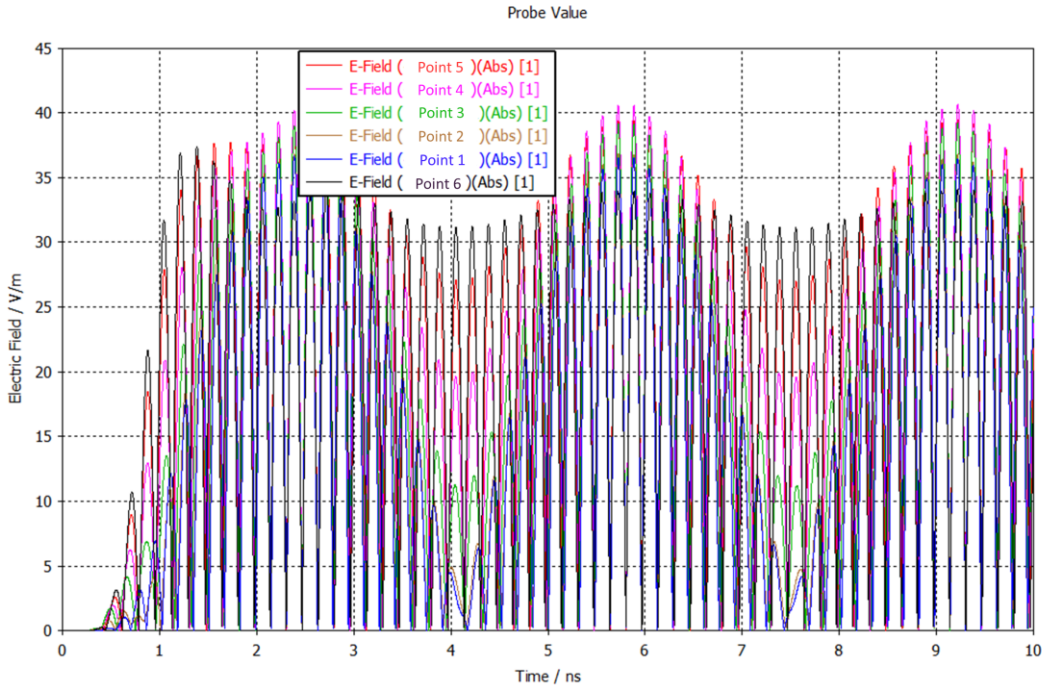

Figure 4.15: Electric field at probe points outside the RF finger was performed in the transient domain solver in CST

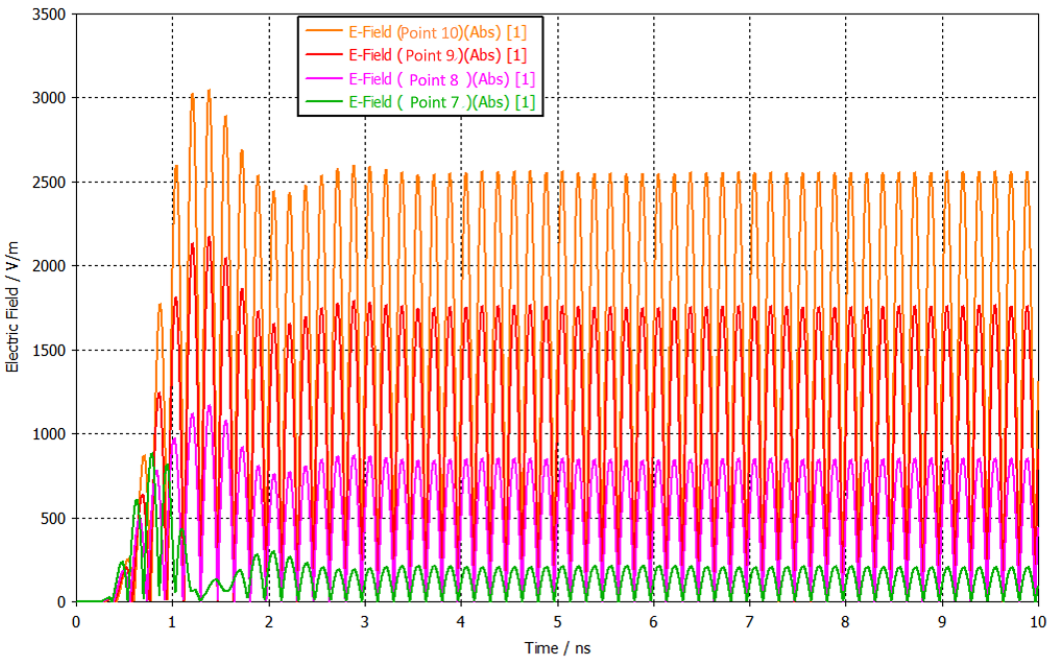

Figure 4.16: Electric field at probe points inside the RF finger was performed in the transient domain solver

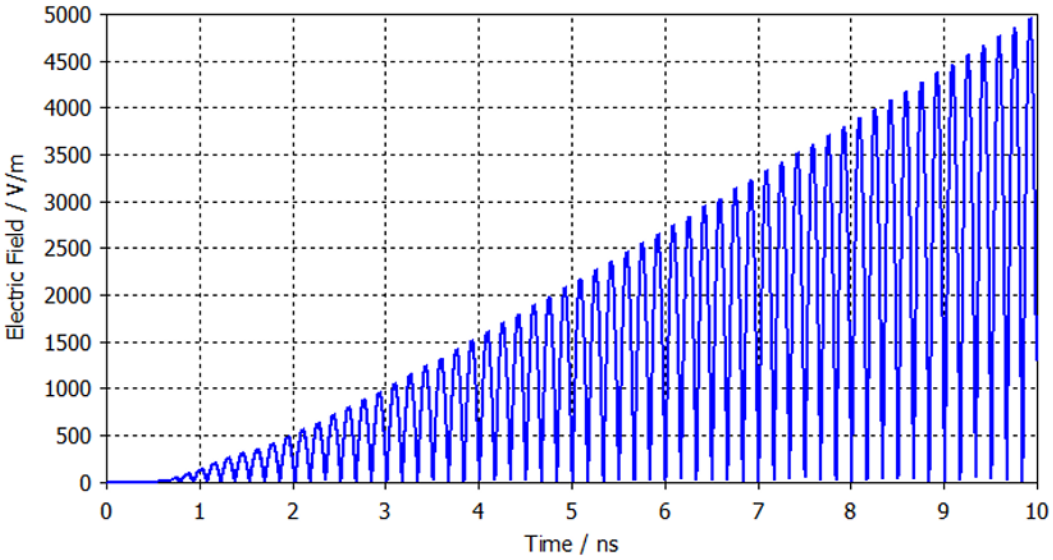

Figure 4.17: Electric field behavior at the tip of the pin-cathode during 10 ns of RF injection was analyzed in the transient domain solver

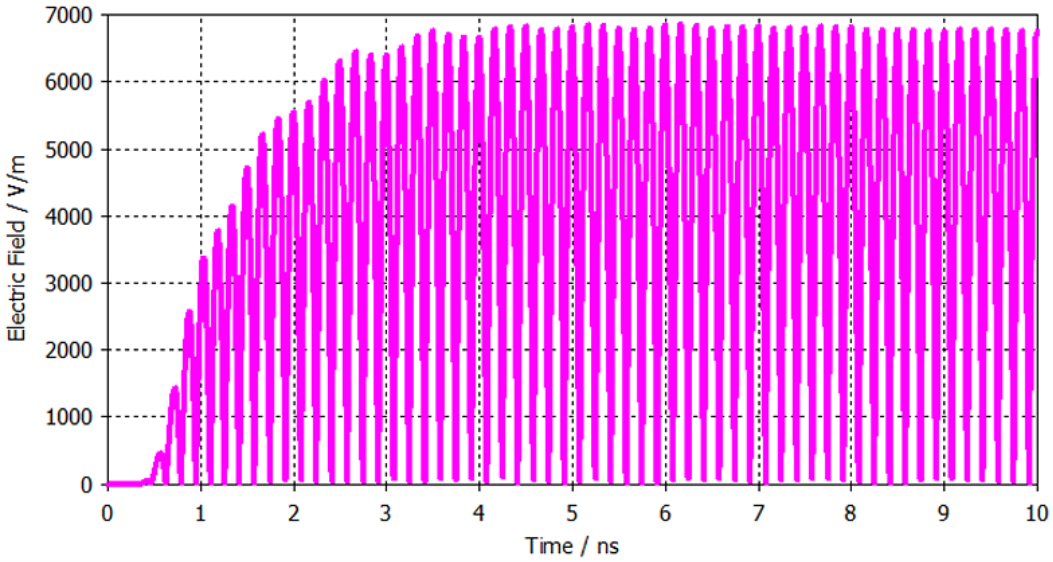

Figure 4.18: Electric field behavior at the tip of the antenna during 10 ns of RF injection was performed in the transient domain solver

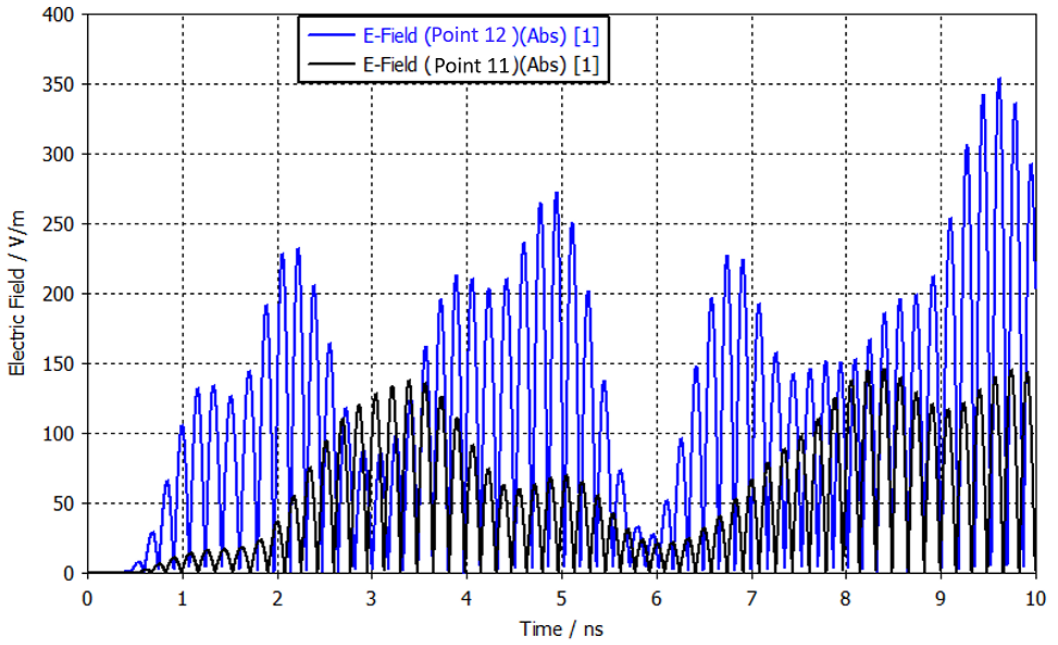

Figure 4.19: Electric field on the probes in the choke filter area was performed in the transient domain solver

4.2 Vacuum simulation

The cavity is cleaned and prepared in such a way that the pressure inside the cavity is in the range of $1 \times 10^{-9}\ mbar$ in order to reduce the possibility of sparks and increase the surface quality. For this reason, in the design of cavity and couplers, vacuum considerations were also taken into account in order to achieve this range of pressure. The vacuum simulation is performed using Molflow+ software [31], which is a Windows program to calculate the steady-state pressure based on the Monte Carlo method. It is very common and practical to use this software for simulating Ultra High Vacuum (UHV) systems in particle accelerators and complex geometries [37].

It is important to perform this simulation separately for both unbaked and baked vacuum chambers. It is estimated that 99% of the gases in unbaked systems are water vapor [38], [39]. The thermal outgassing rate of water vapor escaping the inner surface of the vacuum chamber depends on pumping time and can be calculated using this experimental formula [40]:

$$Q(t) = \frac{2 \times 10^{-9}}{t\,[h]} \quad torr\ \frac{l}{s}\frac{1}{cm^2} \tag{4.1}$$

The outgassing rate will therefore be equal to $2 \times 10^{-10}\ \ torr\ \frac{l}{s}\frac{1}{cm^2}$ after 10 hours of pumping. A turbomolecular pump HiPace 300 is used in the actual setup, which pumps water molecules at 255 l/s [41]. In Figure 4.20, the RF gun geometry can be seen in Molflow+ software. By applying thermal outgassing, temperature, pumping speed, and the molecular mass of 18 g/mol for water, the pressure profile on the path of electrons from the cathode up to 30 cm away (red line in Figure 4.20) can be simulated. Vacuum specialists perform this technique routinely in order to simulate an unbake vacuum system [42]. Figure 4.21 illustrates that the pressure profile in the new geometry can be more favorable than that of prototype I, but the pressure is still in the range of 1E-8 mbar, which is one order of magnitude away from the optimal pressure required to operate the cavity at high powers.

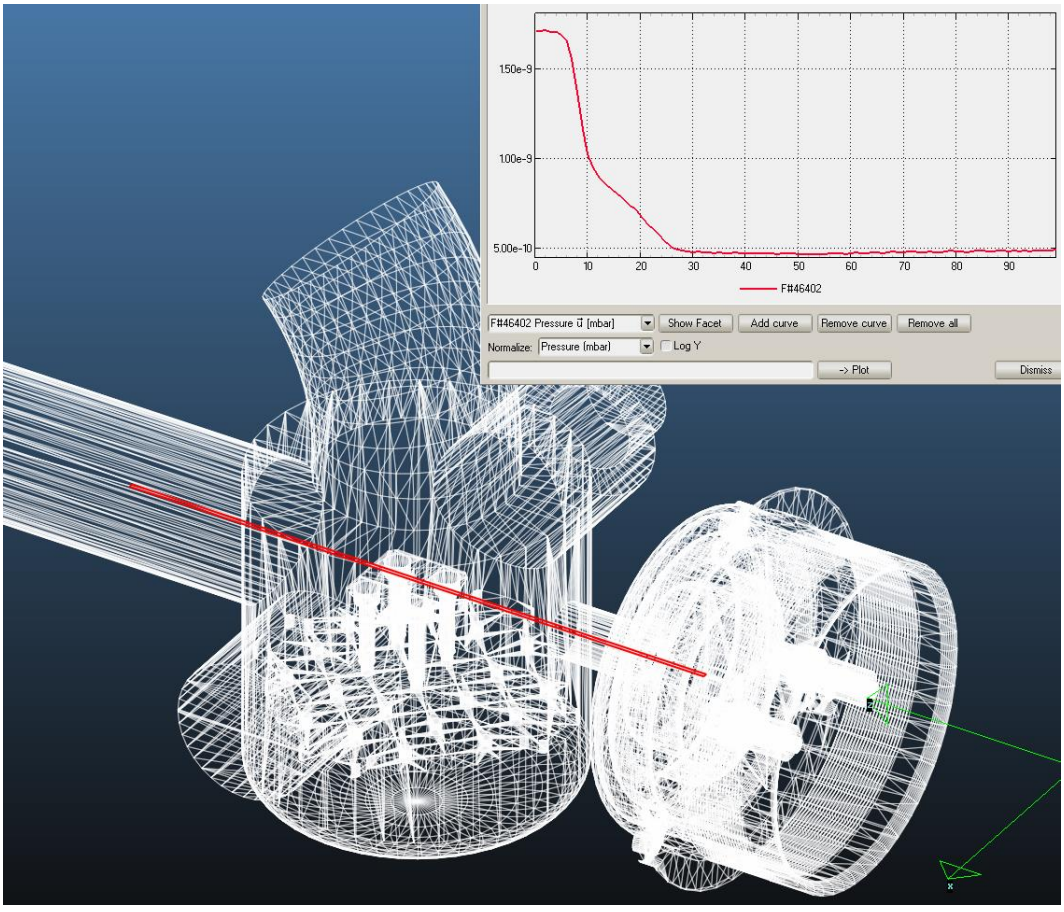

Figure 4.20: Geometry of the RF gun in Molflow+ for simulation of pressure profile

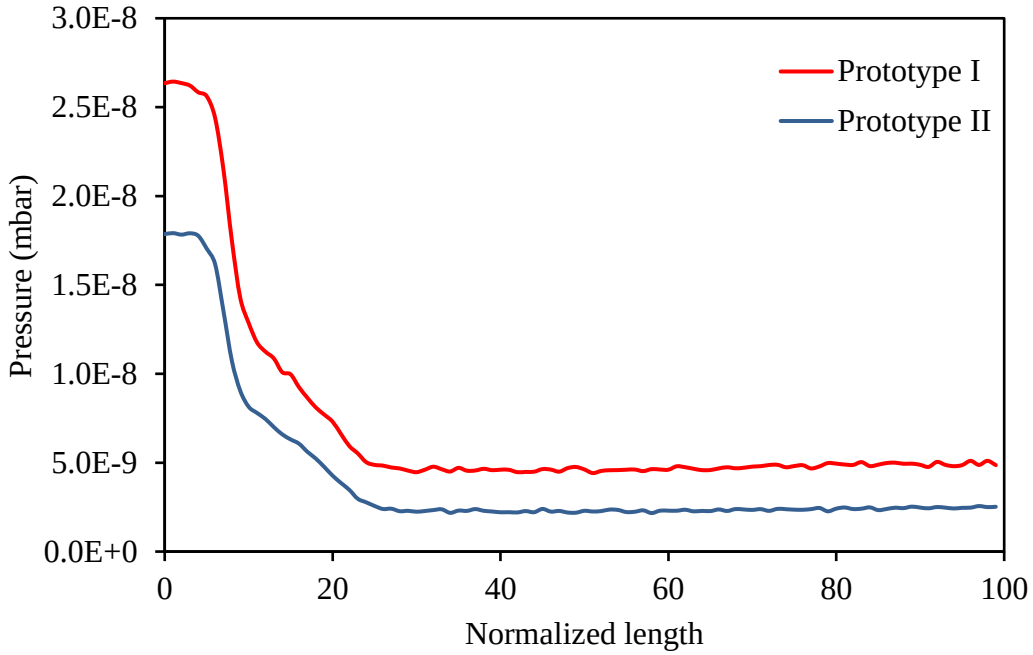

Figure 4.21: Comparison of the pressure profiles for the first and second RF gun prototypes in the unbaked state, simulated with Molflow+ software.

Most of the economic effort that goes into attaining UHV conditions is devoted to reducing water outgassing. The most effective technique for reducing the outgassing of H_2O is in-situ bake-out. The outgassing of baked vacuum systems is dominated (99%) by H_2. Following a standard cleaning and baking-out of the vacuum system for 24 hours at 200 ºC, the thermal outgassing will be approximately $Q = 1 \times 10^{-11}\ torr\ \frac{l}{s}\frac{1}{cm^2}$ [42], [43]. Hydrogen molecules are pumped at 220 l/s by this turbomolecular pump.

The pressure profile in the baked vacuum chamber is shown in Figure 4.22. Hence, the maximum pressure within the cavity is equal to 1.43E-9 mbar, indicating that this vacuum system must be baked in order to reach the desired pressure range for operating the cavity. Figure 4.23 also shows the texture of the pressure profile on the surfaces of the RF Gun vacuum chamber in Molflow software.

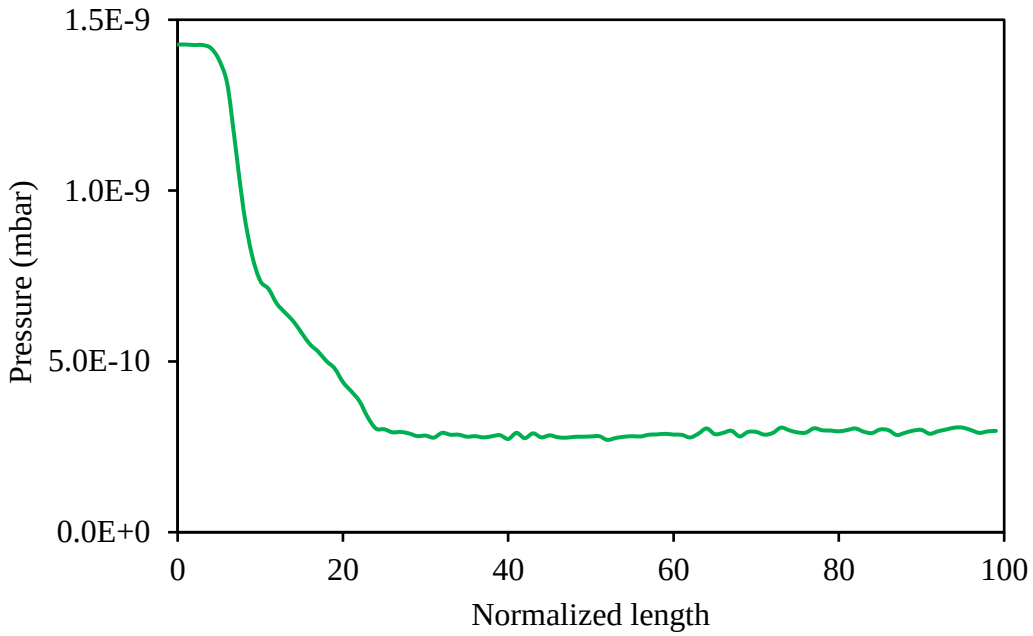

Figure 4.22: Pressure profile of the RF gun prototype II as a baked vacuum system

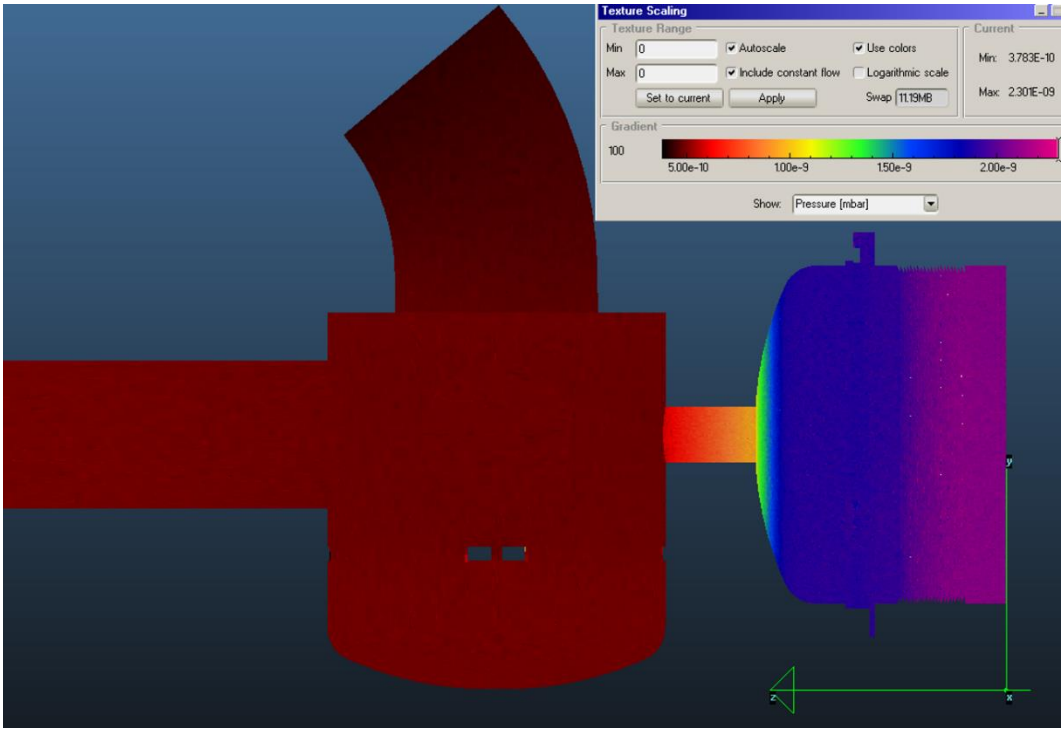

Figure 4.23: Texture of the pressure profile on the surfaces of the RF Gun vacuum chamber in Molflow software

4.3 Beam dynamic simulation

This section focuses on introducing and investigating the quantities used to describe the electron beam in a photoinjector. A potential application of this RF gun is as an injector for a booster, as indicated in the introduction section. Therefore, it is essential to investigate and optimize the electron beam characteristics produced by the RF gun, such as energy, transverse and longitudinal emittance, bunch length, and transverse bunch size during injection into the booster.

As discussed in Chapter 2, the cavity and solenoid of the RF gun are designed so that the electron beam is focused both transversely and longitudinally 8 cm downstream of the photocathode in the vacuum chamber attached to the cavity. This is due to the fact that electrons must be focused on the THz-driven booster. Since the entrance aperture of the booster is approximately 100 μm in diameter [44], the transverse size of the electron beam should be such that most electrons may pass through it. Furthermore, since the THz pulse with a frequency of 300 GHz is used for acceleration of electrons in the booster, the length of the electron beam must be within the range where electrons can be effectively accelerated by the electric field.

4.3.1 Acceleration in an RF cavity

The acceleration of charged particles in a standing wave accelerating structure can be represented in the following way. The reference theory for the beam dynamics inside RF standing-wave electron guns is that of Kim [45]. The amplitude of the electric field on the axis of the standing wave structure at a specific time t is a function of the longitudinal coordinate along the structure and this field oscillates in time according to the harmonic law:

$$E_z(0,z,t) = -E_{acc,0}\, cos(k_{RF} z)\, sin(\omega_{RF} t + \varphi) \tag{4.2}$$

The usual relations between the RF wave number $k_{\mathrm{RF}} = 2\pi/\lambda_{\mathrm{RF}}$ and the angular frequency $\omega_{\mathrm{RF}} = ck_{\mathrm{RF}}$ hold, while φ is the initial RF phase of the structure when electrons leave the cathode. The momentum of an electron passing an accelerating structure is:

$$p_z = p_0 + \int_0^T eE_{acc,0}\, cos(k_{RF} z) \cdot sin(\omega_{RF} t + \varphi) dt \tag{4.3}$$

Where p_z is the momentum of the particle downstream the structure, p_0 is the momentum of the particle upstream the structure, e is the electrical charge of the

particle and T is the time of flight of the particle through the cell. Based on a simple mathematical calculation the particles momentum gain is:

$$p_z = p_0 + p_M \cdot \cos(\varphi) \tag{4.4}$$

Where p_M is the maximum momentum gained by an electron passing through the accelerating structure shown in Figure 4.24. A model of the acceleration of an electron bunch by an RF cavity is shown in Figure 4.24. The resulting momentum of a particle coming to the cavity at phase φ is:

$$p_z = p_0 + p_M \cdot \cos(\varphi - \varphi_0) \tag{4.5}$$

When an electron enters the cavity at phase φ_0, it will obtain the highest possible momentum gain. The RF phase of the electric field in the cavity increases from left to right in Figure 4.24. The head of the bunch is arriving in the cavity first, meaning that it is coming in an earlier phase than the tail. Thus, if the whole bunch enters the cavity earlier than phase φ_0 with a phase difference of $\Delta\varphi$, the tail of the bunch will experience higher acceleration than the head. As a result, the whole bunch will have a momentum chirp - the longitudinal momenta and longitudinal positions of electrons within the bunch will be correlated.

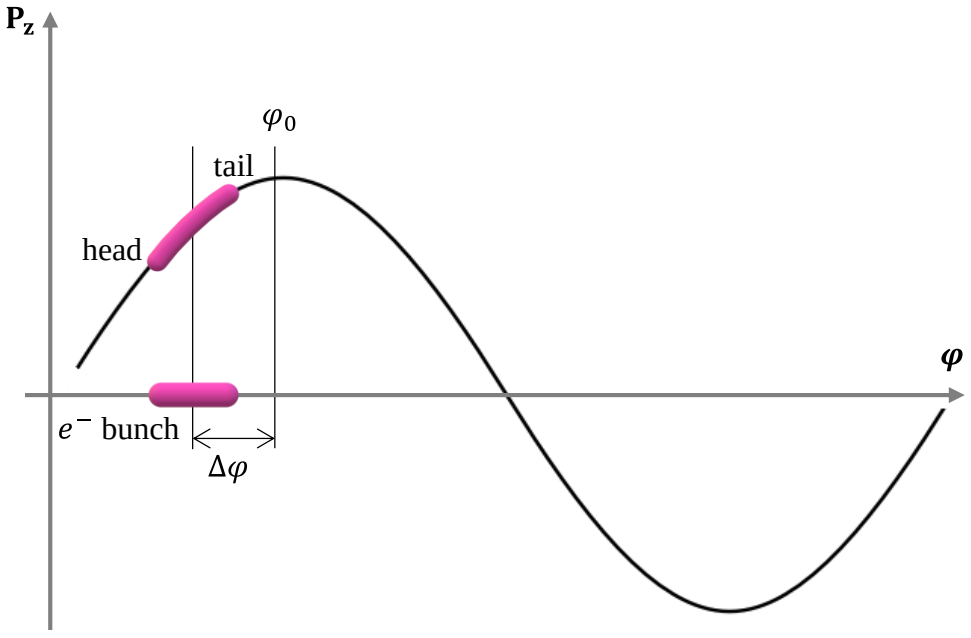

Figure 4.24: Model for acceleration of an electron bunch by an RF cavity. The electron momentum gain is shown with the black curve as a function of the RF phase at which the electrons enter the cavity.

As shown in Figure 4.7, the electric field distribution within the cavity corresponds to 1 Joule of energy injected into the cavity. Upon injection of a 10 kW peak power solid-state amplifier pulse into this cavity, the electric field enhancement at the cathode is expected to exceed 102 MV/m. Figure 4.25 illustrates the electric field enhancement at the cathode versus the propagation distance, Z. This electric field and the magnetic field of the solenoid can be used to study beam dynamics using ASTRA software. To focus electrons 8 cm downstream of the photocathode, a peak magnetic field of 0.18 T was considered.

Figure 4.26 illustrates the influence of the RF phase on the rms bunch length (σ_z), the rms transverse size of the bunch (σ_x), and the energy of the electrons. UV beam characteristics in this simulation include a rms temporal duration of 2 ps and a rms beam size of 40 μm. As discussed earlier, since electrons will be injected into the THz-driven booster, we aim to focus the beam down to less than 10 μm beam size and 25 μm longitudinal size as well as to have the transverse and longitudinal focus almost at the same point [46]. This is why the electric field phase and the magnetic field are important. We will see later, however, that the characteristics of the laser pulse have a considerable effect on the emittance of the electron beam, and so a suitable strategy must be followed in order to determine the optimal configuration.

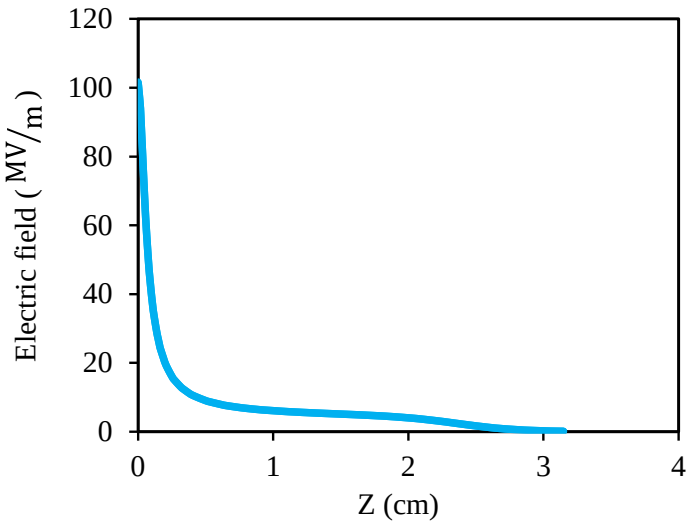

Figure 4.25: Field enhancement at the cathode vs propagation distance, Z

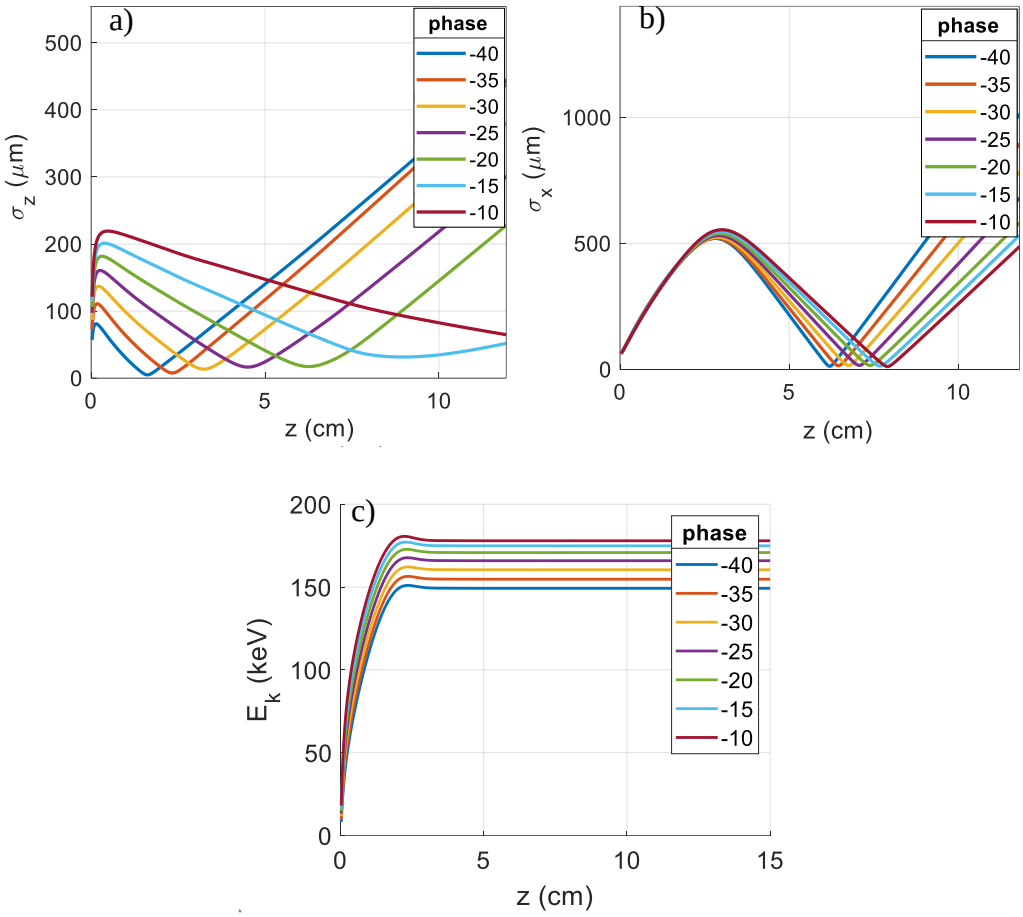

Figure 4.26: a) rms bunch length (σ_z), b) the rms transverse size of the bunch (σ_x), and c) the energy of the electrons vs propagation distance, Z, in different electric field phase (φ)

4.3.2 Beam Emittance

The emittance of charged particles is one of the most important characteristics in accelerator physics. This quantity refers to the area occupied by the beam in a position-and-momentum phase space [47]. Each particle in a beam can be described by its position and momentum along each of the three orthogonal axes, for a total of six position and momentum coordinates. On a two-dimensional graph plotting position and momentum for a single axis, the average spread of the coordinates on this plot is termed emittance. In photoinjectors, the horizontal ε_x and vertical

emittance ε_y are almost identical. The rms transverse (horizontal) emittance is defined as:

$$\varepsilon_x \equiv \sqrt{\langle \Delta x^2 \rangle \langle \Delta x'^2 \rangle - \langle \Delta x \Delta x' \rangle^2} \tag{4.6}$$

Where x is the particles transverse coordinates, x' is the particles transverse divergences calculated as $x' = p_x/p_0$, and p_0 is the particles longitudinal momentum, with $\Delta x \equiv x - \langle x \rangle$ and $\Delta x' \equiv x' - \langle x' \rangle$. As it has been done for the transverse plane, a rms longitudinal emittance can also be defined:

$$\varepsilon_z \equiv \sqrt{\langle \Delta z^2 \rangle \langle \Delta p_z{}^2 \rangle - \langle \Delta z \, \Delta p_z \rangle^2} \tag{4.7}$$

With $\Delta z \equiv z - \langle z \rangle$ and $\Delta p_z \equiv p_z - \langle p_z \rangle$.

The total transverse emittance is primarily composed of three components:

- **Cathode emittance**

Electrons emitted from the photocathode have random directions independent of their position on the cathode. The lower limit of the emittance of an electron bunch emitted from the photocathode of an RF gun is the cathode emittance. Cathode emittance is also frequently refered to thermal emittance is the consequence of a non-vanishing initial transverse momentum of the emitted electrons due to the excess energy. This value depends on the material work function and the applied RF gradient, but is definitely less than 1 eV for common operating conditions in RF photoinjectors [48].

- **RF induced emittance**

Electrons are exerted a radial force by the accelerating field in the cavity as a result of the radial electric field, $E_r(r)$, and azimuthal magnetic field, $B_\theta(r)$. According to equation (4.2), the force experienced by a electron depends on its launch phase. As a result of the finite duration of the laser pulses used to extract the electrons, the RF focusing force is influenced by the internal longitudinal bunch coordinate. This variation of the transverse momenta along the bunch causes an increase in the total emittance.

$$F_{\mathrm{r}}(r) = e \cdot [E_r(r) - \beta c \cdot B_\theta(r)] \tag{4.8}$$

- **Space charge-induced emittance**

Electrons as charged particles produce an electric space charge-field which defocuses the electron bunch and therefore increases the emittance. According to Kim [49], the strength of the transverse space charge force scales with $1/\gamma^2$

$$F_{sc} = \frac{e}{\gamma^2} \cdot E_{sc} \tag{4.9}$$

Here, E_{sc} represents the electric field caused by the charge of the electrons in the bunch rest frame. According to this equation, space charge forces are predominant at low beam kinetic energies, i.e., immediately after the emission of electrons from the photocathode.

4.3.3 Electron beam properties influenced by laser pulse parameters

In order to achieve the most effective emission compensation process, the optimal laser pulse profile, both temporal and transverse, is determined by considerations of the electron bunch shape. These considerations are presented in the following by examining the main characteristics of the laser pulse separately - the laser pulse energy, the transverse laser pulse shape and the temporal laser profile.

4.3.3.1 Laser pulse energy

The amount of extracted charge is determined primarily by the laser pulse energy. Furthermore, the charge can be further enhanced by the electric field amplitude during emission or diminished by the mirror charge fields [50]. Despite the fact that the first effect results in an increased bunch charge, the second effect can significantly alter the longitudinal phase space distribution and cause particle loss at the cathode if the strength of the mirror charge field compensates the external accelerating field. Although less than the desired bunch charge is extracted, this effect disrupts the emittance compensation process and results in an increase in transverse emittance. For these detrimental effects to be avoided, the laser spot size on the photocathode must be increased in order to reduce the charge density oat emission.

4.3.3.2 Transverse laser pulse shape

Transverse laser spot size determines the amount of cathode emittance and, therefore, the lower limit of the total transverse emittance. As a result, a smaller laser spot size is advantageous. In contrast, a smaller laser spot size will result in an

increase in the transverse space charge forces and therefore the transverse emittance. Consequently, it is necessary to find an optimum beam size that is a compromise between the cathode emittance and space charge forces. A diagram of the dependencies discussed so far can be seen in Figure 4.27. In this case, a temporal Gaussian laser profile with a 2 ps duration is used to illustrate how the transverse emittance is affected by the laser spot size.

For each laser spot size, the optimum RF phase and magnetic field were calculated so as to obtain the minimum transversal emittance and maximum electron kinetic energy. The optimal laser spot size is determined by $x_{rms} = 32\ \mu m$ according to the figure. For laser spot sizes smaller than $32\ \mu m$, the emission becomes space charge dominated and a fraction of the extracted charge cannot leave the cathode. For laser spot sizes larger than $32\ \mu m$ the cathode emittance starts to dominate the total transverse emittance.

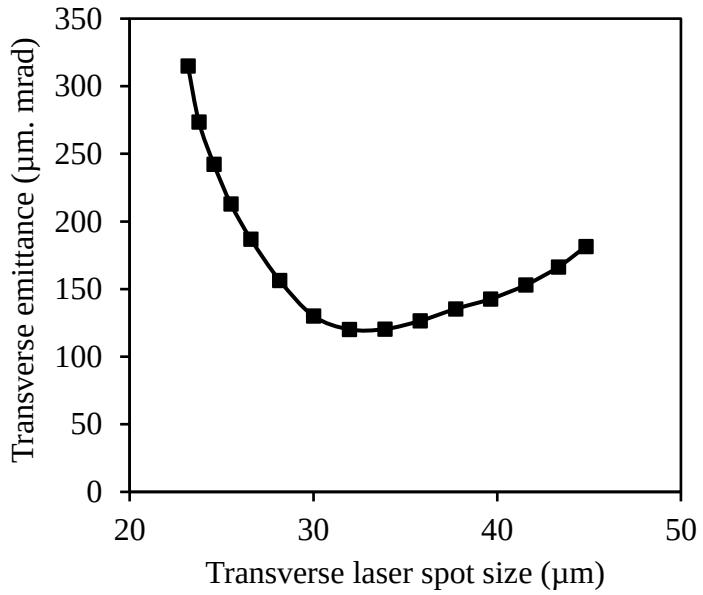

Figure 4.27: Simulated total transverse emittance at 8 cm downstream of the photocathode versus the transverse laser spot size.

4.3.3.3 Temporal laser pulse shape

As the actual electron bunch does not have an infinite length, the transverse space charge forces at the head and tail are smaller than those at the center. In this simulation, the temporal laser pulse shape is assumed to be Gaussian, so that we can know what emittance we will achieve during the initial phase of commissioning

the RF gun as an injector. In the following, however, we will examine how far we can optimize the beam parameters by improving the laser pulse shape (flat-top or ellipsoid).

A balance must be struck between several considerations in order to determine the optimal laser pulse duration. Generally, a longer laser pulse duration is preferred in order to reduce the strength of transverse space charge fields. Conversely, FEL operation requires large electron bunch currents, which require a compression of electron bunches [51]. Due to this reason, it is more beneficial to use short laser pulses.

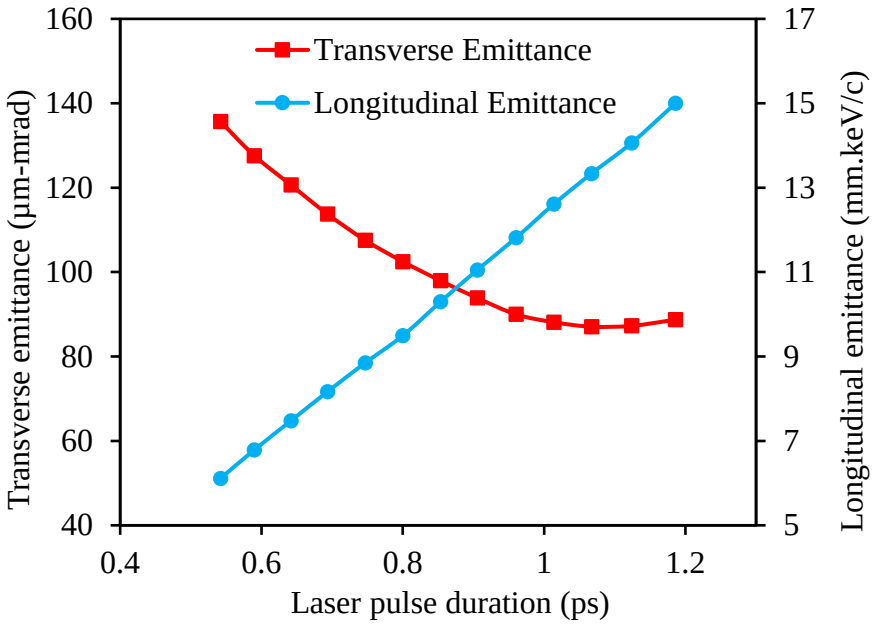

Figure 4.28: Simulated transverse and longitudinal emittance versus laser pulse duration.

As a demonstration of the described situation, Figure 4.28 illustrates the variation of transverse and longitudinal radiation values with respect to the duration of the laser pulse. Based on numerical optimization of the machine parameters for the lowest transversal emittance, the given numbers were determined. In order to reach a compromise, a RMS pulse duration of 0.85 ps was chosen.

4.3.3.4 The optimized laser pulse properties

Optimisation of the machine parameters was performed with regard to the Gaussian profile of the transverse and temporal laser pulses in order to establish a baseline for further investigation of deviations from that profile. As a result of the

optimization, a transverse emission of $\varepsilon_x = 98\,\mu m.mrad$ was obtained for the machine parameters summarized in Table 2.

Table 2: Optimized machine parameters for minimum transverse emittance at 8 cm downstream of the photocathode.

Parameter	Value
RF input power	10 kW
Bunch charge	100 fC
RF emission phase	13 º
Solenoid peak field	0.18 T
UV pulse duration	0.85 ps (rms)
UV spot size	49 µm
UV wavelength	267 nm
Transverse and longitudinal shape of laser pulse	Gaussian
Transverse Emittance	98 µm. mrad
Longitudinal Emittance	11 mm. keV/c
Kinetic energy	179.6 keV
Relative energy spread	0.8%

Figure 4.29 illustrates the dependence of transverse emittance on the individual parameters. In each case, all other parameters were maintained at their optimal values. According to this figure, the transverse emittance is highly dependent on the RF phase and magnetic field of the solenoid. As can also be seen from Figure 4.28 and Figure 4.29, the transversal emittance is more sensitive to the pulse duration than to the spot size of the laser. Therefore, optimizing the longitudinal laser pulse shape is worthwhile.

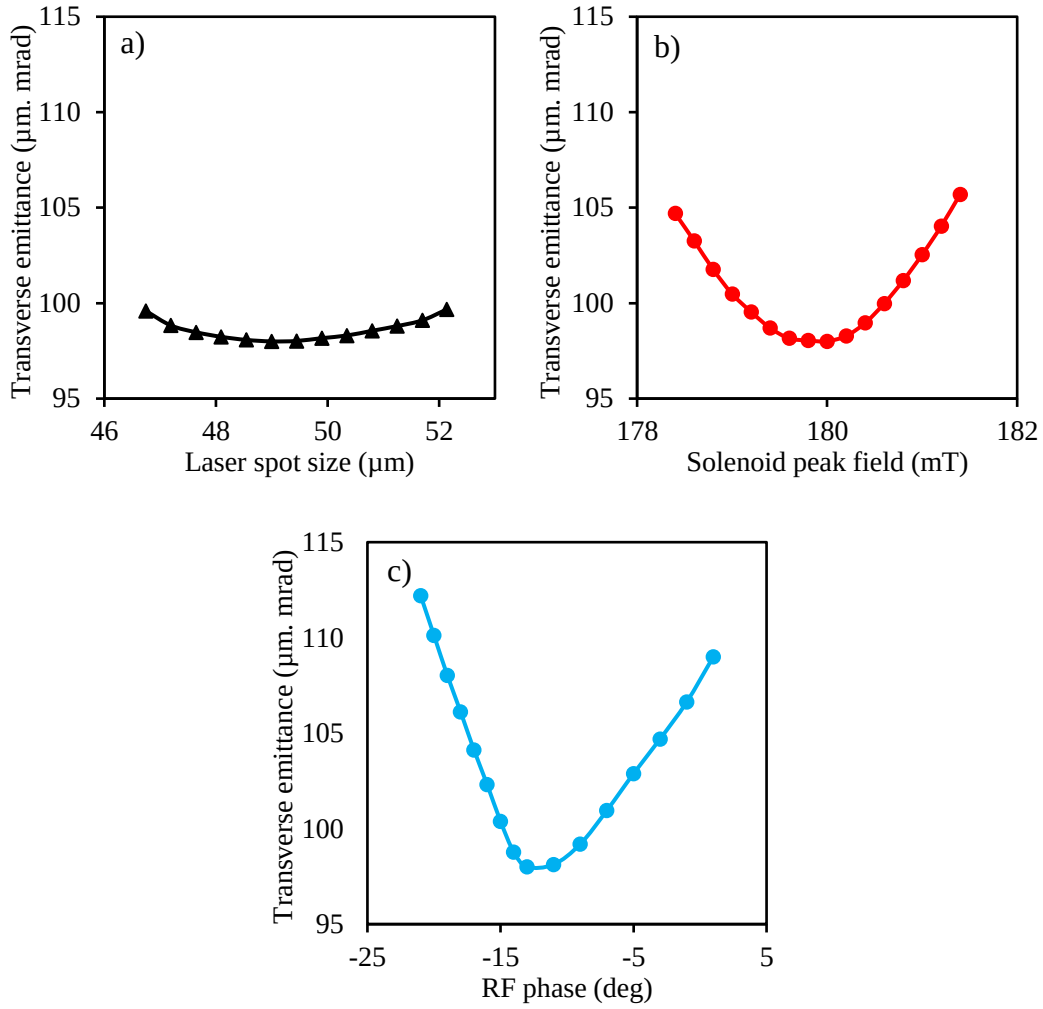

Figure 4.29: A study of the dependence between the optimized parameters and the transverse emittance. a) Transverse emittance vs laser spot size, b) Transverse emittance vs solenoid peak field, c) Transverse emittance vs RF phase.

As well, it is important to know the dimensions of the electron bunch when it is injected into the booster. Based on the optimum parameters of the machine as described in Table 2, Figure 4.30 illustrates the bunch length and transverse size of the bunch as well as the energy of the electrons in terms of propagation distance, Z. At the injection point of the booster, the bunch length is 14 µm, and the transverse bunch size is 21 µm, which appears to be appropriate. Moreover, the relative energy spread at the injection point is approximately 0.8%.

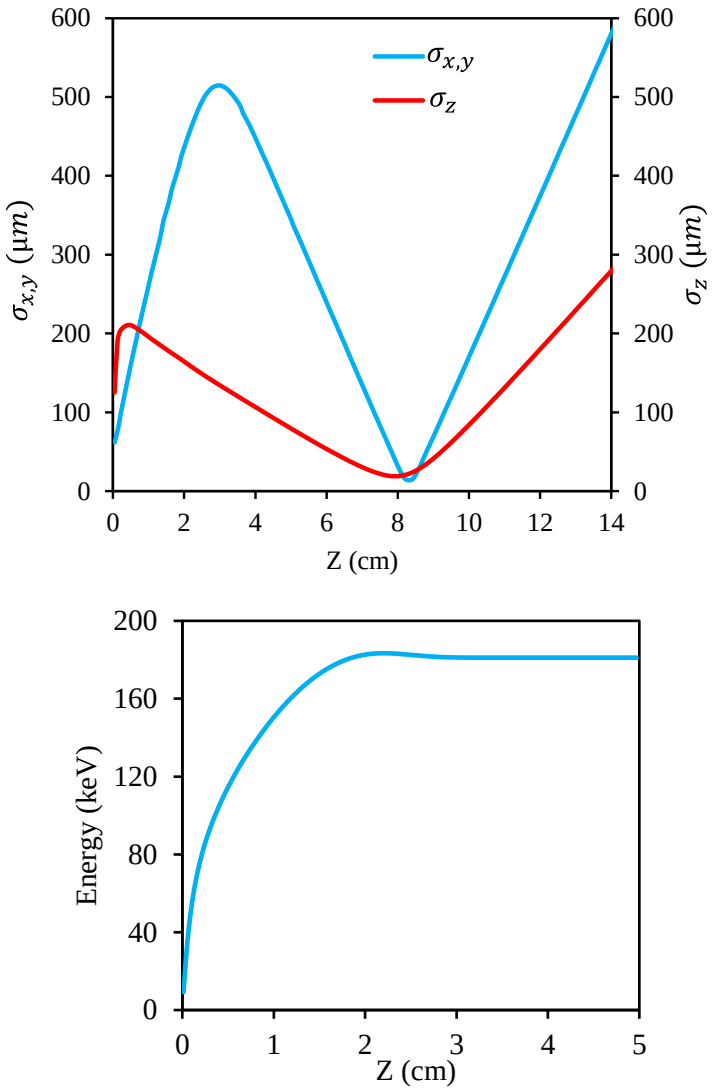

Figure 4.30: top: Focusing and compression of the bunch vz propagation distance, Z, bottom: Acceleration dynamics of the electron bunch vs propagation distance.

4.4 Design and fabrication

A cavity coupling system was modified based on the experiences gained from the first RF gun prototype. Major changes include:

- Back chamber has been removed to avoid RF resonance there
- RF couplers are perpendicular to the cathode to allow a smooth cavity

- Couplers are shortened as much as possible to reduce mechanical / thermal movements
- Couplers are fixed to the chamber by additional metal straps to reduce mechanical vibrations
- The fixture plate got thicker to increase mechanical stability
- No more vent holds of the couplers but stacking of parts to reduce RF leakage

The RF leakage we observed last time necessitated full simulations of the RF coupling. Based on microwave simulations, 2.998 GHz resonance frequency can be well tuned into the cavity with a high quality factor. In addition, eigenmode simulations were performed to determine the optimal conditions of the cavity for a coupling coefficient equal to 1. As a result of the transient domain simulation performed on the RF gun, different parts of the cavity, including the choke filter, the RF finger in the coupler, etc., are operating at their optimal performance. Furthermore, the vacuum simulation showed that it is possible to achieve 10^{-9} mbar by baking out the vacuum chamber, and this can be useful in preventing sparks in the cavity, speeding up conditioning, and overcoming the multipacting.

It is depicted in Figure 4.31 how the cathode part is designed and how the couplers are attached to the vacuum chamber. A brazing process was used in the vacuum furnace at a temperature above 500 degrees to connect copper to copper parts as well as copper to the stainless steel 316 vacuum chamber and CF150 flange. In this process, there are several points of brazing between different parts that must be performed simultaneously in order to prevent leakage.

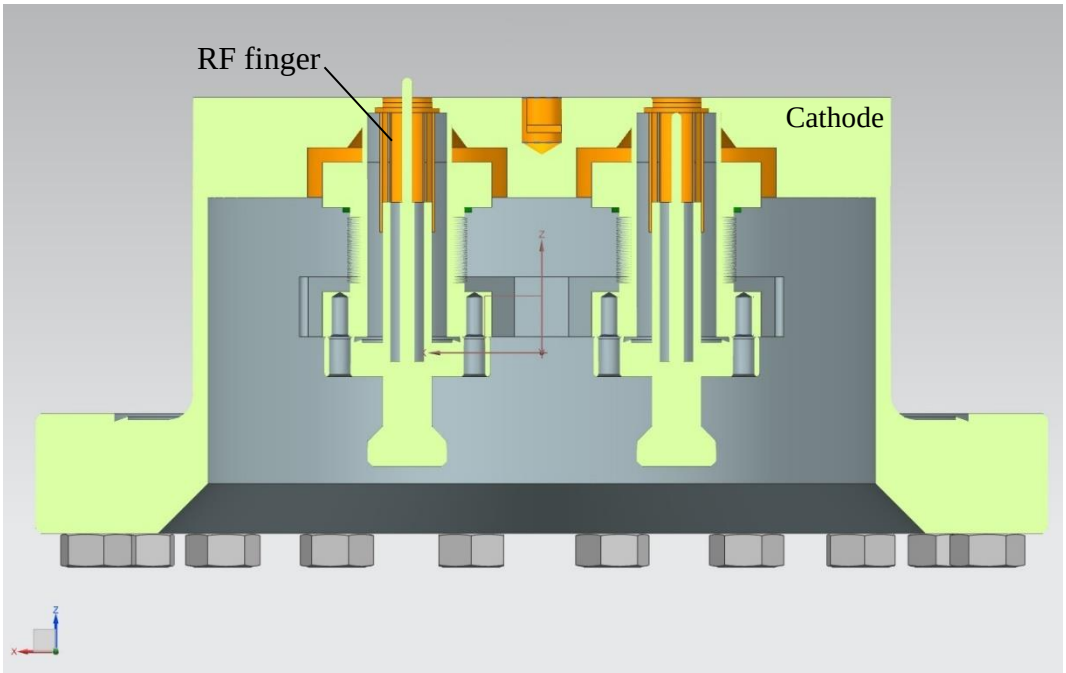

Figure 4.31: Back chamber of the RF gun: Cathode part and couplers

It is also evident from Figure 4.32 that the back compartment of the RF gun is much more compact than that of the first prototype. The compact chamber will make it easier to perform back-illumination, which may be considered in future prototypes [52]. The Figure 4.33 illustrates the several parts of the RF gun back chamber. Since the roughness of the pin-cathode tip plays a significant role in the production of dark charges, this part was made with a roughness of less than 10 nm.

Following the assembly of the vacuum chamber and the successful vacuum and RF coupling tests, the RF gun conditioning process was performed for further investigation of dark charges and multipacting, which will be discussed in the next chapter. As another purpose of this RF gun, it will be used to conduct UED experiments, which will be discussed in more detail in Chapter 7 regarding the required vacuum chambers and diagnostic systems, the photoemission generation process, laser requirements, etc.

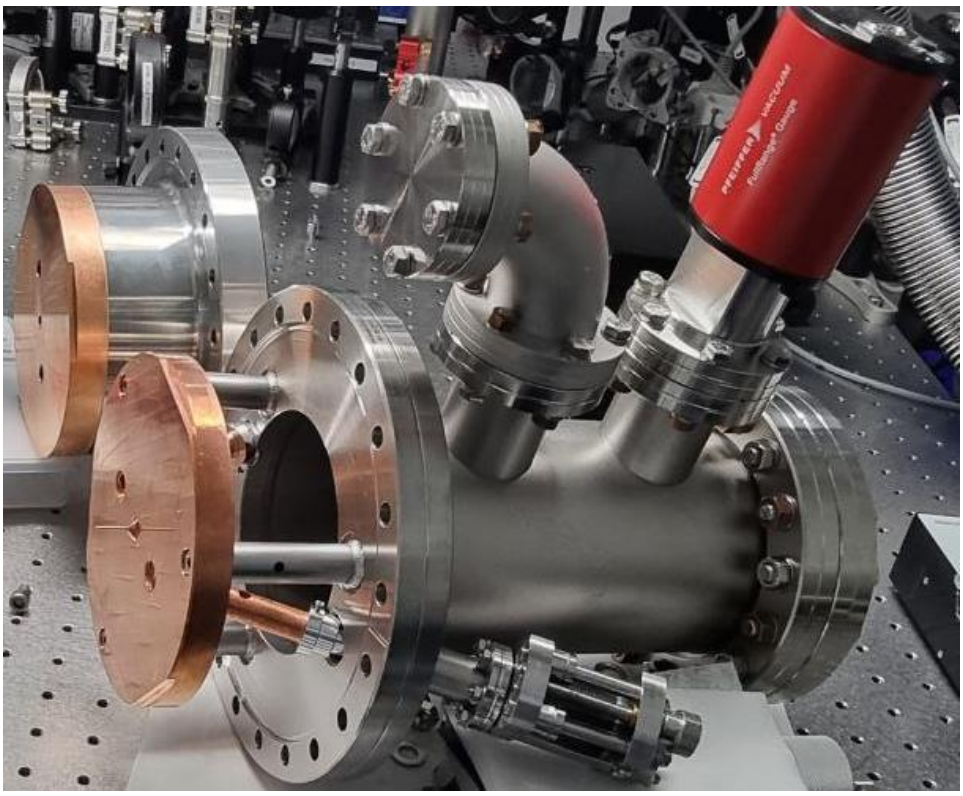

Figure 4.32: Comparison of back chamber prototype I and prototype II

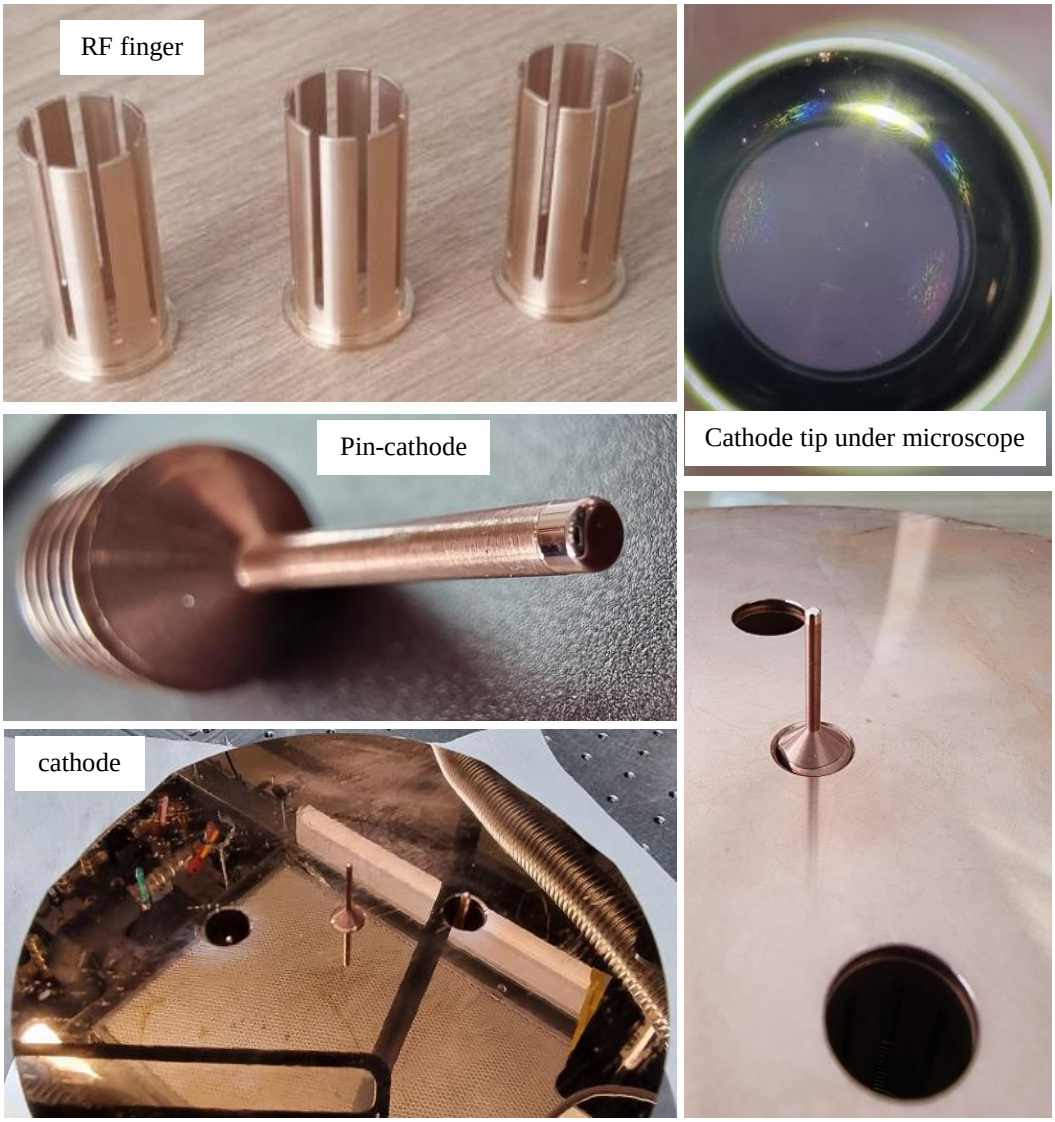

Figure 4.33: several parts of the RF gun back chamber

Chapter 5

Multipacting

In RF equipment with electric surface fields electrons can be emitted from the surface and accelerated. On surface impact secondary electrons can be produced, which are again accelerated in the RF field. At certain field levels it can happen that the particle movement and the RF are in synchronism, and more secondaries are produced. If the Secondary Emission Yield (SEY) is larger than 1 an exponential multiplication of electrons can take place, called multipacting [53]. This process is always characterized by an exponential growth of the number of free electrons in the vacuum chamber.

The multipactor discharge is an undesirable phenomenon. It can lead to problems of RF system operation, for example vacuum breakdown, RF power loss, overheating and damage to RF components and, in the case of superconducting cavities, it may cause a quench when the material becomes normal conducting. Multipacting is often found at lower field levels and after certain time of RF conditioning the SEY goes down and these multipacting barriers can be surpassed. However, if multipacting occurs at field levels close to normal operating fields, then the operation may be severely impacted and even damage of structure is possible.

5.1 Multipacting 3D simulation

Simulations of multipacting improves our understanding of this process and helps to identify critical locations within the cavity. Additionally, it is possible to determine the effects of different parameters such as solenoid current, surface cleaning, bake-out process, etc. on multipacting.

The multipacting simulations employ three parts of the CST studio: CST Microwave studio for the RF field simulations using the Eigenmode solver, CST EM studio for the external magnetostatic fields (the solenoids fields) using the magnetostatic solver, and the CST Particle In Cell (PIC) solver for particle tracking in combination of RF and static fields. The results of eigenmode and magnetostatic simulations have been presented in Figure 4.7 and Figure 2.11. This simulation will be completed by coupling them with the PIC solver and entering the parameters of the field-emission electrons and secondary emission yield of the cavity material.

5.1.1 Particle source

The electric field on the pin-cathode surface of this compact RF gun is not uniform. Figure 5.1 illustrates the distribution of the electric field around the pin-cathode as well as the magnitude of the electric field on the surface of a pin-cathode with a diameter of 0.8 mm.

In the multipacting simulation, the pin-cathode edge (Figure 5.2) was chosen as the electron source, where the direction of the electric field in this area has different angles to the z axis. Simulations indicate that these electrons cannot leave the cavity, but instead they strike the opposite surface of the cavity (anode part) and produce secondary electrons.

The emission time of 333 ps was set in this simulation, which corresponds to the RF period (for the 3 GHz case) to encompass all phases of dark current emission. Initially, the particles have a kinetic energy of 0.04 eV, a kinetic spread of 50%, an angular spread of 45°, and a total charge of 1 pC [54]. During the emission time, the current was generated using a Gaussian emission model, as shown in Figure 5.2, which displays the source settings and a schematic presentation of the temporal structure.

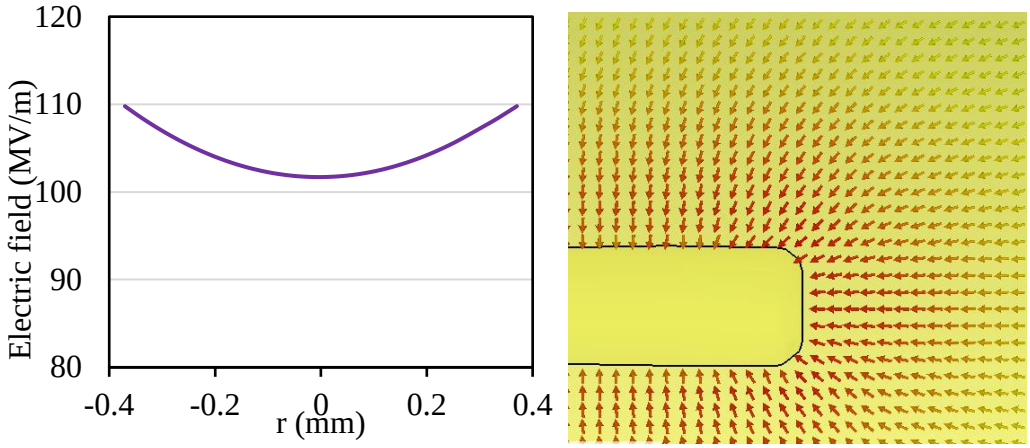

Figure 5.1: left: magnitude of the electric field on the surface of a pin-cathode with a diameter of 0.8 mm, right: distribution of the electric field around the pin-cathode

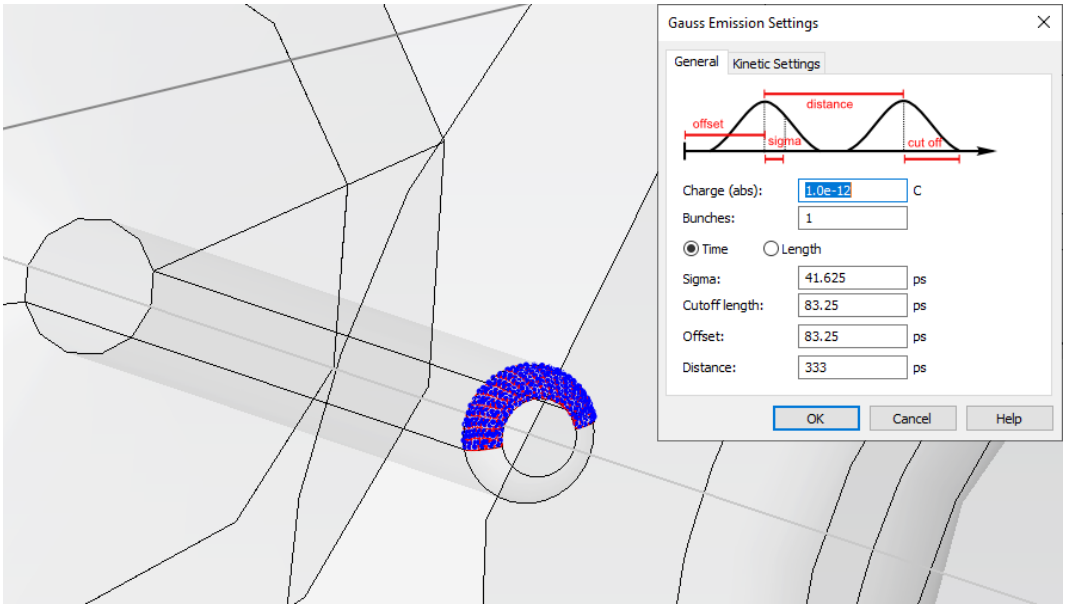

Figure 5.2: Particle source with Gaussian Emission setting in CST particle-in-cell studio.

5.1.2 Material and Secondary Emission Yield

A commonly used parameter to describe secondary electron emission is the Secondary Emission Yield (SEY), which is defined as a ratio between the number of emitted electrons and the number of incident electrons. The SEY varies depending on the type of material, surface treatment, coating of the metal (if any) and the impact energy of the primary electron. Any insulating layers (e.g. oxides as

well as adsorbed water) significantly enhance the emissivity of surfaces. Figure 5.3 illustrates an example of secondary electron emission yield for various technical materials [55].

The Furman model [56] of the secondary emission for copper is used with the default CST parameters for particle tracking simulations. Apart from the pin-cathode as a primary electron source, we consider other surfaces in the cavity as surfaces that may be capable of producing secondary electrons. This simulation uses copper with a maximum SEY of 2.1 at 250 eV impact energy.

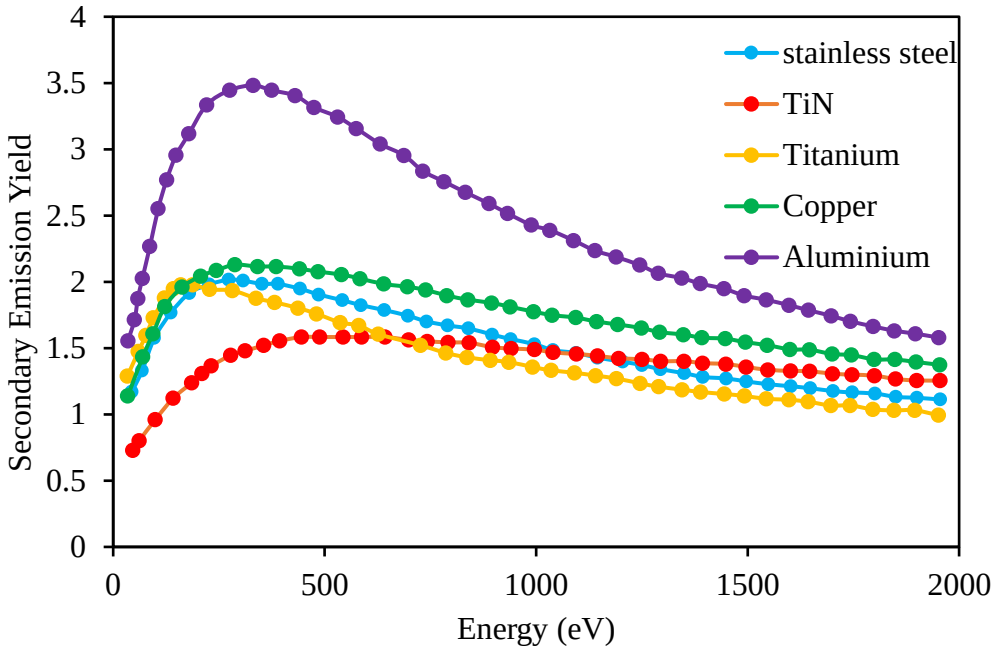

Figure 5.3: Secondary Emission Yield (SEY) of various materials [55]

5.1.3 Results

Evaluation of the number of particles in the cavity volume over time is a common strategy for multipacting indication and verification. As a matter of fact, the presence of multipacting in the simulated geometry with the defined field configuration can be inferred from the growth of electrons number. In order to determine the effects of a solenoid magnetic field on multipacting, we investigated multipacting in two modes with and without solenoid.

5.1.3.1 Multipacting without solenoid

Based on the simulation results, it was determined that most of the particles emitted from the cathode edge were not able to be transported to the beamline. With 10 kW input power, the electrons can reach the cavity surface after 140 ps and most of them hit the cavity surface and produce secondary electrons which are shown in Figure 5.4.

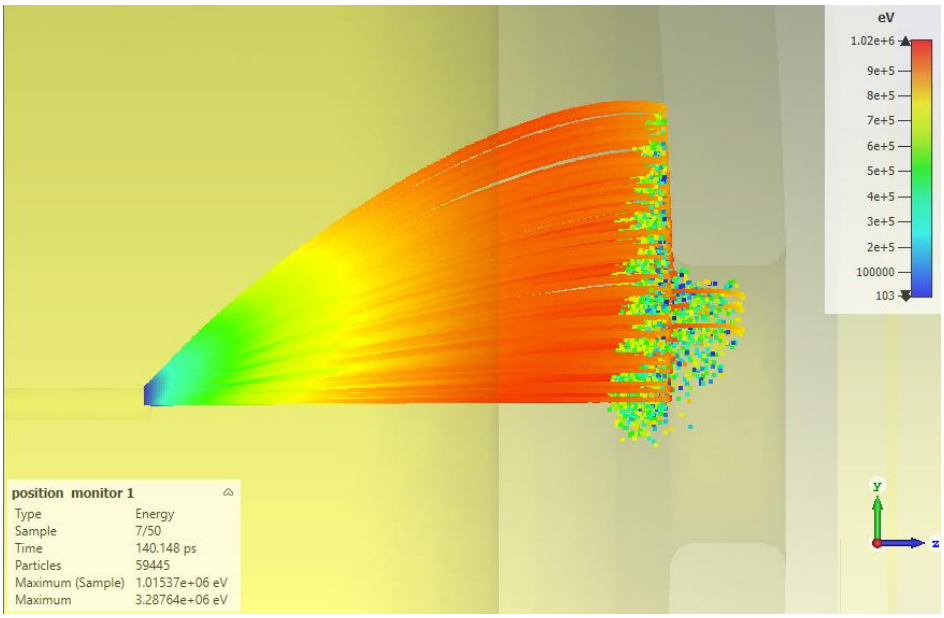

Figure 5.4: Trajectory of electrons with 10 kW input power and without solenois in PIC solver of CST.

Figure 5.5 illustrates the multipacting effect by plotting the number of particles in the gun as a function of time until 10 ns. The simulation results indicated a gradual decrease in the number of electrons over 3 ns. Thereafter, the electrons gradually lose energy and form more secondary electrons. Figure 5.6 depicts the energy spectrum of the particles at a time of 10 ns. The majority of particles have low energy, which makes them capable of generating more secondary electrons. As mentioned in Chapter 3, the RF injection pulse into the cavity has a duration of approximately 5 μs, which will result in a significant increase in the number of electrons. However, when the solenoid is off, the plot of particle number versus time is linear from 3 to 10 ns, indicating that the multipacting disappears relatively quickly following RF gun conditioning.

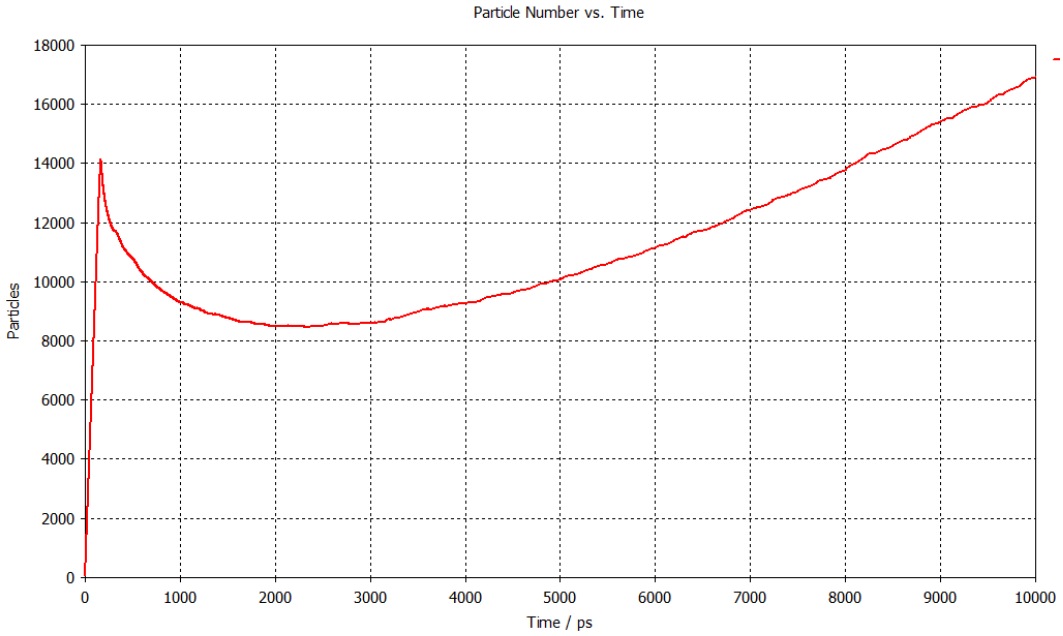

Figure 5.5: Particle number versus time, without solenoid, for 10 kW input power

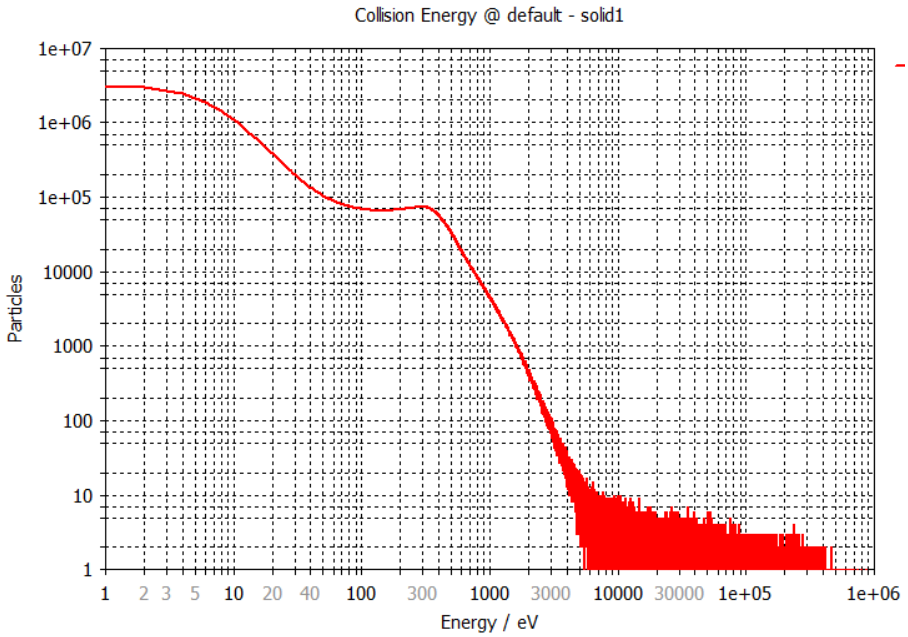

Figure 5.6: Energy spectrum of the particles after 10 ns.

Due to the radial component of the RF electric force, electrons fly up at an angle θ_1 when the direction of the electric field is to the left (Figure 5.7). Having moved closer to the anode, electrons move downwards with the alternating electric field at

an angle θ_2, where $\theta_2 < \theta_1$. This is the reason why electrons become trapped at the corner of the cavity over time. Figure 5.8 illustrates the location of electrons accumulation after 10 ns.

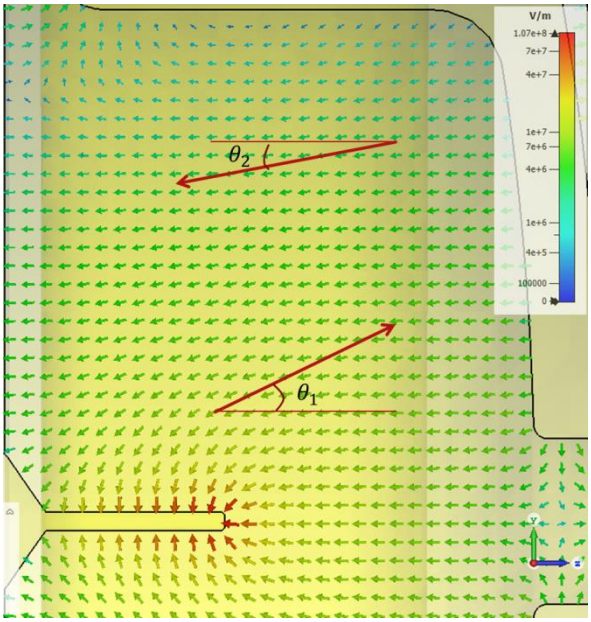

Figure 5.7: Electron trajectory in an alternating field as influenced by the distribution of the electric field inside the cavity.

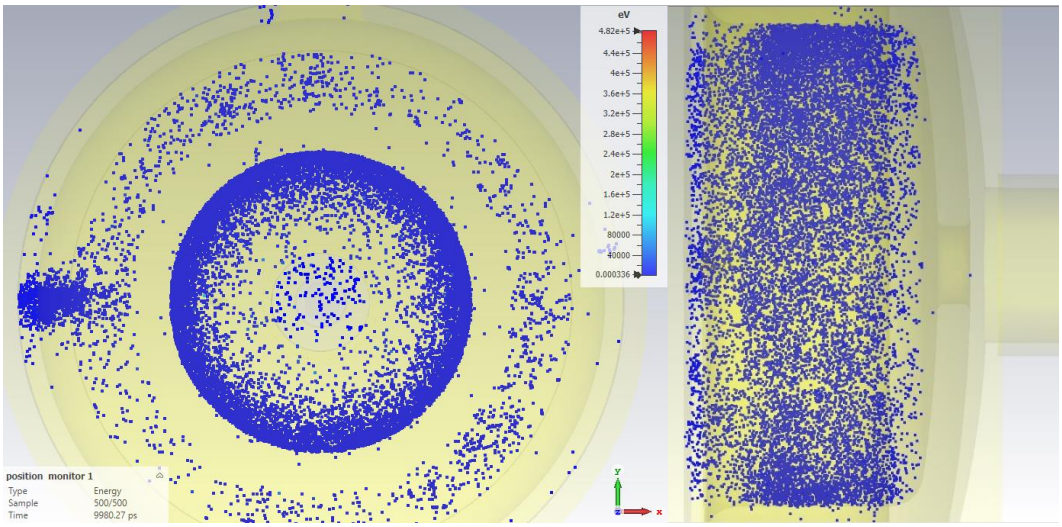

Figure 5.8: Location of electrons accumulation after 10 ns, without solenoid field.

5.1.3.2 Multipacting with the solenoid

The electron trajectory can be seen in Figure 5.9 by applying the solenoid magnetic field (with a maximum magnetic field of 0.18 T). Even when the magnetic field is applied, the dark charge emitted from the pin-cathode edge cannot escape the cavity towards the beamline. In Figure 5.10, the electrons are trapped and accumulated in the right corner of the cavity after 10 ns of tracking.

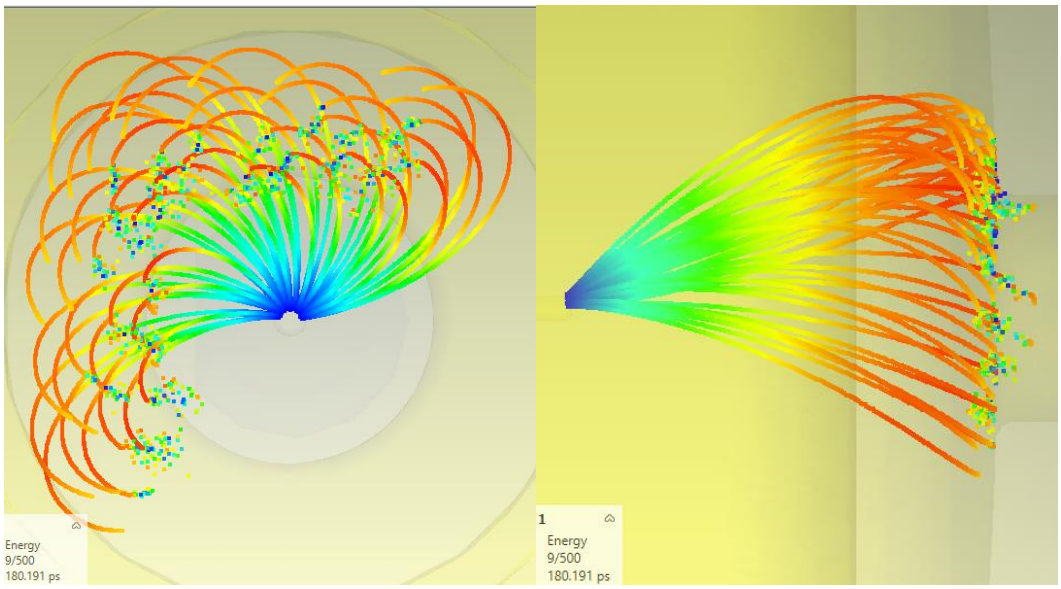

Figure 5.9: Trajectory of electrons in presence of both RF and magnetic fields

It can be seen in Figure 5.8 that, in the absence of a magnetic field, the electrons are trapped at the corner of the cavity, but they are distributed approximately equally in the longitudinal direction (Z-axis). As a result, the electrons, synchronizing with the RF field, strike the surface of the anode and cathode and produce secondary electrons, resulting in two-sided multipacting, and the number of particles will increase linearly as time passes. By applying the magnetic field, however, electrons accumulate on the right side of the cavity (near the anode) and lead to one-sided multipacting. As a result, the frequency of electrons hitting the anode surface will increase, resulting in a greater number of secondary electrons being produced. Figure 5.11 illustrates the exponential growth of electron numbers over a period of 10 ns. Moreover, Figure 5.12 shows the generation of secondary electrons over time. According to the figure, every 333 picoseconds, the electrons collide with the anode surface and a large number of secondary electrons are produced.

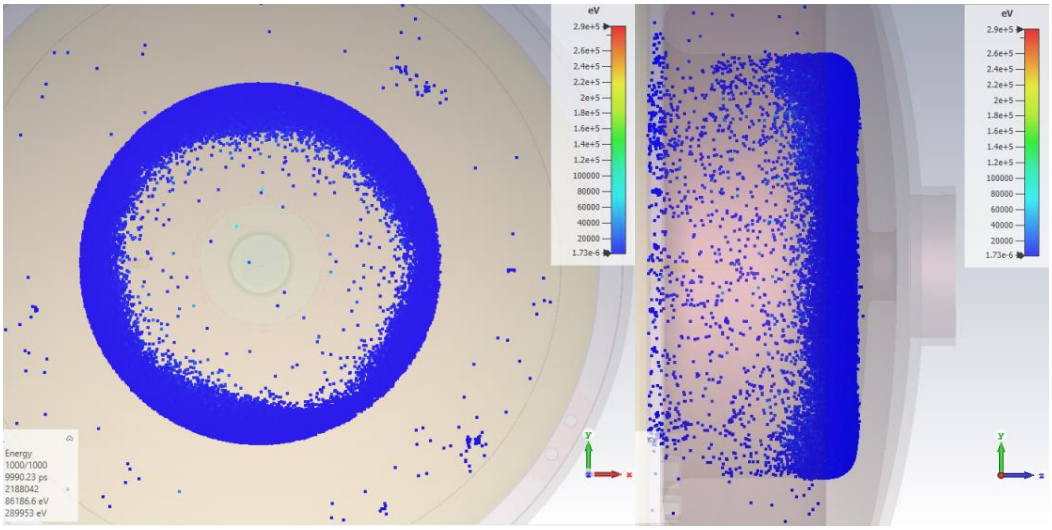

Figure 5.10: Accumulation of electrons on the right corner of the cavity with exerting the solenoid field, afetr 10 ns of tracking.

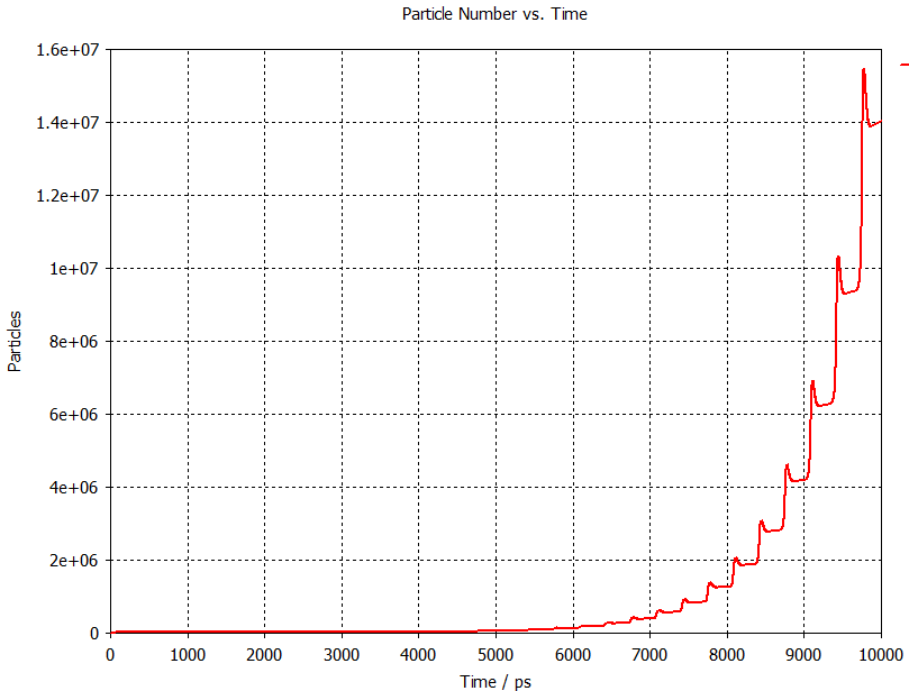

Figure 5.11: Particle number versus time, with solenoid field and 10 kW RF power.

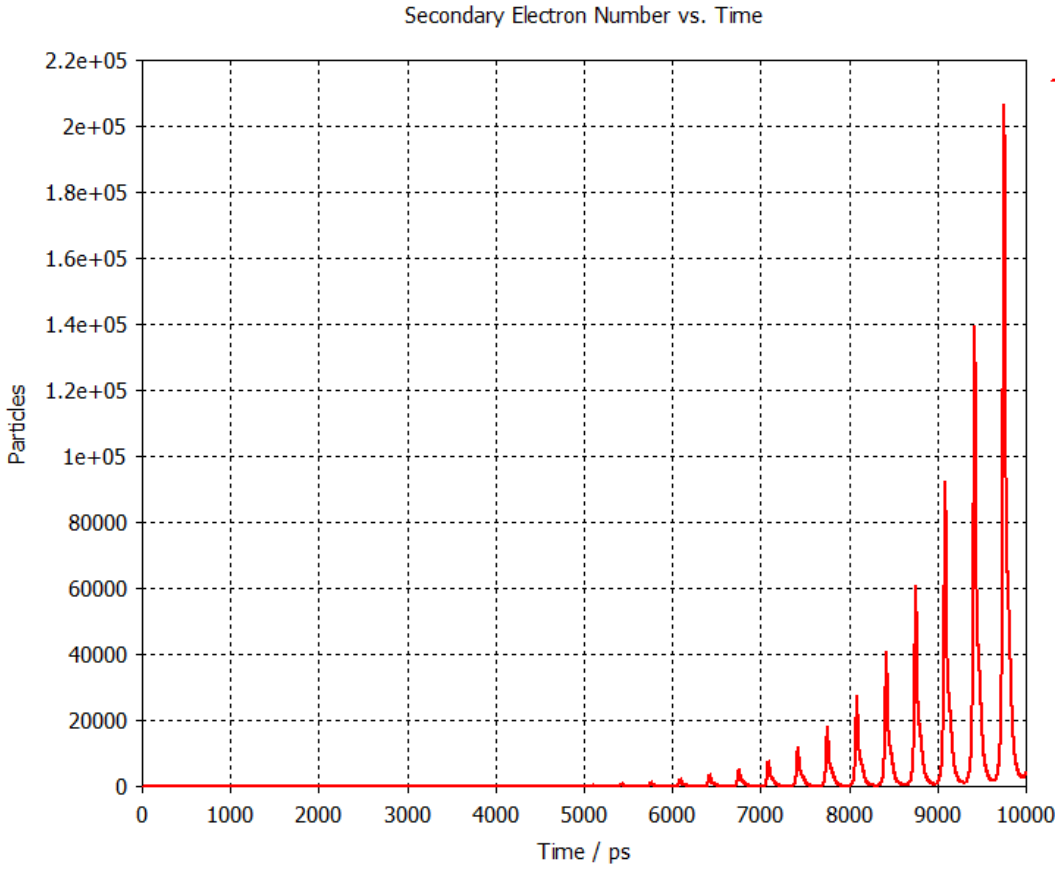

Figure 5.12: Secondary electron number versus time, with solenoid field and 10 kW RF power.

5.2 Multipacing suppression methods

It has been shown in the simulations and confirmed in the experiment that there is a high multipacting in cavity, for which it is necessary to investigate the methods of suppressing it. In addition to surface cleaning in a variety of ways, in-situ bake-out, and the dose effect on the surface caused by electron bombardment, surface roughness can also be changed to reduce secondary emission yield. Additionally, we examine the effects of applying DC voltage to this cavity, which reduces the production of secondary electrons and suppresses multipacing.

5.2.1 Cleaning effect on the multipacting

A very effective way to avoid resonance discharge is to eliminate electron multiplication by using materials with a secondary emission yield less than 1 for RF devices. In this way, the number of newly emitted electrons decreases exponentially with the number of impacts, and the discharge is no longer able to self-sustain. In the RF field, suitable conductors with low resistive losses, such as copper, aluminum, and silver, and superconductors such as niobium, have secondary emission yields ranging from 1.5 to 2.5 and are highly dependent on the oxidation and surface contamination status [57], [58].

Figure 5.13 illustrates the difference between pure metals and technical surfaces [55]. The graph shows the variation in the SEY for a copper sample in its as-received state (covered with natural oxides and contaminants) and after two different in-situ treatments: a 300 bake-out and an argon glow discharge (AGD). It was found that the highest SEY (more than 2) was obtained at an initial energy of 300 eV for the as-received sample. The SEY of the as-received samples is significantly reduced by baking under vacuum (e.g. up to 300 °C), a process that mainly results in the removal of water vapor adsorbed on their surface. In the case of samples that are baked under vacuum at 300°C, this value is reduced to 1.8.

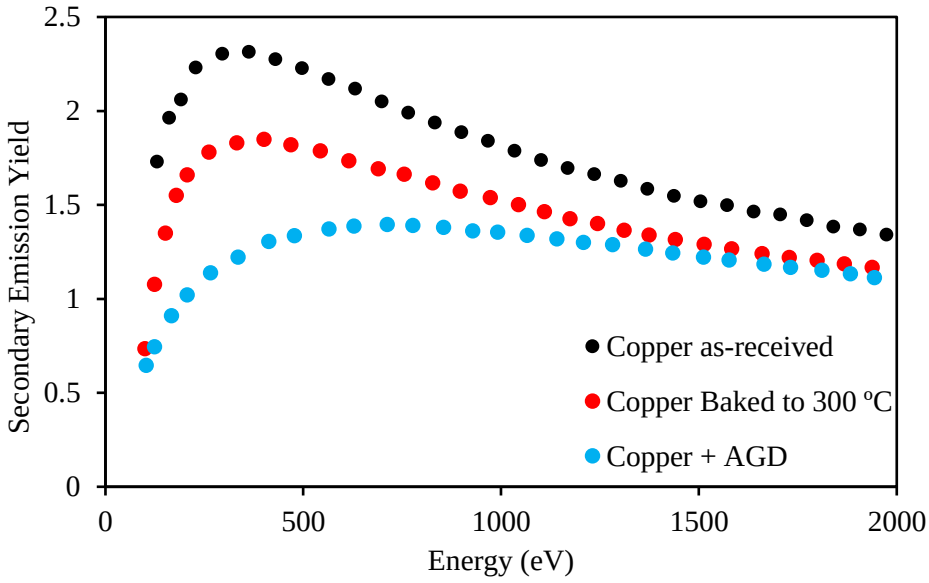

Figure 5.13: The SEY of copper for various surface treatments [55].

- **Cleaning effect on the multipacting, without solenoid**

Without the solenoid, we observed earlier in the multipacting simulation that electrons grow linearly over time. Therefore, we expect it to disappear easily after cleaning the gun and baking-out the RF gun vacuum system. Consequently, copper SEY has been reduced from 2.1 to 1.8 in order to evaluate this effect. The situation depicted in Figure 5.14 does not exhibit multipacting.

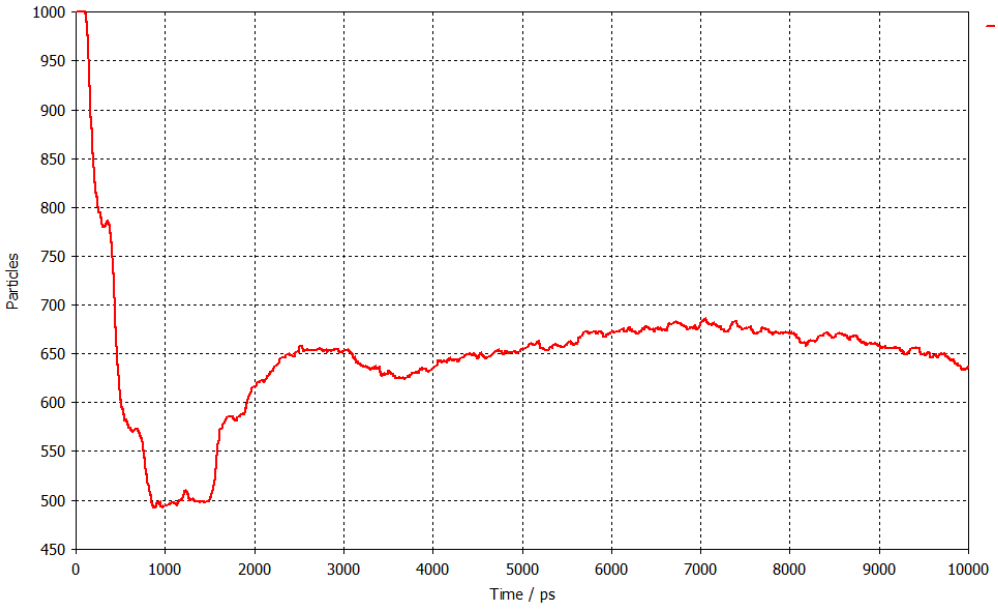

Figure 5.14: Particle number versus time, without solenoid, power of 10 kW, SEY=1.8

- **Cleaning effect on the multipacting, with solenoid**

Previous simulations of multipacting in the presence of a solenoid were performed using SEY of 2.1, demonstrating an exponential increase of electrons inside the cavity. To determine at what level of SEY multipacting will be suppressed, we will check SEY from 2.1 to 1.5 in this simulation. RF power is assumed to be 10 kW, and the magnetic field resulting from the solenoid is 0.18 T. Figure 5.15 illustrates the logarithmic evolution of electrons over time based on a variety of SEYs. According to this figure, using SEY equal to 1.8 (equivalent to baking-out at 300 ^{o}C), the number of electrons decreases by 25 times after 10 ns.

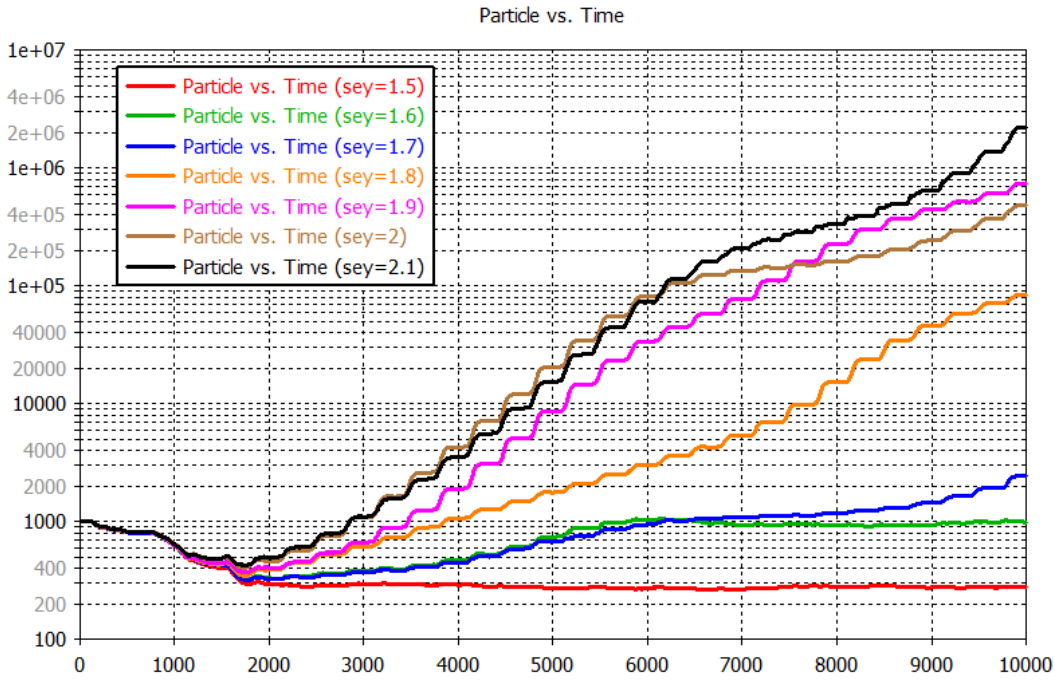

Figure 5.15: Particle number versus time in different SEY from 1.5 to 2.1

Based on the findings of the previous measurements, air exposure strongly affects the SEY of technical materials [59]. An argon ion glow discharge treatment can significantly reduce the SEY of copper, however, once it is exposed to air, this effect is almost completely lost. For this purpose, in-situ cleaning methods should be employed so that the cavity is no longer exposed to air. Therefore, the process of baking out the vacuum chamber, which is performed in-situ, is extremely beneficial prior to conditioning the RF gun. The amount of SEY, however, has not yet been reduced to 1.6, indicating that an appropriate cleaning procedure must be selected.

The dry-ice sublimation-impulse cleaning (DIC) technique has been proven to be an effective method for cleaning niobium and copper surfaces [60]. In tests conducted on several FLASH and XFEL cavities that had been cleaned in this manner, there were no detectable field emissions up to 36 MV/m. During this type of cleaning, liquid carbon dioxide passes through a ring-type nozzle, expands into a dry-ice / gas mixture, and is accelerated by the surrounding nitrogen.

As a result, in order to achieve lower values of SEY, following the DIC cleaning method, the vacuum chamber needs to be baked out, and to further reduce SEY, the "dose effect" in the RF gun conditioning procedure should be considered.

5.2.2 Dose Effect

Electron bombardment of the copper surface with an energy of a few hundreds of electron volts results in a decrease in SEY [61]. According to Figure 5.16, SEY variation is plotted against electron dose for an unannealed copper sample [62], [63]. As doses exceed $10^{-6}\ C/mm^2$, SEY decreases, and its maximum is almost 1.2 for doses greater than $10^{-3}\ C/mm^2$.

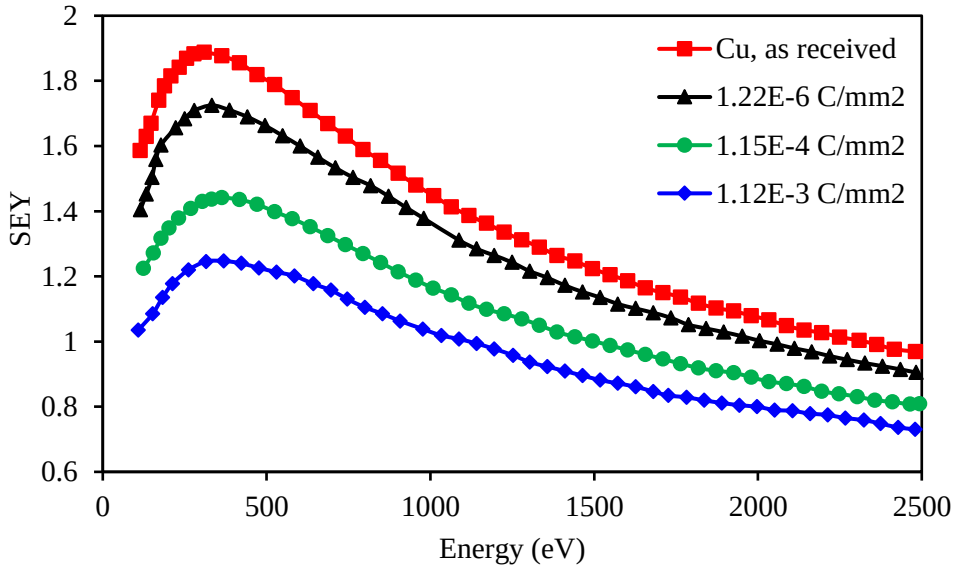

Figure 5.16: Variation of the SEY of copper with the incident electron dose [62], [63]

For all primary electron energies, the dose effect decreases SEY, although this effect is more prominent for lower primary electron energies. According to Figure 5.17, SEY is affected by the dose of electrons impacting with different energies [62], [64].

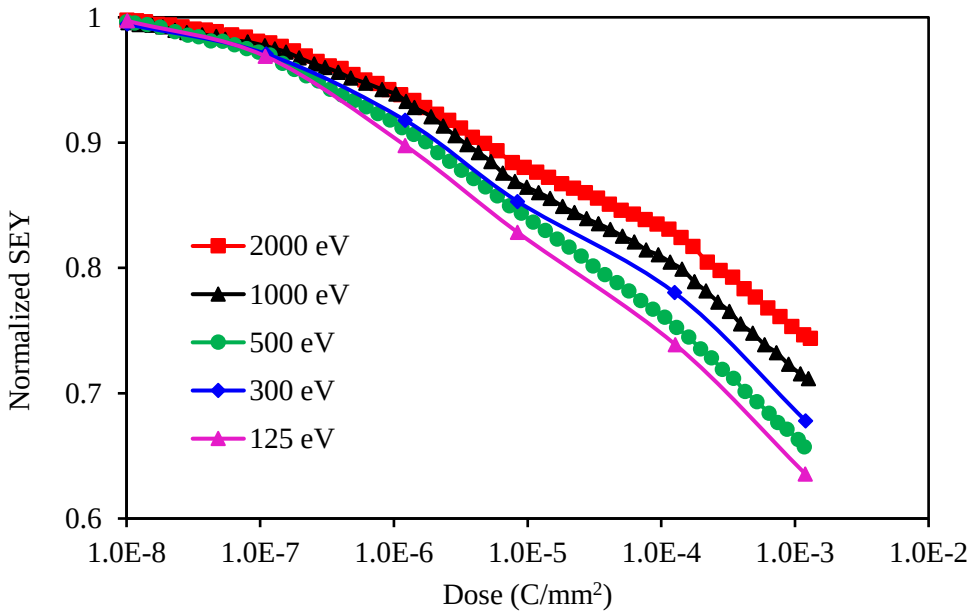

Figure 5.17: The variation of the secondary electron yield with the incident electron dose, normalised to 1 before bombardment [62], [64].

The multipacting process is now being examined from a different perspective with a view to enhancing the surface quality through electron bombardment. With the injection of RF into the cavity, and the impact of energetic electrons generated by the field emission on the copper walls within the cavity, in addition to gas desorption, it stimulates the surface to generate secondary electrons. By synchronizing secondary electrons with electromagnetic fields, more collisions will occur, resulting in more electrons being generated. It has also been shown that these electron bombardments in a cavity reduce SEY significantly [65].

In accelerators, these phenomena are commonly used to operate radio frequency devices and are referred to as "conditioning". In order for RF guns to operate under nominal conditions, such conditioning is necessary. The purpose of this study is to evaluate the time required for the conditioning of the RF gun. Nevertheless, it is difficult to adapt this estimate to the experiment, as it heavily depends on the surface quality. While the properties of the as-received copper are assumed in this simulation, the fabrication and preparation conditions can have a profound effect on the RF gun performance. Thus, this estimate may serve as a minimum conditioning time for suppressing multipacting.

Here, we apply the multipacting simulation that has been presented so far to determine the dose of electrons striking the surface inside the cavity. As shown in Figure 5.10, electrons accumulate in a specific area of the cavity after a short period of time. We therefore place a probe in that part of the cavity in order to count how many electrons with energies between 60 and 1500 electron volts collide with the surface of the cavity. Using this value and considering the RF pulse length and repetition rate, one can calculate the dose of incident electrons.

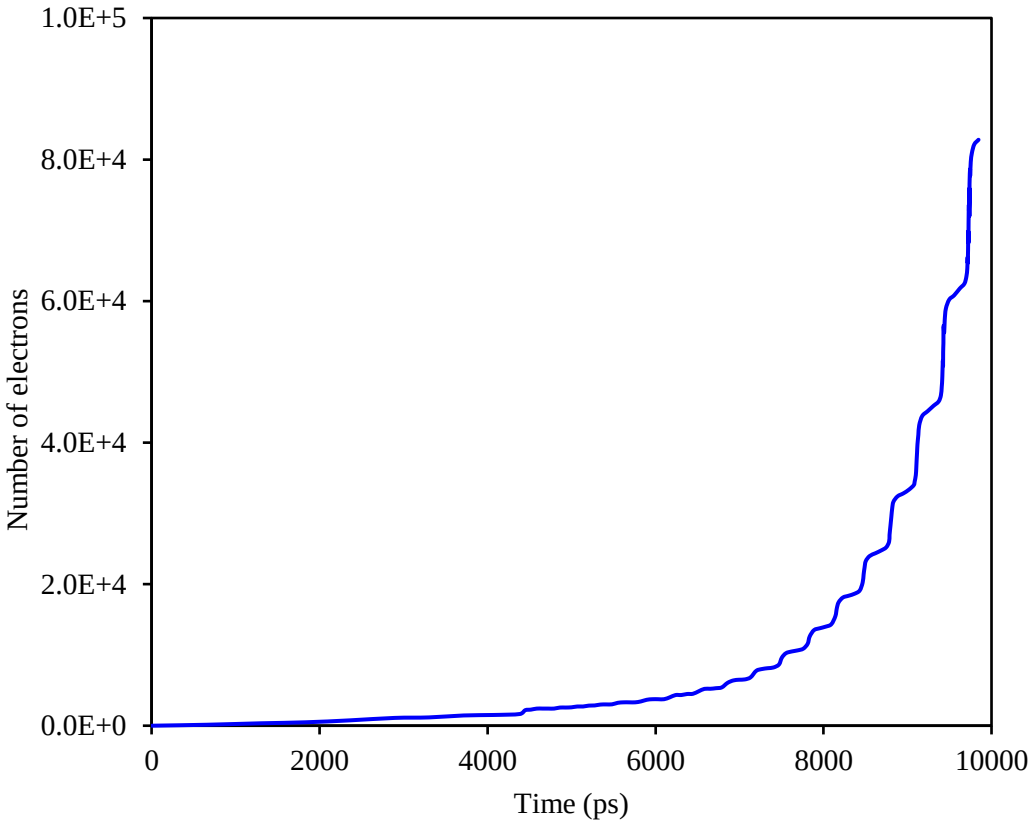

Figure 5.18: The number of electrons with an energy between 60 and 1500 electron volts that impact the dose calculation probe.

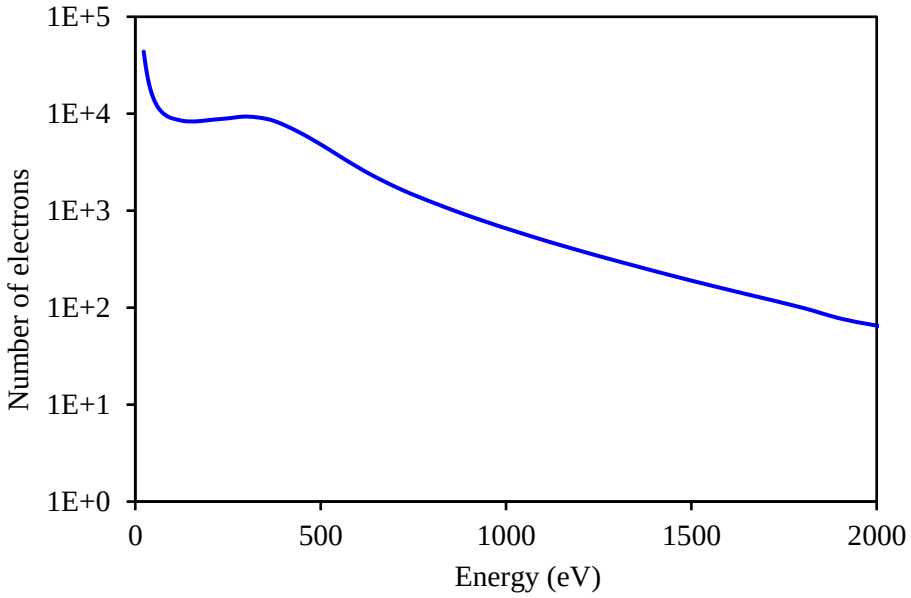

Figure 5.19: The energy spectrum of electrons hitting the probe during a time period of 10 ns.

It is evident from Figure 5.18 that the number of electrons on the probe increases exponentially over time, and therefore there should be a limit on the simulation time. At the initial injection of RF power in the first prototype RF gun, during multipacting, approximately 1 nC of charge exited the cavity as measured by the Faraday cup. A similar result was also observed in the experiment on the second RF gun prototype, which will be discussed in more detail in the experiment part of this chapter. Consequently, the simulation will continue until the number of secondary electrons reaches 6E+9. In order to calculate the dose of electrons, we assumed that the pulse length and repetition rate of the RF signal were equal to 5 μs and 50 Hz, respectively.

The horizontal axis in Figure 5.20 indicates the conditioning time, the vertical axis indicates the amount of electron dose, and the SEY value corresponds to the electron dose, which is obtained from the data in Figure 5.17. For instance, after one hour of conditioning, the dose of electrons will be 7E-6 C/mm^2, whose SEY is 1.89. According to Figure 5.19, electrons have energies ranging from 60 to 1500 electron volts. on the other hand, the SEY changes with the amount of energy, as shown in Figure 5.17. Consequently, the average value of SEY in Figure 5.20 is determined based on the electron's energy histogram.

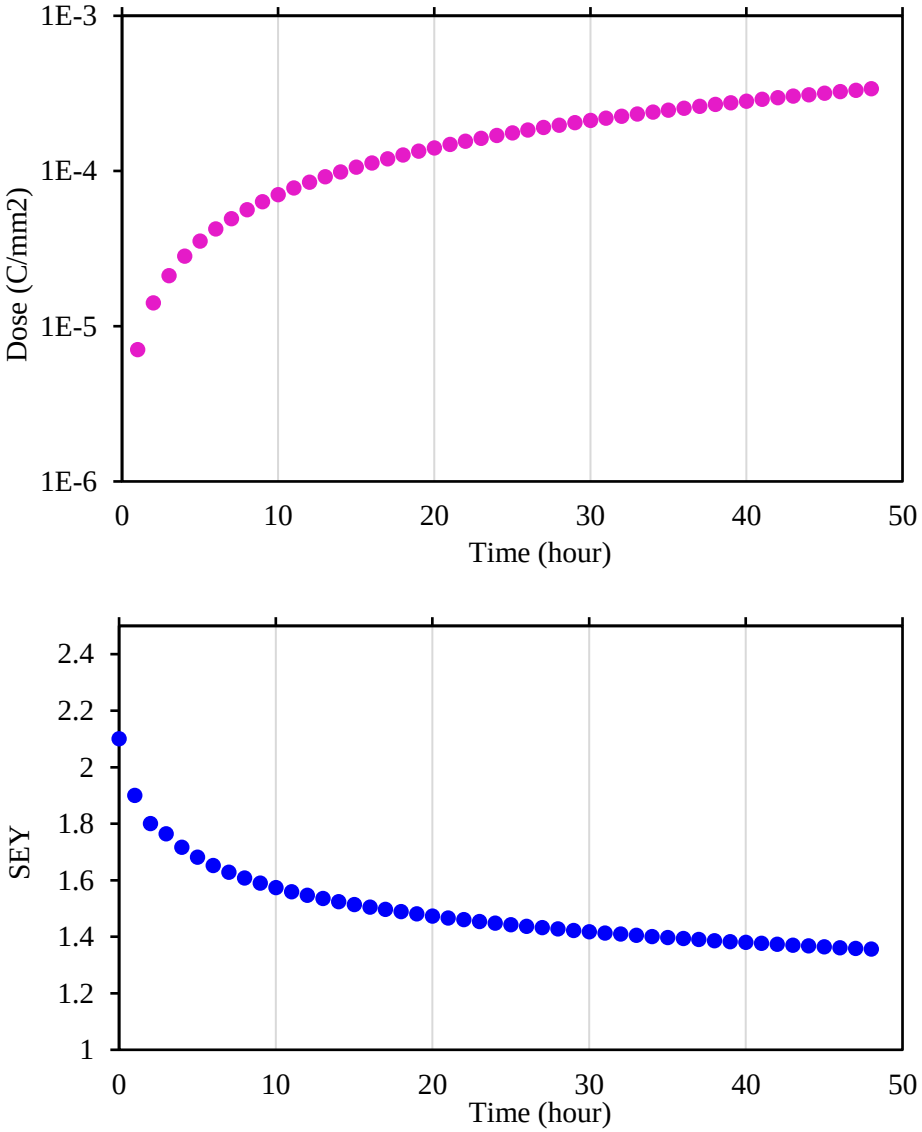

Figure 5.20: Dose of electrons and SEY according to conditioning time of RF gun with 10 kW power and the solenoid field peak of 0.18 T.

Based on the data in Figure 5.20, the secondary emission gain will be equal to 1.4 after 34 hours of electron bombardment in the cavity. In this case, multipacting can be significantly reduced. However, secondary electrons are still generated and have a substantial impact on the amount of dark charge in the system. For this effect to be minimized, SEY should equal 1, which requires a significantly higher dose.

5.2.3 DC voltage

In the previous section, it was demonstrated that a magnetic field created by the solenoid causes electrons to accumulate in the corner of the cavity over time, resulting in one-sided multipacting that can not be eliminated by applying a SEY of 1.8 (chamber baking to 300°C). The purpose of the present study is to determine whether the multipacting can be suppressed by applying a DC voltage to the cavity. In contrast to conventional RF guns, this compact design uses a choke filter and separates the cavity into anode and cathode sections, allowing this voltage to be applied operationally.

A DC potential is applied to the RF gun and the distribution of electric fields inside the cavity is shown in Figure 5.21. This DC field is added to the multipacting simulation in the PIC solver, along with the RF field with a power of 10 kW and the magnetic field of the solenoid with a peak of 0.18 T. Additionally, the secondary emission yield in this simulation is considered in two variations of 2.1 and 1.8. After 10 ns, the number of particles inside the cavity is determined for different DC voltage values.

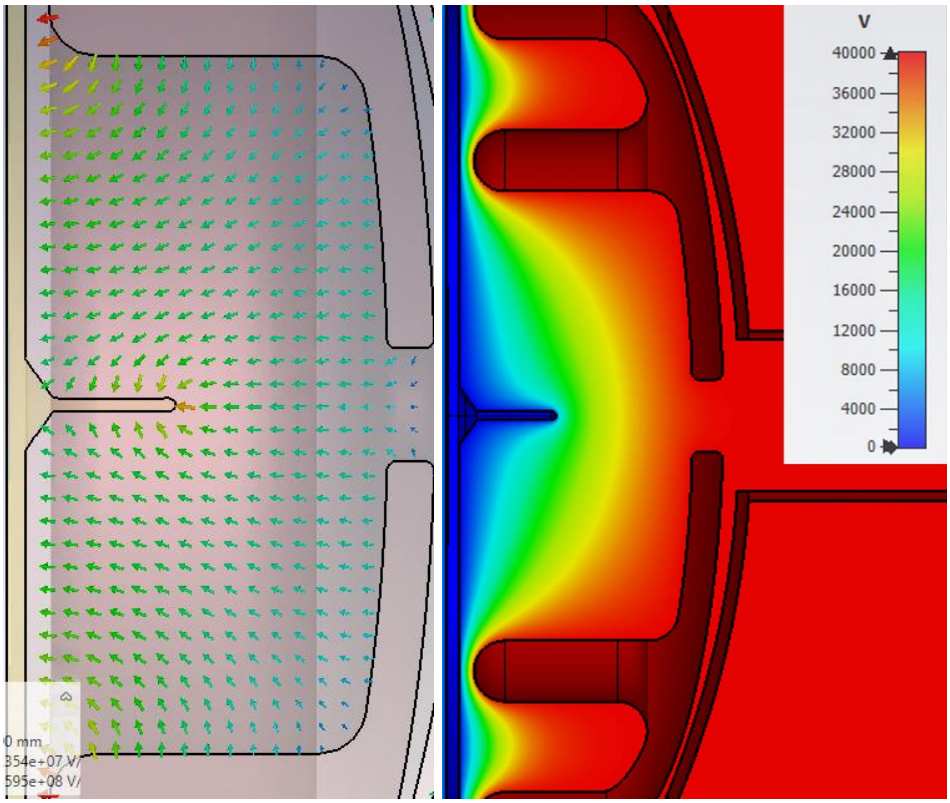

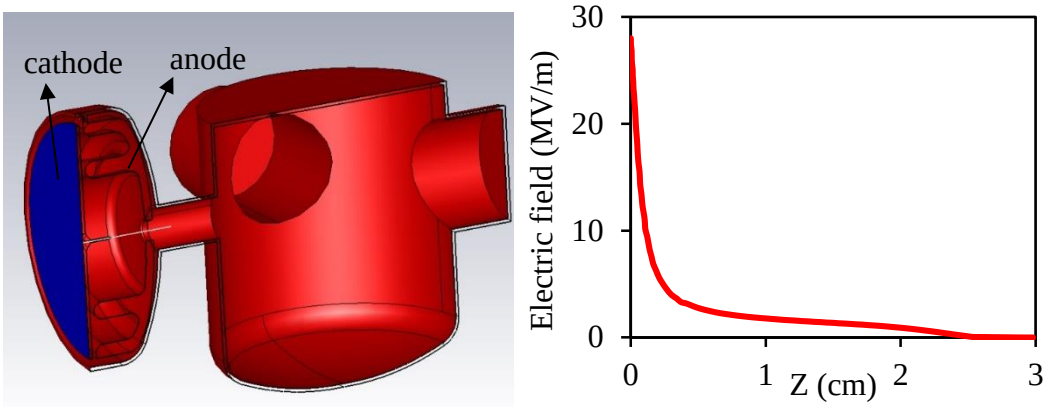

Figure 5.21: The DC potential in the RF gun, Electric distribution vs propagation distance, Z

Based on the data provided in Figure 5.22, a decrease in the number of particles after 10 ns is observed with increasing DC voltage. In the case of SEY of 2.1, the potential difference of 70 kV is not sufficient to completely eliminate multipacting. However, when SEY is equal to 1.8, applying voltages higher than 40 kVcan be useful for suppressing the multipacing.

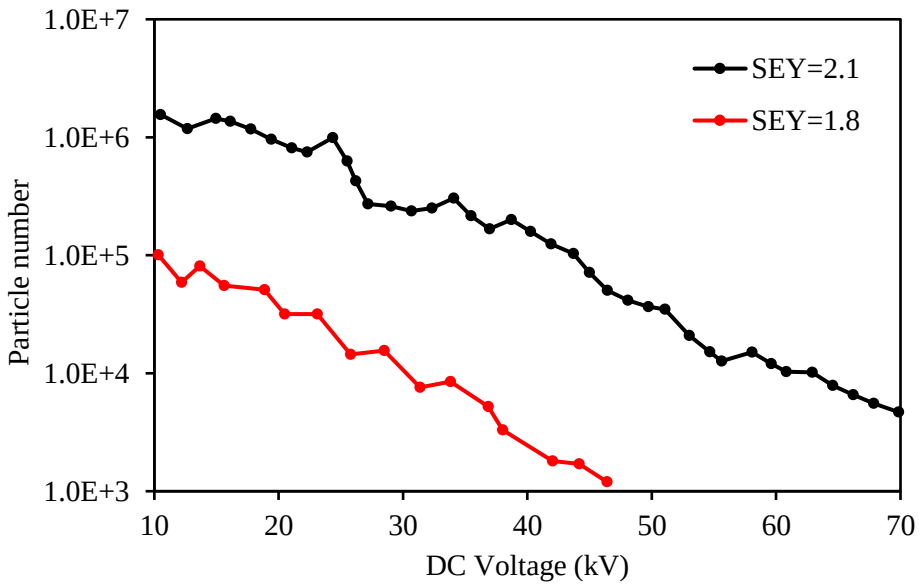

Figure 5.22: The number of particles after 10 ns of simulation time, expressed as a DC voltage for two values of SEY

At a DC voltage of 40 kV at anode and SEY equal to 1.8, Figure 5.23 shows the accumulation of electrons within the cavity after 10 ns. As a result of RF and magnetic fields, electrons accumulate in the corner of the cavity, resulting in one-sided multipacting. In Figure 5.23, it can be seen that electrons are still accumulating in the same corner of the cavity when DC voltages are applied, however, their synchronization with the alternating field is lost. In fact, if we assume the total electric field of $E_{DC} + E_{RF}$ applied to electrons at time t_0, then upon a 180º phase change, the total electric field will be $E_{DC} - E_{RF}$.

In conclusion, the simulations demonstrate that if we bake an as-received copper to a temperature of 300 degrees, then apply 40 kV DC voltage to the anode part of the cavity, the multipacting can be suppressed. In addition to eliminating multipacting, applying 40 kV potential difference to the cavity increases the energy of the electrons. Figure 5.24 illustrates the energy of electrons affected by RF and DC fields versus propagation distance, Z.

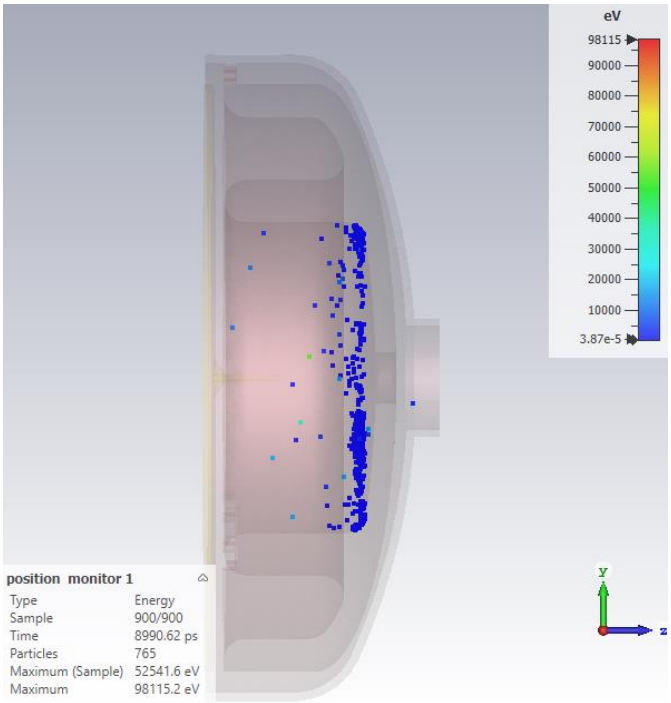

Figure 5.23: Accumulation of electrons on the cavity with DC voltage of 40 kV and RF power of 10 kW, and solenoid magnetic field of 0.18 T.

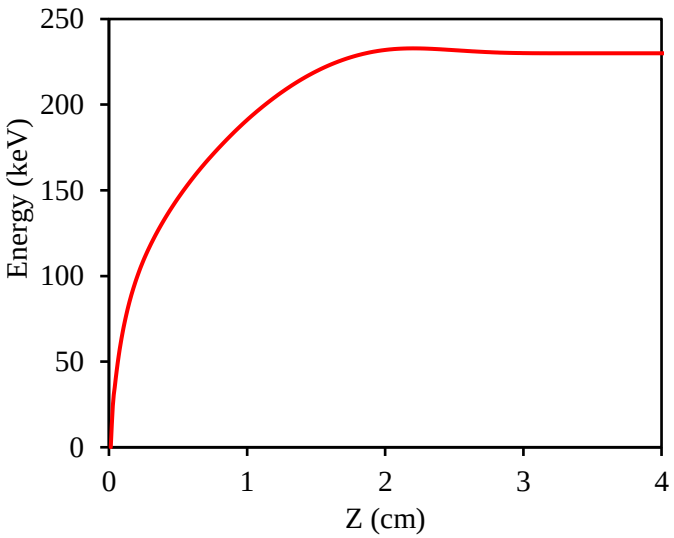

Figure 5.24: Energy of electron bunch affected by RF and DC fields versus propagation distance, Z.

5.3 Dependence of multipacting on RF power and solenoid field

In advance of conditioning the RF gun and ramping up the RF power and magnetic field of the solenoid, it would be beneficial to estimate what their effect will be on the multipacting and to estimate how the experiment will proceed.

The multipacting simulation was carried out over a range of RF power values between 0 and 10 kW and solenoid magnetic field values between 0 and 0.18 T to investigate the growth of electrons after 10 ns. The number of primary particles was 1000 in these simulations and SEY was assumed to be equal to 1.8.

As shown in Figure 5.25, while the solenoid is off, the growth of electrons is plotted against RF power with a resolution of 100 W. The simulation indicates that multipacting decreases at higher RF powers. In fact, decreasing secondary emission yield is predicted as the electron energy increases, which is illustrated in Figure 5.3.

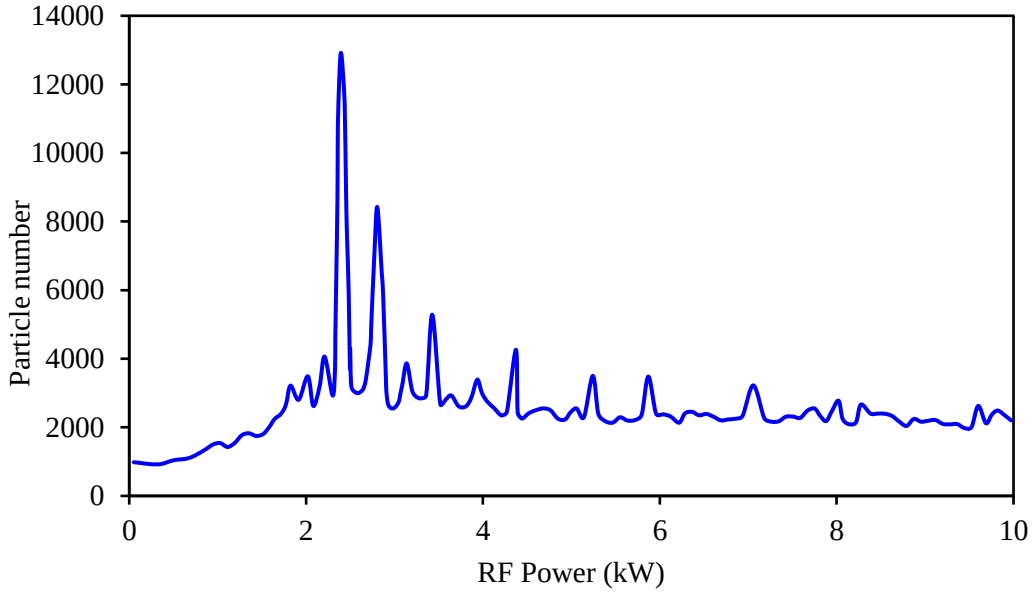

Figure 5.25: Particle number in different power range between 0 to 10 kW with a resolution of 100 W

Figure 5.26 illustrates the number of particles inside the cavity after 10 ns as a function of the magnetic field from 0 to 0.18 T when the RF power is equal to 10 kW and SEY is equal to 1.8. As can be seen, the multipacting is much stronger at higher magnetic fields. It is therefore preferable to apply the magnetic field of the solenoid during RF gun conditioning so that the process of cleaning the internal surfaces of the cavity due to the collision of electrons can be accomplished more quickly.

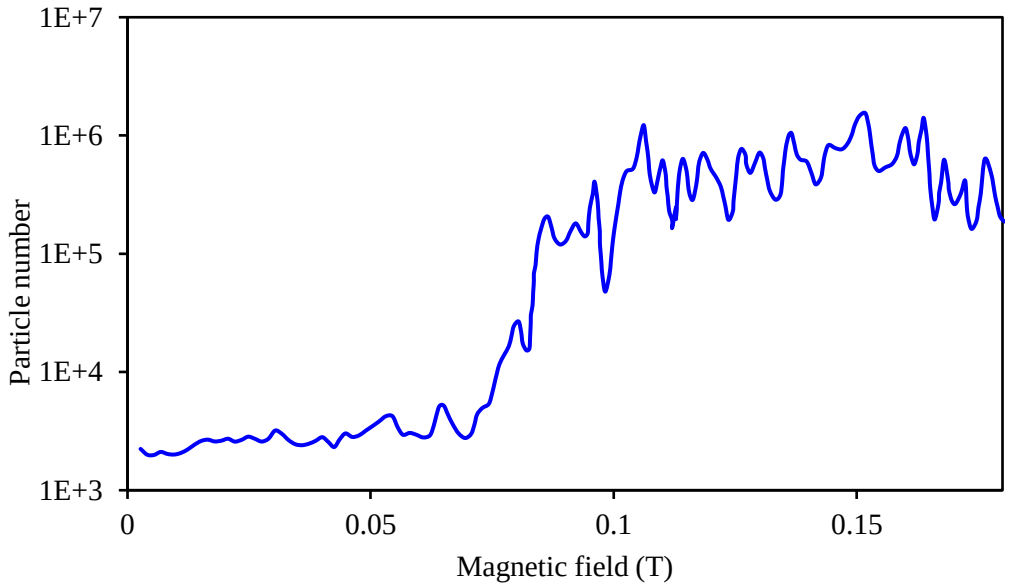

Figure 5.26: Particle number in terms of sweeping the magnetic field of solenoid in power of 10 kW.

Chapter 6

Characterization of RF gun prototype II

Following the assembly of RF Gun Prototype 2, in order to evaluate its performance, it was transferred to the Control System Test Laboratory in MSK Group, Desy, which is equipped with RF signal generators and LLRF control systems. The results of the measurements of safety group D3 showed that no radiation beyond the background signal could be detected at a power of 10 kW and a solenoid current of 180 A, so it is possible to work in this room without shielding. We aim to first measure the stability of resonance frequency and cavity coupling efficiency, and then to investigate the spark, dark charge, and multipacting of the RF gun by injecting RF power into the cavity. Additionally, the effects of baking-out of the vacuum chamber and the effect of conditioning at different RF power levels and solenoid currents can also be examined on the behavior of dark charge and multipacting. Following the successful conditioning of the RF gun, the laser required to conduct the photoemission process will be then installed.

6.1 RF coupling test

According to Figure 4.3 and Figure 4.4, by adjusting the length of the antenna and the gap between the anode and the cathode, the optimal conditions for cavity coupling can be established so that the resonance frequency is equal to 2.998 GHz.

According to Figure 6.1, Using a vector network analyzer, the frequency response of the cavity was determined and a loaded quality factor of 5,800 was measured with a reflection S_{11} reaching below -50 dB. The difference between this amount of quality factor and what was predicted by the simulation (6,000) can be attributed to the quality of the copper's inner surface.

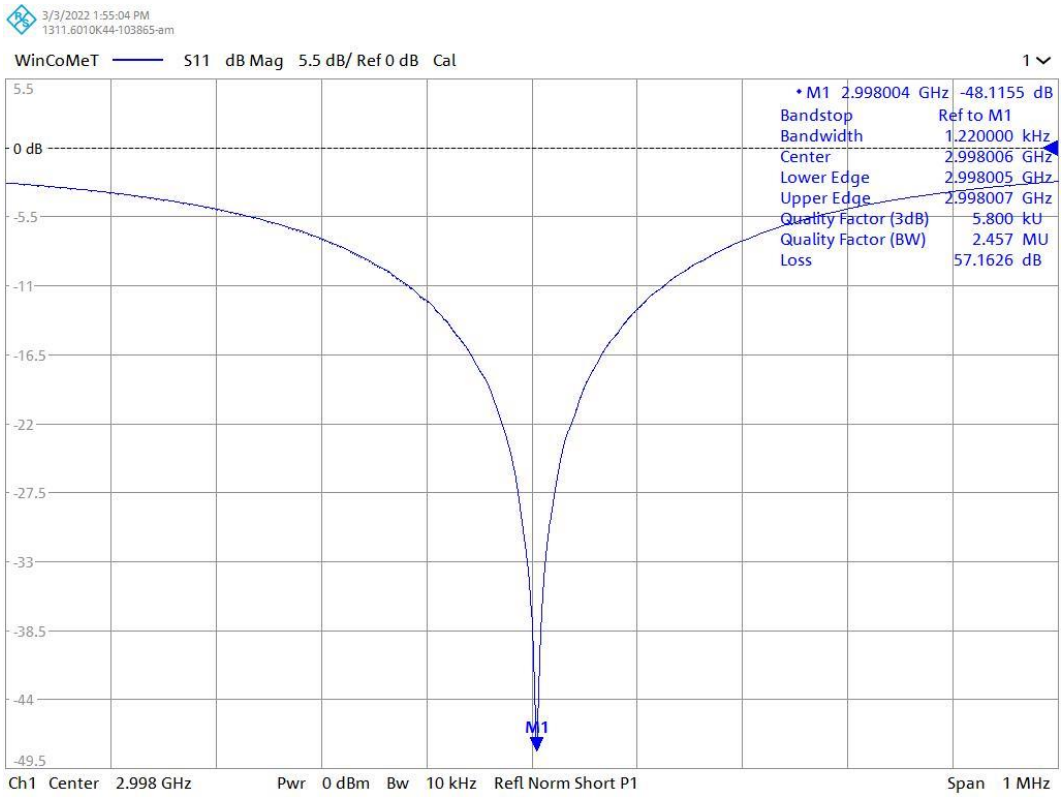

Figure 6.1: The frequency response of the cavity was determined by a vector network analyzer, and a loaded quality factor of 5,800 was measured with a reflection S_{11} reaching below -50 dB

Figure 6.2 illustrates the frequency response of the cavity over a wider frequency span, demonstrating that the side resonance frequencies are sufficiently far from 2.998 GHz.

Contrary to the previous prototype, the frequency response of the current cavity appears to be very stable, and no fluctuations are observed in the S_{11} parameter, and no electromagnetic field leakage was detected to other parts of the RF gun. Because of the simpler design and shorter length of the antennas, couplers are easier to work with, less equipment is required, and optimal conditions are easier to achieve. Upon injecting RF power into the cavity, the LLRF control system (Figure 6.3) reports that the reflection signal (the signal is reflected from the cavity back to the RF source) approaches zero, indicating that effective coupling has occurred.

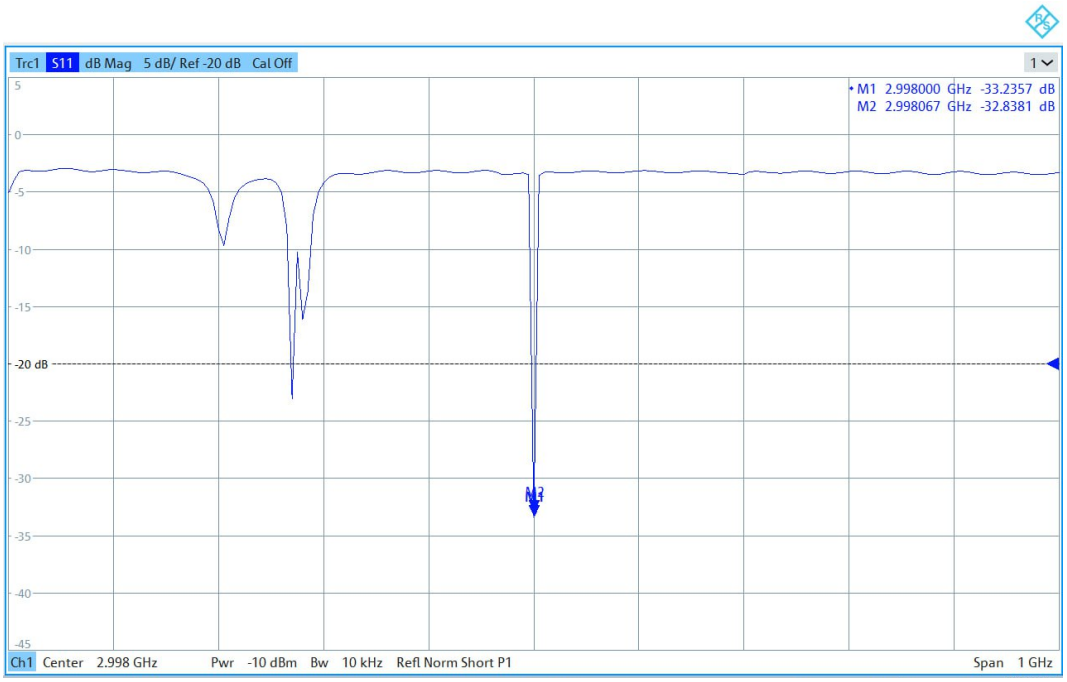

Figure 6.2: The frequency response of the cavity over 1 GHz frequency span.

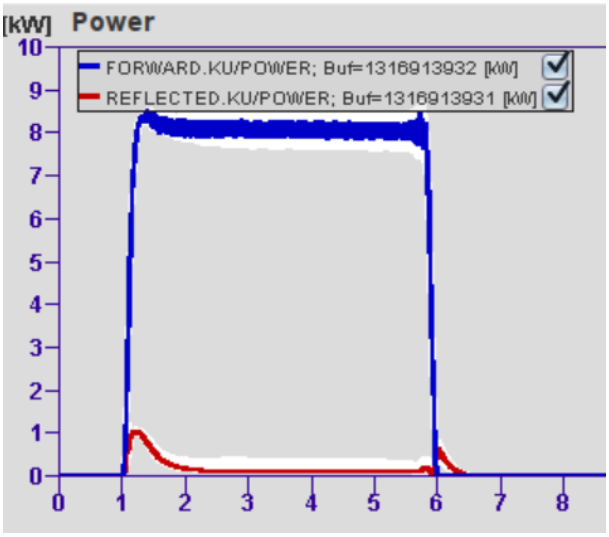

Figure 6.3: The forward power (blue) and reflection power (red) of the cavity are shown on the control panel of the RF gun.

6.2 Faraday Cup

Using a Faraday cup in this experiment, we are able to measure the dark charge as well as capture the image of the electron beam by placing a scintillator on the copper surface. In the beginning, LYSO was considered as the scintillator material, but testing in REGAE revealed that it wasn't effective at low energies, so YAG scintillator was substituted. A Faraday cup containing a YAG scintillator measuring 2 x 2 cm^2 is shown in Figure 6.4. This scintillator has a thickness of 300 microns and is marked with a dark spot of 983 microns in order to facilitate calibration and to find the beam position on the scintillator more easily.

Using a CCD camera mounted on the cross-flange of the Faraday cup, it is possible to image the electron beam impacting the Faraday cup at an angle of 45 degrees. On the vacuum chamber of the RF gun, Figure 6.5 illustrates the location of the Faraday cup and the required camera. Connecting an SMA cable from the Faraday cup feedthrough to an oscilloscope allows the measurement of the voltage generated by the dark charge.

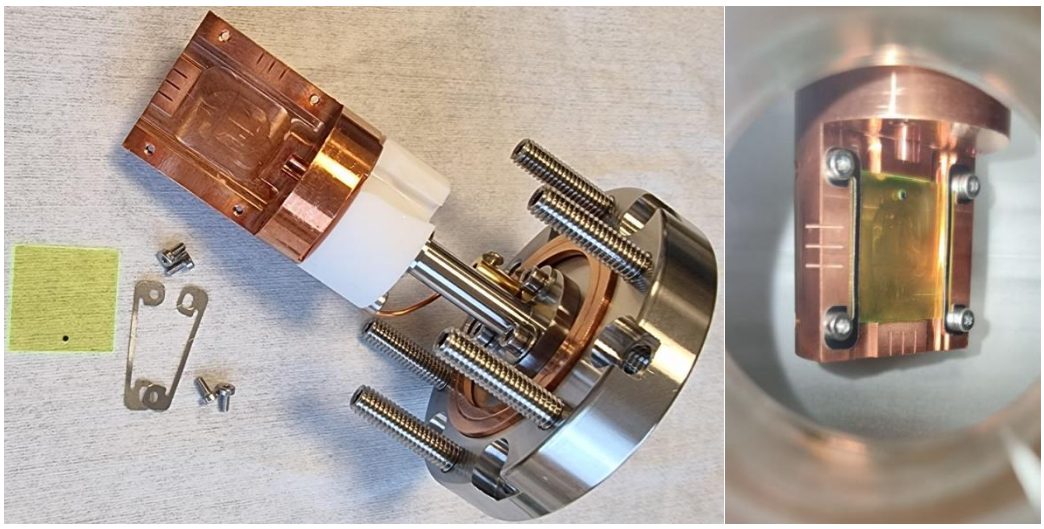

Figure 6.4: A Faraday cup containing a YAG scintillator measuring 2 x 2 cm^2

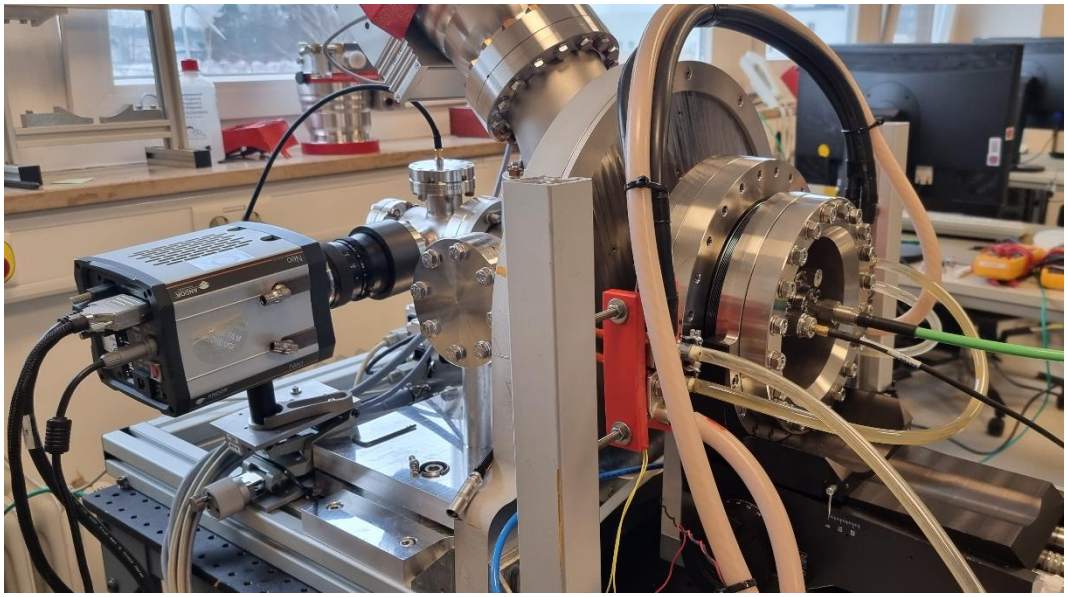

Figure 6.5: The location of the Faraday cup and the required camera

6.3 Conditioning & Multipacting

Secondary electron emission, RF discharge or multipactor might be a serious obstacle for normal operation of cavities and couplers. When the electron trajectories oscillate in a resonance with the RF field, it causes exponential growth in the number of electrons by secondary emission. According to the previous

chapter, baking out the vacuum system at 300 ºC for 24 hours significantly reduces secondary emission yield of untreated copper. The maximum temperature of 150 ºC has been chosen for baking-out of this RF gun, owing to the concern that a higher temperature may cause sudden damage to certain components of the RF gun (RF finger, scintillator, brazed joints, etc.) whose temperature sensitivity we are not yet familiar with.

The baking-out process also improves the pressure level of the vacuum system. In fact, the main source of outgassing in the vacuum system is water molecules, carbon oxides, and hydrocarbons that are bound to the surface and can be partially removed by bakeout at relatively low temperatures (100-150°C) [66].

According to the experience gained from the DESY vacuum group, the temperature rise and fall during the baking-out should be programmed at a maximum of 0.2 Kelvin per minute, and the window ports should be covered with aluminum foil to reduce thermal stress on the glass.

Four days of bakeout at 150°C resulted in a base pressure of 5×10^{-10} mbar at room temperature, which is slightly better than the conservative vacuum simulation conducted previously.

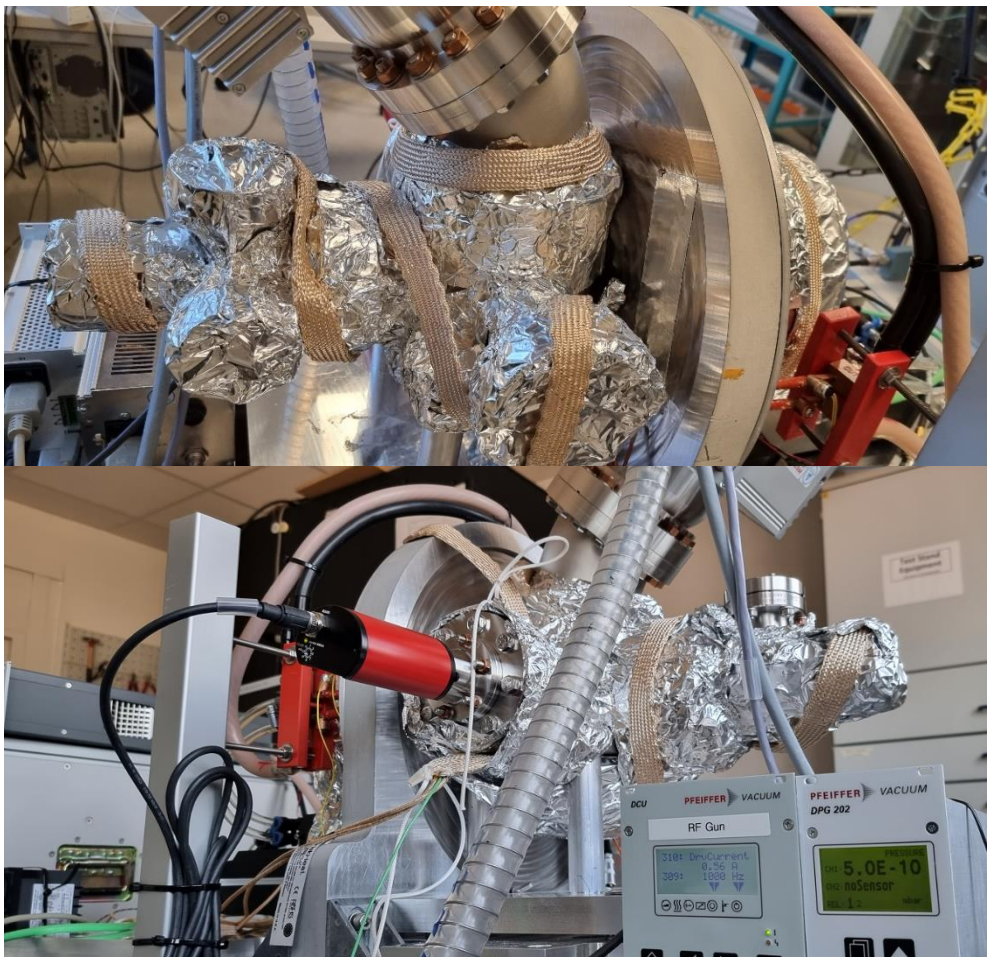

Figure 6.6: Baking out the vacuum system of the RF gun, and base pressure of 5×10^{-10} mbar after four days of bakeout at 150°C

After the baking process, the solid-state amplifier injects gradually RF power from 0 to 10 kW into the cavity to initiate the conditioning. During the RF injection, no sparking was observed in this second prototype even at high powers, and both probe and reflection signals were completely stable. This indicates that the RF finger and the entire coupling design are functioning well and transmitting RF power into the cavity effectively. When 10 kW of RF power is injected into the cavity with the solenoid turned off, Figure 6.7 illustrates the forward signal, the reflection signal from the cavity, and the probe signal within the cavity.

As another important result, no multipacting was observed during the ramping of the RF power from 0 to 10 kW, as predicted from simulations with a lower SEY due to the bakeout process.

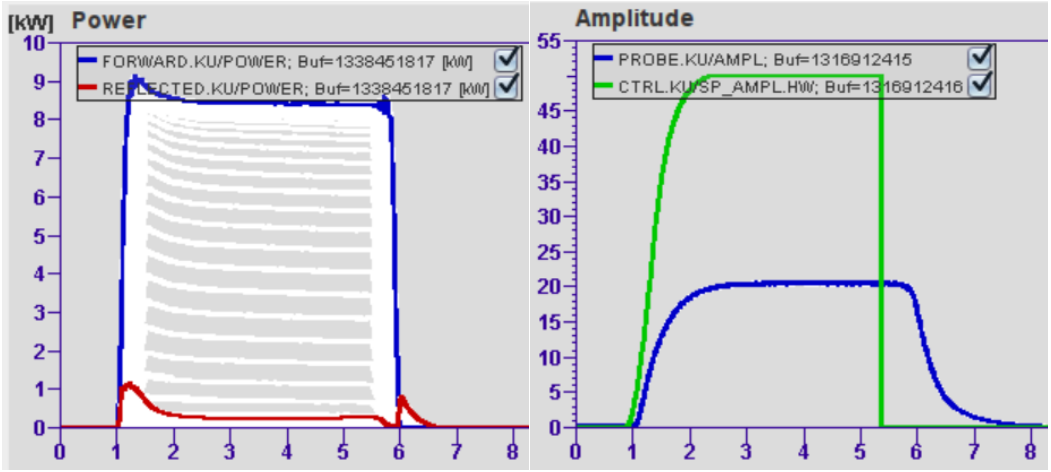

Figure 6.7: left: The forward signal (blue), and the reflection signal (red) in kW, right: probe signal inside the cavity with an arbitrary scale (blue), on the LLRF control panel.

We now maintain the RF power at 10 kW, activate the solenoid and increase its current gradually. As expected, electrons will accumulate at the corner of the cavity when the solenoid current is applied, and the multipacting within the cavity will be evident, especially at higher currents. For example, the first multipacting occurred at a current of 24 A and disappeared after 2 minutes, Then, a stronger multipacting occurred at a current of 30 A, causing the pressure to rise to 2.2e-8 mbar, and it took about 5 minutes to vanish. An illustration of a probe, forward, and reflection signals of the LLRF control panel for 24 and 30 A currents can be found in Figure 6.8.

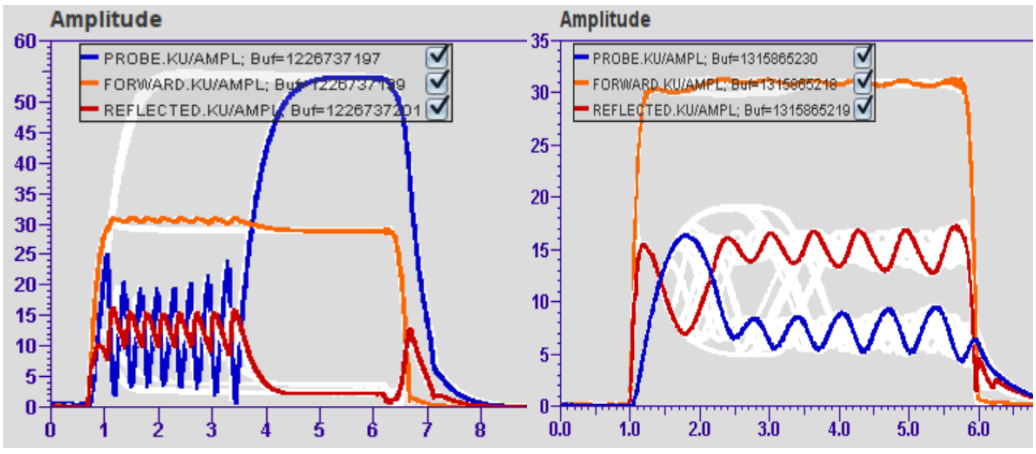

Figure 6.8: The forward (orange), reflection (red), and probe (blue) signals in arbitrary amplitude vs RF pulse length (μs), for 24 A (left) and 30 A (right) currents of the solenoid.

In order to condition the RF gun, the solenoid current is gradually increased so that the interior surfaces are continuously cleaned. As well as observing LLRF signals, which are intuitive and not quantitative, one method of identifying multipacting is to measure the dark charge. As experience has shown, the stronger the multipacting, the greater the dark charge recorded on the Faraday cup. The increasing trend in vacuum pressure can also be interpreted as a sign of multipacting, but our experience in these experiments has shown that it cannot be as reliable as the dark charge.

For the purpose of measuring the voltage produced on the Faraday cup under weak dark charges, the Faraday cup feedthrough was connected to a 1MΩ resistor of the oscilloscope. As an example, Figure 6.9 illustrates the voltage generated on the Faraday cup at a solenoid current of 30 A. Multipacting and the produced cycles of Figure 6.8 are clearly visible on this measurement, as well as the amount of dark charge can also be determined, which is equivalent to 120 pC.

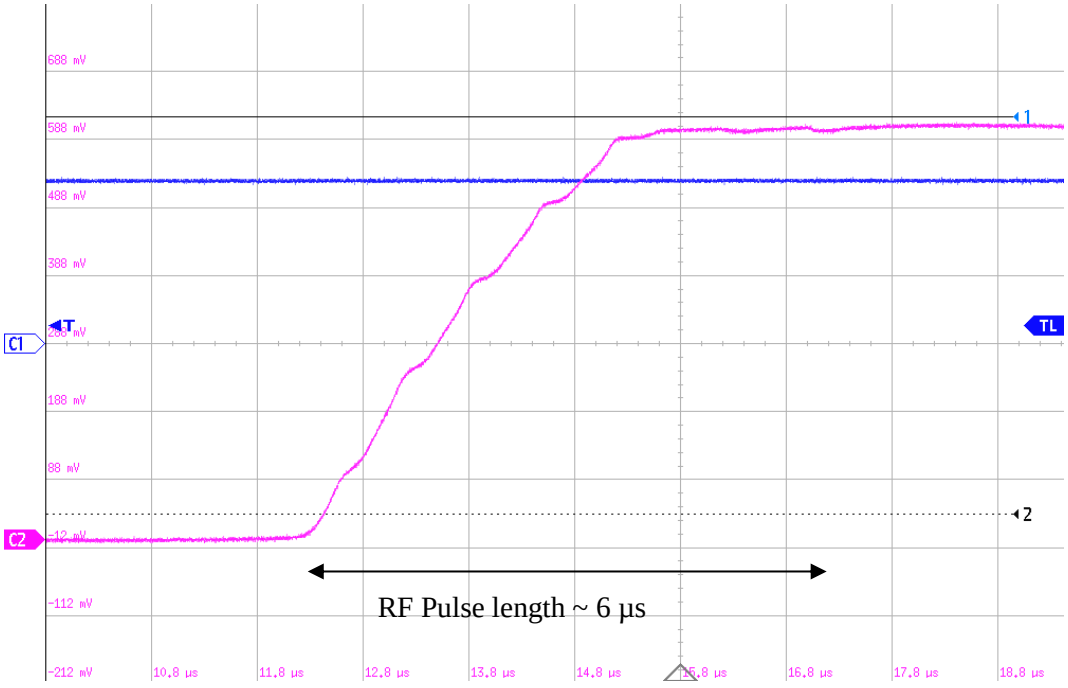

Figure 6.9: The voltage generated on the Faraday cup at a solenoid current of 30 A and RF power of 10 kW.

With the gradual increase in solenoid current when the RF power is fixed at 10 kW, the amount of dark charge was recorded for each specific current to observe the multipacting behavior. In Figure 6.10, the dark charge measurement is shown for

different solenoid currents, indicating that there is greater multipacting at higher currents. Based on these results, it can be concluded that there is a good correlation between the results of the experiment and those of the multipacting simulation, as shown in Figure 5.26.

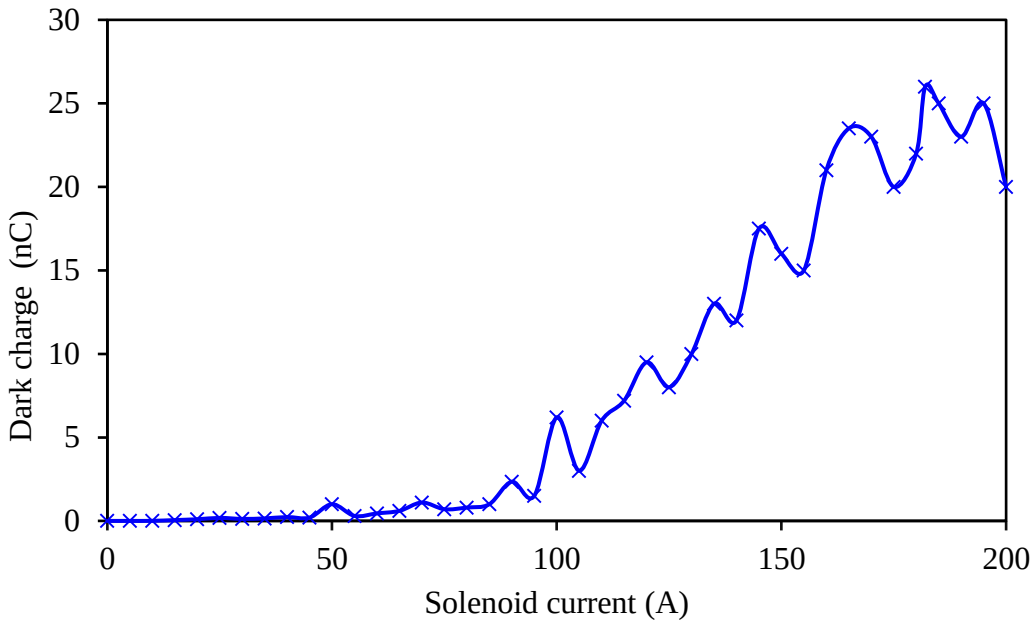

Figure 6.10: The dark charge measurement for different solenoid currents at 10 kW RF power.

This experiment confirms that, as discussed in section 3.3, there is robust multipacting at the current of 180 A and the RF power of 10 kW. Figure 6.11 illustrates the LLRF signals along with the image produced on the scintillator of the Faraday cup when a 180 A current is applied. By increasing the solenoid current from zero to 200 A, the dark charge can be detected on the Faraday cup scintillator at currents exceeding 120 A, however, the electrons are focused and the brightest light is obtained at 175 to 183 A current.

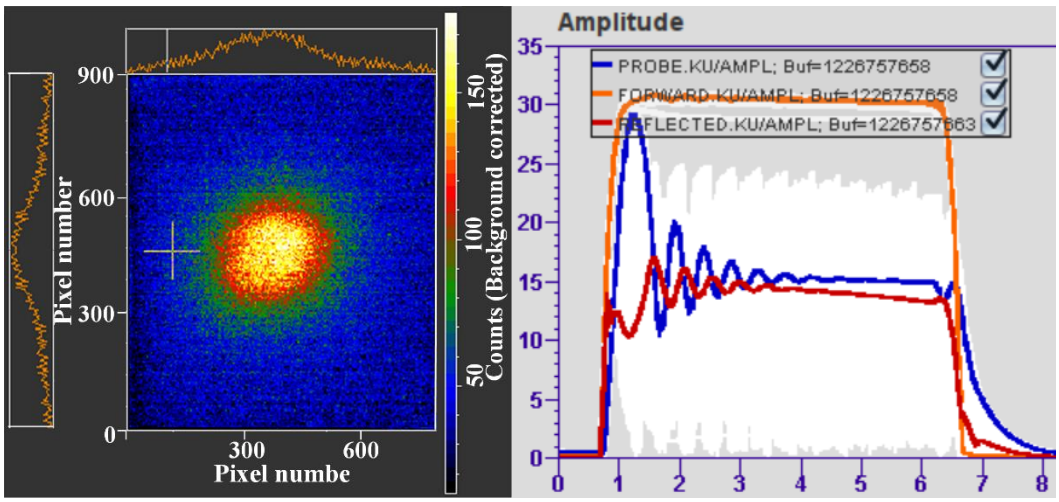

Figure 6.11: The LLRF signals along with the image produced on the scintillator of the Faraday cup at 180 A solenoid current and 10 kW RF power

In order to determine the effect of conditioning time on dark charges, we allow the RF gun to be conditioned with a current of 180 A and a power of 10 kW. As shown in Figure 6.12, the dark charge changes with respect to these parameters over time. Due to the bombardment of secondary electrons, the dark charge in this graph has decreased, indicating the cleaning of the inner surface of the cavity. After approximately 19 hours, the amount of dark charge decreases sharply, indicating that multipacting has been suppressed. At the same time, LLRF signals are stable and do not exhibit cyclic characteristics, confirming the dissolution of multipacting. There is no doubt that the multipacting or exponential growth of the number of electrons is relatively stopped after 19 hours, but the amount of dark charge is still high. As shown in Figure 6.13, the probe signal has not entirely returned to its initial state, which indicates that there are still secondary electrons within the cavity that absorb some of the stored power. Here, SEY is less (refer to simulation result in Figure 5.20), which prevents the number of electrons from increasing exponentially and causing discharge. Following 6 days of conditioning the RF gun at 10 kW power and 180 amps of current, the amount of dark charge had decreased to 100 fC.

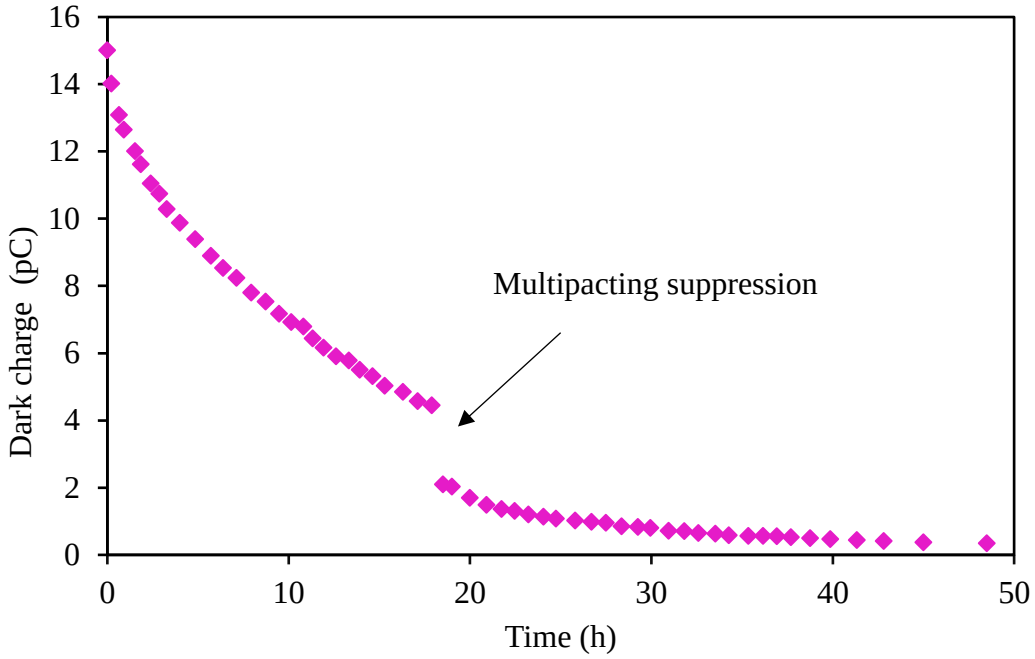

Figure 6.12: The dark charge changes over the conditioning time, with respect to 180 A solenoid current and 10 kW RF power.

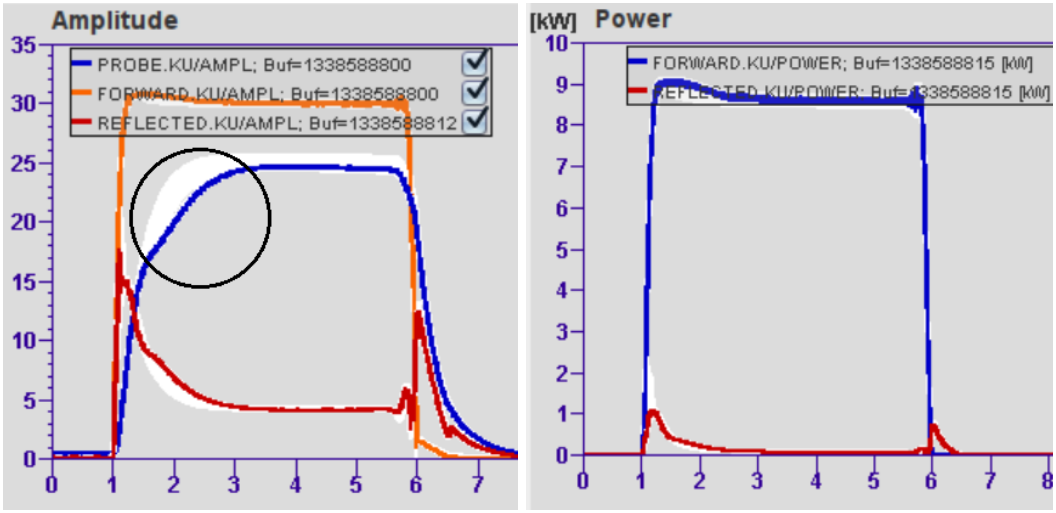

Figure 6.13: *left*: The forward (orange), reflection (red), and probe (blue) signals in arbitrary amplitude vs RF pulse length (μs), *right*: The forward signal (blue), and the reflection signal (red) in kW, on the LLRF control panel, after the multipacting is suppressed.

Chapter 7

RF Gun for Ultrafast Electron Diffraction

Ultrafast electron diffraction (UED), also known as femtosecond electron diffraction (FED), has become an important tool for probing atomic-scale structure due to the orders-of-magnitude higher interaction cross sections and orders-of-magnitude lower damage per scattering event relative to X-ray diffraction [67]. In addition, electron probes provide increased sensitivity to hydrogen atoms, which are fundamentally important for biological systems [68]. These properties, in conjunction with a significantly lower fabrication cost than comparable X-ray sources, make electron sources highly attractive for ultrafast atomic-scale research.

As a result of the space charge broadening effect in electron accelerators, it is important to minimize the acceleration and propagation times in order to prevent excessive pulse broadening prior to the interaction with the target sample. Simply stated, the longer the time it takes the pulse to arrive at the specimen, the more space-charge induced pulse-broadening will occur and the longer the electron pulse. It is essential to keep the electron pulse as short as possible to probe the dynamics of interest. For this reason, the electric fields have to be maximized, while the acceleration distance has to be minimized. Traditionally, UED sources are inexpensive, DC photoelectron guns capable of delivering high-coherence electron bunches with energies typically in the range of 50 – 100 keV. At these energies,

coulombic repulsion, also referred to as “space-charge” forces, induce a rapid spatiotemporal expansion of the beam that degrades the brightness and temporal resolution of the UED instrument, critical for generating high-quality diffraction patterns and resolving fast chemical processes. To combat these effects, the bunch charge and propagation distances should be minimized. This approach, however, requires long acquisitions at high repetition rates and hence a high degree of reproducibility in both the sample and its dynamics, limiting the type of samples that can be studied. Short gun-sample distances also restrict the complexity of the sample delivery system and prevent investigation of certain classes of samples, such as those in a liquid phase, which are increasingly becoming important for understanding biological processes. The low electron energies also bring other challenges, including temporal walk-off between the electrons and copropagating pump laser pulses initiating the interaction, as well as increased probability of multiple-scattering events which limit sample thicknesses to the few-nanometer range, which can be difficult to implement [69].

An alternative to DC fields for the purpose of rapid acceleration of charged particles to highly relativistic energies is the application of RF-fields in normal or superconducting cavities are commonly used for the acceleration of electrons to energies ranging up to the MeV range. The acceleration in RF-cavities happens within very short periods of time by the application of high electric field gradients, which are resultant of the collection of RF-waves in the geometrically constrained spaces of the metallic cavities. The propagation speed of RF waves within these constrained dimensions leads to the fast alternating character of the fields, with frequencies typically ranging in GHz can produce very short electron pulses with high peak currents, making them ideal for studying ultrafast phenomena.

However, multi-MeV RF guns, typically driven by klystrons, require a level of cost and infrastructure not accessible to the majority of small, university-scale labs, restricting the user base and thus the growth of the scientific field. Here, we propose an intermediate solution between the DC-gun and RF-gun technologies which is still low cost and requires low levels of infrastructure, but significantly increases electron energies beyond what is typically feasible with DC guns: a compact RF gun driven by a low-average-power solid-state amplifier which harnesses field-enhancement at a pin-shaped photocathode to increase field strengths, electron energies and hence bunch quality. A prototype, designed to reach 180 keV with a single power supply and 270 keV with a second unit has been constructed and is currently undergoing conditioning and characterization. We present the design

concept of the gun and report on measurements of the cavity performance during the successful conditioning phase of the prototype.

Subject to achievement of high brightness electron bunches we plan to conduct UED studies of phonon dynamics in lithium niobate to improve THz generation for the AXSIS project and eventually use a duplicate of this electron gun as a photo injector for the AXSIS source.

7.1 Beam dynamics simulation of the compact RF gun

The RF cavity, based on a half-cell pill-box, was designed expressly for the UED application by combining both acceleration and compression of the electron bunch in a single device. By implementing a pin-shaped photocathode with a flat 0.8 mm tip, strong enhancement of the RF-field strength in the vicinity of the cathode is achieved which substantially reduces the power requirements, and hence the cost and complexity of the device. The fields, which peak over 100 MV/m (based on Figure 4.25) using only a 10-kW peak power solid-state amplifier, both accelerate the electrons to 180 keV and impart a linear velocity chirp onto the bunches, allowing them to compress via velocity bunching to sub-100 fs durations at a distance of 8 cm from the cathode. A solenoid lens is placed directly in front of the anode for beam collimation.

In UED experiments, pulse duration plays an important role since it establishes the maximum temporal resolution that can be achieved. Electrons are bombarding the sample during the pulse duration, resulting in the formation of a diffraction pattern. Consequently, a shorter pulse duration will result in a higher time resolution. In order to determine the duration of a pulse, two factors must be considered: the length of the beam and the velocity of the electron.

In preparation of the electron beam for the UED experiment, it is recommended to focus the electron beam temporally on the specimen (8 cm away from the cathode), while simultaneously collimating the electron beam in the transverse direction at this point by the solenoid magnetic field. A collimated electron beam is crucial for precise probing of specimens, ensuring high-resolution diffraction patterns. By maintaining focus and reducing beam spread, collimation enhances signal clarity and minimizes background noise, crucial for accurate data interpretation. Knowledge of the final energy and energy spread of electrons is also beneficial.

It is important to note that how these conditions are achieved depends on the laser pulse duration ($T_{l,rms}$), laser spot size ($XY_{l,rms}$), and electron bunch charge. Additionally, for a specific $T_{l,rms}$ and $XY_{l,rms}$, it must be identified under which phase of the electric field (φ_E) and magnetic field of solenoid (B_s) these conditions will be established. As an example, with a bunch charge of 10 fC and $T_{l,rms} = 0.4\ ps$ and $XY_{l,rms} = 5\ \mu s$, Figure 7.1 shows the bunch length (σ_z) in rms in terms of φ_E and B_s, so that the blue line indicates the minimum of σ_z and the dashed green line indicates the point at which the electron beam is collimated.

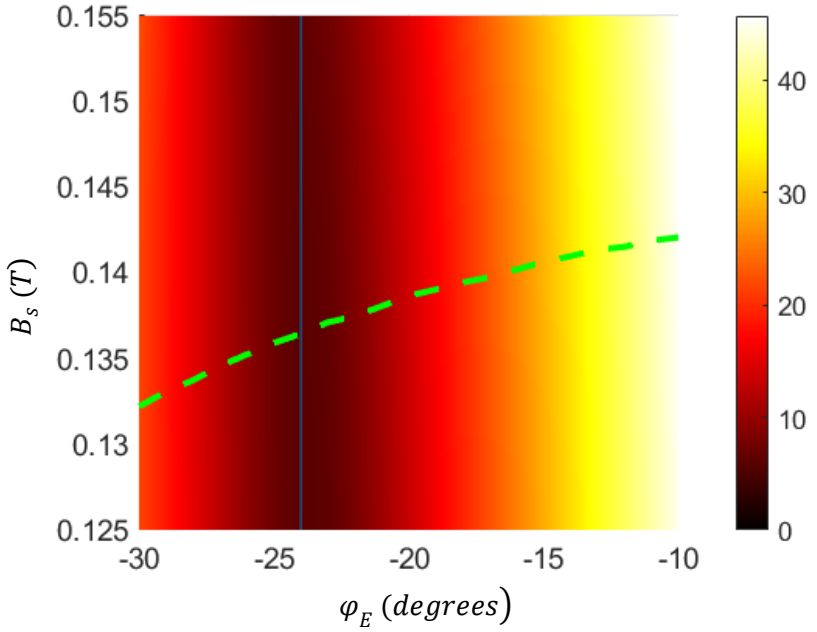

Figure 7.1: Bunch length (σ_z) in color map and collimated beam plot (green line) when $T_{l,rms} = 0.4\ ps$ and $XY_{l,rms} = 5\ \mu s$.

Consequently, the intersection point of these two lines will provide the solution to the UED experiment conditions. This intersection point is calculated for a wide range of $T_{l,rms}$ and $XY_{l,rms}$, and finally, in Figure 7.2, the minimum possible bunch length σ_z in fs is plotted for a bunch charge of 10 fC. The ASTRA particle tracking solver is used to investigate the beam dynamics in the gun. Also, Figure 7.3 and Figure 7.4 show respectively the average energy of electrons and the spot size of the electron bunch at the specimen in terms of $T_{l,rms}$ and $XY_{l,rms}$. Moreover, the simulation indicates that for the above $T_{l,rms}$ and $XY_{l,rms}$ values, the maximum energy spread of electrons on the specimen will be 0.92% (Figure 7.5).

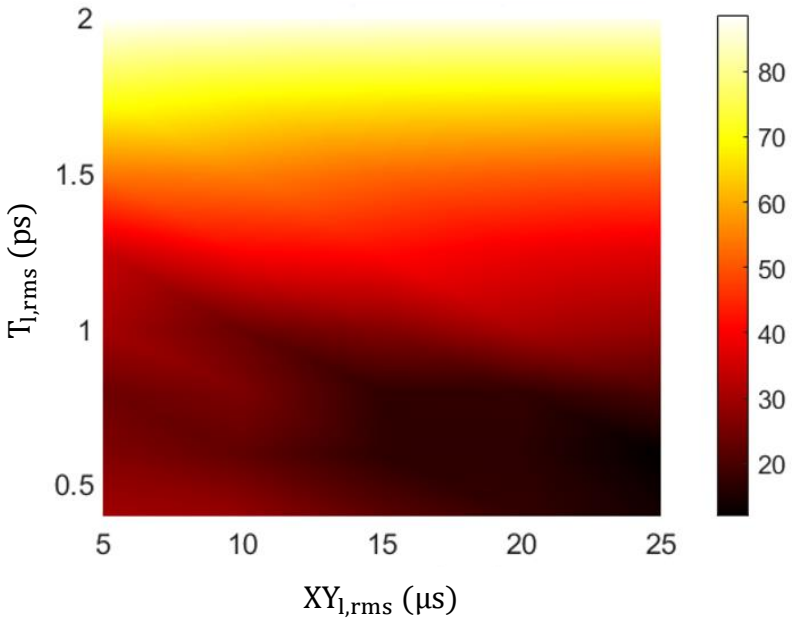

Figure 7.2: The color map illustrates the minimum rms electron bunch duration (σ_z) in fs in terms of $T_{l,rms}$ and $XY_{l,rms}$ for electron bunch charge of 10 fC.

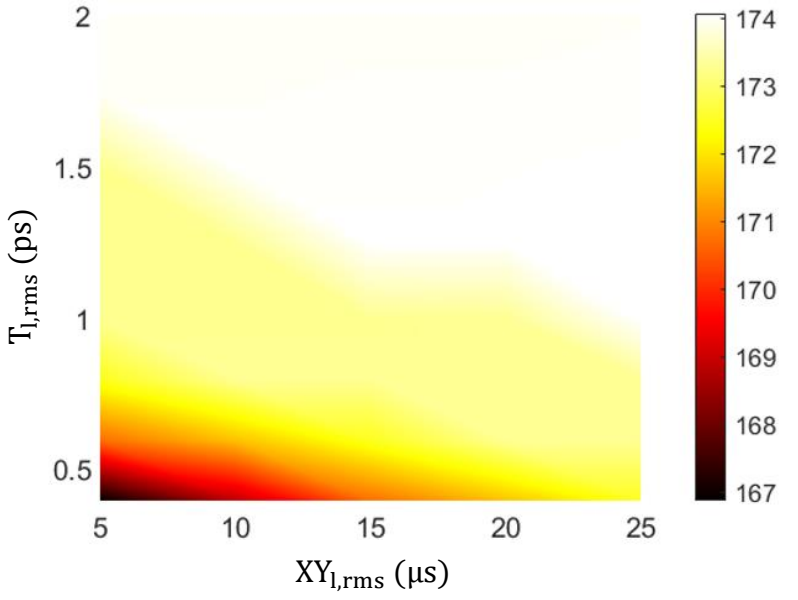

Figure 7.3: The energy of electrons on the specime in keV expressed in terms of $T_{l,rms}$ and $XY_{l,rms}$.

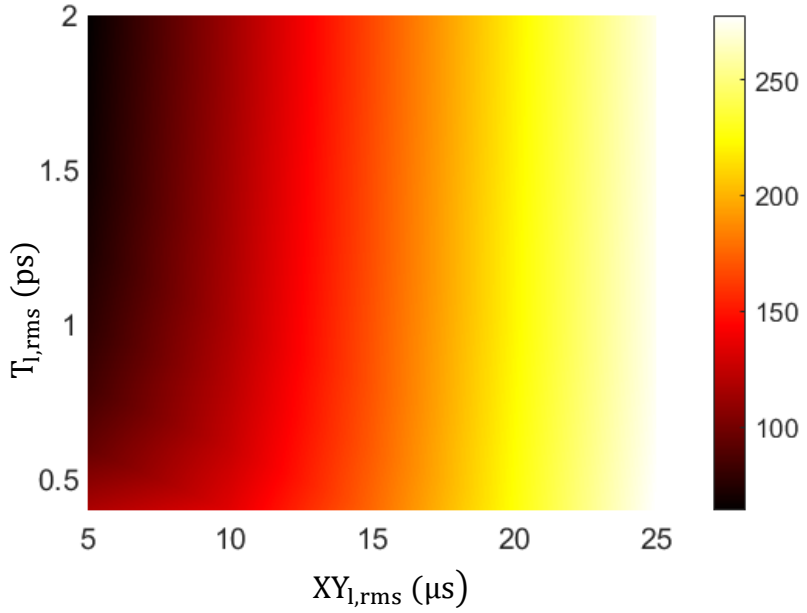

Figure 7.4: The spot size of the electron bunch in μm at the specimen in terms of $T_{l,rms}$ and $XY_{l,rms}$.

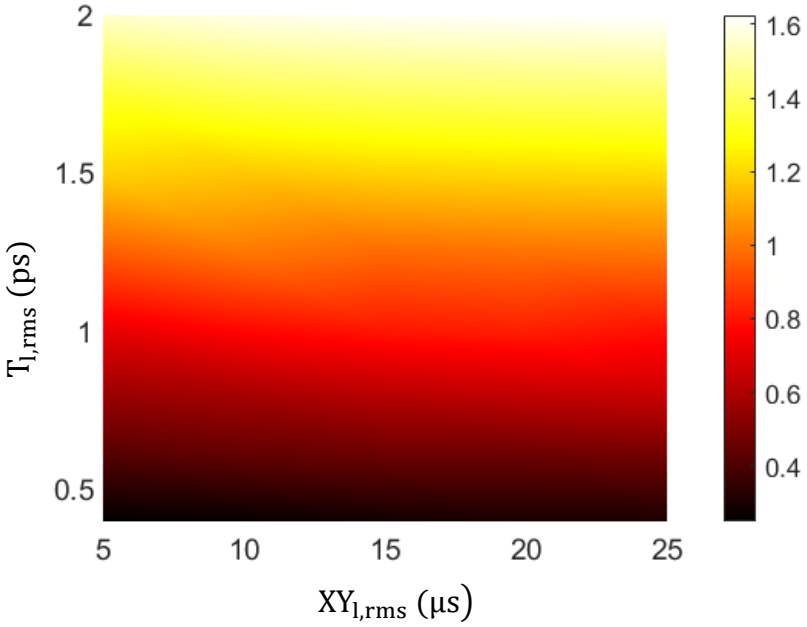

Figure 7.5: The energy spread of electrons on the specimen in keV expressed in terms of $T_{l,rms}$ and $XY_{l,rms}$.

In order to capture the fastest structural rearrangements on the Å scale, a temporal resolution of order 10 femtoseconds (fs) is required [70], implying the generation of electron pulses of similar duration with sufficient brightness. According to the result above, the pulse duration of the electron bunch will be approximately 10 fs at the optimum point, assuming that the bunch change is equal to 10 fC. Using $T_{l,rms} = 0.5\,ps$ and $XY_{l,rms} = 25\,\mu m$, Figure 7.6 illustrates the bunch length and spot size of the electron bunch along the propagation path. The bunch length is focused at the specimen, while the beam is transversely collimated, and the RMS radius of the beam is 135 µm. In order to achieve this result, the phase of the electric field and the magnetic field of the solenoid must be -25° and 0.135 T, respectively.

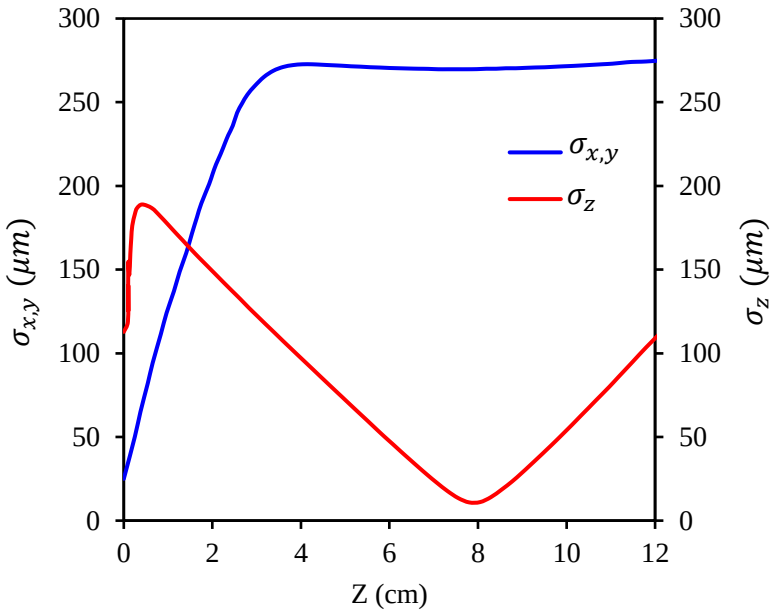

Figure 7.6: The bunch length and spot size of the electron bunch along the propagation path, using $T_{l,rms} = 0.5\,ps$ and $XY_{l,rms} = 25\,\mu m$

An important parameter in electron diffraction experiments is the transverse coherence length, which is defined as the maximum distance between two electrons over which interference is still visible [71]. The transverse coherence length can be expressed as:

$$L_x = \frac{\hbar}{mc}\frac{\sigma_x}{\varepsilon_{n,x}} \tag{7.1}$$

where ħ is Planck's constant divided by 2π, m is the electron mass, c is the speed of light, σ_x is the rms beam size and $\varepsilon_{n,x}$ is the transverse normalized emittance defined by $\varepsilon_{n,x} = \frac{1}{mc}\sqrt{\langle x^2\rangle\langle p_x^2\rangle - \langle x p_x\rangle^2}$. In the case of 10 fC bunch charge, the transverse coherence length will be equal to 2.9 nm at the optimum conditions.

7.1.1 Influence of electron bunch charge on optimum configurations

The optimal laser spot size and laser duration depend on the transverse space charge and the cathode emittance, as discussed in chapter 4. The strength of the transverse space charge forces is highly dependent on the bunch charge, and the simulated optimal duration of 10 fs and rms radius of 135 μm is only valid for a 10 fC bunch charge. Based on practical experience, a bunch containing more than 10^5 electrons is required to acquire a diffraction signal with sufficient contrast [72]. The diffraction signal becomes stronger as the number of electrons increases. However, as the bunch charge increases, the transverse space charge forces will increase, resulting in a different optimal laser spot size, optimal laser pulse duration, as well as electron bunch properties at the specimen.

Figure 7.7 illustrates the pulse duration of electron bunches on the specimen in femtosecond as a function of laser pulse duration and laser spot size when the electron bunch charge is equal to 100 fC. As can be seen, the space charge has a significant effect on the pulse duration $T_{l,rms}$ smaller than 0.8 ps. The minimum pulse duration of the electron bunch at the specimen will be equal to 50 femtoseconds, and the optimal point for $T_{l,rms}$ and $XY_{l,rms}$ differs from that calculated for 10 fC bunch charge. Figure 7.8 and Figure 7.9 illustrate the average kinetic energy of electron bunch and their transverse size at the specimen as a function of $T_{l,rms}$ and $XY_{l,rms}$. In the optimal state, by elevating the bunch charge from 10 to 100 fC, the electron energy is reduced slightly from 174 to 170 keV. In addition, the radius of the electron bunch at the specimen is 150 μm.

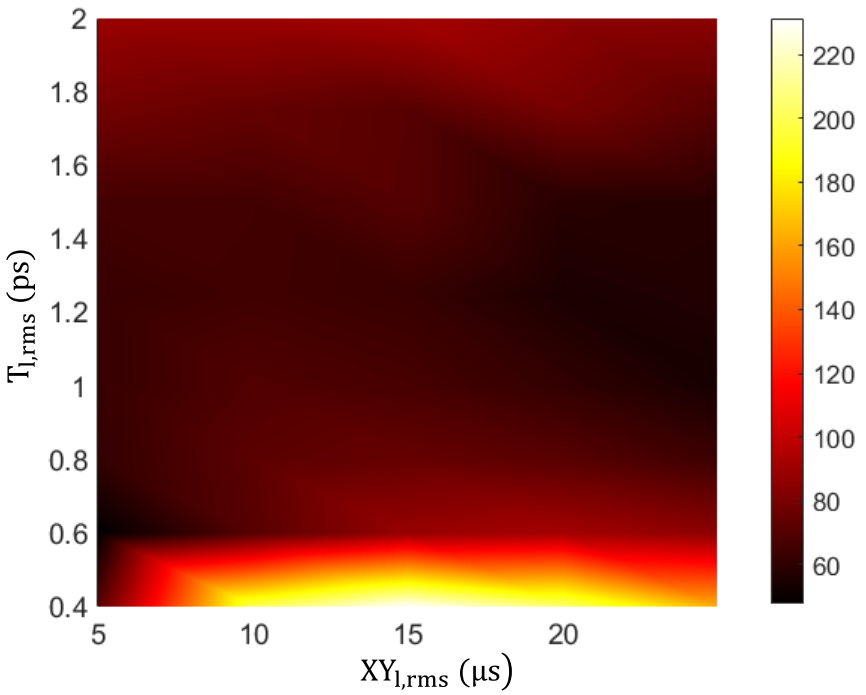

Figure 7.7: The color map illustrates the minimum rms electron bunch duration in fs in terms of $T_{l,rms}$ and $XY_{l,rms}$ for electron bunch charge of 100 fC.

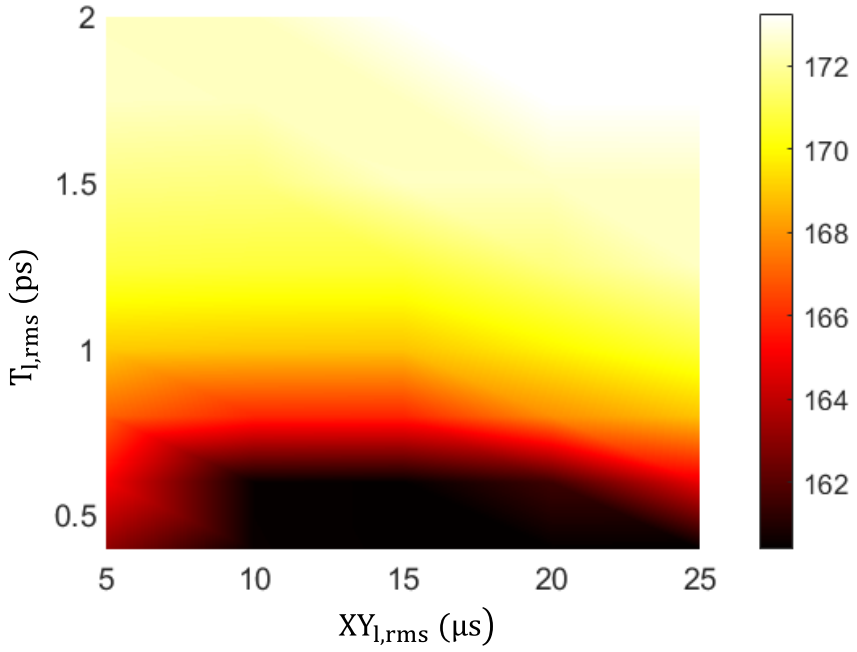

Figure 7.8: The average energy of electrons on the specimen in keV expressed in terms of $T_{l,rms}$ and $XY_{l,rms}$ for 100 fC bunch charge.

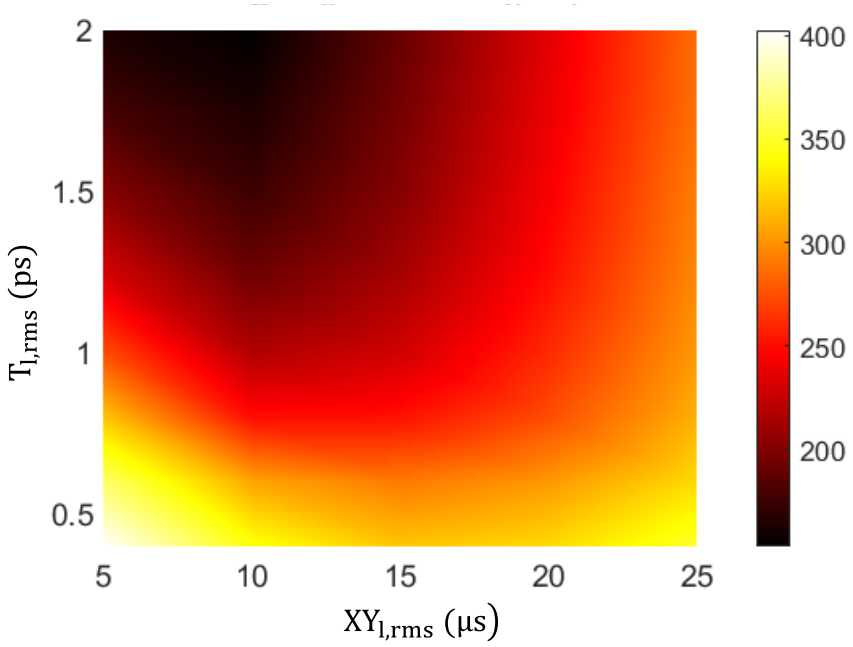

Figure 7.9: The spot size of the electron bunch in μm at the specimen in terms of $T_{l,rms}$ and $XY_{l,rms}$, for 100 fC bunch charge.

The effect of the longitudinal and transverse distribution of electrons in an electron bunch on the temporal bunch length is also investigated. In the simulations above, gaussian distributions of electrons were considered both longitudinally and transversely. As mentioned in Chapter 4, the space charge field also includes nonlinear defocusing components that result in increased emittance. These non-linear forces depend on the type of electron beam distribution and therefore on the spatial distribution of the laser pulse. An ideal shape of the electron bunch is a homogeneous ellipsoid [73], [74], since the space charge field will be linear in all directions during compression. With a charge of 100 fC and a laser pulse spot size of 25 μm, Figure 7.10 shows the dependence of electron bunch duration on the laser pulse duration $T_{l,rms}$ in a variety of laser pulse shape such as gaussian, flat-top, and ellipsoidal.

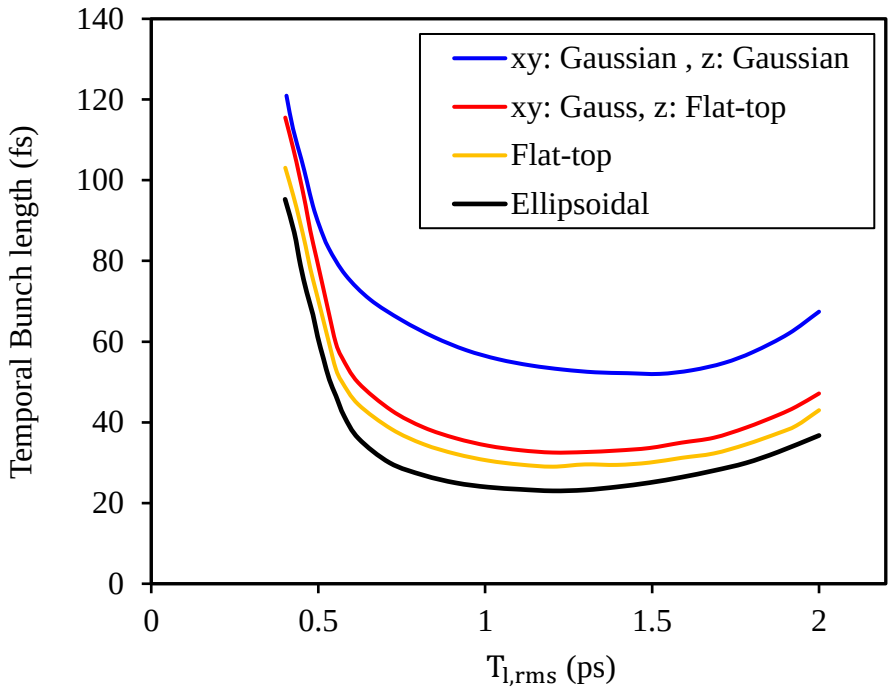

Figure 7.10: The electron bunch duration vs laser pulse duration for different laser pulse shape in 100 fC

According to the figure, the uniform distribution in the z direction has a greater impact on reducing the temporal bunch length than the transverse distribution, and the space charge effect is quite evident at lower $T_{l,rms}$ for different distributions. It is therefore reasonable to make greater efforts to improve the temporal distribution of the laser beam. Although it is difficult to achieve an ellipsoidal shape of the temporal laser pulse in practice [75], laser beam injection into the photocathode using a temporal flat-top profile with a short rise and fall times and a transverse shape of a circular flat-top appears to be feasible [75]–[77]. During our experiments on laser beam shaping, which will be discussed in the following sections, we approached a flat-top distribution. According to Figure 7.10, by changing the laser pulse shape from Gaussian to flat-top with 10 % rise and fall times, the temporal duration of electron bunch at the specimen can be reduced from 53 to 29 fs.

7.2 The femtosecond laser system

The laser beam line is driven by a Coherent Legend Elite Duo amplifier comprised of a diode pump laser, an oscillator, and a regenerative amplifier. The fundamental wavelength of the system at the amplifier output is 800 nm with a maximum energy of 5 mJ per pulse. This system also produces pulses with a duration of 35 fs and a maximum repetition rate of 3 kHz.

Through the third harmonic generation by two BBO crystals, the fundamental wavelength of 800 nm is converted to the UV regime with 267 nm wavelength in order to efficiently extract electrons from the photocathode material from the cavity front-side. A fraction of the laser power is divided through a beam splitter to be used as a pump for the UED experiment. A linear translation stage is included in the pump beamline, which is designed to insert a controlled delay between the arrival times of the pump and the probe beam. Figure 7.11 illustrates how the UV beam and the pump beam is directed toward the specimen via the flange on the side of the specimen chamber.

Table 3: A list of the equipment used in the tripling layout of the fundamental laser pulse as well as the temporal stretching beamline of the UV beam

beamline	items
Tripling	4:1 telescope to reduce beam size
	0.5 mm 29° BBO= SHG xtal
	70fs-350 fs calcite retarder plate
	800/400 nm dual wave plate
	0.1 mm 43° BBO tripling xtal
Stretching	Aluminum mirrors M1, M2, M3
	Brewster cut fused silica prism pairs P1, P2

Figure 7.13 illustrates the tripling layout of the fundamental 800 nm laser pulse as well as the beamline corresponding to the temporal stretching of the 267 nm UV beam. Table 3 provides a list of the equipment used in this layout. Prior to being sent to the third harmonic generator (THG), the fundamental beam is horizontally

polarized. Therefore a horizontal (p-polarized) UV beam is obtained at the end of the TGH (Figure 7.12). Thus, the UV beam will strike the prism at Brewster angle and pass through it to be streched.

Temporal shaping to the required picosecond timescale for effective RF cavity compression is accomplished by a four-prism stretcher. Figure 7.13 illustrates the configuration of the bowtie prism stretcher, which includes four prisms. Based on the results of our experiment, four prisms in a double bowtie stretcher have the advantage of reducing the distance (approximately 1 m) between the dispersers by four times, compared to using two simple stretcher prisms. In this way, the UV beam stretching setup will be more compact and more stable when it comes to vibrations and distortions. THG beamline efficiency is approximately 0.5% at 200 mW input power. Additionally, the temporal stretcher configuration is about 80% efficient. Due to the fact that copper has a work function of 4.5 eV and a quantum efficiency of 10^{-5}, there is the possibility of more than 10^{6} electrons being extracted from photo-emission.

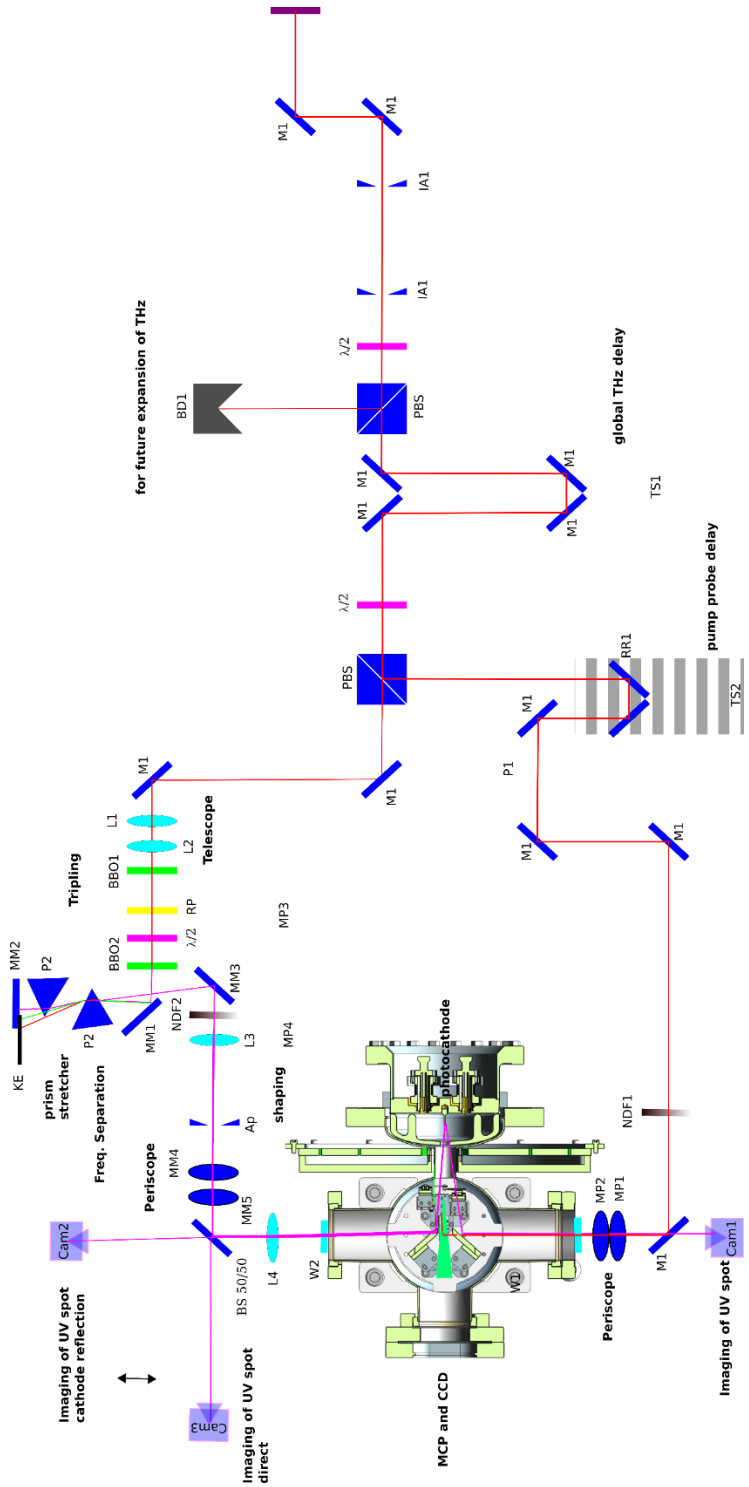

Figure 7.11: Layout of the laser beamline for injecting into the photocathode and specimen

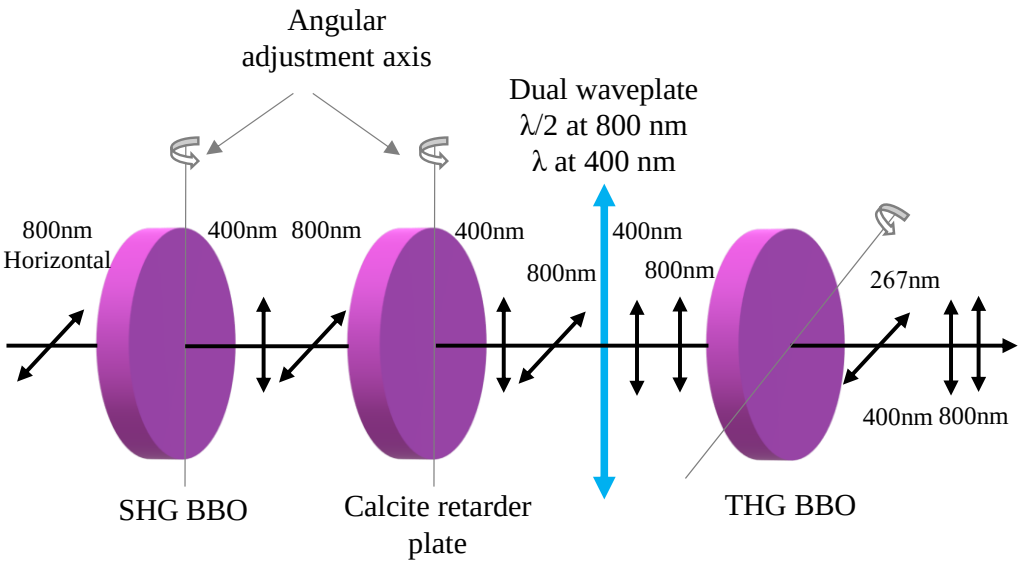

Figure 7.12: Optical Layout of third harmonic generation

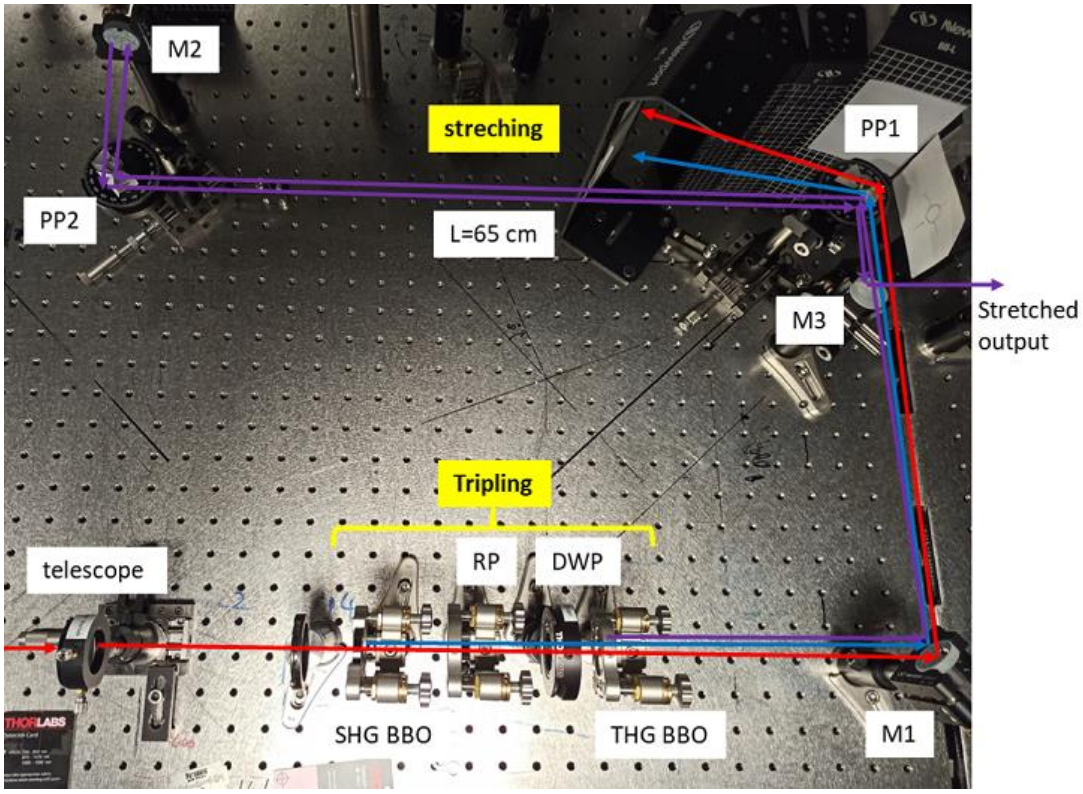

Figure 7.13: Tripling layout of the fundamental laser pulse as well as the temporal stretching beamline of the UV beam.

Transverse beam shaping is accomplished by 2:1 imaging of an illuminated 50-micron pinhole onto the photocathode, and we have demonstrated a one sigma truncated Gaussian beam profile of 26 µm diameter, approximating the ideal 'half circle' radial profile desired for linear space charge expansion dynamics.

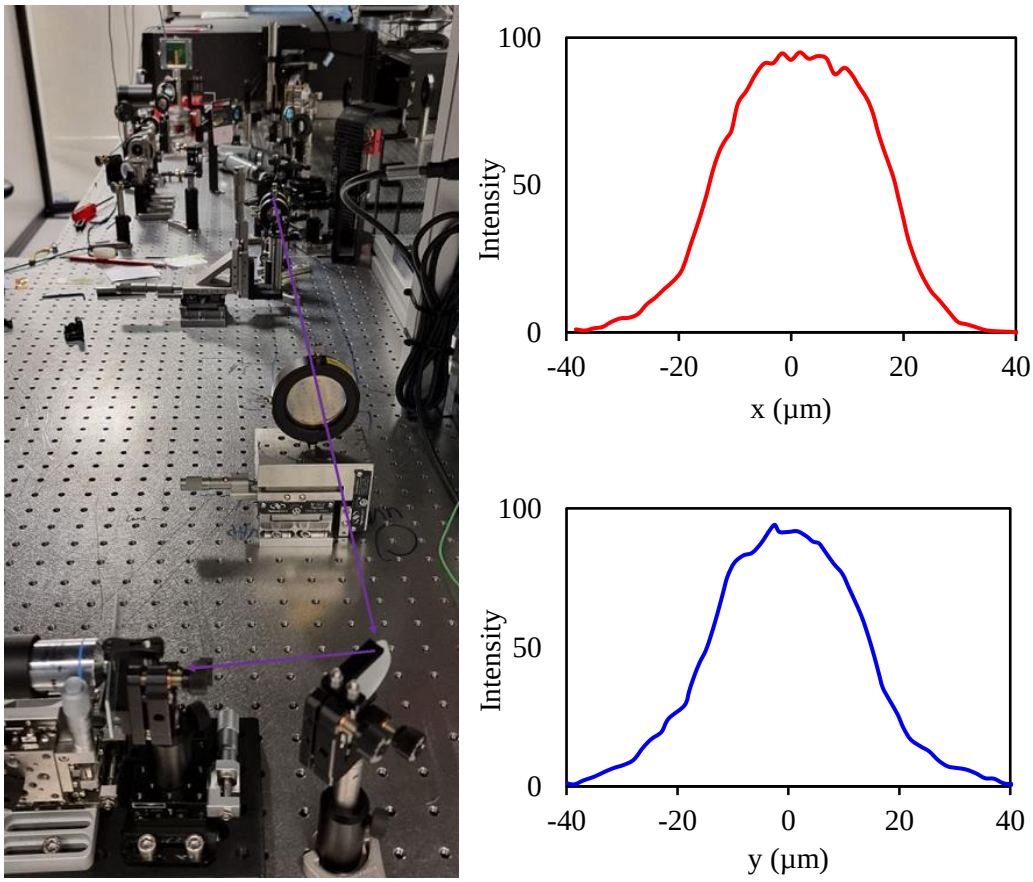

Figure 7.14: Transverse beam shaping of UV beam, with a quasi half-circle radial profile

7.3 Specimen chamber

The specimen chamber is, as its name suggests, a chamber in which various specimens and diagnostics are placed, as well as the UV beam can be coupled to photocathodes using a suitable design. Due to the mechanical limitations of the solenoid position between the cavity and the specimen chamber, as well as the limitation of the solenoid saturation in small thicknesses, a minimum distance of 8 cm was considered for positioning the specimen relative to the photocathode for the

purpose of achieving the shortest electron bunch length possible at the specimen position. A cross-sectional view of the compact RF gun is shown in Figure 7.15, including the structure of the cavity, solenoid, energy spectrometer, specimen chamber, as well as the coupling of the UV and IR beams.

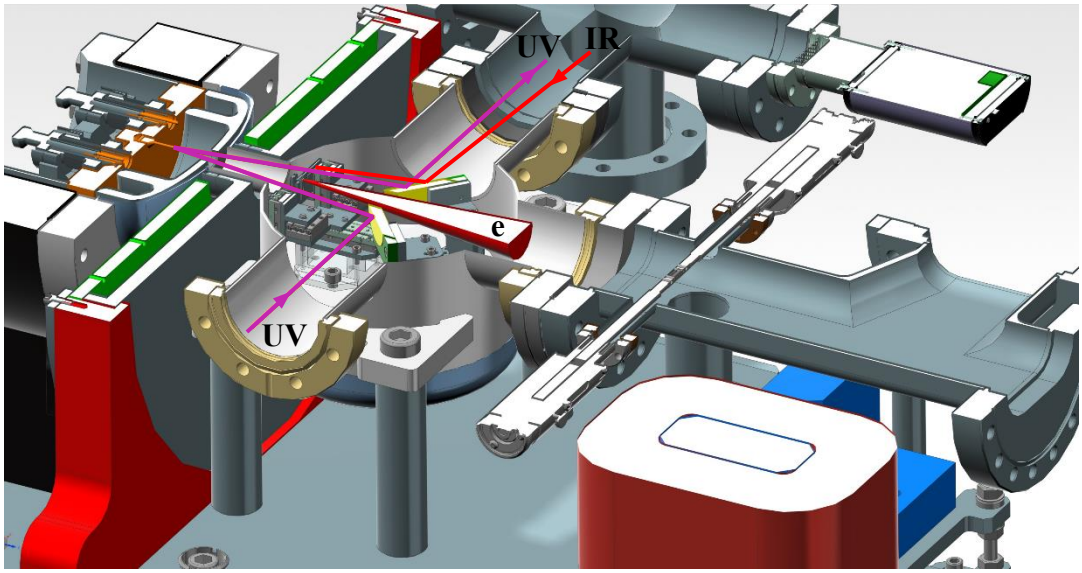

Figure 7.15: Sectional view of Compact RF gun including the cavity structure, solenoid, specimen chamber, and energy spectrometer.

An interior view of the specimen chamber is shown in Figure 7.16, along with the location of the mirrors, streak camera, and sample holder. After passing through the UV vacuum window and reflecting from the M1 aluminum mirror, the UV beam will reach the photocathode. The reflected UV from the cathode surface will be transferred out through the IR vacuum window so that beam shape imaging can be performed to ensure the UV coupling on the pin-cathode. The IR beam, which will be used as a pump pulse, enters through the IR window, then is reflected by the M2 aluminum mirror and radiates on the photoswitch of the streak camera.

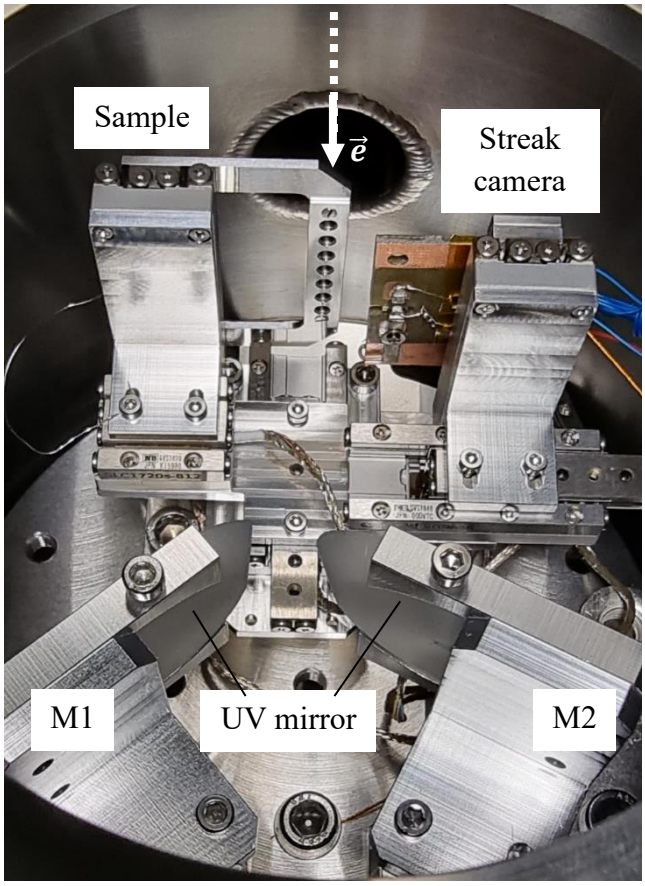

Figure 7.16: Interior of the specimen chamber, showing electron beam aperture, specimen and streak camera assemblies.

Considering the small inner radius of the solenoid tube (12 mm) and the presence of other components within the chamber, it may be operationally difficult to couple the UV, receive its reflection for imaging, and irradiate the IR beam in such a compact space, which calls for a precise design of the components within the chamber.

From the vacuum point of view, adding such components in the specimen chamber and connecting the side cross chambers for coupling the UV and the pump rays as well as the downstream diagnostic chamber, will increase the thermal outgassing and volume of the vacuum system. For this purpose, a compact NexTorr D 500-5 pump (combination of NEG pump and ion pump) has been added to this system to provide UHV conditions along with the turbo pump. The vacuum simulation shows that the base pressure inside the cavity is equal to 1.6×10^{-9} mbar, and after RF gun conditioning, the maximum dynamic pressure inside the cavity will be equal to

7.3×10^{-9} mbar. This pump along with the RF gun and other equipment used in the UED experiment mounted on an optical table can be seen in Figure 7.17.

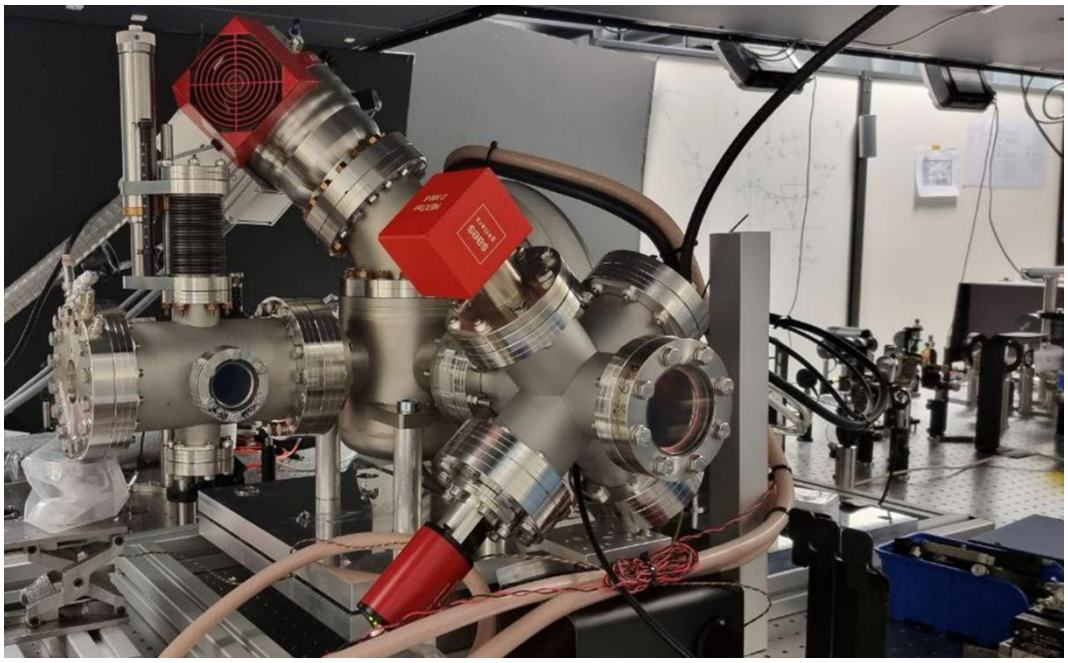

Figure 7.17: An overview of the RF gun used for the UED mounted on an optical table.

7.4 Dignostics:

7.4.1 UV alignment and monitoring:

Previously, the UV beam was imaged using a suitable scintillator and a microscopic objective at a distance equal to the pin-cathode position, as shown in Figure 7.14. Then we want to align the UV beam on the pin-cathode inside the cavity and monitor its coupling remotely. A screen scintillator (a microscope cover slide with a thickness of 100 µm) is set on the pin-cathode from the downstream diagnostic chamber (Figure 7.19-a). Following this, the scintillated beam is observed by a far-view camera along with the telescope objective, which is placed at the focal distance (60 cm from the pin-cathode), as shown in Figure 7.18. For the UV beam to be focused more precisely on the photocathode, we need to align the two-inch UV lens on a 3D stage directly in front of the UV window (Figure 7.20).

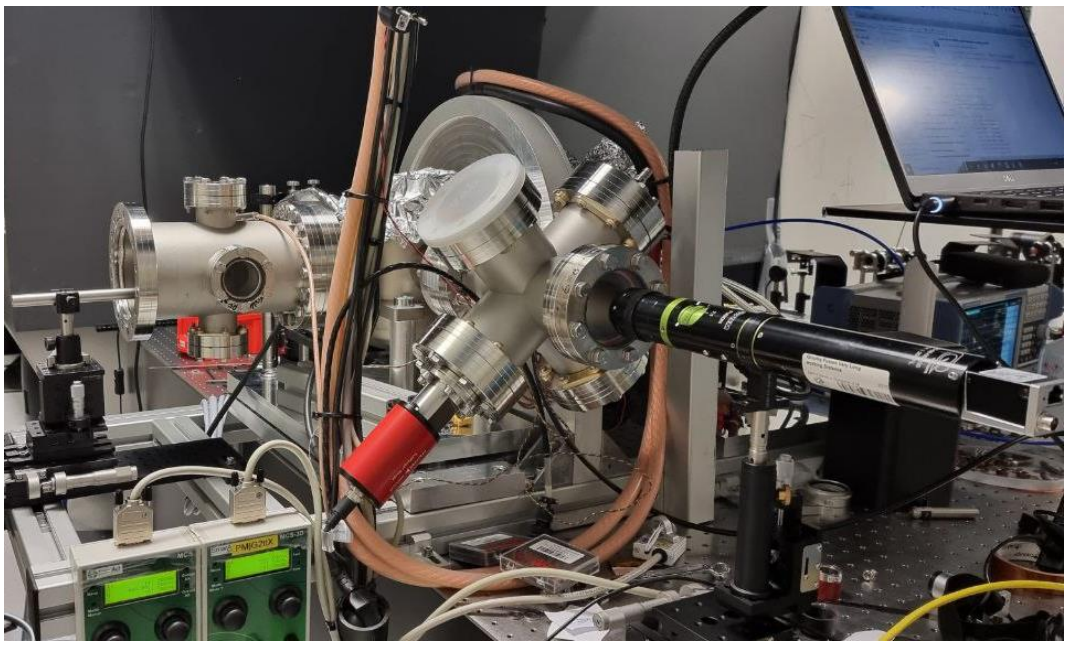

Figure 7.18: Alignment of UV beam on the pin-cathode using a UV scintillator and a far-view camera

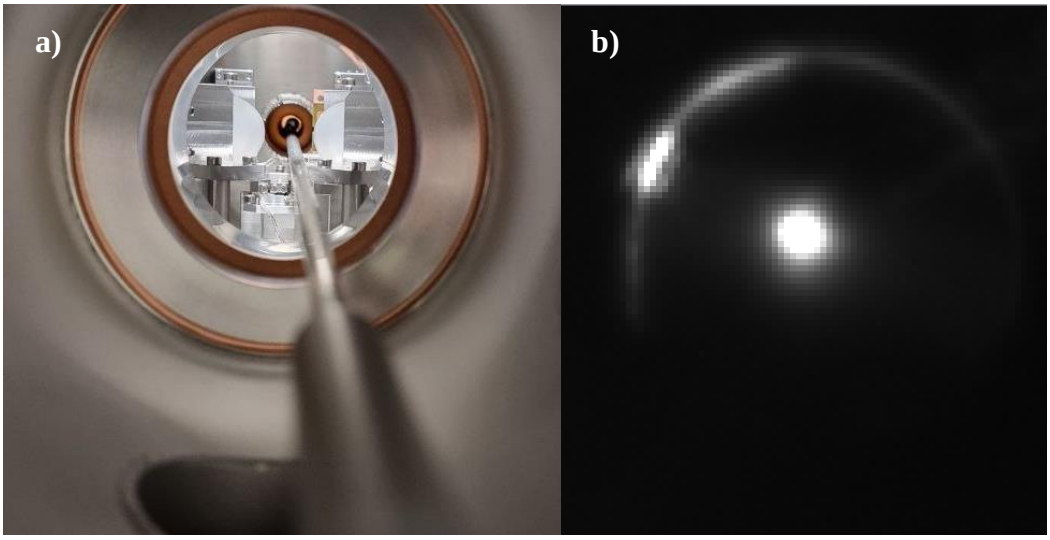

Figure 7.19: a) Alignment of the scintillator on the pin-cathode from the back chamber, b) UV beam being aligned on the center of the circular cross-section of the pin-cathode can be observed through the imaging system.

In Figure 7.19-b, an example of the UV beam being aligned on the center of the circular cross-section of the pin-cathode can be seen. Since there is no scintillator on the pin-cathode after vacuuming the system, we create a UV imaging system

similar to the one we created previously for monitoring the UV beam profile right after the IR vacuum window. Figure 7.20 illustrates the reflected UV beam emerging from the vacuum window and the location of the IR beam.

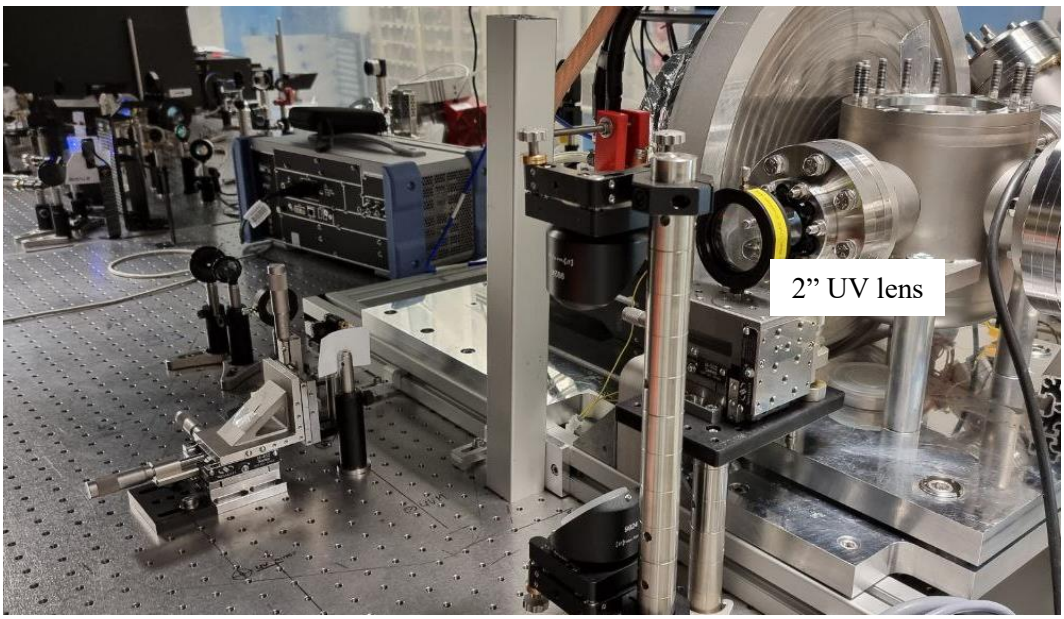

Figure 7.20: UV beam shaping before injecting to the side-chamber of the RF gun.

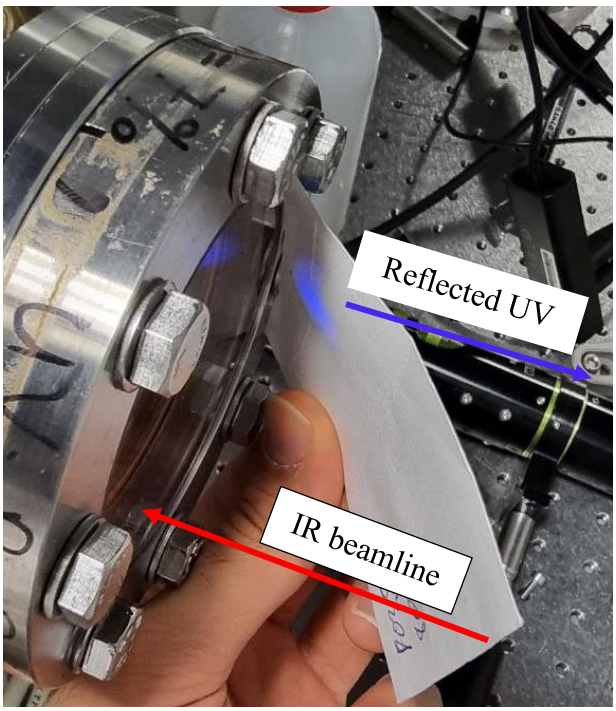

Figure 7.21: The reflected UV beam emerging from the vacuum window and the location of the IR beamline

7.4.2 Streak camera

Electron beam diagnostics include a streak camera featuring a gallium arsenide photoconductive semiconductor switch (GaAs PCSS) for sub-100 fs resolution electron bunch profiling and arrival time jitter measurement. The latter has been developed in collaboration with the Max Planck Institute for the Structure and Dynamics of Matter (MPSD).

Figure 7.22 illustrates the streak camera with a millimeter-scale streak plate length and a sub-millimeter plate separation. In addition to minimizing temporal smear caused by a finite electron energy bandwidth, the compact design of the device allows a larger electric field to exist between the streak plates in comparison to centimeter-scale streak cameras, leading to a significant increase in sensitivity [78].

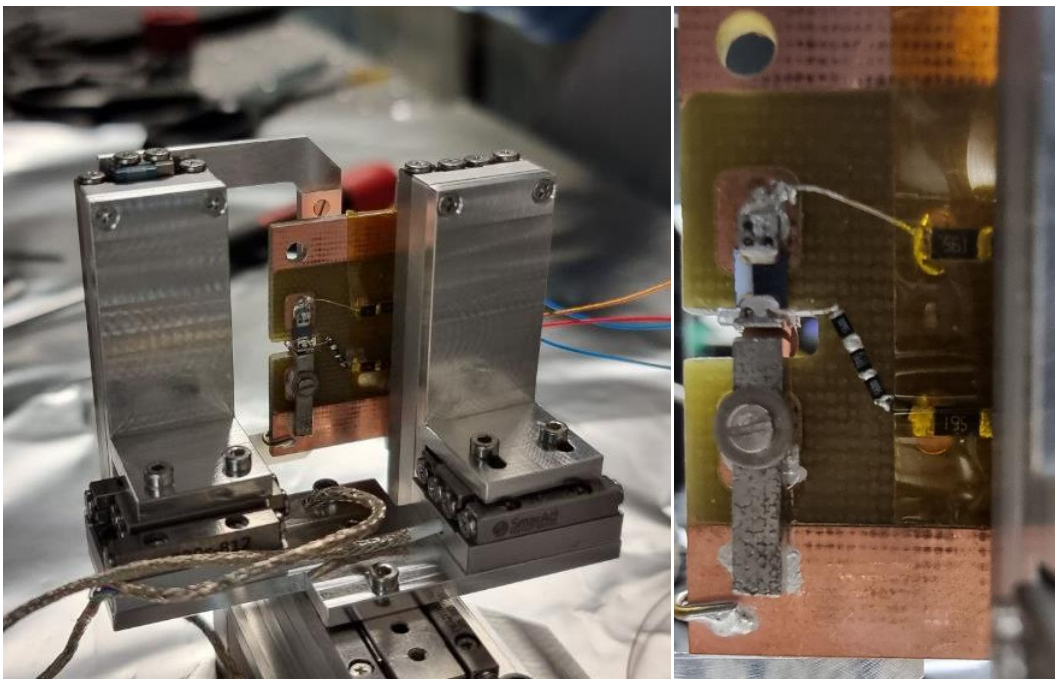

Figure 7.22: A streak camera featuring a gallium arsenide photoconductive semiconductor switch (GaAs PCSS) for sub-100 fs resolution electron bunch profiling and arrival time jitter measurement [78].

7.4.3 Faraday cup

A detailed discussion of the Faraday cup, which is used to measure the charge of an electron beam, was included in Chapter 6. In order to utilize this Faraday cup in the UED experiment, since it is placed before the MCP detector (Figure 7.17), a beam blocker has been integrated at the end of the previous design (Figure 7.23), which blocks the main photoemission beam, improving the contrast of the diffracted beam on the MCP.

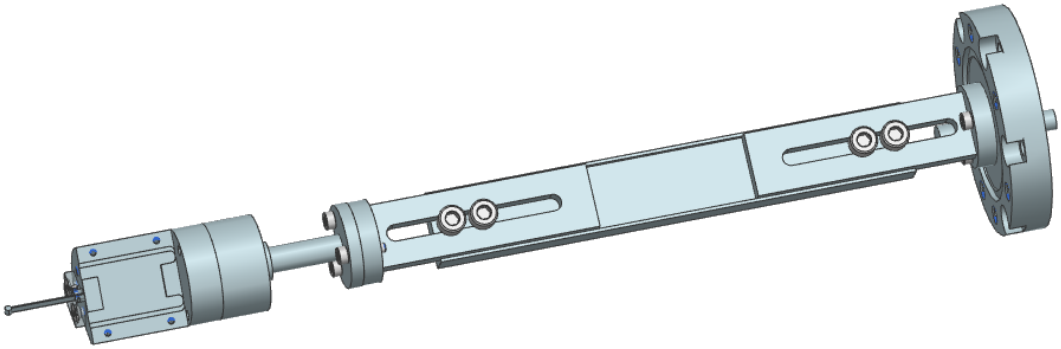

Figure 7.23: Faraday cup equipped with a beam blocker.

7.4.4 MCP

Considering the high quantum efficiency of the MCP detector coupled 1:1 with the CCD camera, it appears to be appropriate to detect both the photo-emitted electrons and the diffracted electron beam. The MCP model BOS-40-6, manufactured by Beam Imaging System, features two microchannel screens with a 40mm diameter active area, a P-43 phosphor screen assembly, and MHV high voltage vacuum feedthroughs, housed in a 6-inch conflat flange with glass viewport.

This MCP is located at the end of the diagnostic chamber, and a home built MCP protection box is also integrated to it, as shown in Figure 7.24. MCP input is divided 50:50 by two 10MΩ resistors, with a 2MΩ in series as protection, so that both MCPs have a more balanced voltage with some overcurrent protection. Phosphor plate is also coupled to the power supply in series with a 20MΩ. By providing ground to the MCP front as well, it is possible to apply a different bias to the MCP front (for example, a slight negative bias to reject photo electron background).

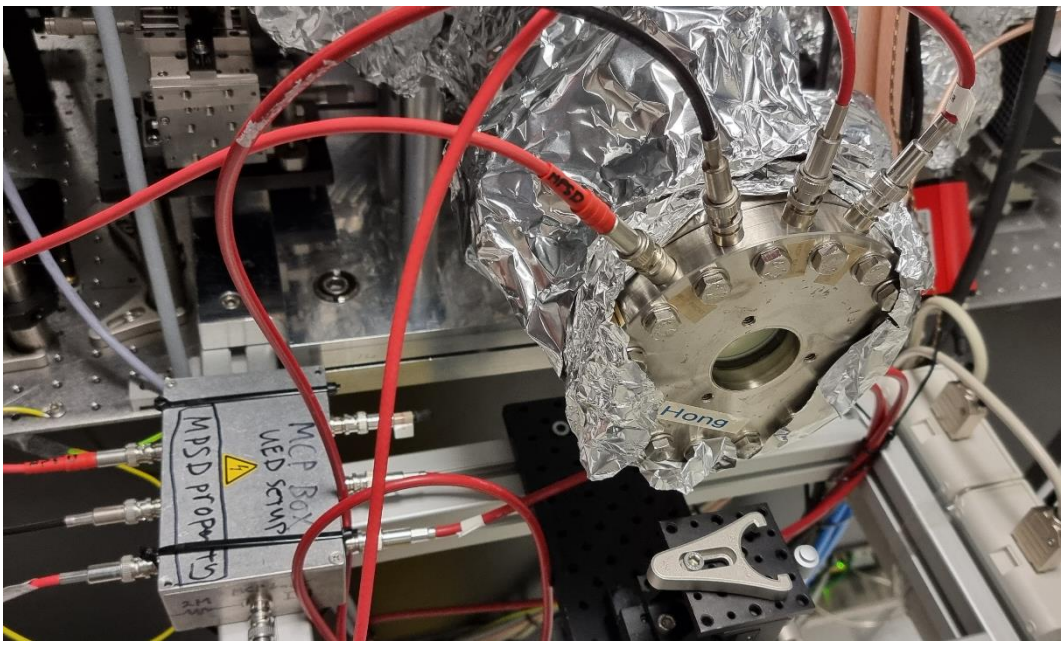

Figure 7.24: A MCP detector with a protective box is positioned at the end of the diagnostic chamber.

7.4.5 Energy spectrometer

To measure the energy and spread energy of electrons resulting from photoemission, we need an energy spectrometer, which is usually accomplished by deflecting electrons through a magnetic field. Considering the fact that we are in the initial phase of characterizing the RF gun's performance and since the RF gun has not yet been precisely synchronized with the laser, the energy of the electron bunch varies in different RF phases, so it is the best to design a spectrometer that can detect the electron bunch energy in a single shot and over a broad range.

A broadband single-shot electron spectrometer with a large momentum acceptance and sufficient resolution has been developed for this RF gun, as shown in Figure 7.25 and Figure 7.26. This energy spectrometer uses a compact tunable dipole magnet, and the specific design of the poleshoes is such that electron bunches within 40-180 keV are focused onto a 4cm long image plane where the scintillator is directly mounted to increase the energy resolution.

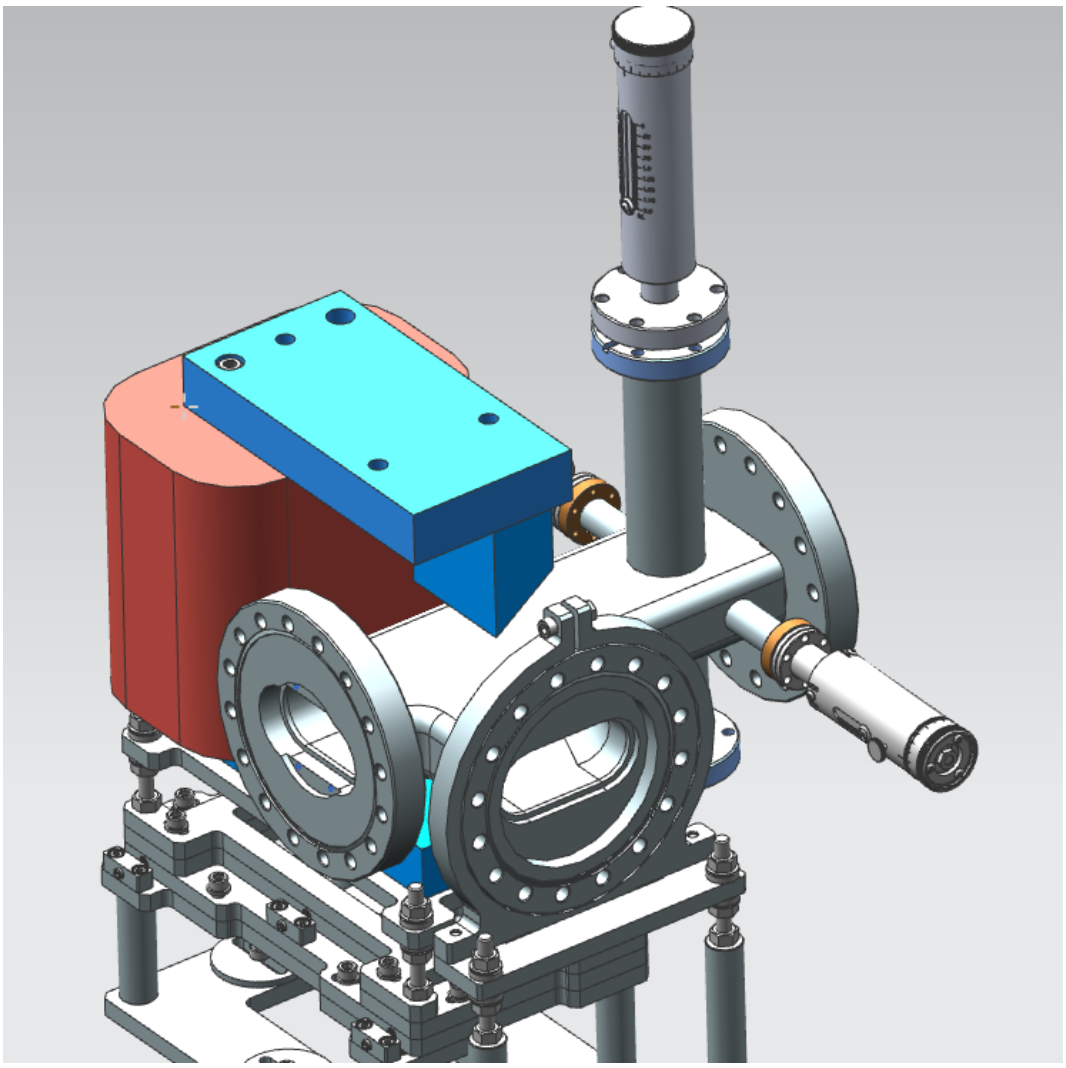

Figure 7.25: Electron energy spectrometer of the RF gun

A simulation of the electrons' trajectory through the magnetic field demonstrated that the dispersion function on the image plane is linear and proportional to the electrons' energy, which greatly simplifies the calibration of this energy detector. Since the electrons are focused on the scintillator plane and their collision is close to perpendicular, it will result in a high light yield and resolution.

As a result of the slit system, the amount of charge entering the spectrometer is controlled. Slit width affects resolution; the narrower the slit, the higher the resolution. A narrower slit, however, reduces the strength of the signal as well. These two factors must be balanced when selecting a slit size. Figure 7.27 illustrates the resolution calculation for a variety of electron energies. Using the slit system at

the entrance of the spectrometer, 0.45% relative resolution ($\Delta E/E$) can be achieved. The slit blades are made of tungsten and have a thickness greater than the energy range of the most energetic electrons. For electron detection, a MCP equipped with a P-43 phosphor screen and a CCD camera with 1:1 imaging will be employed.

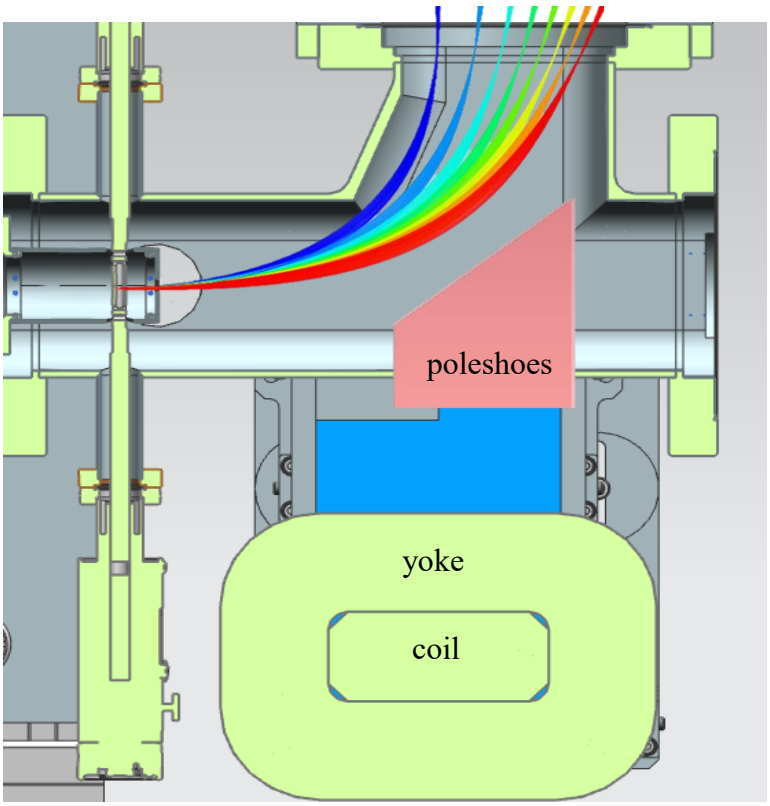

Figure 7.26: A sectional view of the electron energy spectrometer, showing the trajectory of the electrons with energies ranging from 40 to 180 keV through the magnetic field of the dipole magnet.

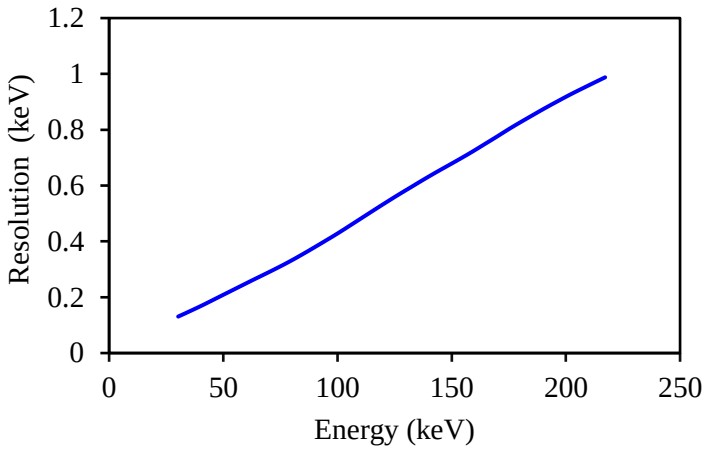

Figure 7.27: Resolution calculation for a variety of electron energies on the image plane, using a slit system at the entrance of the spectrometer.

7.5 Photoemission Experiment

After aligning the UV beam on the pin-cathode, we are now interested in investigating the production of photoemission. This can be achieved by conditioning the RF gun, synchronizing the RF pulse with the laser beam, and then shining the UV beam onto the pin-cathode. The photo-emitted electrons are then detected by the downstream MCP.

In light of knowledge gained during the previous tests discussed in chapter 6, the preparation of the RF gun was done successfully. Following the bake-out of the RF gun in-situ for 3 days at a temperature of 150 ºC (Figure 7.28), the base pressure reached 10^{-9} mbar. After this, the RF gun was subjected to RF conditioning at 10 kW RF peak power with a 50 Hz repetition rate and 180 A solenoid current for several days in order to eliminate multipacting and reduce the amount of dark charge to 200 fC. Figure 7.29 shows the amount of probe power (P_{21}) and reflected power (P_{11}) stabilized in the RF gun after conditioning, as well as the dark charge on the MCP detector.

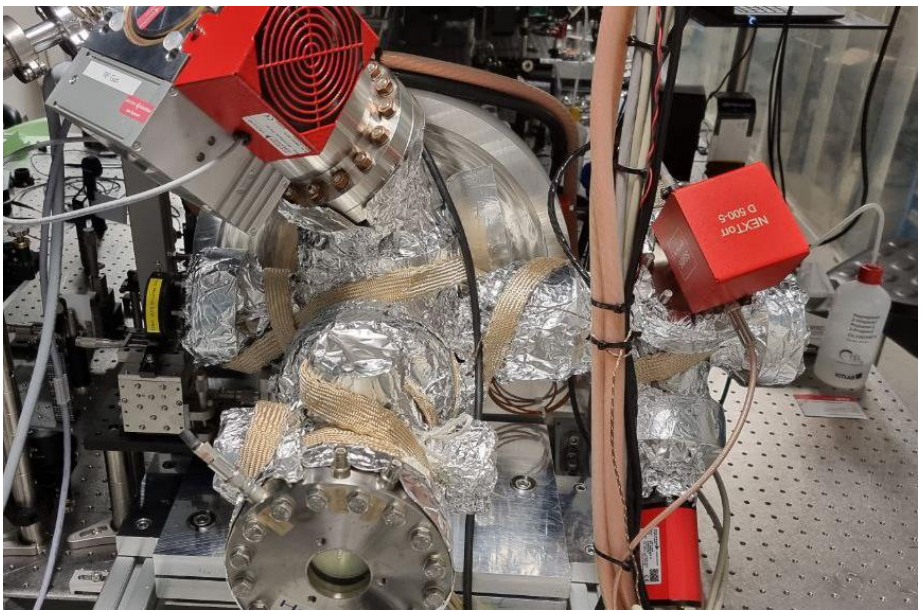

Figure 7.28: Bake-out of the RF gun in-situ for 3 days at a temperature of 150 ºC

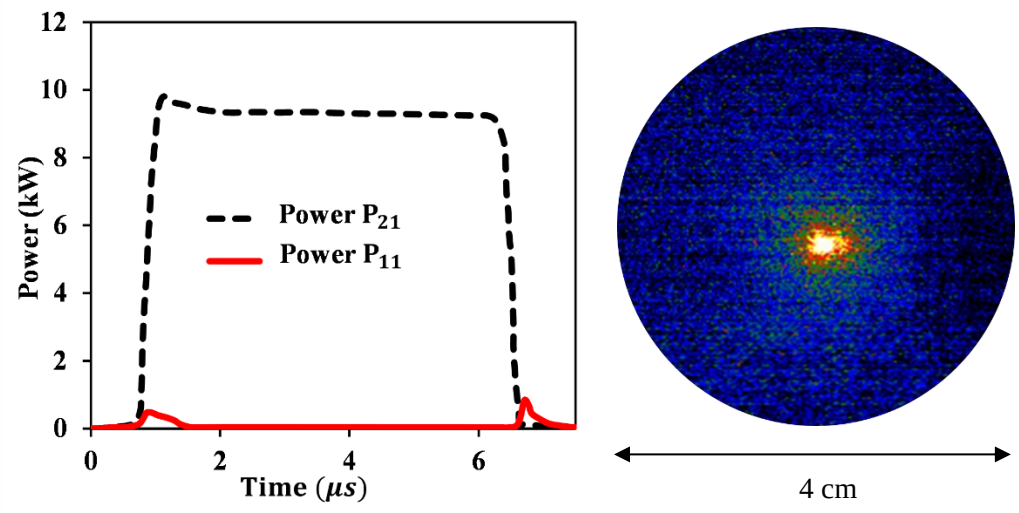

Figure 7.29: The probe power (P_{21}) and reflected power (P_{11}) stabilized in the RF gun after conditioning, and the dark charge on the MCP detector.

Synchronizing the laser to RF pulse is the most challenging aspect of this experiment. The synchronization scheme relies on the proven MicroTCA technology provided MSK, DESY, and a low noise Rohde&Schwarz RF signal generator combined with a Balanced Optical-Microwave Phase Detector (BOMPD) from Cycle GmbH.

A typical synchronization procedure in REGAE, FLASH, and XFEL uses the RF signal generator as a master clock for trigging the laser oscillator equipped with an adjustable cavity. Nevertheless, due to the non-adjustability of the laser oscillator that is currently being used, the oscillator signal must be considered as the master clock. To monitor RF-laser synchronization, we will use the BOMPD diagnostic device that compares a 3GHz RF signal with an 80MHz pulse train through electro-optic elements and outputs a voltage proportional to the phase difference. The acquired BOMPD from Cycle GmbH will operate at a frequency of 3 GHz +/- 5 kHz.

For this purpose, the RF gun cavity should be tuned at 3.000 GHz. According to section 4.1, this design of the cavity is capable of resonating at a wide range of frequencies by varying the gap between the anode and cathode parts (D). We measured the resonance frequency inside the cavity and the corresponding quality factor with respect to different gaps, as shown in Figure 7.30. Thus, frequencies between 2.93 and 3.1 are capable of resonating in the cavity, although the value of the quality factor determines which range will be worthwhile.

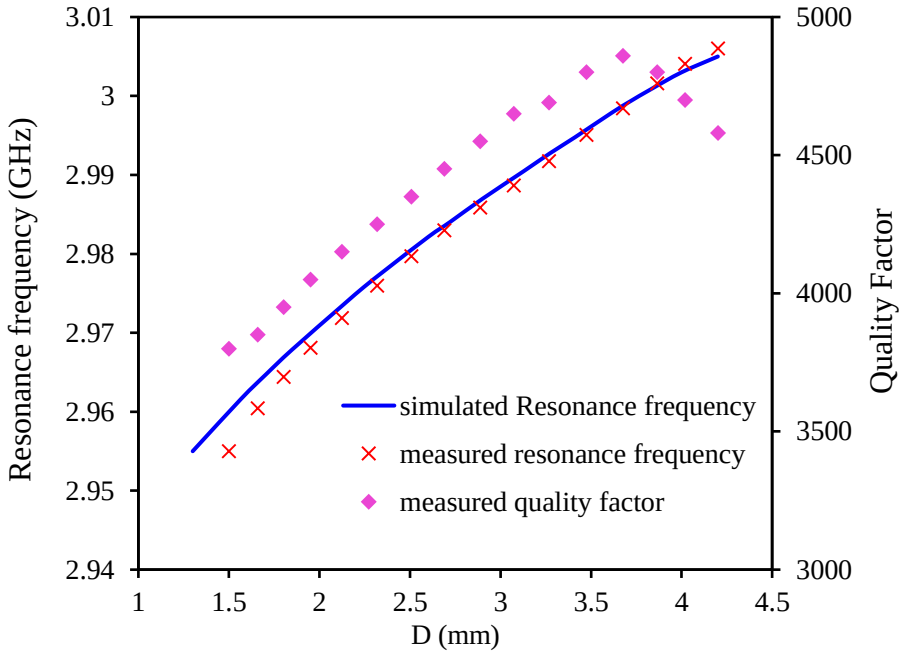

Figure 7.30: Measured resonance frequency inside the cavity and the corresponding quality factor with respect to different gaps

To make progress with synchronization, it is necessary to overlap the RF amplifier burst signal with the SDG signal for amplified laser pulses. We connect both signals to the oscilloscope, ramp up the LLRF system as usual, and set the R&S signal generator to external reference with the measured Vitara repetition rate (80.02265 MHz), then set the RF delay on the LLRF control panel so that it looks as shown in Figure 7.31.

Figure 7.31: Overlaping the RF amplifier burst signal (pink) with the SDG signal for amplified laser pulses (blue) on a scope.

Following the UV beam irradiation on the pin-cathode, it was observed that the photo-emitted electrons were flashing continually on the MCP. Figure 7.32 shows the dark charge electrons (in the center of the MCP) as well as the photo-emitted electrons, whose position can be easily adjusted by shifting the solenoid. However, precise synchronization is not achieved since there is a huge shot to shot variation in the electron beam shape and position on the screen.

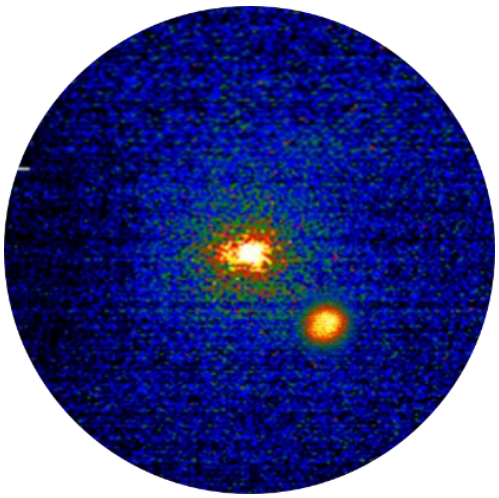

Figure 7.32: Dark charge and photoelectrons on MCP

Chapter 8

Conclusion

S-band RF guns are highly developed to produce relativistic electron bunches with low emittance, which are typically driven by klystrons. Therefore, they are prohibitively expensive and require large-scale infrastructure, making them unaffordable for small and university-scale laboratories. Here, we present an intermediate solution between DC-guns and RF-guns that is still low-cost and requires a minimal level of infrastructure, but significantly increases electron energies over what is typically achieved with DC guns: a compact S-band gun powered by a low average power solid-state amplifier that employs field enhancement in a pin-shaped photocathode to increase field strength, electron energy, and thus beam quality. A prototype of a normal-conducting compact gun designed to achieve 180 keV with a single power supply has been constructed and is currently being conditioned and characterized.

An innovative design of the compact RF gun with 2.998 GHz resonance frequency is presented in Chapter 2, along with implementation of a pin-shaped photocathode with a flat tip of 0.8 mm, in order to achieve a strong increase in RF field strength near the cathode. This reduces the device's cost and complexity as well as significantly reducing the power requirement. Chapter 3 discusses the characterization of the first prototype of the RF gun. Although sparks occurred

inside the RF gun at high RF powers, and the coupling system was not completely stable, the experiments provided us with valuable experiences in the coupling, conditioning, dark charge, and multipacting, which can be used in the design and experiment of the second iteration.

For the purpose of preventing sparks and achieving more effective RF pulse transmission, we have developed a simpler design, and detailed microwave simulations have been conducted in order to prevent RF leakage and to design an optimal coupling. Due to the potential for the RF gun to serve as a photoinjector into a THz-driven booster in AXSIS, beam dynamic simulations are performed to determine the optimal conditions for the operation of the RF gun as well as the influence of laser beam properties on the quality of the electron beam. At a power of 10 kW, optimal conditions are achieved with an RF phase of 13º, a solenoid magnetic field of 0.18 T, a rms UV duration pulse of 0.85, and rms UV spot size of 49 μm. As a result, the average energy of electrons at the point of injection will be 180 keV with a relative energy spread of 0.8%, the transverse emittance will be equal to 98 μm.mrad, along with a rms electron bunch length of 14 μm, and rms transverse bunch size of 21 μm.

An initial challenge during operation was multipacting, which is further exacerbated by the solenoid magnetic field. Through a better understanding of this phenomenon using simulations and development of a careful conditioning protocol, elimination of multipacting was achieved. In addition to surface cleaning in a variety of ways, in-situ bake-out, and the dose effect on the surface caused by electron bombardment, in chapter 5, I investigated the impact of applying DC voltage to this cavity, which reduces the generation of secondary electrons and suppresses multipacting.

In Chapter 6, investigations on the second prototype RF gun demonstrate that the coupling system works very efficiently, with a loaded quality factor of 5800 and a reflection (S_{11}) reaching below -50 dB at 2.998 GHz frequency resonance. During the RF injection, no sparking was observed even at high powers, the frequency response of the cavity appears very stable, and no electromagnetic field leakage was detected to other parts of the RF gun. In response to four days of bakeout at 150°C, a base pressure of 5E-10 mbar was achieved, and no multipacting was observed during the ramping of the RF power from 0 to 10 kW in the absence of a solenoid, as predicted from simulations. It can be concluded that there is a good correlation between the results of the experiment and those of the multipacting simulation.

In chapter 7, electron beam dynamics of the RF gun for UED application were described in detail. Simulations predict that very bright electron bunches with an rms duration of 10 fs, a radius of 135 μm, and a spatial emittance of 0.1 mm-mrad are achievable for a bunch charge of 10 fC. This chapter also describes the development of an appropriate UV beam with a half-circle transverse profile with a diameter of 30 microns, along with stretching in the required range of picoseconds, UED setup along with diagnostic tools including a MCP imaging detector, Faraday cup, and a streak camera featuring a GaAs PCSS for sub-100 fs resolution electron bunch profiling.

Upon aligning the UV beam on the cathode and injecting 10 kW of RF into the cavity, it was observed that the electrons generated by photoemission were focused on the MCP about 60 cm away from the cathode. Following the completion of the conditioning phase and successful synchronization as described in Chapter 7, the next round of testing will target characterization of the energy, energy spread, and emission of the beam. A favorable beam characterization will then lead to the development of a dedicated UED instrument based on this platform.

For the purpose of increasing the energy output of the electron bunch, cryogenic temperatures could be considered, which appear to be fully functional in the compact design of this RF gun. In addition, elevating the resonance frequency of this compact gun towards the X-band, allows for a greater gradient of electric field inside a smaller cavity.

References

[1] R. L. Sheffield, “Photocathode rf guns,” in *AIP Conference Proceedings*, American Institute of Physics, 1989, pp. 1500–1531.

[2] K. Batchelor *et al.*, “Performance of the Brookhaven photocathode RF gun,” *Nucl Instrum Methods Phys Res A*, vol. 318, no. 1–3, pp. 372–376, 1992.

[3] S. Humphries, *Principles of charged particle acceleration*. Courier Corporation, 2013.

[4] F. X. Kaertner *et al.*, “AXSIS: Exploring the frontiers in attosecond X-ray science, imaging and spectroscopy,” *Nucl Instrum Methods Phys Res A*, vol. 829, pp. 24–29, 2016.

[5] N. H. Matlis *et al.*, “Progress on Development of AXSIS: A Femtosecond THz-Driven MeV Accelerator and keV X-Ray Source,” 2022.

[6] R. J. D. Miller, “Femtosecond crystallography with ultrabright electrons and x-rays: Capturing chemistry in action,” *Science (1979)*, vol. 343, no. 6175, pp. 1108–1116, 2014.

[7] W. E. King *et al.*, “Ultrafast electron microscopy in materials science, biology, and chemistry,” *J Appl Phys*, vol. 97, no. 11, p. 8, 2005.

[8] P. Zhu *et al.*, “Femtosecond time-resolved MeV electron diffraction,” *New J Phys*, vol. 17, no. 6, p. 063004, 2015.

[9] H. Daoud, K. Floettmann, and R. J. Dwayne Miller, “Compression of high-density 0.16 pC electron bunches through high field gradients for ultrafast single shot electron diffraction: The Compact RF Gun,” *Structural Dynamics*, vol. 4, no. 4, p. 044016, 2017.

[10] K.-J. Kim, “Emittance growth in laser-driven RF electron guns,” in *High gain, high power free electron laser: physics and application to TeV particle acceleration*, 1989.

[11] K. Flottmann, S. Lidia, and P. Piot, “Recent improvements to the ASTRA particle tracking code,” Lawrence Berkeley National Lab.(LBNL), Berkeley, CA (United States), 2003.

[12] B. E. Carlsten, “New photoelectric injector design for the Los Alamos National Laboratory XUV FEL accelerator,” *Nucl Instrum Methods Phys Res A*, vol. 285, no. 1–2, pp. 313–319, 1989.

[13] M. Otevrel *et al.*, “Report on Gun conditioning activities at PITZ in 2013,” *Proc. IPAC*, vol. 14, pp. 2962–2964, 2014.

[14] V. Ayvazyan *et al.*, “Generation of GW radiation pulses from a VUV free-electron laser operating in the femtosecond regime,” *Phys Rev Lett*, vol. 88, no. 10, p. 104802, 2002.

[15] L. H. Yu *et al.*, “First ultraviolet high-gain harmonic-generation free-electron laser,” *Phys Rev Lett*, vol. 91, no. 7, p. 074801, 2003.

[16] M. Krassilnikov, R. Cee, and T. Weiland, “Impact of the RF-gun power coupler on beam dynamics,” in *EPAC*, 2002, p. 1640.

[17] J. D. Jackson, “Classical electrodynamics.” American Association of Physics Teachers, 1999.

[18] D. Hall and A. Dicker, “A review of the equivalent circuit model of RF accelerating cavities in the context of an analysis of the 1.3 and 3.9 GHz cavities at FLASH,” 2021.

[19] H. Wiedemann and H. Wiedemann, *Synchrotron radiation*. Springer, 2003.

[20] T. P. Wangler, “Introduction to linear accelerators,” 1993.

[21] M. Steer, *Microwave and RF design*. NC State University, 2019.

[22] H. Daoud, K. Floettmann, and R. J. Dwayne Miller, “Compression of high-density 0.16 pC electron bunches through high field gradients for ultrafast

single shot electron diffraction: The Compact RF Gun," *Structural Dynamics*, vol. 4, no. 4, p. 044016, 2017.

[23] "German patent application DE 10 2016 105 443.7. 23. March 2016.".

[24] B. E. Carlsten, "New photoelectric injector design for the Los Alamos National Laboratory XUV FEL accelerator," *Nucl Instrum Methods Phys Res A*, vol. 285, no. 1–2, pp. 313–319, 1989.

[25] M. Reiser, *Theory and design of charged particle beams*. John Wiley & Sons, 2008.

[26] V. Kumar, "Understanding the focusing of charged particle beams in a solenoid magnetic field," *Am J Phys*, vol. 77, no. 8, pp. 737–741, 2009.

[27] D. M. Pozar, "Microwave Engineering Book, JohnWiley & Sons." Inc, 2012.

[28] W. Xu, S. Belomestnykh, I. Ben-Zvi, and H. Hahn, "Improvement of the Q-factor measurement in RF cavities," Brookhaven National Lab.(BNL), Upton, NY (United States), 2012.

[29] P. J. Petersan and S. M. Anlage, "Measurement of resonant frequency and quality factor of microwave resonators: Comparison of methods," *J Appl Phys*, vol. 84, no. 6, pp. 3392–3402, 1998.

[30] D. H. DOWELL, "NORMAL CONDUCTING RF INJECTORS".

[31] R. Kersevan and J.-L. Pons, "Introduction to MOLFLOW+: New graphical processing unit-based Monte Carlo code for simulating molecular flows and for calculating angular coefficients in the compute unified device architecture environment," *Journal of Vacuum Science & Technology A: Vacuum, Surfaces, and Films*, vol. 27, no. 4, pp. 1017–1023, 2009.

[32] D. Reschke *et al.*, "Dry-Ice cleaning: The most effective cleaning process for srf cavities?," *SRF2007, Beijing, China*, 2007.

[33] E. U. Condon, "Forced oscillations in cavity resonators," *J Appl Phys*, vol. 12, no. 2, pp. 129–132, 1941.

[34] G. Romanov, "Simulation of multipacting in HINS accelerating structures with CST particle studio," *LINAC08, Victoria, BC, Canada*, 2008.

[35] S. Shee and S. Dwivedi, “Parametric Analysis of Reltron Modulation Cavity and Q-factor Calculation from S-parameter,” in *2018 IEEE MTT-S International Microwave and RF Conference (IMaRC)*, IEEE, 2018, pp. 1–4.

[36] Y. Liu *et al.*, “Design of a V-band high-power sheet-beam coupled-cavity traveling-wave tube,” *Progress In Electromagnetics Research*, vol. 123, pp. 31–45, 2012.

[37] N. Plambecka, “Vacuum System Related Simulations for PETRA IV Using Numerical and Monte-Carlo Methods,” Vakuumsysteme, 2019.

[38] H. C. Hseuh, “PRESSURE LIMITS IN ACCELERATOR VACUUM SYSTEM,” Brookhaven National Lab.(BNL), Upton, NY (United States), 1983.

[39] A. Berman, “Water vapor in vacuum systems,” *Vacuum*, vol. 47, no. 4, pp. 327–332, 1996.

[40] D. Edwards Jr, “An upper bound to the outgassing rate of metal surfaces,” *Journal of Vacuum Science and Technology*, vol. 14, no. 4, pp. 1030–1032, 1977.

[41] “HiPace® 300 with TC 400, DN 100 CF-F.” [Online]. Available: www.pfeiffer-vacuum.com

[42] L. Schulz, “private communication,” May 2020.

[43] I. Chun, B. Cho, and S. Chung, “Outgassing rate characteristic of a stainless-steel extreme high vacuum system,” *Journal of Vacuum Science & Technology A: Vacuum, Surfaces, and Films*, vol. 14, no. 4, pp. 2636–2640, 1996.

[44] T. Kroh *et al.*, “Single-Sided Pumped Compact Terahertz Driven Booster Accelerator,” in *13th International Particle Accelerator Conference (IPAC’22), Bangkok, Thailand, 12-17 June 2022*, JACOW Publishing, Geneva, Switzerland, 2022, pp. 625–627.

[45] K.-J. Kim, “RF and space-charge effects in laser-driven RF electron guns,” *Nucl Instrum Methods Phys Res A*, vol. 275, no. 2, pp. 201–218, 1989.

[46] M. Fakhari, “Internal documentation for the UFOX project on Confluence,” 2020.

[47] D. A. Edwards and M. J. Syphers, *An introduction to the physics of high energy accelerators*. John Wiley & Sons, 2008.

[48] J. Maxson, P. Musumeci, L. Cultrera, S. Karkare, and H. Padmore, “Ultrafast laser pulse heating of metallic photocathodes and its contribution to intrinsic emittance,” *Nucl Instrum Methods Phys Res A*, vol. 865, pp. 99–104, 2017.

[49] K.-J. Kim and Y.-J. Chen, “RF and space-charge induced emittances in laser-driven RF guns,” 1988.

[50] X. J. Zhou *et al.*, “Space charge effect and mirror charge effect in photoemission spectroscopy,” *J Electron Spectros Relat Phenomena*, vol. 142, no. 1, pp. 27–38, 2005.

[51] M. Ferrario, K. Flöttmann, B. Grigoryan, T. Limberg, and P. Piot, “Conceptual design of the XFEL photoinjector,” *TESLA FEL Report*, vol. 3, 2001.

[52] K. Flöttmann and H. Delsim-Hashemi, “private communication,” 2022.

[53] R. F. Parodi, “Multipacting,” *arXiv preprint arXiv:1112.2176*, 2011.

[54] Y. Li and W. Cui, “Prediction of multipacting breakdown in microwave components using an electromagnetic-based Particle-In-Cell simulator,” in *2011 International Conference on Electronics, Communications and Control (ICECC)*, IEEE, 2011, pp. 4431–4433.

[55] V. Baglin *et al.*, “The secondary electron yield of technical materials and its variation with surface treatments,” 2000.

[56] M. A. Furman and M. T. F. Pivi, “Probabilistic model for the simulation of secondary electron emission,” *Physical review special topics-accelerators and beams*, vol. 5, no. 12, p. 124404, 2002.

[57] A. Septier, “Surface studies and electron emissions,” in *Workshop on RF superconductivity*, 1980.

[58] R. F. Parodi, “Multipacting,” *arXiv preprint arXiv:1112.2176*, 2011.

[59] I. Bojko, N. Hilleret, and C. Scheuerlein, “Influence of air exposures and thermal treatments on the secondary electron yield of copper,” *Journal of Vacuum Science & Technology A: Vacuum, Surfaces, and Films*, vol. 18, no. 3, pp. 972–979, 2000.

[60] A. Brinkmann and J. Ziegler, “Dry-ice cleaning of RF-structures at DESY,” in *28th Linear Accelerator Conference*, HF-Technik Supraleitung, 2016.

[61] M. Lavarec, P. Bocquet, and A. Septier, “Variation of the secondary emission coefficient of real surfaces under the effect of primary electronic bombardment,” *CR Acad. Sci. Paris, B*, vol. 288, no. SLAC-TRANS-0201, pp. 77–80, 1982.

[62] V. Baglin *et al.*, “The secondary electron yield of technical materials and its variation with surface treatments,” 2000.

[63] N. Hilleret, E. Mercier, V. Baglin, C. Scheuerlein, and B. Henrist, “Ingredients for the Understanding and the Simulation of Multipacting,” SIS-2001-053, 2000.

[64] B. Henrist, C. Scheuerlein, N. Hilleret, M. Taborelli, and G. Vorlaufer, “The variation of the secondary electron yield and of the desorption yield of copper under electron bombardment: origin and impact on the conditioning of the LHC,” 2002.

[65] O. Bruning *et al.*, “Electron cloud and beam scrubbing in the LHC,” in *Proceedings of the 1999 Particle Accelerator Conference (Cat. No. 99CH36366)*, IEEE, 1999, pp. 2629–2631.

[66] D. J. Santeler, “Estimating the gas partial pressure due to diffusive outgassing,” *Journal of Vacuum Science & Technology A: Vacuum, Surfaces, and Films*, vol. 10, no. 4, pp. 1879–1883, 1992.

[67] R. J. D. Miller, “Femtosecond crystallography with ultrabright electrons and x-rays: Capturing chemistry in action,” *Science (1979)*, vol. 343, no. 6175, pp. 1108–1116, 2014.

[68] W. E. King *et al.*, “Ultrafast electron microscopy in materials science, biology, and chemistry,” *J Appl Phys*, vol. 97, no. 11, p. 8, 2005.

[69] Z. Tao, H. Zhang, P. M. Duxbury, M. Berz, and C.-Y. Ruan, "Space charge effects in ultrafast electron diffraction and imaging," *J Appl Phys*, vol. 111, no. 4, p. 044316, 2012.

[70] S. Manz *et al.*, "Mapping atomic motions with ultrabright electrons: towards fundamental limits in space-time resolution," *Faraday Discuss*, vol. 177, pp. 467–491, 2015.

[71] T. Van Oudheusden, E. F. De Jong, S. B. Van der Geer, W. t Root, O. J. Luiten, and B. J. Siwick, "Electron source concept for single-shot sub-100 fs electron diffraction in the 100 keV range," *J Appl Phys*, vol. 102, no. 9, 2007.

[72] R. P. Chatelain, V. R. Morrison, C. Godbout, and B. J. Siwick, "Ultrafast electron diffraction with radio-frequency compressed electron pulses," *Appl Phys Lett*, vol. 101, no. 8, p. 081901, 2012.

[73] O. J. Luiten, S. B. Van der Geer, M. J. De Loos, F. B. Kiewiet, and M. J. Van Der Wiel, "How to realize uniform three-dimensional ellipsoidal electron bunches," *Phys Rev Lett*, vol. 93, no. 9, p. 094802, 2004.

[74] M. Ferrario *et al.*, "Direct measurement of the double emittance minimum in the beam dynamics of the sparc high-brightness photoinjector," *Phys Rev Lett*, vol. 99, no. 23, p. 234801, 2007.

[75] M. Krasilnikov, J. Bähr, M. Hänel, F. Stephan, and I. Will, "Experimental optimization of the cathode laser temporal profile," in *Proceedings of DIPAC*, Citeseer, 2007.

[76] R. Lemons *et al.*, "Noncolinear Synthesis of Picosecond Flat-Top Laser Pulses to Increase Electron Photoinjector Brightness," Thomas Jefferson National Accelerator Facility (TJNAF), Newport News, VA …, 2022.

[77] C. Vicario *et al.*, "Laser temporal pulse shaping experiment for SPARC photoinjector," 2004.

[78] G. H. Kassier *et al.*, "A compact streak camera for 150 fs time resolved measurement of bright pulses in ultrafast electron diffraction," *Review of Scientific Instruments*, vol. 81, no. 10, p. 105103, 2010.